



Università degli Studi di Messina
Dipartimento di Scienze Matematiche, Informatiche, Fisiche e Scienze della Terra
(MIFT)
Dottorato di Ricerca in Fisica
XXXI CICLO

**Biocompatible Nanoparticles: Synthesis,
Analysis and Applications
in Biological and Medical fields**

PhD Student:
Nancy RESTUCCIA

PhD Tutor:
Chiar.mo Prof. Lorenzo TORRISI

Referee:
Prof. Mackova Anna
Prof. Ronca Sara

Settore Scientifico Disciplinare FIS/01
2017-2018

REFEREES:

- Professor Mackova Anna
Nuclear Physics Institute (ASCR), 25068 Rez, Czech Republic
Mail: mackova@ujf.cas.cz
- Professor Ronca Sara
Loughborough University, Department of Materials
Leicestershire, UK, LE11 3TU
Mail: S.Ronca@lboro.ac.uk

INTRODUCTION

This Thesis reports the work I have done at the Department of Mathematics, Informatics, Physics and Earth Sciences (MIFT) of the University of Messina under the supervision of Prof. Lorenzo Torrisi, from 2015 to 2018. The study carried out in this period was focused on the use of metallic nanoparticles in the medical and biological fields.

In recent years, technological development has allowed us to prepare, manipulate and characterize more nano-sized materials. The nano prefix, which derives from the Greek nanos and means ‘dwarf’, describes materials, technologies or properties with dimensions on the nanoscale (10^{-9} m). Nanotechnology is an interdisciplinary field that involves the study and application of natural sciences and engineering to develop tools at the nanoscale. The nanotechnology applied to life sciences has led to improve knowledge about cellular and molecular processes and factors that cause a variety of diseases. The understanding of novel disease pathways has acted as a catalyst for the development of nanomedicine. Advances in this field promise to increase the accuracy and specificity of medical diagnoses and treatments of diseases. Metallic nanoparticles (NP), based on Ti, Au, Ag, Bi and others, embedded in an insulating medium behave like ionizing radiation absorbing centers, being able to show certain absorption resonances bands at specific wavelengths, thank to the Surface Plasmon Resonance (SPR) absorption effect [1]. Their size distribution in a fluid changes the electronic and mass density and the material equivalent atomic number. In the present study the behaviour of metallic nanoparticles in therapy and in diagnostics was determined experimentally, in particular by calculating the ratio of the delivered dose to a given depth and the delivered dose to the surface in various media (water, adipose tissue and compact bone) in presence or not of the nanoparticles. The choice of gold, as starting material to prepare nanoparticles, is not accidental. In fact, gold is stable, not oxidable and biocompatible for humans and, more in general, also for other living beings. In the

light of these results, the medicine demonstrates a particular interest to the gold nanoparticles for different aspects concerning prosthesis, interface adhesion, high Z contrast medium for X-ray images.

The anticancer potential of the gold nanoparticles is generated by the different advantageous physico-chemical properties. Numerous studies have demonstrated the safety and biocompatibility of gold both in vitro and vivo, suggesting that the gold nanoparticles can be administered safely with minimal inflammatory activation and few local or systemic side effects [2] enhancing the equivalent Z-value of the tissue at significant concentrations.

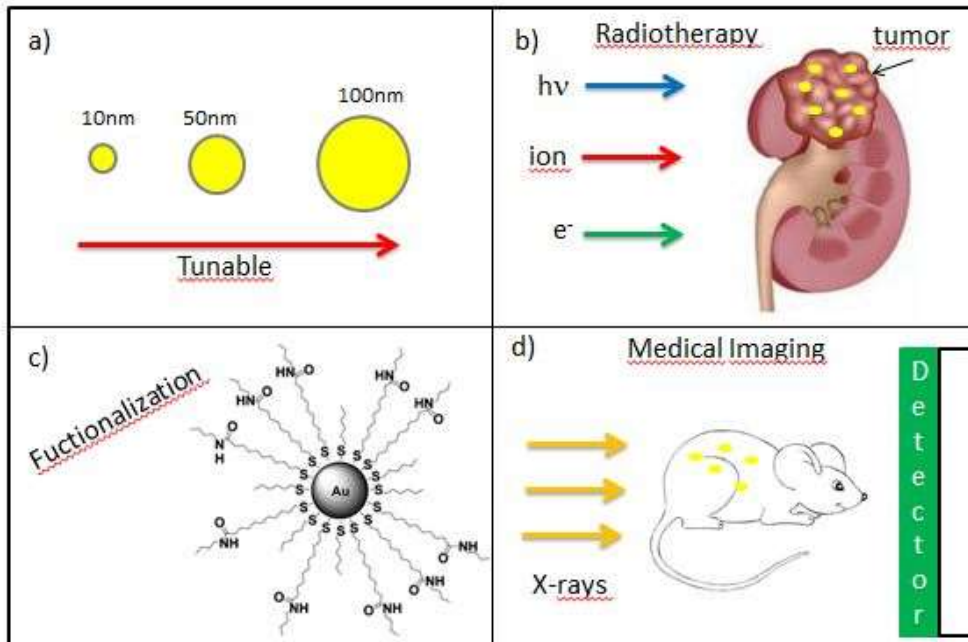


Fig. 1- . Au NPs with various shapes and size (a), bio-functionalized with various biomolecules (c), creates bioconjugates. The subministration can take place in various ways, such as intratumoral injection, intravenously and by means of suitable drugs. The NPs have the ability to enhance radiation therapy of tumors (b), as well as serve as high Z imaging contrast agents (d).

Figure 1 shows Au NPs of various shapes and sizes (a), their functionalization with particular molecules (c) which allows the transfer to the tumor sites via or biological processes or use of drugs by localized injection into the tumor zone.

The so attached metallic NPs to the tumor have the ability to improve radiotherapy and imaging of localized tissues (b, d).

The high atomic number of gold (Au, $Z = 79$) allows a high absorption and enhancement of ionizing radiation, as well as the X-ray attenuation and X-ray characteristic line fluorescence for better imaging applications [3].

The inclusion of metallic nanoparticles in a liquid, at different concentrations, modifies significantly the solution properties, especially in physical terms concerning the surface tension, density, viscosity, thermal and electric conduction, vapour pressure, and other parameters [4].

The wettability of the liquid changes introducing specific nanoparticles and the resulting adhesion of the liquid to a surface may be drastically modified. This aspect is of special interest in Biology and Medicine because it has been demonstrated that the wetting ability determines the protein absorption and the cellular response [5] and that it represents a key parameter for the success of prostheses implantation and functionality in human body [6].

The main goals of this thesis work are three: i) to synthesize various metallic nanoparticles (such as Au, Bi,...) by laser ablation in water; ii) to characterize the so obtained nanoparticles by means of different spectroscopy techniques; iii) to apply them in some interesting biological and medical fields. In particular, the thesis consists of six chapters. The first two chapters are an overview of metallic nanoparticles, their properties, the synthesis methods and the characterization systems. The main chapters are the third, fourth and sixth.

The third shows our obtained results in modifying the materials by adding nanoparticles.

The fourth chapter shows the obtained results by exploiting the nanoparticles (Au, Ag and Bi) in the field of imaging.

Finally, in the last chapter we propose a theoretical study of a clinical case of breast cancer treated with radiotherapy; the behavior of Au nanoparticles in radiotherapy was determined by calculating in particular the ratio between the released dose at the tumor depth and the released dose on surface.

INDEX

INTRODUCTION	I
1. Nanoparticles and Biomaterials	1
1.1. Nanoparticles.....	2
1.2. Surface Plasmon Resonance	4
1.3 Biomaterials	10
1.3.1 <i>Metallic Biomaterials</i>	12
1.3.2 <i>Polymeric Materials</i>	14
1.3.3 <i>Ceramic Biomaterial</i>	17
2. Synthesis and Characterization of Nanoparticles	21
2.1. Synthesis of Nanoparticles.....	22
2.2. Nanofabrication by “Top Down” Methods.	24
2.2.1 <i>Laser Ablation</i>	24
2.2.2 <i>Our set up for Laser Ablation</i>	26
2.2.3 <i>The Laser Ablation: Theoretical background</i>	28
2.2.4 <i>Temperature Dependence</i>	29
2.2.5 <i>Irradiation, Energy, Wavelength and Time Depedence</i>	31
2.2.6 <i>Photochemical effects of Laser</i>	33
2.3. Nanofabrication by “Bottom-Up” Methods	35
2.4. Physical Characterization of Nanoparticles	39
2.5.1 <i>Electron Microscopy: TEM and SEM</i>	40
2.5.2 <i>Optical Spectroscopy (UV-Vis Spectroscopy)</i>	46
2.5.3 <i>X-Ray Diffraction (XRD)</i>	49
2.5.4 <i>Raman Spectroscopy</i>	52
3. Modification of the material using Metallic Nanoparticles	55
3.1. Wettability.....	56
3.2. Wettability of Biological Liquids with Metallic Nanoparticles	59
3.2.1 <i>Used Materials</i>	60

3.2.2	<i>Methods of analysis</i>	60
3.2.3	<i>Results</i>	63
3.3.	Optical and mechanical properties: Static and dynamic characterization of biomedical polyethylene laser welding using biocompatible nano-particles. 72	
3.3.1	<i>Materials</i>	73
3.3.2	<i>Physical Characterization</i>	74
3.3.3	<i>Mechanical Characterization</i>	75
3.3.4	<i>Results</i>	76
3.4.	Gold Nanoparticles produced by Laser Ablation in water and in graphene oxide suspension	81
3.4.1	<i>Experimental set up</i>	82
3.4.2	<i>Results</i>	85
4.	Use of Metallic Nanoparticles for Biological and Medical Diagnostics	95
4.1.	Contrast Agents in X-ray imaging and computed Tomography	96
4.1.1	<i>Contrast agents for CT</i>	97
4.1.2	<i>Gold nanoparticles as x-ray contrast agents</i>	98
4.1.3	<i>Contrast enhancement</i>	100
4.1.4	<i>Design of AuNPs as x-ray contrast agents</i>	102
4.2.	Laser-produced Au nanoparticles as X-ray contrast agents for diagnostic imaging	104
4.2.1	<i>Used Materials</i>	107
4.2.2	<i>Mechanism of X-ray absorption in liquids and tissue</i>	109
4.2.3	<i>X-ray diagnostic enhanced by Au NPs</i>	112
4.3.	Comparison between Au and Ag Nanoparticles generated by laser in liquid as contrast medium.	116
4.3.1	<i>Used Materials</i>	117
4.3.2	<i>Results</i>	118
4.4.	Laser-generated Bismuth Nanoparticles for application in Imaging and Radiotherapy.....	120
4.4.1	<i>Materials</i>	121
4.4.2	<i>Results</i>	124
4.5.	Comparing different types of Nanoparticles as X-ray contrast agents for diagnostics imaging	129

5.	Radioterapy and Thermootherapy	134
5.1.	Radiotherapy	135
5.1.1	<i>Radiation with Photons</i>	137
5.1.2	<i>Radiotherapy with Electrons</i>	138
5.1.3	<i>Protontherapy</i>	139
5.2.	Different Types of radiotherapy	142
5.3.	Radiotherapy Techniques and Criteria	144
5.3.1	<i>Doses given to the Patient</i>	145
5.4.	Radiotherapy enhancement with Gold Nanoparticles	147
5.4.1	<i>Properties of gold nanoparticles</i>	148
5.4.2	<i>Physics of Metal-Enhanced Radiotherapy</i>	150
5.4.3	<i>Therapy using Gold Nanoparticles in mice</i>	151
5.5.	Thermaltherapy (Hyper-Thermia)	154
6.	Theoretical Case Study: Radiotherapy with Gold Nanoparticles of Breast Cancer	158
6.1.	Calculation of the Dose Ratio between the surface and the depth at which the tumor is located.	162
6.1.1	<i>Protons</i>	163
6.1.2	<i>Electrons</i>	167
6.1.3	<i>Photons</i>	171
	CONCLUSIONS	I
	REFERENCES	I

1. Nanoparticles and Biomaterials

1.1. Nanoparticles

In the last three decades nanoparticles have received increasing interest from scientific research. This is due to the dimension-dependent unique properties of nanoparticles, they have often been thought of as a distinct and intermediate state of matter between the individual atoms and the massive material [7].

The properties of the nanoparticles are presented as a consequence of the confinement of the electronic wave function and of an extremely high proportion of the surface of the atoms; both these factors are directly dependent on the nanoparticle size [8]. Indeed the possibility to check the properties, adjusting the nanoparticle size, has been the cause and the subject of so much research. Unlike bulk materials that have constant physical properties indifferent to mass, the nanoparticles offer unique opportunities for control when varying their diameter and they have alterable electronic, magnetic and optical properties. These effects arise because the energy levels for small particles are not continuous, as in bulk, but discrete due to the confinement of the wave function electron. The physical properties of the nanoparticles are therefore determined by their size and by the relatively small physical dimension in which the wave function is confined (Fig. 1.1).

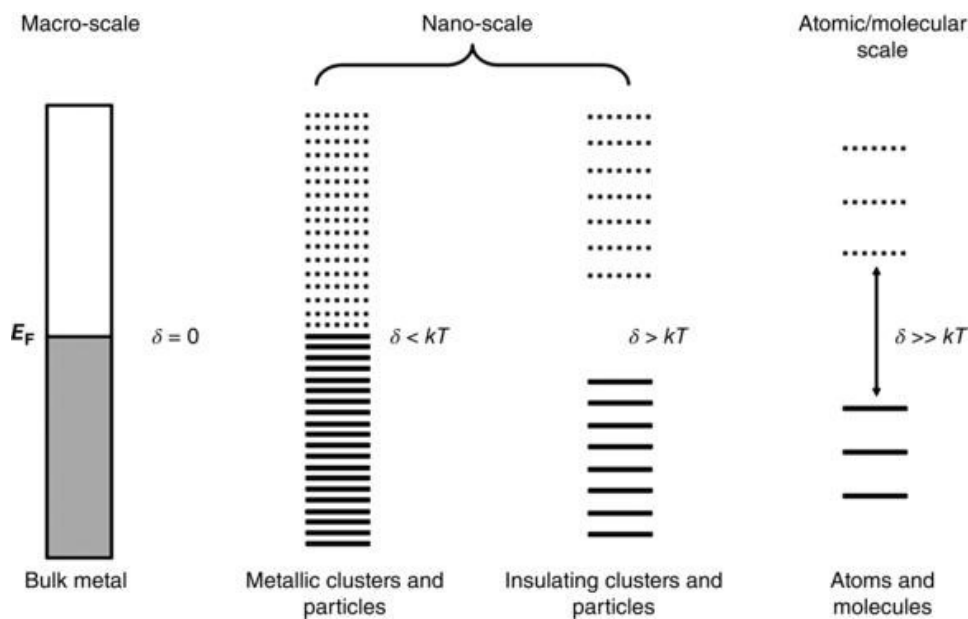


Fig. 1.1- The evolution of the band gap and the density of states as the number of atoms in a system grows (from right to left). E_F is the Fermi energy level of the material and δ is the Kubo gap [9].

The energy level of Fermi (E_F) is the highest level of energy occupied by the system in its ground state (lower energy). The band gap (E_g) of these systems is the energy space between the highest unoccupied and the lowest occupied by the energy states. In these systems, from discrete atoms to bulk materials, the energy ranges are determined by the extent of the overlap between the electronic orbitals of the material. The individual atoms have well-known atomic orbitals. They can be combined into molecules to form molecular orbitals and also extensive band structures, such as metals or semiconductors. The value of E_g is proportional to E_F divided by the number of delocalized electrons in the extended band structure. For a bulk metal, the number of delocalized electrons in the band structure is equal to the number of atoms in the mass of the material. This results in a very low E_g value, and therefore observed only at low temperature. Under a normal temperature, the delocalized metal electrons can easily be promoted to a higher energy state, and can move freely in the structure. This gives the material its electrically conductive nature. In traditional semiconductor materials the number of delocalized electrons is significantly lower than the number of atoms. This is evidenced by a higher value of E_g which is significant at room temperature. This means that in a semiconductor the electrons will not be free to move and conduct current without some additional energy input. The following Equation 1.1 gives us the average level of electronic energy that distances successive quantum levels (known as the Kubo gap).

$$\delta = \frac{4E_F}{3n} \quad (1.1)$$

where δ is the Kubo gap, E_F is the Fermi energy level of the bulk material, and n is the total number of valence electrons. Because of the Kubo gap in nanoparticles, properties like electrical conductivity and magnetic susceptibility show quantum size effects. These effects have led the nanoparticles to be used in many applications since catalysis, at optics up to medicine.

1.2. Surface Plasmon Resonance

The excitation of surface plasmons (SPs) in metallic nanoparticles (NPs) induces optical properties hardly achievable in other optical materials, yielding a wide range of applications in many fields. Surface plasmon (SP) resonance is the most outstanding optical property of metallic nanostructures. It consists of a collective oscillation of conduction electrons excited by the electromagnetic field of light. SP resonance is the origin of optical properties hardly achievable with other physical processes [10]. In the case of metallic nanoparticles (NPs), where the electrons are confined in the three dimensions, the electron oscillations induces an electric field around the NP that can be much larger than the incident light one. SPs are one of the best examples that are different at the nanoscale. When the size of a metallic particle is reduced to a few nanometers, the optical properties are dramatically modified by the appearance of SPs and its resulting behavior is completely different from the bulk metal one. SPs open the possibility to amplify, concentrate and manipulate light at the nanoscale, overcoming the diffraction limit of traditional optics and increasing resolution and sensitivity of optical probes [11-14]. Consequently, SPs can be used in a wide range of fields, including biomedical [15], energy [16-18], environment protection [19-21], sensing [22] and information technology [23] applications. Nowadays, there are well-established applications of SPs that increase rapidly with the development of our capabilities to fabricate and manipulate nanomaterials. Moreover, NPs are not the only metallic nanostructures exhibiting SPs. Films, wires and patterned media exhibit also SPs [24-25]. In the case of NPs, the confinement of electrons leads to localized SPs, while other structures with large dimensions compared with light wavelength (wires and films) hold extended SPs that propagate along the interface between the metal and the dielectric medium. There is a third case corresponding to mesoscopic systems, with dimensions comparable to wavelength. In this case SP modes can also be excited. The scientific study of SPs started in the early 20th century when Gustav Mie published his pioneering work explaining the surprising optical properties of metallic colloids [26]. However, SPs in NPs have been empirically used for a long time, particularly for glass colouring. After Mie's work in the early 20th century,

the origin of the optical properties of metallic NPs was understood, but further exploitation was limited by the capabilities to synthesize and manipulate NPs in a controlled way. It was not until the development of nanotechnology at the end of 20th century that the applications of SPs spread quickly in many fields. SPs correspond to an interaction between matter and the electromagnetic field of the light. Thus, the exact analysis of SPs implies solving the Maxwell equations with the appropriate boundary conditions. The solution of these equations is only possible for certain conditions and even in this case, the results are mathematical series that do not explain what are SPs. However, a simplified classical picture can be more useful to understand the physical meaning of SPs. A metallic NP can be described as a lattice of ionic cores with conduction electron moving almost freely inside the NP (the Fermi sea) as figure 1.2 illustrates. When the particle is illuminated, the electromagnetic field of the light exerts a force on these conduction electrons moving them towards the NP surface. As these electrons are confined inside the NP, negative charge will be accumulated on one side and positive charge in the opposite one, creating an electric dipole. This dipole generates an opposite electric field to that of the light that will force the electrons to return to the equilibrium position.

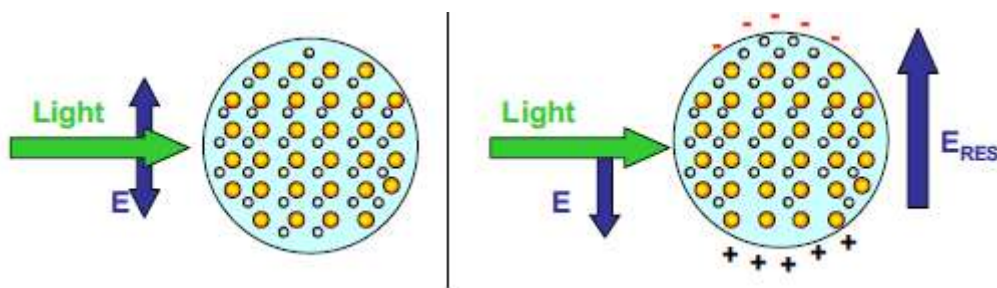


Fig. 1.2- Scheme of the light interaction with a metallic NP. The electric field of the light induces the movement of conduction electrons which accumulate at the NP surface creating an electric dipole. This charge accumulation creates an opposite electric field to that of the light [10].

The larger the electron displacement, the larger the electric dipole and consequently the restoring force. The situation is similar to a linear oscillator with a restoring force proportional to the displacement from the equilibrium position. If the electrons are displaced from the equilibrium position and the field is removed later, they will oscillate with a certain frequency that is called the resonant frequency; in

the case of SPs it is named the plasmonic frequency. Actually, the electron movement inside the NP exhibits some degree of damping.

The ionic cores and the NP surface partially damp the electron oscillations. Thus, the system is similar to a linear oscillator with some damping. When an alternating force is applied to a linear oscillator, the system oscillates with the same frequency as the external force but the amplitude and phase will depend on both the force and the intrinsic parameters of the oscillator. In particular, the oscillating amplitude will be maxima for the resonant frequency (Fig. 1.3(a)). It is quite straightforward to understand that, if the frequency of the external force is the same as the plasmonic frequency of the NP, it will be easy to make the electrons oscillate, but as we move far away from this frequency the movement of electrons will be more difficult, i.e. with reduced amplitude. We cannot directly observe the movement of electrons to determine their oscillating amplitude. However, we can determine this amplitude indirectly. The electronic oscillation implies an increase in kinetic and electrostatic energies associated with the electric fields of the dipole. As energy must be conserved, this increase in energy must be provided by the illuminating light. Therefore, the light extinguishes partially when exciting SPs inside the NP. The larger the electron oscillations, the larger the light extinction, so the optical absorption spectrum allows one to detect the excitation of SPs.

The resonant frequency for these oscillations in metallic NPs corresponds typically to UV–Vis light and consequently, the SPs arise absorption bands in this region of the spectrum as Fig. 1.3(b) illustrates.

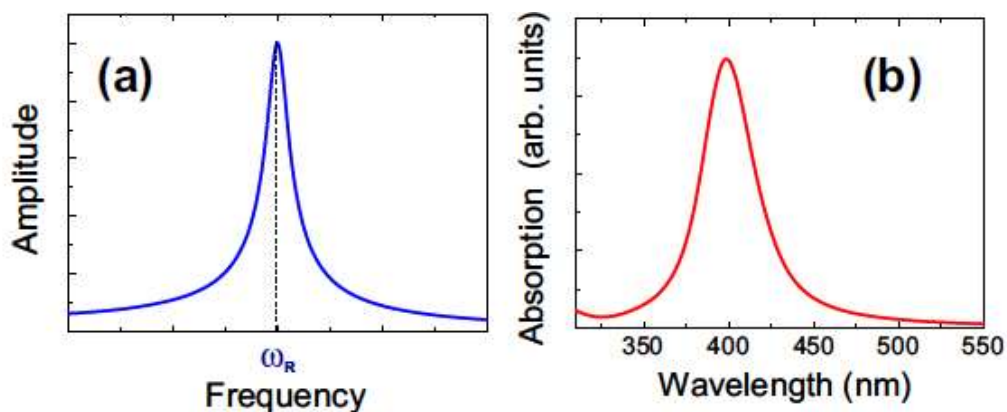


Fig. 1.3- (a) Oscillation amplitude for a linear oscillator as a function of the external force frequency. (b) Optical absorption spectrum corresponding to 10 nm silver NPs embedded in a silica glass [10].

At this stage, SPs can be considered as another electronic process in which light is absorbed to promote electrons from the ground level to an excited one. What makes the SPs unique are the numbers of these processes. The absorbing efficiency of a particle is given by its absorption cross section. Classically it corresponds to the geometrical section of an ideal opaque particle absorbing the same number of photons as the studied particle. As figure 1.4 illustrates, we could replace the absorbing NP by a perfect opaque one (absorbing any photon reaching its surface) that will absorb the same number of photons as our real particle. The section of this ideal particle represents the absorption cross section of the NP. For instance, if we have an NP absorbing half of the photons reaching its surface, the absorption cross section will be half of its geometrical section. In addition to absorption, light interacting with matter can be scattered, changing the propagation direction and eventually also energy and momentum. For this process, we can define also the scattering cross section as the geometrical section of an ideal scattering particle (that scatters any photon reaching its surface) with the same scattering efficiency as the real particle. The sum of absorption and scattering cross section is defined as the extinction cross section that represents the efficiency of the particle to remove photons from an incident beam (by both absorption or scattering processes). The maximum possible value of the extinction cross-section for perfect opaque particles is the particle section ($\pi \cdot R^2$).

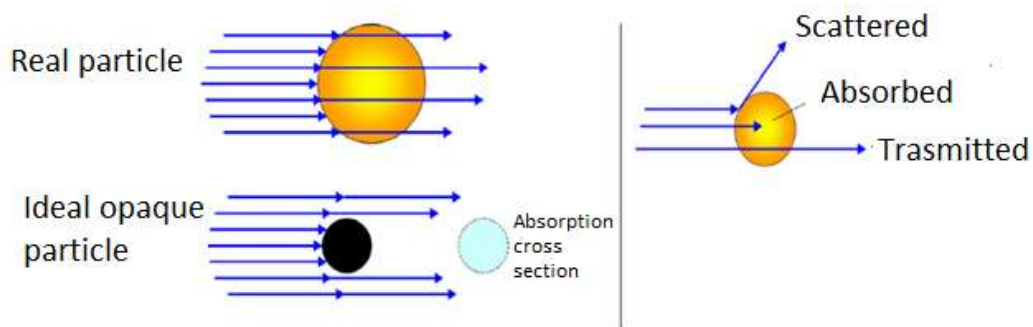


Fig. 1.4- Left: illustration of absorption cross section concept. Right: picture describing transmission, absorption and scattering processes[10].

It is found that for noble metal NPs the extinction cross section can be up to 10 times their geometrical section; that is, the NP is capable of absorbing and scattering photons even away from its physical position. Somehow, the excitation of the SP is equivalent to concentrate the light passing by the NP to induce a huge extinction. It is worth noting that the light absorption has an exponential dependence on the absorption cross section. A light beam propagating across a medium with metallic NPs decay in intensity as

$$I(x) = I_0 e^{-C \cdot \sigma \cdot x} \quad (1.2)$$

I_0 being the initial intensity, C the concentration of NPs per unit volume, σ their extinction cross section and x the travelled distance. Therefore, a moderate increase in the extinction cross section can lead to a huge enhancement of light absorption. A more direct example of the huge extinction in metallic NPs due to SP excitation is provided by a comparison with interband transitions. In addition to SPs, there are other possible electronic excitations in metallic NPs. In a metallic material, valence and conduction bands overlap forming a continuous spectrum of available states. However, some inner levels do not split enough to overlap these bands so the system may exhibit interband transitions similar to those in semiconductors. Transitions between these inner levels and the conduction band induce an absorption edge similarly to the case of semiconductors. Actually, some metals present a weak luminescence emission due to electron decay between these bands. For bulk materials these transitions are very unlikely and optical absorption and emission associated with these transitions are very weak. For instance, a weak photoluminescence associated with interband transitions has been measured for bulk gold corresponding to transitions between the 3d level and the conduction band. However, for NPs with a reduced number of atoms, energy bands are not so well formed because of the limited number of atoms and interband transitions become more prominent. Figure 1.5 shows the optical absorption spectrum of Ag and Au NPs. In the case of Ag, both SP band and interband transition absorption edges are well resolved. For Au NPs, both absorptions overlap. This overlapping is important when analysing the shape of the SP. In particular, the width of the SP band (related to the NP size) must be determined separating the contribution of the interband transitions. We may observe how the SP absorption is larger than that of

the interband transitions despite the fact that the absorbing centre is the same for both processes. The reason for this surprising behaviour can be qualitatively explained with the same classical picture of SPs.

When the incident light reaches the NP, the conduction electrons move resulting in a charge accumulation at the NP surface. This charge creates a field inside the NP (the restoring field) but also out of the NP. The large electron density and mobility in the metallic NP produces a large charge accumulation at the NP surface and consequently intense fields in a region larger than the NP size. There are wide regions where the electric field created by the particle is opposite to that of the light, so the interference is destructive, leading to light extinction beyond the NP volume [27]. For other regions, the result of the interference between both electric fields is a net field with other propagating direction, hence inducing light scattering. This mechanism explains qualitatively the huge extinction cross section of metallic NPs when SPs are excited [28-30]. Actually, the excitation of SPs with laser sources can even yield a modification of the NP shape by local increase in the temperature associated with the huge absorption.

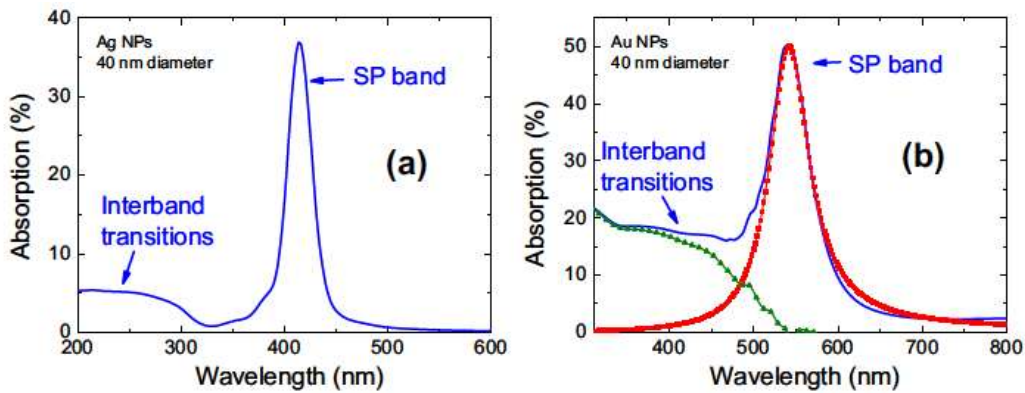


Fig. 1.5- Optical absorption spectra for (a) Ag and (b) Au NPs with 40 nm size (embedded in a silica matrix with $\epsilon = 2.25$). For Au NPs, the contributions to the optical absorption of interband transitions and SPs are resolved [10].

1.3 Biomaterials

The "Biomaterials" term have alternatively been used to describe materials derived from biological sources and/or materials used for therapies in the human body. The first and foremost requirement for the choice of the biomaterial is its acceptability by the human body (Fig. 1.6).

The success of a biomaterial or an implant is highly dependent on three major factors:

- 1) the properties (mechanical, chemical and tribological) of the biomaterial.
- 2) biocompatibility of the implant.
- 3) the health condition of the recipient and the competency of the surgeon

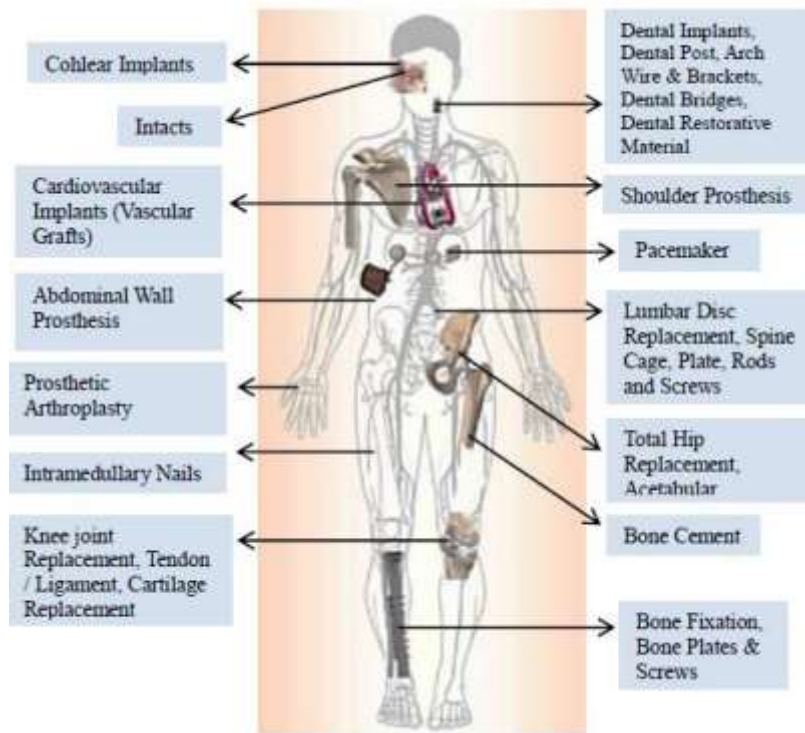


Fig.1.6- Significance of Implants for Human Anatomy

As shown in Fig.1.7, over the years a wide variety of polymer based biomaterials have been developed for various biomedical applications. A biomaterial is a material that interfaces with biological systems to evaluate, treat, increase or replace any organ tissue, organ or function [31].

Any biomaterial causes a biological response of the organism in which it operates, which in turn causes a process of degradation in the biomaterial itself. Therefore there is talk of a double interaction between the two systems. We must not make the mistake of considering an inert biomaterial with respect to the organism in which it is implanted. The human organism has the possibility to activate numerous and complex biological mechanisms that have defense functions against events considered harmful. In general, these mechanisms consist of complicated sequences of processes, each of which is regulated by precise activation / inhibition equilibria. Sometimes these processes can be altered pharmacologically to achieve an increase or decrease in the effectiveness of natural defenses. The natural defense mechanisms, although obviously indispensable for the survival of the organism, constitute the main obstacle to the application of medical devices. Like any traumatic event, even the insertion of a medical device, from the simple injection needle to the more complex artificial organ, is "experienced" by the biological organism as an event from which to defend itself. This attitude of "waste" derives essentially from the fact that the acceptance of a device by the body takes place on the basis of molecular recognition mechanisms of the materials of which the device is constituted and not on the evaluation of the functions that these materials (and the device) can play. A fundamental concept with regard to biomaterials is that of biocompatibility, which indicates the aptitude of a material to be well tolerated by the host organism in which it must operate, determining an appropriate response in relation to the application by the latter. Biocompatibility is the paramount criterion that must be met by every biomaterial. The biocompatibility of a biomaterial must be conserved for the entire duration of the application for which it is intended. For example, a prosthesis must guarantee functioning and biocompatibility throughout the life of the patient.

Generally, there are two fields of use for biomaterials:

- extracorporeal: equipment, analysis instruments, surgical instruments;
- body: means of osteosynthesis, orthopedic prostheses, dental prosthesis.

The biocompatibility of the used materials must be respected for both fields of use, but naturally the materials to be used within the body must comply with more stringent specifications.

Biomaterials can be classified according to their chemical nature. Figure 1.7 shows the classification of biomaterials and shows the percentage of use of each family.

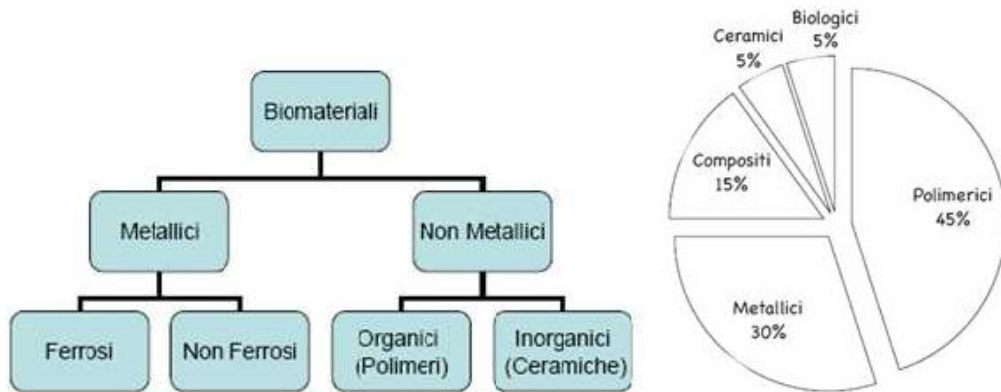


Fig. 1.7- Classification of biomaterials and percentage of use of the various types.

1.3.1 Metallic Biomaterials

The most used metals as biomaterials are stainless steels, cobalt-chrome alloys and titanium alloys. They are widely used mainly as materials for the construction of biomedical devices [32]. Some common applications of metal biomaterials concern the manufacture of surgical instruments, orthopedic and dental prostheses and osteosynthesis devices. In fact, the metallic materials, presenting mechanical properties that make it possible to produce prostheses able to withstand high loads with small sections, lend themselves well to solving problems related to the replacement of hard tissues such as bones and teeth. Figure 1.8 shows examples of prostheses partly or entirely constructed of biocompatible metal material.

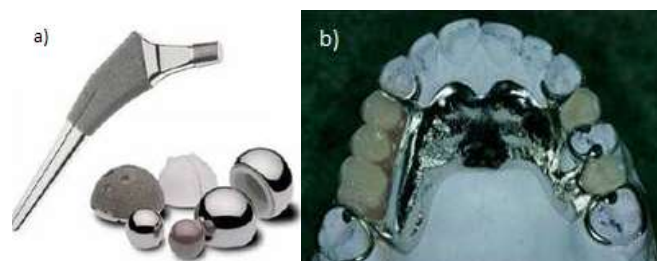


Fig. 1.8- Examples of prostheses made from metal biomaterials: a) hip prosthesis, b) dental prosthesis.

The most important advantages of metal biomaterials are the following:

- high elastic modulus (about 100, 200 GPa);
- high yield strength (about 300, 1000 MPa). They can therefore withstand high loads without breaking or deforming;
- good ductility. Consequently, if the stress exceeds the yield limit, the biomaterial deforms plastically rather than breaking brittlely. This usually allows to intervene by replacing the deformed component before it breaks;
- absence of viscoelasticity;
- high resistance to mechanical fatigue. The fatigue strength also depends solely on the number of cycles and not on their frequency.

On the other hand, however, they have the following disadvantages:

- on average they have a higher specific weight than polymeric and composite biomaterials;
- they are generally more difficult to manufacture than biopolymers;
- tend to corrode and wear due to contact with biological fluids.

Metal biomaterials can be processed using most of the traditional technologies and often their mechanical properties can be modified appropriately before the workpiece reaches its final shape.

To guarantee high biocompatibility it is necessary to take care of manufacturing technologies, above all with regard to surface finishing. Biocompatibility is connected, in the case of metals, to the problem of corrosion in a biological environment; in fact, in this type of environment, organic fluids have a high corrosive power towards metals. The consequences of corrosion are the loss of metallic material by the plant, with the possibility of loss of functionality of the plant itself and contamination of biological tissues.

Most of these problems, however controllable, are related to implanted devices, while for non-implanted devices, as in the case of surgical instruments, the metals have minor drawbacks and are the most used materials where high mechanical properties and reliability over time are required. From a corrosionist point of view, the human body can be assimilated to an aqueous solution with a temperature around 37 ° C, containing chloride ions and with an average pH of about 7.4 (the pH is actually variable depending on the area and can suffer strong fluctuations in

the presence of infections, as a result of surgical interventions and pharmacological applications). This solution is also strongly oxygenated and contains a high amount of salts and organic and inorganic compounds and therefore has a fairly high electrical conductivity. For all these reasons, the human organism is the ideal environment for the establishment of corrosion cells on metals. The corrosion resistance of metals depends on several factors, including the composition, the microstructure, the internal stresses and the surface finish.

1.3.2 Polymeric Materials

The use of polymers in medicines gave birth to the polymer science, virtually every early synthetic polymer found their way into the experimental surgical studies soon after their invention and many endured to become staples of clinical practice. The polymers remain important in clinical medicine as essential components of permanent prosthetic devices including hip implants, artificial lenses, large diameter vascular grafts, catheters, etc., and research continues to optimize the stability and performance of these materials in vivo. Whereas the original uses of polymers in surgery centered primarily on replacements for connective tissues, a host of new applications is emerging as a result of major advances in the sciences of molecular cell biology and developmental biology. An array of new protein and nucleic acid based drugs, which cannot be taken in classical pill form, is providing impetus for new implantable polymers for controlled drug delivery and gene therapy [33]. Applications in the relatively new field of tissue engineering, where polymers are used to assist the regeneration of three-dimensional tissue and organ structures, are more promising and are more assimilated with biological demands. A large number of polymers such as polyethylene (PE), polyurethane (PU), polytetrafluoroethylene (PTFE), polyacetal (PA), polymethylmethacrylate (PMMA), polyethyleneterephthalate (PET), silicone rubber (SR), polysulfone (PS), polyetheretherketone (PEEK), poly lactic acid (PLA), and poly glycolic acid (PGA) are also used in various biomedical applications. HA/PE, silica/SR, carbon fiber/ultrahigh molecular weight polyethylene (CF/UHMWPE), carbon fiber/epoxy (CF/epoxy), and CF/PEEK are few examples of polymer composite

biomaterials. The application of polymeric materials for medical purposes is growing very fast. Polymers have found applications in such diverse bio-medical fields as tissue engineering, implantation of medical devices and artificial organs, prostheses, ophthalmology, dentistry, bone repair, and many other medical fields. Polymer-based delivery systems enable controlled slow release of drugs into the body. The application of synthetic polymers for gene therapy has also been investigated. They may provide a safer way of gene delivery than use of viruses as vectors. Polymeric materials have also extensively been used for biosensors, in testing devices, and for bio-regulation. Suitable polymeric material for a biomedical application must be 'biocompatible', at least on its surface. Strictly speaking many polymeric systems used for implantation of medical devices into the body are considered to be 'biocompatible', though after implantation they become isolated from the tissues of the body by collagenous encapsulation. An implanted polymeric material may be considered to be 'biocompatible', if its insertion into the body does not provoke an adverse reaction. A thrombus is formed very fast when polymers contact blood cells. Materials with non-thrombogenic blood compatible surfaces must, therefore, be used in contact with the blood stream. Truly biocompatible polymers, used for medical purposes, should be able to recognize and cooperate in harmony with bio-assemblies and living cells without any non-specific interactions. Polymers have taken an important role in medical applications. In most of these applications, polymers have little or no competition from other types of materials. Their unique properties are:

1. Flexibility.
2. Resistance to biochemical attack.
3. Good biocompatibility.
4. Lightweight.
5. Availability in a wide variety of compositions with adequate physical and mechanical properties.
6. Possibility to be easily manufactured in products with the desired shape.

Biomaterials play a fundamental role in the engineering of tissue structures, working as an artificial extracellular matrix and three-dimensional support environment for cells (dragged in vitro or in vivo migration from host tissue) to

regenerate a wound site. Because of their mechanical versatility and resemblance to the structural characteristics of the fabric, polymers are the most popular biomaterials in tissue engineering. Polymeric biomaterials are currently dominated by thermoplastic polyesters such as polylactic acid (PLA), glycolic acid (PGA), poly caprolactone (PCL) and their mixtures or copolymers. Polyester is a category of polymers that contain the ester functional group in their main chain. Esters are chemical compounds derived from a carboxylic acid (COOH group) and a compound hydroxyl (OH), usually an alcohol. Many esters, such as fatty acids, are endogenous compared to human metabolism and therefore biocompatible. Many polyesters can degrade to natural metabolic products by simple hydrolysis. Although these biomaterials have been well characterized and fabricated to adapt to the biochemical properties of soft tissues, the mechanical compatibility between implants of thermoplastic polymers and living tissues generally lacks. Biodegradable synthetic polymers have attracted considerable attention to applications in medical devices and will play an important role in the design and function of medical devices. Drug eluting stents (DES) have been widely used as the default treatment for patients with coronary artery disease. The biodegradable polymers are always used as a biodegradable and bioabsorbable coating on stents to control drug delivery. In addition to being used as biodegradable coatings, biodegradable polymers are also candidate materials for completely biodegradable stents due to their properties for controlled drug delivery and good mechanical performance to prevent stents from deformation or fracturing. Orthopedic devices made of biodegradable materials have advantages in metallic or non-degradable materials. They can transfer stress over time to the damaged area while healing, allowing the tissues, and there is no need for a second surgery to remove the implanted devices. These biodegradable polymers have been used to prepare some single-use medical devices and will probably have an increasing commercial demand. A new dimension for the use of polymeric materials as drug delivery devices involves incorporation of biodegradability into the system. A number of degradable polymers are potentially useful for this purpose, including a variety of synthetic and natural substances. The use of intentionally degradable polymers in medicine has been brought into prominence with new innovations in drug delivery

systems. In some cases, erosion or dissolution of the polymer contributes to the release mechanism. Degradable polymers such as poly lactic acid and polyorthoesters, are used for drug delivery systems.

1.3.3 Ceramic Biomaterial

The field of nanotechnology is playing a pivotal role in the fields of electronics, biology and medicine. It also introduced several new concepts into medicine and thus makes these large cross disciplinary fields to join together. Nanomedicine encompasses many common technical issues like analytical tools, nanoimaging, nanomaterials and nano-devices, novel therapeutics and Drug Delivery Systems, clinical, regulatory and toxicological issues. Among the varieties of nanomaterials, nanostructured ceramics, cements and coatings are being considered for major applications in orthopaedic and dental treatments. Biocompatible Ceramics, also known as bioceramics, include both macro and nano materials mainly used for bone, teeth and other medical applications. Nanostructured ceramics, cements and coatings are being considered for major orthopaedic, dental and other medical applications. The development of novel biocompatible ceramic materials with improved biomedical functions is at the forefront of health-related applications all over the world [34]. Ceramics are also unique used biomaterials used for repairing and regenerating several parts of the human body. The widely used ceramic nanobiomaterials include (see Fig. 1.9), Calcium Phosphate (CaP), Tri-Calcium Phosphate (TCP), Hydroxy-Apatite(HAP), TCP+HAP, Si substituted HA, Calcium Sulphate and Carbonate, Bioactive Glasses, Bioactive Glass Ceramics, Titania-Based Ceramics, Zirconia Ceramics, Alumina Ceramics and Ceramic Polymer Composites.

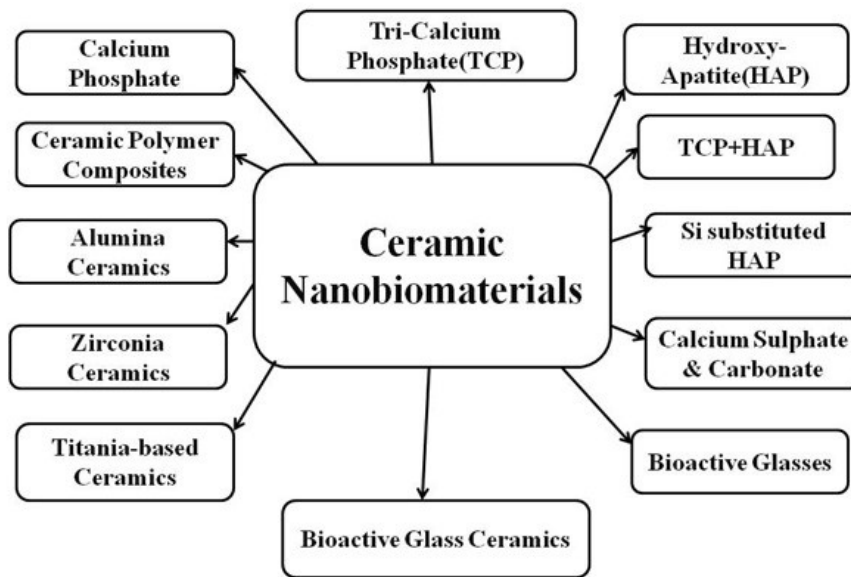


Fig. 1.9- Widely used ceramic nanobiomaterials.

Ceramics are compounds between metallic and non-metallic elements; they are most frequently oxides, phosphates, nitrides, and carbides. There are wide range of ceramic materials like clay minerals, cement, and glass used for various applications. These materials are typically insulators to electricity and heat, and are highly resistant to harsh chemical environments than metals and polymers. With regard to their mechanical behaviour, ceramics are very hard and brittle. At nanoscale also, ceramic materials exhibit higher hardness, excellent heat and corrosion resistance, and electrical insulation properties. Typical examples include china clay, firebricks, cements and glass. In addition to these properties, Fine Ceramics (also known as “advanced ceramics”) have many advanced mechanical, electrical, electronic, magnetic, optical, chemical and biochemical characteristics. One of the major field of application of bioceramics is tissue generation. The major parameters considered to optimize the biomaterials for the tissue generation include, a) Structural Components (physical, mechanical and chemical properties) and b) Biochemical Components (immobilized signals, diffusable signals, and living components).

The bioceramics have good biocompatibility, osteo conductivity, osteoinductivity, biodegradability, resorbability, and hydrophilicity. Yet another major field of application of bioceramic is clinical dentistry.

Bioceramics are materials used to repair and replacement of diseased and damaged parts of musculoskeletal systems. Based on their inherent properties, they are classified into three major categories as:

- Bioactive ceramics (CaP, HAP, Bioactive Glass (BAG), and Glass Ceramics (GC) which form direct chemical bonds with bone or even soft tissues of living systems,
- Bioresorbable ceramics (TCP) that actively participate in the metabolic process of an organism
- Bioinert high strength ceramics (alumina and zirconia)

Based on their applications, ceramic biomaterials are further classified into:

- ✓ Cardiovascular biomaterials
- ✓ Dental Biomaterials
- ✓ Orthopedic biomaterials
- ✓ Biomaterials to promote tissue generation.

Nanomaterials of CaP, HAP, TCP, BAG, GC and Calcium sulphate form good ceramic-based bone graft substitutes. Hydroxyapatite (HAP) has been widely used as a biocompatible ceramic in many areas of medicine, but mainly for contact with bone tissue, due to its resemblance to mineral bone. HAP has exceptional biocompatibility and bioactivity properties with respect to bone cells and tissues. As a result of excellent favorable osteoconductive and bioactive properties, it is widely preferred as the biomaterial of choice in both dentistry and orthopaedics.

The hydroxyapatite has a few favorable bioactive and osteoconductive properties which help in rapid bone formation, with a strong biological fixation to bony tissues. It also has very low mechanical strength and fracture toughness, which is an obstacle to its applications in load-bearing areas.



Fig 1.10- HA for accelerating the reconstruction of the bone tissue on the metallic implant surface creating a rapid bonding.

HAP can incorporate the drug molecules either physically or chemically so that the drug retains intact until it reaches to the target site. It could also gradually degrade and then deliver the drug in a controlled manner over time. Titanium comes under the category of Technical ceramics. The technical ceramics are divided into oxides and non-oxides like Aluminium Oxide, Ceramics, Carbide Ceramics, Nitride Ceramics, Oxide Ceramics, Silicon Carbide Ceramics, Silicon Nitride Ceramics, and Zirconium Ceramics Dioxide. The fact that titanium is strong, light, non-toxic and does not react without bodies makes it a valuable medical resource and used to make surgical implements and implants, such as hip joint replacements that can stay in place for up to 20 years. Although other photocatalytic materials are available, researchers have found that titanium dioxide provides the best performance in sunlight. Titanium nanomaterials have been clinically successful as orthopedic or dental implant material.

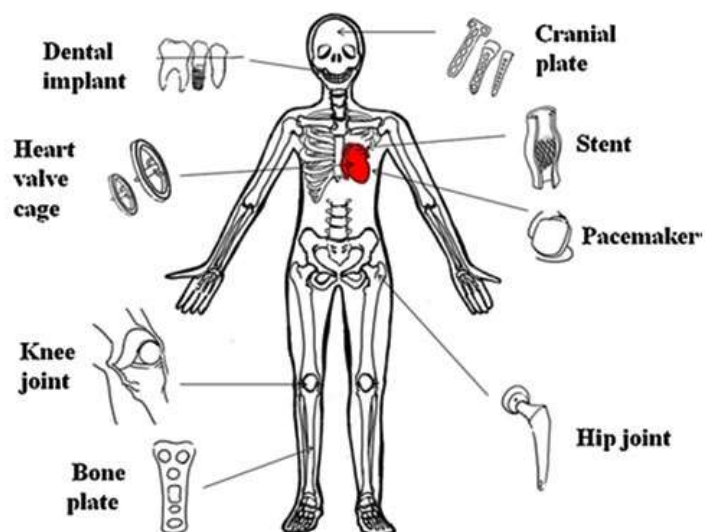


Fig 1.11- Biomedical application of titanium and its alloys

2. Synthesis and Characterization of Nanoparticles

2.1. Synthesis of Nanoparticles

The importance and benefits of nanotechnology in biology and medicine are now well-recognized by scientists, technologists, as well as various governmental and private research funding agencies. The basis that enables the application of nanotechnology is the availability of nanostructured materials. Therefore, it is essential to provide an insight on the state-of-the-art methods to manufacture various nanostructures. The methods for synthesis and patterning for many of these nanostructures are founded on basic, well-known techniques and their modifications, as is described in this chapter. The nanofabrication processes can be divided into the two well-known approaches: “top-down” and “bottom-up.” The “top-down” approach uses traditional methods to guide the synthesis of nanoscale materials. The proper paradigm of its definition generally dictates that in the “top-down” approach it all begins from a bulk piece of material, which is then gradually or step-by-step removed to form objects in the nanometer-size regime. The top-down approach for nanofabrication requires a thorough understanding of the short-range forces of attraction, such as Van der Waals forces, electrostatic forces, and a variety of interatomic or intermolecular forces. Since it is not possible to have various minute things come together without some attractive force or active field of force in the region, having the fundamental forces “doing all the work” for us is the key principle underlying this approach.

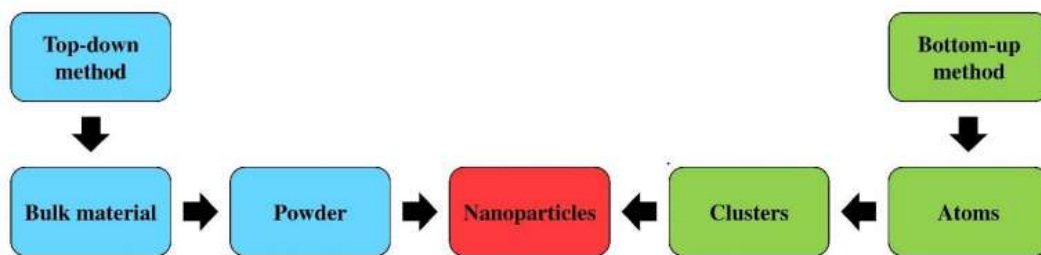


Fig. 2.1- Synthesis Process

Some examples of such a synthesis route starting from atoms and molecules are methods like self-assembly of nanoparticles or monomer/polymer molecules, chemical or electrochemical reactions for precipitation of nanostructures, sol-gel processing, laser pyrolysis, chemical vapor deposition (CVD), plasma or flame spraying synthesis, and atomic or molecular condensation [35-37].

The bio-assisted synthesis of nanomaterials also belongs to this approach. However, despite being so promising and inviting, our ability to build things from the bottom up is fairly limited in scope. While we can assemble relatively simple structures, we cannot produce complex, integrated devices using the bottom-up approach. Any kind of overall ordered arrangement aside from repeating regular patterns cannot be done without some sort of top-down influence, like lithographic patterning. Until we have fully mastered the bottom-up synthesis approach, we will not be able to fully exploit its speed and accuracy. The important factor is that they are two different approaches to creating nanostructures which can be applied according to the specific needs for each application, often in a complementary way.

2.2. Nanofabrication by “Top Down” Methods.

Over the past few decades, a wide variety of top-down production techniques have been developed that have been implemented using different media ranging from chemical and electrochemical media to photofabrication, laser processing, ecc. Here, we describe only the technique Laser Ablation in liquids.

2.2.1 Laser Ablation

Laser ablation is a method for fabricating various kinds of nanoparticles including semiconductor quantum dots, carbon nanotubes, nanowires, and core shell nanoparticles. In this method, nanoparticles are generated by nucleation and growth of laser-vaporized species in a background gas [38]. The extremely rapid quenching of vapor is advantageous in producing high purity nanoparticles in the quantum size range (<10 nm). The most critical characteristic of nanoparticles is that the properties electrical, optical, magnetic, and so on depend strongly on the size and size distribution of the particles. Many kinds of nanoparticles exhibit special characteristics (ferromagnetism, paramagnetism, pinned emission, fluorescence, spin quantum effect, etc.) when the size of a particle is at the nanoscale level. The special characteristics are significantly impacted by the size and size distribution of the particles. Laser ablation is a method that utilizes laser (which is an acronym for light amplification by stimulated emission of radiation) as an energy source for ablating solid target materials. In this process, extremely high energy is concentrated at a specific point on a solid surface to evaporate light-absorbing material. The term ‘ablation’ refers to the removal of surface atoms and involves not only a single photon process (breaking the chemical bonds) but also multiphoton excitation (thermal evaporation). High-purity nanoparticles can be generated by laser ablation because the purity of the particles is basically determined by the purity of the target and ambient media (gas or liquid) without contamination from the reactor. However, it is difficult to control size distribution, agglomeration, and crystal structure in the conventional laser ablation process since nanoparticles are built by random (Brownian) motion of molecules. Therefore,

several advanced laser ablation techniques have been developed for fabricating morphology-controlled nanoparticles.

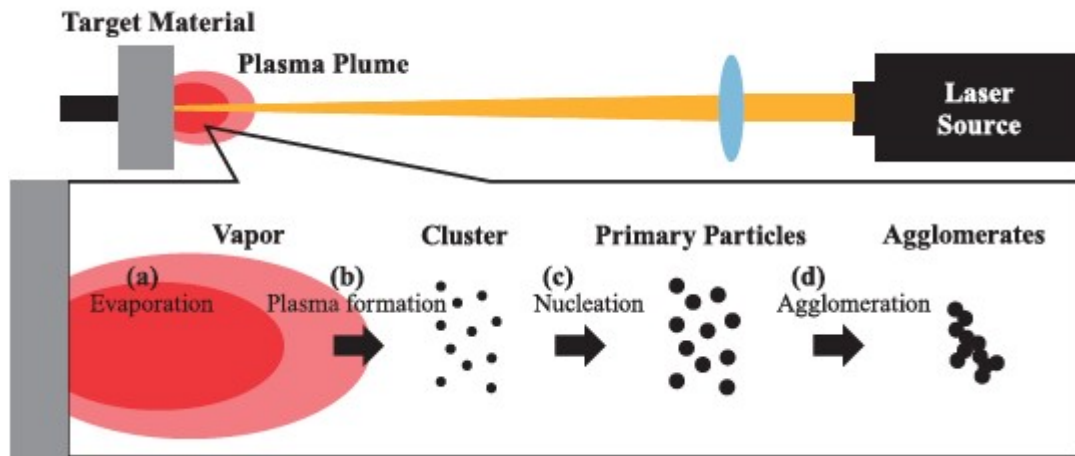


Fig. 2.2 - Schematic of particle generation procedure in the laser ablation process.

Fig. 2.2 is a schematic of the nanoparticle formation process by laser ablation. When the laser beam is focused on the surface of a solid target material in the ambient media (gas or liquid), the temperature of the irradiated spot rapidly increases, vaporizing the target material. The collisions between the evaporated species (atom and clusters) and the surrounding molecules result in excitation of the electron state coupled with light emission and generation of electrons and ions, forming a laser-induced plasma plume. The plasma structures (size of the plume and its emission spectrum) depend on the target material, ambient media (liquid or gas), ambient pressure, and laser conditions. Laser ablation in liquid is employed to confine the plasma plume in a small region to directly disperse nanoparticles in the liquid phase. In any case, the ambient media must be carefully selected because the laser-generated particles easily react with surrounding molecules to create complexes such as oxides and other undesirable species. Coagulation is another critical phenomena that must be finely controlled in the later stages of nanoparticle formation. Since laser-generated particles have a very clean surface, agglomerated particles create chemical bonds at the contact point (neck), which significantly compromise the properties of primary particles. The low-pressure gas process is advantageous not only for reducing the size of the primary particles but also for preventing coagulation. For the fabrication of nanoparticles of the desired size and structure, the selection of a suitable laser system is one of the most critical decisions.

The evaporation rate of the target material is generally determined by the laser parameters (laser source, wavelength, fluence, pulse width and frequency), the light absorption efficiency of the target material, and the condition of the ambient media. Laser energy per unit area on the target material is defined as fluence of the laser F , which is given as

$$F = \frac{I}{A} \quad (2.1)$$

where I [J/pulse] is the laser power and A [m^2] is the area of the laser spot. The wavelength of the laser is another important parameter that determines the absorption efficiency of the target. The absorption depth and spot (focusing) area are also influenced by laser wavelength. In early studies of the nanoparticle synthesis by laser ablation, excimer lasers in the ultraviolet spectrum (193 nm for ArF, 248 nm for KrF) are often used as a light source. Recently, Q-switch pumped pulsed YAG (Yttrium Aluminum Garnet) lasers are more commonly used for laser ablation because they do not require hazardous gases. The wavelength of Nd:YAG laser (1064 nm for fundamental wave) can be changed by employing nonlinear optical crystals. The pulse width of the laser is also another important parameter that determines peak energy. Recently picosecond and femtosecond lasers have been applied to enhance the photon absorption efficiency of the target surface to break chemical bonding.

2.2.2 Our set up for Laser Ablation

A Nd:YAG laser operating at the fundamental wavelength of 1064 nm with a pulse energy of 200 mJ, 3 ns pulse duration, and a repetition rate of 10 Hz, was employed at 10^{10} W/ cm^2 intensity. The horizontal laser beam, 1 cm^2 in diameter with a Gaussian profile, was vertically deflected by a mirror and focused on the gold sample at about 1 mm^2 spot size, placed in a polyethylene holder, through a lens with a focal length of 50 cm (Fig. 2.3). The laser-generated plasma, containing the gold ions and electrons, expanded in the liquid and condensed to form spherical nanoparticles, as reported in the literature [39-40].

Au-NPs are immediately produced, in times comparable with the laser pulse and transforming the liquid in a solution as a consequence of the 10 Hz laser irradiation for times ranging between 10 and 30 minutes, in order to obtain different solution concentrations.

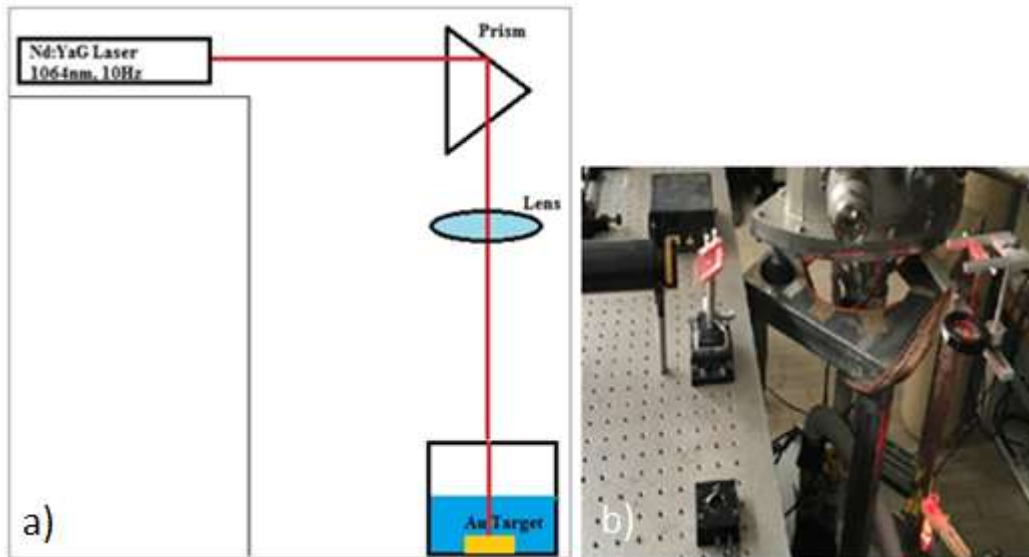


Fig.2.3- Laser Ablation in liquid set up a) scheme, b) photo of set up in our laboratory.

Generally, from 1mg/ml up to 10 mg/ml of gold nanoparticles in distilled water is obtained, but higher concentration can be easily produced. In order to reduce the effect of particle coalescence with the times, a very little quantity of tension active liquid is added ($\sim 10\mu\text{g}$ trisodium citrate) which covers the surface of the nanoparticles greatly reducing their coalescence [41]. The liquid and the target where particles are generated are in movement during laser ablation using the 10 Hz repetition rate. This movement is not due to motors, mechanical stirrers or continuum liquid flux, but it is due to the high used laser intensity (10^{10} W/cm^2), which produces high shock waves determining a continuum horizontal oscillating movement of the target (the target is clamped inside a polyethylene cavity holder so that only horizontal movements are possible) and continuum liquid oscillations and mixing (drops liquid jumping on liquid with heights up to even 10 cm, maintained inside the long used glass tube).

2.2.3 The Laser Ablation: Theoretical background

Comprehension of the aerosol formation as inevitable process in laser micromachining technology is established and the application of laser ablation in the production of nanoparticles is widely spread. However, characteristics of particles generated by laser ablation are not fully known. Therefore, the studies of particles concentration and their size distribution are hot topics in current laser ablation investigations recently [42]. Nanoparticle generation by laser ablation is used for a variety of applications such as biotechnology, electronic industry, etc. The laser ablation is also an intensive source of submicron particle generation and their possible leakage into ambient air, therefore investigations of the particle formation kinetics in ambient air are essential for the evaluation of potential generation of particles by laser and their impact on human health. For example, during laser processing, particles formed of metals (e. g. iron, aluminum), especially toxic (e. g. manganese, zinc) or carcinogenic substances (e. g. chromium (VI) compounds, nickel), might penetrate into a human organism and cause health concerns. The physical process of particle generation begins with the absorption of laser irradiation in the beam/material interaction zone. Depending on the wavelength of the laser beam and the material properties, kinetic energy is transformed into thermal (in metals 10–13 s), which cuts off chemical bonds in the material. The phase transition occurs if the energy threshold for that material is reached. As a result, the material can be melted, vaporized or sublimated and the particle generation process begins. Both the particle concentration and size distribution depend on laser operating parameters such as wavelength, pulse duration, energy and repetition rate, beam scanning speed. Studies show that experimental conditions during the laser ablation could be established in order to control the particles size and distribution. Besides, the medium (ambient air, argon, water, etc.) in the ablation chamber also plays an important role in the particle formation process. It was experimentally estimated that the mass of generated nanoparticles in ambient air was up to 100 times higher than in water.

2.2.4 Temperature Dependence

During the interaction of the laser beam and material, the light absorption is a general physical process [43-45]. The energy coupled into material causes thermal heating, melting and vaporization of material, plasma formation and particle emission. In metals, free electrons interact with the intense electromagnetic irradiation. The energy is instantly absorbed by electrons and further distributed to the lattice. The laser pulse duration τ_L is important for understanding what happens with the energy in the beam / material interaction zone. $\tau_i = \frac{C_i}{\gamma}$ is the lattice heating time, $\tau_e = \frac{C_e}{\gamma}$ is the electron cooling time, where C_e and C_i are electron and lattice thermal capacities, respectively, and γ is the electron– lattice coupling parameter specific to every material. Based on the two-temperature diffusion model the laser beam/material interaction can be described by electron and lattice subsystem temperatures T_e and T_i , respectively:

$$C_e \frac{\partial T_i}{\partial T} = -\frac{\partial Q(z)}{\partial z} - \gamma(T_e - T_i) + S \quad (2.2)$$

$$C_i \frac{\partial T_i}{\partial T} = \gamma(T_e - T_i) \quad (2.3)$$

where $Q(z)$ is the heat flux, S is the heat source (laser pulse). For picosecond pulses, the condition $\tau_e \ll \tau_L \ll \tau_i$ is fulfilled. The laser pulse duration is shorter than the lattice heating time. Particles from the material are removed partly by the solid state – vapor transition and the direct breaking of chemical bonds. For picosecond pulses the electron temperature T_e becomes quasi-stationary:

$$\frac{\partial}{\partial z} \left(-k_e \frac{\partial T_i}{\partial z} \right) - \gamma(T_e - T_i) + I_a \alpha \exp(-az) = 0 \quad (2.4)$$

where k_e is the electron thermal conductivity, α is the absorption coefficient, I_a is the laser intensity transmitted to the material, z is the depth of laser beam

penetration into material perpendicular to the surface. In this case, lattice temperature T_i is

$$T_i = \frac{t}{\tau_i} \int_0^t \exp\left(-\frac{t-\theta}{\tau_i}\right) T_e(\theta) d\theta + T_0 \quad (2.5)$$

where T_0 is the initial electron temperature. Taking this into account Eq. (2.5) can be simplified due to quasi-stationary condition of electron temperature:

$$T_i \approx T_e \left(1 - \exp\left(-\frac{t}{\tau_i}\right)\right) \approx \frac{t}{\tau_i} T_e \quad (2.6)$$

where t is the time after the laser exposure. It means that electron cooling temperature T_e stays longer than lattice heating temperature T_i after exposure to picosecond laser pulses. Electron cooling temperature T_e at the end of the pulse is

$$T_e \approx \frac{I_a \alpha}{\gamma} \exp(-\alpha z) \quad (2.7)$$

Lattice heating temperature T_i at the end of the laser pulse is

$$T_e \approx \frac{F_a \alpha}{C_i} \exp(-\alpha z) \quad (2.8)$$

where F_a is the absorbed laser fluence, which is $F_a = I_a \tau_L$. By using the condition of strong evaporation it can be described as

$$F_a \geq F_{th} \exp(-\alpha z) \quad (2.9)$$

where F_{th} is the threshold laser fluence for evaporation. Equations (2.7) and (2.9) describe how laser intensity, material transmissivity and thermal capacities influence the temperature of the electron and lattice. In the second case for nanosecond pulses, the condition $\tau_L \gg \tau_i \gg \tau_e$ is fulfilled. Equations (2.1), (2.2) for nanosecond pulses are

$$C_i \frac{\partial T}{\partial t} = \frac{\partial}{\partial z} \left(k_0 \frac{\partial T}{\partial z} \right) + I_a \alpha \exp(-\alpha z) \quad (2.10)$$

where k_0 is the conventional equilibrium thermal conductivity of a metal and T represents general temperature of the subsystem, because in case of ns-laser ablation $T_e = T_i = T$.

The energy absorbed by electrons is fully transferred to the lattice during the laser pulse duration. Material is heated due to the absorbed energy of the lattice. In this case, solid material melts, the beam/interaction zone spreads and particles are evaporated from liquid state. Metals have good thermal conductivity properties, thus increasing energy loss due to lattice heating for nanosecond pulses.

2.2.5 Irradiation, Energy, Wavelength and Time Dependence

Irradiation of a solid target in a liquid with a laser beam results in the generation of metal flakes by laser fragmentation. The particles are refined by irradiation with the laser beam a second time. The laser beam reduces the size of the generated nanoparticles or produces particles with a specific size distribution. The interaction of the laser beam with the liquid also affects the particle formation. Bubbles and cavitation result from laser-induced plasma generation and affect nanoparticle fragmentation [46]. In addition, the aqueous solution influences the formation of clusters of nanoparticles. Nanoparticle size and dispersion can be controlled by varying the laser parameters. The wavelength of the laser pulse also affects the nanoparticle generation. When a laser of different wavelength with the same pulse width is used, the fragmentation effect increases with decreasing pulse wavelengths. This is because the shorter the pulse wavelength, the greater the absorption cross section. In addition, liquids other than deionized water may be used, and they can contribute to the nanoparticle formation and stability. The laser pulse width is a predominant determinant of nanoparticle size and distribution. Laser pulse widths in the femtosecond, picosecond, and nanosecond regions can be used to induce the laser fragmentation [47-49]. Several studies have evaluated the interactions of picosecond or femtosecond laser pulses with materials. Such ultrafast laser pulses cause nonlinear multiphoton absorption due to their high peak power. Because of this, energy cannot be transferred from the electrons to the ion

grids in femtoseconds or picoseconds, which enables the processing of materials that are little affected by heat. Irradiation with a nanosecond pulsed laser beam results in thermal diffusion at the particle surface.

It is important to compare the diffusion time and the pulse width. In general, the thermal diffusion in metal nanoparticles requires 50 to 100 ps, and the diffusion time can be used to classify laser fragmentation mechanisms into short and long pulse-width categories. At a pulse width of less than a few picoseconds, the electron and phonon temperatures in the particle are different. In this case, to determine the particle temperature distribution, a model with different electron and phonon temperatures should be applied.

Also, since the laser beam absorption time is shorter than that of heat diffusion, it is appropriate to assume that the boundary condition of particles is adiabatic. In this model, the energy absorption by laser irradiation is a function of the fluence and absorption cross-sectional area of the laser. This correlation affects the electron temperature and phonon temperature of nanoparticles; that is, as the pulse width decreases, the peak laser power and the electron temperature increase. This results in a release of electrons from the particle; moreover, a Coulomb explosion may occur. Coulomb explosions are a major mechanism of the femtosecond laser fragmentation.

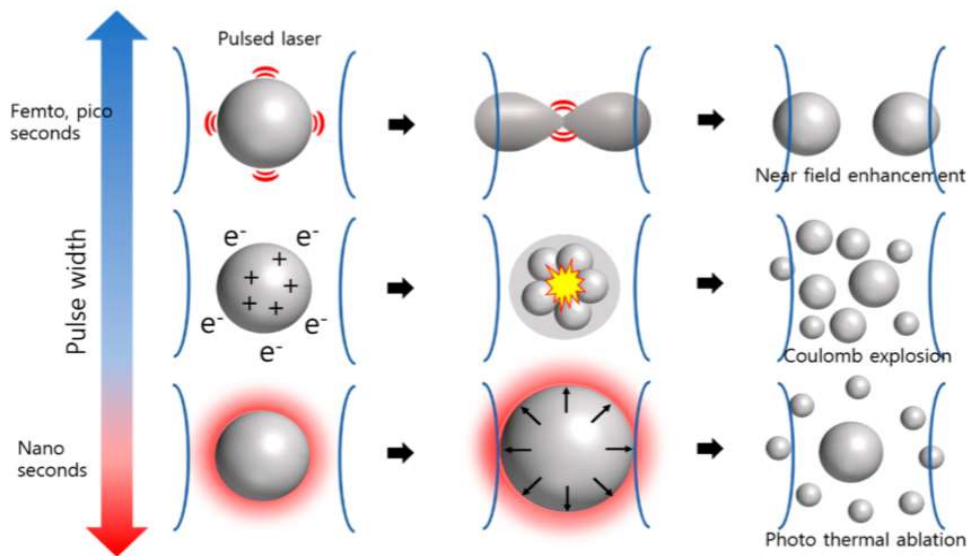


Figure 2.4- Mechanisms causing laser fragmentation for different laser pulse widths.

When the pulse width increases from femtoseconds to picoseconds, the energy transfer tends to resolve the energy imbalance in the nanoparticles. In this case, the effect of Coulomb explosions in the particles decreases. Near-field enhancement at the nanoparticle surface also occurs using ultrafast laser pulses. When a nanostructure is irradiated with a short laser pulse, the electromagnetic field is amplified at the point at which an abrupt change in shape occurs. This results in a sudden energy concentration at that point, leading to particle fragmentation. A model with constant electron and phonon temperatures can be used for lasers with nanosecond pulse widths. Also, since there is enough time for thermal diffusion within the particle, the heat at the interface interacts with the surroundings during laser irradiation. Therefore, the photothermal effect becomes dominant. Melting, evaporation, or both occur at the particle surface as a result of the temperature imbalance between the particle surface and interior, which likely also causes particle fragmentation. The three above-mentioned mechanisms of laser fragmentation are summarized in Figure 2.4. The effect on the nanoparticle formation of mechanical shock waves generated by the laser-induced generation of plasma is shown in Figure 2.5.

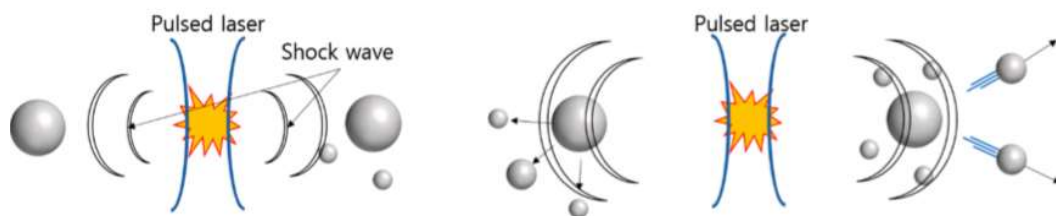


Figure 2.5- Effect of shockwave propagation on the laser fragmentation.

2.2.6 Photochemical effects of Laser

There are four major categories of light-tissue interactions that lead to alteration of the tissue structure/composition:

- Photochemical: Absorption of light by molecules present or added to tissue.
- Photothermal: Biological effects due to deposition of thermal energy in tissue.

- Photoablative: in UV, photons possess sufficient energy to cause photo-dissociation of bio-polymers and subsequent desorption of fragments (a substance is released from or through a surface).
- Photomechanical: it occurs at high fluence rates where dielectric breakdown of tissue is induced which can lead to plasma formation. Rapid plasma expansion generates a shock wave which can rupture tissue [50].

Light can induce chemical effects and reactions within macromolecules or tissues. Photodynamic therapy (PDT): spectrally adapted chromophores are injected into the body.

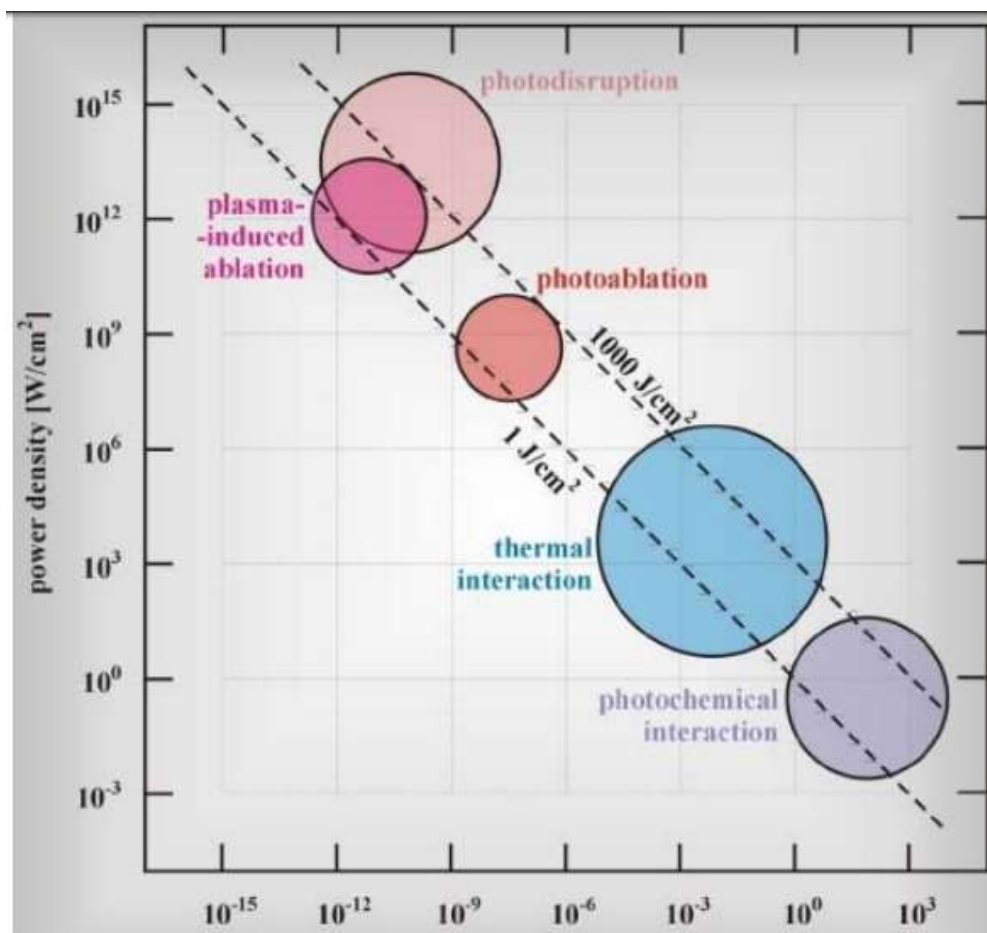


Fig. 2.6- Map of the power density value in relation to the exposure time.

Monochromatic irradiation (usually red) may then trigger photochemical reactions, resulting in certain biological transformations. A chromophore which is capable of causing light-induced reactions in other non-absorbing molecules is called photosensitizer (PS) (organic dyes). After absorption of laser photons, PS is transferred to S1. After this, a radiative decay might occur to an excited triplet state (intercrossing system) (T_1) besides other alternatives such as non-radiative decays or radiative singlet decay to the single ground state. Radiative singlet and triplet decays: fluorescence (ns) and phosphorescence (ms-s). PS are compounds whose energy difference $T_1 - S_0$ is close to the energy needed for oxygens molecules to be excited from the triplet ground state to a excited singlet state (energy is transferred to the oxygen molecule). The excited singlet oxygen resulting from this process are very reactive and lead to lipids and protein oxygenation and other destructive processes, which could start necrosis of cancer cells (PDT: photodynamic therapy). The main disadvantage of PDT is the long time of the compound's decay and removal from the patient body became photosensitive from several days to weeks after application of such drugs and the related effects (toxicity etc.)

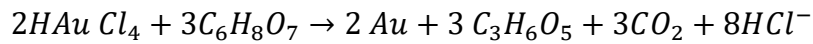
2.3. Nanofabrication by “Bottom-Up” Methods

The NPs obtained thanks to the Bottom-Up strategy, are the result of the natural manifestation of interaction between the constituent elements, that is organize to form the desired structure. The bottom up approach uses atomic or molecular raw materials as the source of the material that it must be chemically converted into larger nanoparticles. This method has the advantage of being, potentially, much more controllable than the top down approach. This has led to the development of many general strategies of bottom up.

In general, two main chemical methods can be used for the AuNP preparation: co-precipitation and chemical reduction. In both cases, the presence of a surfactant is necessary to control the process of growth. Co-precipitation reactions involve the thermal decomposition of the organometallic gold predecessors, while the chemical reduction that occurs in the colloidal solution is another approach to the formation

of Gold nanoparticles controlled by size. Au-NPs can be produced by the reduction of chloroauric acid (HAuCl₄), which after dissolution causes the reduction of Au₃⁺ ions into neutral gold atoms.

A possible reaction to synthesize Au from chloroauric acid is as follows:



Gold gradually begins to precipitate in the form of subnanometers particles that blend with each other. The nucleation kinetics of AuNPs has been studied by Szymongdy e Svedberg [51] who have seen that the size of the AuNPs that come to forming strongly depend on the salt ratio of gold / reducing agent.

The use of the reducing agent is due to the aim of reducing to zero state the elements from which nanoparticles are to be obtained.

To make the synthesis efficient, however, it is also necessary to use stabilizers that control the initial growth of nanoclusters and their eventual agglomeration.

For example, in the synthesis of AuNPs, sodium citrate can be used both the function of reducing agent and that of stabilizing agent (acts then as a "capping agent", ie as a stabilizer and an inhibitor of the coalescence effect). The layer of citrate anions absorbed on the surface of nanoparticles separates from these and the presence of this Colloidal suspension can be detected by the reflection of a laser beam from particles. The stabilizing agent is usually a charged molecule that surrounds the NP and makes it into so that they repel and remain distant: these molecules have an end that is adsorbed or chemically bound to the surface of the gold, while the other end is facing the solution. The procedure with sodium citrate, is the most cited method for the synthesis of colloids of gold. With this method the obtained nanoparticles have size between 10 and 20 nm.

To produce larger particles, it is necessary to add less sodium citrate (possibly up to 0.05%): the lower is its quantity present in solution, the greater the diameter of the obtained particles will be. Indeed, the reduction of the amount of sodium citrate will reduce the amount of citrate ions available to stabilize the particles, and this will cause the latter to aggregate into larger structures. The liquid-chemical methods are instead based on the precipitation of a solid from a solution or the chemical conversion of a colloidal dispersion into a gelatinous body. The Sol-Gel technique (Figure 2.7) is part of the latter class, and consists of the passage from a liquid phase

of sol (chemical solution), which acts as a precursor, to a gel solid (integrated network of particles) through hydrolysis and condensation reactions. The drying and post-heat treatments solidification are generally used to eliminate the liquid phase from the gel, promote further condensation and increase properties mechanical. Finally, oxides will be formed.

The sol consists of particles suspended in a liquid having a conventionally included diameter between 1 nm and 1 μm and is typically obtained from precursors such as alkoxides of metals or metalloids.

These are obviously just some of the methods of synthesis: infact in the las years research in the field of nanomaterials has allowed the development of many other ways.

Among the advantages of the chemical synthesis of AuNPs we have: the possibility to use different solvents / reaction environments and good control of the form and the NP size. However, the disadvantages are not negligible at all they are mainly linked to the presence of stabilizers and binders on the surface of AuNPs. These, although necessary, can complicate further functionalization of NPs because it makes the superficial atoms less accessible. This situation is particularly disadvantageous in the field of catalysis where a highly accessible and free contaminants surface is required, or in the study of AuNP physico-chemical interactions in certain environments, since the role of the metal core is hidden.

Furthermore, the use of different reagents during synthesis and the presence of stabilizers on the finished product also raise a further problem concerning biocompatibility. Last but not least, it is the problem of product purification: this is a very long process, which can bring to the production of large quantities of waste material and it is possible that traces of toxic substances remain in the purified product. Today both the physical and chemical syntheses of Au-NPs, conducted with laser ablation or with chemical reactions, have the advantage of being simple, fast, cheap and well reproducible, so there are no excessive difficulties in the preparation of NPs.

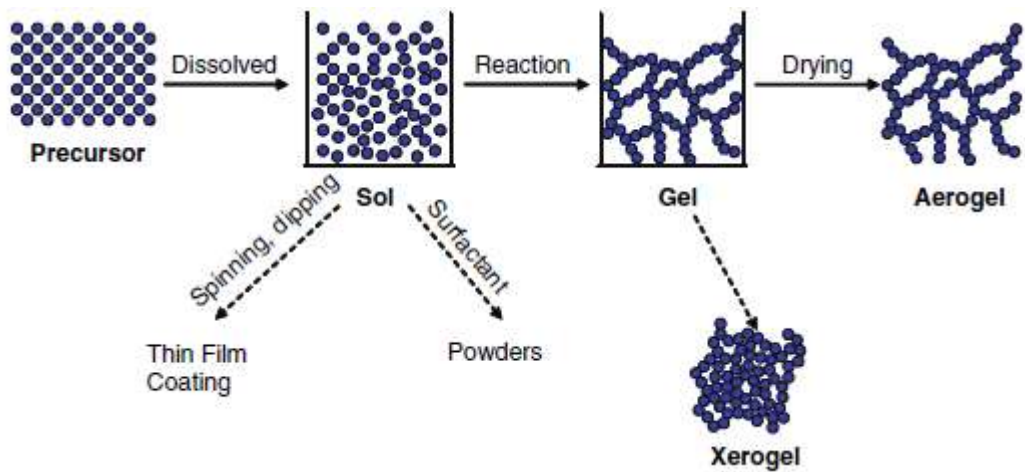


Fig. 2.7- Basic flow of a sol-gel process.

2.4. Physical Characterization of Nanoparticles

The characterization of nanoparticles consists of going to study them through different physical techniques such as:

- TEM (transmission electron microscopy): through a beam of electrons that goes through the sample, it is possible to analyze possible mixings, twins and defects present in it. The beam must pass along the optical axis for a complex system of magnetic lenses that will drive the electrons.
- SEM (scanning electron microscopy): even in this case the source of radiation is not light, but a beam of electrons, which will hit the sample, from which many particles are emitted, such as secondary electrons, which will give us a two-dimensional or three-dimensional image of the sample surface, and backscattered electrons, which instead provide information on the chemical composition of the sample.
- EDX (Energy Dispersive X-ray Spectrometry) is an analytical technique used for the elemental analysis or chemical characterization of a sample. Its characterization capabilities are due in large part to the fundamental principle that each element has a unique atomic structure allowing a unique set of peaks on its electromagnetic emission spectrum (which is the main principle of spectroscopy).
- XRD (X-ray diffraction): thanks to this information is obtained on the crystallographic structure and chemical composition of the sample.
- UV-Visible and IR spectroscopy: these are two absorption spectroscopic techniques for the characterization of materials, as well as for the study of chemical bonds in physical chemistry.
- NMR (nuclear magnetic resonance): this technique exploits the magnetic properties of some atomic nuclei and their behavior when they are immersed in an external magnetic field.

Combining the results of these analyses we can determine some characteristics of the nanoparticles, such as the size, the morphology, the degree of crystallinity, the solubility, the aggregation, the porosity. These are just some of the many techniques used to analyze nanoparticles.

2.5.1 Electron Microscopy: TEM and SEM

The electron microscope is a type of microscope that exploits, like source of radiation, a beam of electrons. The power of resolution of a microscope is inversely proportional to the wavelength of the radiation that it uses, therefore, using an electron beam is possible to reach a resolution several orders of magnitude. Therefore, with the electron microscope you get much higher magnifications. In principle, an electron microscope works like a normal optical microscope if you use light with a very low wavelength. Two types of well-known electron microscopes are the transmission electron microscope (TEM) and the scanning electron microscope (SEM) whose internal structures are schematized in the Figure 2.8.

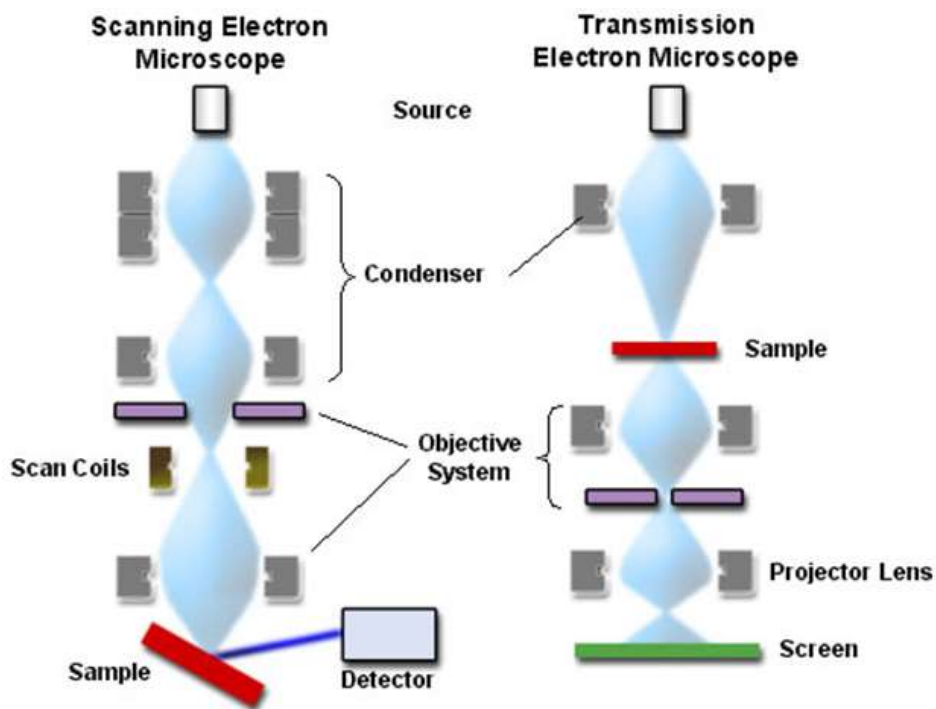


Fig. 2.8 Comparison of ray path diagram between SEM and TEM

Both they employ an electron beam directed at the sample, however, the methods by which the images are produced and enlarged are completely different.

2.5.1.1 TEM (*Trasmission Electron Microscope*)

In TEM the electrons that make up the beam pass through a section in which, previously, the vacuum was created, and then passed completely through the sample. This, therefore, must have an extremely reduced thickness, between 50 and 500 nm. The power of resolution (the minimum distance between two points for which we can distinguish as such and not as one only) is about 0.2 nm, that is about 500 thousand times greater than that of the human eye.

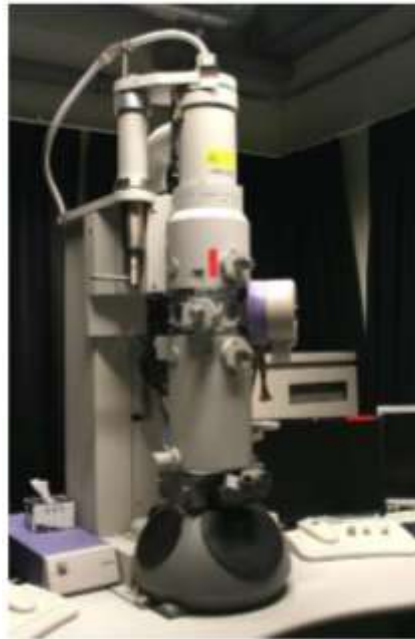


Fig. 2.8- A classic transmission electron microscope (TEM)

This type of microscope is provided, along the electro-optical axis, of complex systems that by exploiting the modification of electric and magnetic fields, are consequently able to drive the electrons through magnetic "lenses" necessary to considerably enlarge the electron beam, already passed through the sample, to ensure that the image is enlarged. The sample consists of sections, as we said, very thin, resting on a small copper or nickel disk (with a diameter of a few millimeters) usually fenestrated to the network ("retino") so that the section can be observed between its meshes without glass interposition (unlike what happens in the optical microscope) that would not be crossed by electrons. The latter in fact can not cross thick materials. The electron beam hits a fluorescent screen (sensitive to them) projecting on it a real and strongly enlarged image of the previously crossed sample

portion. This microscope provides black and white images, but many times there are images obtained from the same that were subsequently processed digitally improving the image [52].

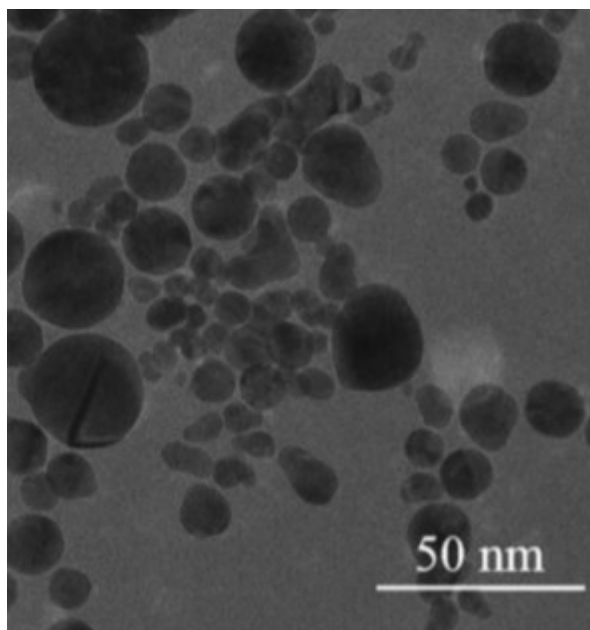


Fig. 2.9- TEM images of the synthesised Au-NPs in DW

2.5.1.2 SEM (Scanning Electron Microscope)

The SEM (Scanning Electron Microscope) is perhaps the most used tool for the characterization of nanomaterials. Thanks to it it is possible to obtain images from secondary electrons of organic and inorganic materials with a resolution of tens of nanometers. SEM exploits a beam of focused primary electrons that hit the sample [53]. The beam is generated by an electronic source, concentrated by a series of electromagnetic lenses and deflected by an objective lens. The latter, in addition to further refocusing the beam, requires a controlled deflection to allow it to scan areas of the sample. One of the possible effects produced by the interaction between the electron and the matter is revealed and transformed into an electrical signal that, when treated and amplified, is modulated in a television signal: 1 pixel of a monochromatic monitor is associated with 1 point of the sample and it is brighter the more the signal is intense. The magnification is given by the ratio between the size of the image and the size of the region on which the scan was performed. These electrons are captured by a detector and converted into electrical impulses that are

sent in real time to a screen (a monitor) where a similar scan is performed simultaneously.

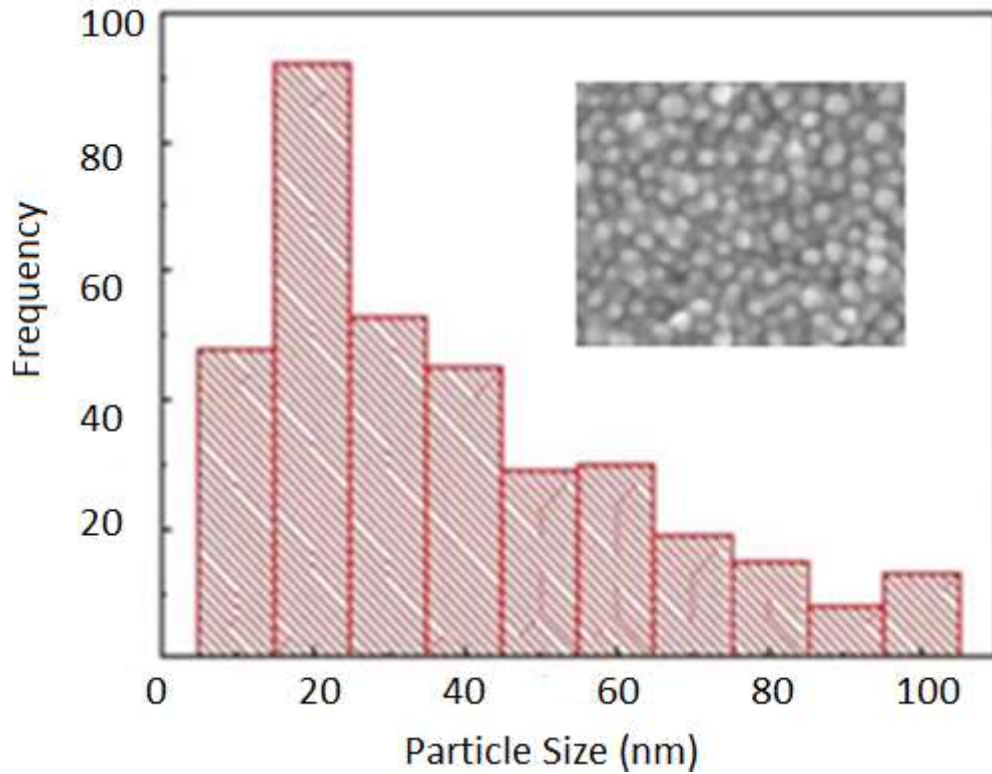


Fig 2.10- Image obtained with the SEM of silver nanoparticles (5 nm size).

The result is a high resolution black and white image with a large depth of field, which has characteristics similar to those of a normal photographic image. The SEM must operate in a vacuum (with pressures below 10^{-3} Pa) and the sample must be conductive and grounded, so as to be able to remove any possible accumulation of charge from the analysis area which would make it impossible to the observation. Non-conductive samples can however be observed at SEM by operating metallic coatings or by dehydrating the wet samples.

2.5.1.3 EDX (Energy-dispersive X-ray spectroscopy)

Each atom has a unique number of electrons that are, under normal conditions, in specific positions, as shown in Figure 2.11. These positions belong to different energy levels. The generation of X-rays in the SEM is a two-step process. In the first phase, the electron beam hits the sample and transfers part of its energy to the sample atoms [54]. This energy can be used by the electrons of atoms to "jump" on a higher energy level or to "jump out" from the atom. If this transition occurs, the electron leaves a hole behind it. The holes have a positive charge and, in the second phase of the process, they attract negatively charged electrons coming from higher energy levels. When an electron fills the hole with a lower energy level, the energy difference of the transition can be released in the form of X-rays.

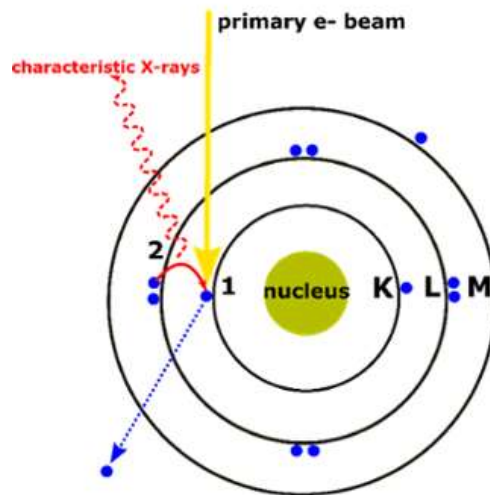


Figure 2.11- The X-ray formation process 1) The energy due to the ejection of the electron leaves a hole behind it 2) Its position is filled by another electron from a higher energy level and the generated X ray.

The X-ray has an energy represented by the difference in energy between these two levels. It depends on the atomic number, which is a unique property of each element. In this way, X-rays therefore represent a "fingerprint" of each element and can be used to identify the different types of elements contained in a sample. To detect them, the most recent EDX systems use the so-called silicon-drift detectors (SDDs). superior to the traditional Si (Li) detectors thanks to the highest count, the best resolution and the fastest analytical skills.

These detectors are positioned at a very close given angle to the sample and have the ability to measure the energy of incident photons, coming from X-rays. The higher the solid angle between the detector and the sample, the greater the probability of detecting X-rays, and thus obtaining better results. The data generated by the EDX analysis consist of spectra with peaks corresponding to all the different elements present in the sample (Fig.2.12).

Moreover, the EDX can be used both in the qualitative analysis (the types of elements) and the quantitative one (the percentage of concentration of each element in the sample). In most SEMs, dedicated software allows the identification of peaks and the calculation of the atomic percentage of each element that is detected. Another advantage of the EDX technique is that it is a non-destructive characterization technique that requires little or no sample preparation.

EDX analysis has become a common technique today and it is so useful that it has become an essential part of the SEM. The image has the ability to know what the sample contains.

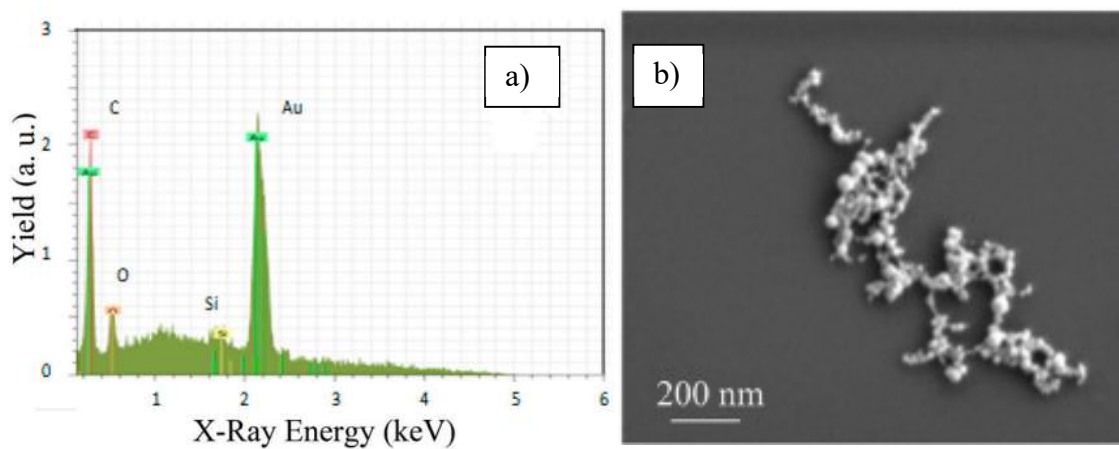


Figure 2.12 a) The EDX spectrum of the Au-NPs suspension, b) SEM photo of AuNps in solution.

2.5.2 Optical Spectroscopy (UV-Vis Spectroscopy)

Optical spectroscopy is based on the Bohr-Einstein relationship:

$$\Delta E = E_2 - E_1 = h\nu \quad (2.11)$$

This relationship links the discrete atomic or molecular energy states E_i with the frequency ν of the electromagnetic radiation. Since the energy levels of matter are quantized, the molecules interact with electromagnetic radiation absorbing or yielding energy, passing from lower energy states to higher energy states (absorption) or from higher energy states to lower energy states (emission). In each possible case, an electron is excited from a full (low energy, ground state) orbital into an empty (higher energy, excited state) anti-bonding orbital. Each wavelength of light has a particular energy associated with it. If that particular amount of energy is just right for making one of these electronic transitions, then that wavelength will be absorbed [55]. The larger the gap between the energy levels, the greater the energy required to promote the electron to the higher energy level. Many compounds absorb electromagnetic radiation in the regions of the visible (vis) and ultraviolet (UV) in the region from 200-800 nm. The absorption of UV or visible radiation corresponds to the excitation of outer electrons. There are three types of electronic transitions which can be considered: transitions involving p, s, and n electrons, transitions involving charge-transfer electrons, transitions involving d and f electrons. When an atom or molecule absorbs energy, electrons are promoted from their ground state to an excited state. In a molecule, the atoms can rotate and vibrate with respect to each other. These vibrations and rotations also have discrete energy levels, which can be considered as being packed on top of each electronic level. Absorption of light in the UV-visible region will only result in the following transitions n and π Fig. 2.12:

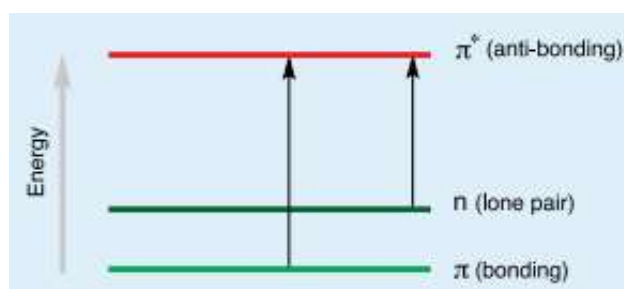


Fig 2.12- Transitions of absorption of light in the UV- Vis region.

UV-visible spectrometers can be used to measure the absorbance of ultra violet or visible light by a sample, either at a single wavelength or perform a scan over a range in the spectrum. The UV region ranges from 190 to 400 nm and the visible region from 400 to 800 nm. The technique can be used both quantitatively and qualitatively. A schematic diagram of a UV-visible spectrometer is shown in Fig. 2.13.

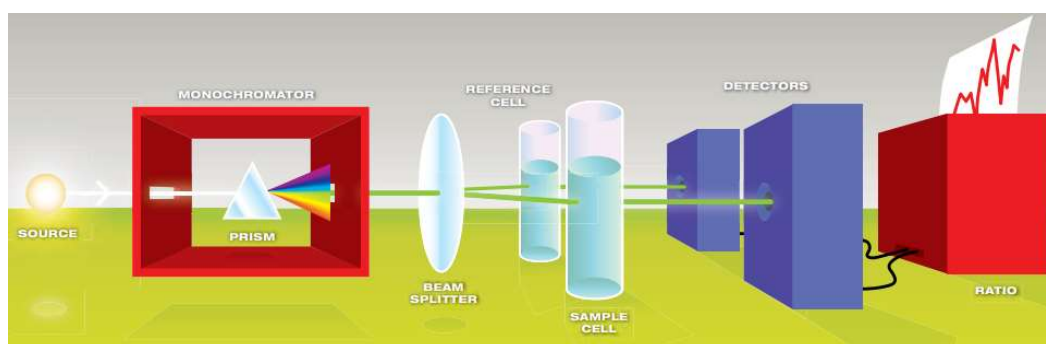


Fig. 2. 13- Schematic diagram of the UV-visible spectrometer

The light source (a combination of tungsten/halogen and deuterium lamps) provides the visible and near ultraviolet radiation covering the 200–800 nm. The output from the light source is focused onto the diffraction grating which splits the incoming light into its component of different wavelength, like a prism but more efficiently. For liquids the sample is held in an optically flat, transparent container called a cell or cuvette. The reference cell or cuvette contains the solvent in which the sample is dissolved. For each wavelength the intensity of light passing through both a reference cell (I_0) and the sample cell (I) is measured. If I is less than I_0 , then the sample has absorbed some of the light. The absorbance (A) of the sample is related to I and I_0 according to the following equation:

$$A = \log_{10} \frac{I_0}{I} \quad (2.12)$$

The detector converts the incoming light into a current, the higher the current the greater the intensity. An acquisition software usually plots the absorbance against wavelength (nm) in the UV and visible section of the electromagnetic spectrum. According to the Beer-Lambert law the absorbance is proportional to the

concentration of the substance in solution and as a result the UV-visible spectroscopy can also be used to measure the concentration of a sample [64]. The Beer-Lambert law can be expressed in the form of the following equation:

$$A = \epsilon cl \quad (2.13)$$

where A is the absorbance, l is the optical path length, i.e. the dimension of the cell or cuvette (cm), c is the concentration of solution ($\text{mol}\cdot\text{dm}^{-3}$) and ϵ is the molar extinction coefficient, which is constant for a particular substance at a particular wavelength ($\text{dm}^3\cdot\text{mol}^{-1}\text{cm}^{-1}$).

An absorption spectrum will show a number of absorption bands corresponding to electronic transitions within the molecule (Fig. 2.14).

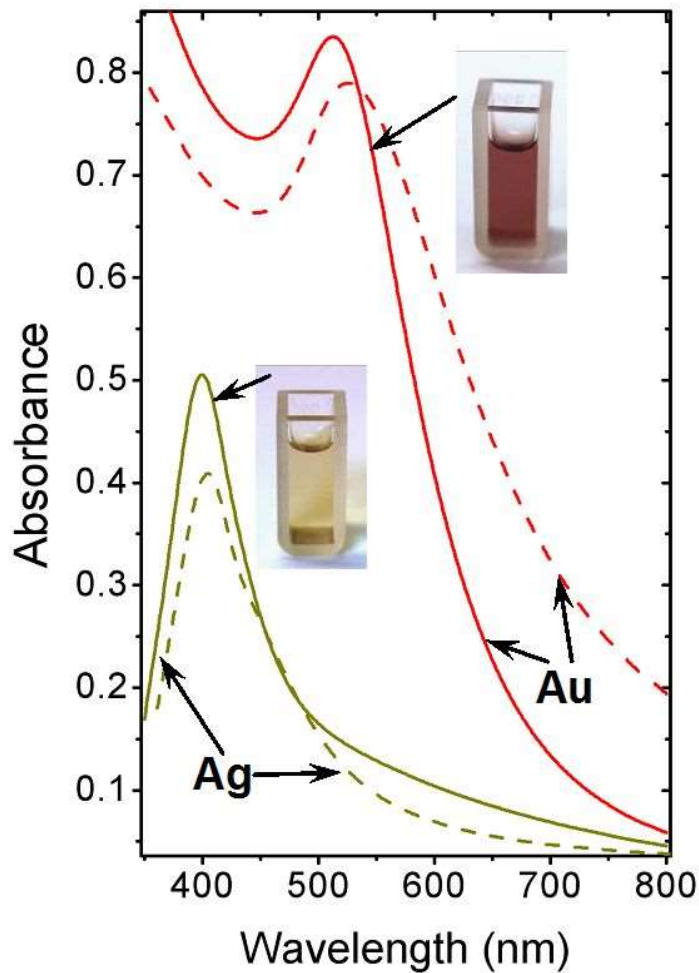


Fig. 2.14- Au NPs and Ag NPs typical absorbance curves.

2.5.3 X-Ray Diffraction (XRD)

X-ray diffractometry (XRD) is a widely used technique for the study of mass properties of a solid. This technique allows to determine:

- the crystallinity of a solid or component
- the estimate of the size of the microcrystals present
- the type of phases present
- the size of the cell unit and the type of atoms that compose it.

The analysis is carried out by making to hit the sample with a collimated beam of X-rays which is only diffracted in particular directions of space, depending on the crystalline phases present following the law of Bragg:

$$n\lambda = 2d \sin \vartheta \quad (2.14)$$

where n is an integer; λ is the wavelength of the incident X-ray; d is the distance between the atomic layers in a crystal and θ is the angle of incidence [56]. The intensity of the diffracted beam is measured as a function of the diffraction angle and the orientation of the sample. This law relates the wavelength of electromagnetic radiation to the diffraction angle and the lattice spacing in a crystalline sample. These diffracted X-rays are then detected, processed and counted. By scanning the sample through a range of 2θ angles, all possible diffraction directions of the lattice should be attained due to the random orientation of the material. The conversion of the diffraction peaks to d -spacings allows identification of the mineral because each mineral has a set of unique d -spacings. Typically, this is achieved by comparison of d -spacings with standard reference patterns. All diffraction methods are based on generation of X-rays in an X-ray tube. These X-rays are directed at the sample, and the diffracted rays are collected. A key component of all diffraction is the angle between the incident and diffracted rays. X-ray diffractometers consist of three basic elements: an X-ray tube, a sample holder, and an X-ray detector.

X-rays are generated in a cathode ray tube by heating a filament to produce electrons, accelerating the electrons toward a target by applying a voltage, and bombarding the target material with electrons. When electrons have sufficient energy to dislodge inner shell electrons of the target material, characteristic X-ray spectra are produced. These spectra consist of several components, the most common being K_{α} and K_{β} . K_{α} consists, in part, of $K_{\alpha 1}$ and $K_{\alpha 2}$. $K_{\alpha 1}$ has a slightly shorter wavelength and twice the intensity as $K_{\alpha 2}$. The specific wavelengths are characteristic of the target material (Cu, Fe, Mo, Cr). Filtering, by foil or crystal monochromator, is required to produce monochromatic X-rays needed for diffraction. $K_{\alpha 1}$ and $K_{\alpha 2}$ are sufficiently close in wavelength such that a weighted average of the two is used. Copper is the most common target material for single-crystal diffraction, with CuK_{α} radiation at a $\lambda=1.5418 \text{ \AA}$. These X-rays are collimated and directed onto the sample. As the sample and detector are rotated, the intensity of the reflected X-rays is recorded. When the geometry of the incident X-rays impinging the sample satisfies the Bragg Equation, constructive interference occurs and a peak in intensity show up. A detector records and processes this X-ray signal and converts the signal to a count rate which is then output to a device such as a printer or computer monitor. The geometry of an X-ray diffractometer is such that the sample rotates in the path of the collimated X-ray beam at an angle θ while the X-ray detector is mounted on an arm to collect the diffracted X-rays and rotates at an angle of 2θ . The instrument used to maintain the angle and rotate the sample is termed a goniometer.

XRD analyses were performed on monometallic or bimetallic nanometric suspensions with the aim of determining the crystalline phases present and the dimensions of nanoparticles. The Debye-Scherrer equation was used to evaluate the crystallite size:

$$d = \frac{K\lambda}{b\cos\theta} \quad (2.15)$$

where b is the width at half height of the reflection, θ is the angle of incidence, λ is wavelength of the incident X ray and $K \sim 0.9-1$.

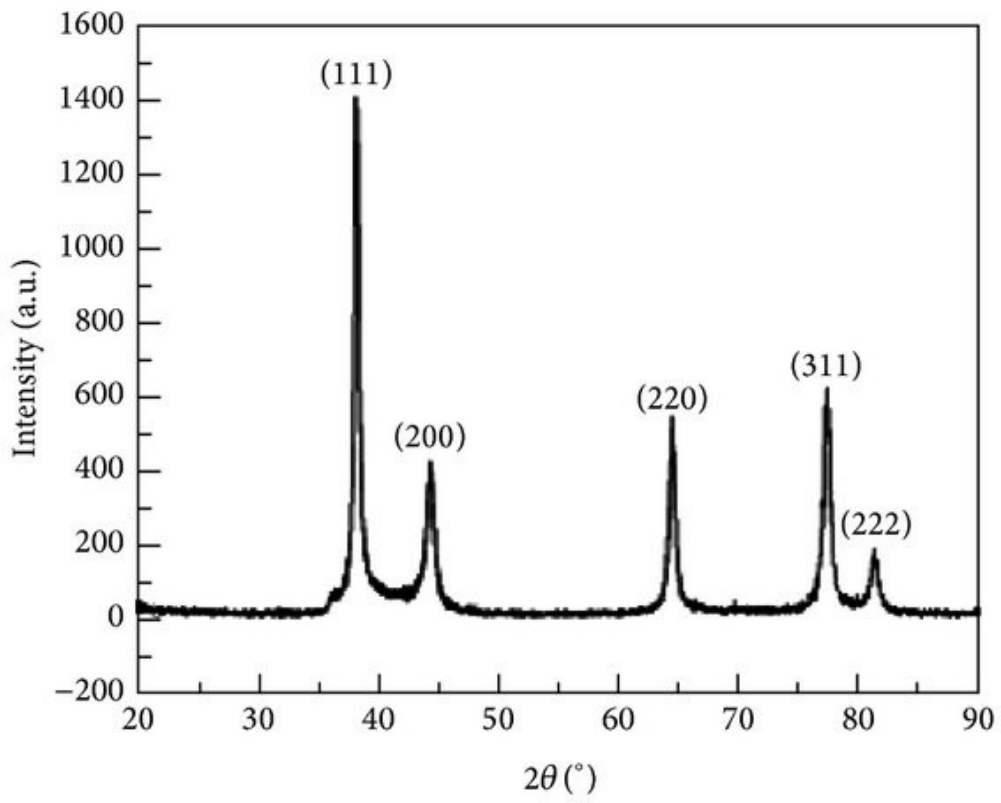


Fig. 2.15- X-ray diffraction pattern of the silver nanoparticles [57].

2.5.4 Raman Spectroscopy

Raman diffusion or scattering means the study of diffused light by a material medium; diffusion occurs when by sending a ray of light onto a material medium we can observe light even in different directions from the initial propagation of the ray. The Raman diffusion experiment is performed by sending on the sample a laser radiation, and therefore highly monochromatic, of frequency ω_L and collecting the diffused radiation of frequency ω_i at a certain angle, usually at 180° (back-scattering conditions). The frequency ω_i may be lower or higher than the incident one. In these cases we speak of anelastic scattering [58]. Usually the different frequency depends on the coupling of the radiation with the vibrations of the sample under examination. Lasers in Raman spectroscopy are very beneficial for the following reasons:

- Diffuse radiation is in itself much weaker than elastic radiation. So using a very intense source like a laser allows us to observe a measurable amount of diffuse radiation.
- The high monochromaticity of a laser source allows us to observe very small Raman shifts. Remembering that the Raman shift is the difference in wave numbers between incident and diffuse radiation, and that the energies that separate the vibrational states are much smaller than the visible laser light energy, it is obvious that if the source is extremely monochromatic does not overlap with diffuse radiation which differs at most by a few thousand cm^{-1} .
- The highly monochromatic radiation also allows us to use selective filters (notch filter) that exclude it from diffuse radiation thus avoiding the blindness of the detector and allowing only the inelastic scattering components to be collected.

In a Raman spectrum three different components can be observed:

- Elastic components: in this case the radiation emitted by the material medium has the same frequency as the incident one, ie $\omega_i = \omega_L$. This type of component is also called Rayleigh scattering.

• Inelastic components: also called Raman scattering, in this case the radiation diffused by the material medium has a different frequency from the incident one, that is $\omega_i \neq \omega_L$. The Raman components in turn are subdivided into Stokes and anti-Stokes. The Stokes have frequency $\omega_i < \omega_L$ while the anti-Stokes have frequency $\omega_i > \omega_L$ (Fig. 2.16).

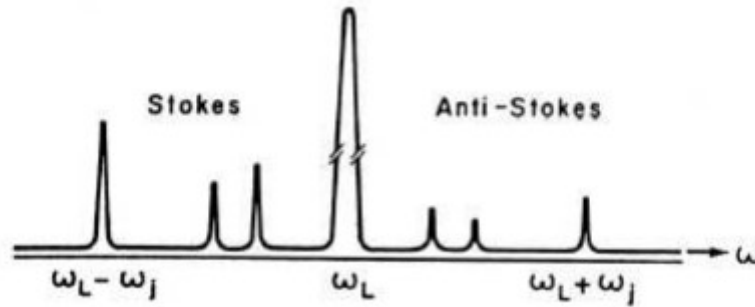


Fig. 2.16- Schematic representation of a Raman spectrum, with the Stokes and anti-Stokes branches.

The vibration modes of the molecules are responsible for Raman scattering phenomena and in the spectrum, the relative position of the peak is independent of the incident frequency ω_L and energy is characteristic of the vibrational state responsible for scattering. In fact, the Raman spectra do not report the absolute frequencies or wavelengths, but rather a difference of these, which makes them independent of the frequency of the incident radiation.

This difference is called Raman shift and is reported in wave numbers:

$$\Delta v = v_L - v_i = \frac{1}{\lambda_L} - \frac{1}{\lambda_i} \quad (2.16)$$

In the Stokes spectra the Raman shift is positive while in the anti-Stokes it is negative. Therefore Raman spectroscopy serves to investigate vibrational states. Stokes and anti-Stokes peaks are symmetrical with respect to Rayleigh's central scattering peak, but in practice only Stokes are observed because they are more intense. A photon with $\hbar\omega_L$ energy of the incident ray is destroyed and the molecule switches to a virtual excited state from which it instantly decays by emitting a photon of energy $\hbar\omega_S$. If the photon emitted has the same energy as the incident photon then it is called Rayleigh scattering and in this case the molecule is excited

by the vibrational state $v = 0$ of the fundamental electronic state in the virtual excited state, then it decays at the vibrational level $v = 0$ of the fundamental electronic state.

If instead the emitted photon has lower energy than the destroyed photon then we are in the presence of Raman-Stokes scattering and in this case the molecule is excited by the vibrational state $v = 0$ of the fundamental electronic state in the virtual excited state, then it decays instantly to the vibrational level $v = 1$ of the fundamental electronic status. It is observed that the difference of energy absorbed and emitted ($\hbar\omega_L - \hbar\omega_S$) corresponds precisely to the energy of the involved vibrational state. In the last case the emitted photon has higher energy than the incident, this because the molecule by thermal effect is already at the vibrational level $v = 1$ of the fundamental electronic state, then excitation takes place in the virtual excited state, after which the molecule decays at the vibrational level $v = 0$ of the fundamental electronic state. Therefore the energy of the emitted photon is

$$\hbar\omega_s = \hbar\omega_L + \hbar\omega_i \quad (2.17)$$

where is it $\hbar\omega_i$ is the energy of the vibrational quantum. The latter case generates the anti-Stokes branch of the spectrum. When the frequency of the incident laser beam is close to or corresponds to that of an electronic transition of the sample under consideration, it is called resonant Raman. In this case the detected signals are more intense but the bandwidth still remains that typical of a vibrational spectrum.

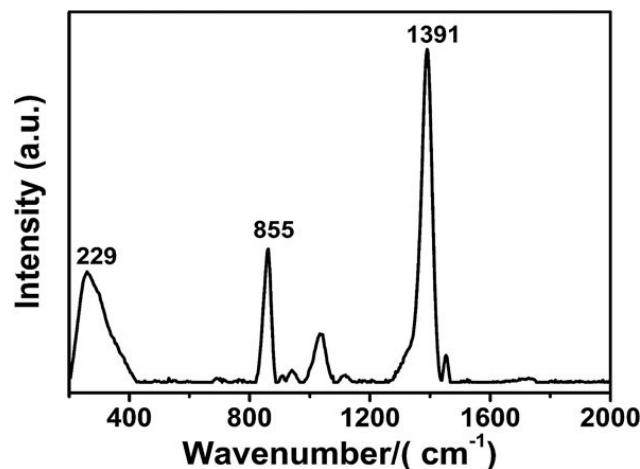


Fig. 2.17- The Raman spectrum of the silver nanoparticles acquired at 785 nm excitation [59].

3. Modification of the material using Metallic Nanoparticles

3.1. Wettability

The introduction of nanoparticles in liquids generally improves the wetting ability and changes other properties of the solution, due to the different distribution of the adhesion forces, to the nature, morphology and concentration of the added nanoparticles. The inclusion of metallic nanoparticles in a liquid, at different concentrations, modifies significantly the solution properties, especially in physical terms concerning the surface tension, density, viscosity, thermal and electric conduction, vapour pressure, and other parameters [60].

Wettability describes the preference of a solid to be in contact with one fluid rather than another. Although the term “preference” may seem odd when describing an inanimate object, it aptly describes the balance of surface and interfacial forces. A drop of a preferentially wetting fluid will displace another fluid; at the extreme it will spread over the entire surface. Conversely, if a nonwetting fluid is dropped onto a surface already covered by the wetting fluid, it will bead up, minimizing its contact with the solid. Wettability studies usually involve the measurement of contact angles as the primary data, which indicates the degree of wetting when a solid and liquid interact. The wetting ability of the liquid on a given surface changes introducing specific nanoparticles at the interface. This aspect is of special interest in Biology and Medicine, especially due to the impact on the protein absorption and the cellular response in ambit of biological tissues-biomaterial interface [61]. The contact angle of the liquid in presence of nanoparticles may be altered depending on the surface properties, such as composition, chemical reactivity, roughness, crystalline structure, grain contours, porosity, permeability, etc. [62]. The contact angle θ depends on the balance of the forces of adhesion and cohesion of the liquid to the substrate in presence of air. If θ is greater than 90° the surface is hydrophobic while if θ is less than 90° the surface is hydrophilic. The contact angle can be calculated by the Young equation 3.1:

$$\cos\theta = \frac{\gamma_{SG} - \gamma_{SL}}{\gamma_{LG}} \quad (3.1)$$

where γ_{SG} is the surface tension of the solid (in equilibrium with the saturated vapour of the liquid), γ_{SL} is the surface tension between solid and liquid, and γ_{LG} is the surface tension of the liquid (in equilibrium with its vapour saturated). Consider a liquid drop resting on a flat, horizontal solid surface (Fig. 3.1) [63].

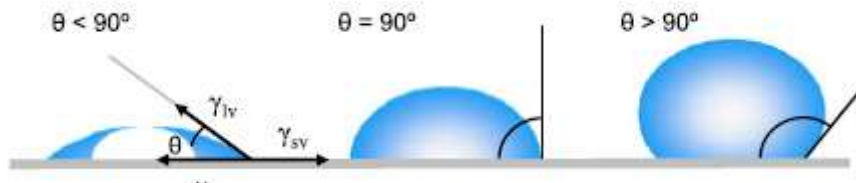


Fig. 3.1- Illustration of contact angles formed by sessile liquid drops on a smooth homogeneous solid surface

The contact angle is defined as the angle formed by the intersection of the liquid-solid interface and the liquid-vapor interface (geometrically acquired by applying a tangent line from the contact point along the liquid-vapor interface in the droplet profile). The interface where solid, liquid, and vapor co-exist is to as the “three phase contact line”. Figure 3.1 shows that a small contact angle is observed when the liquid spreads on the surface, while a large contact angle is observed when the liquid beads on the surface. More specifically, a contact angle less than 90° indicates that wetting of the surface is favorable, and the fluid will spread over a large area on the surface; while contact angles greater than 90° generally means that wetting of the surface is unfavorable so the fluid will minimize its contact with the surface and form a compact liquid droplet. For example, complete wetting occurs when the contact angle is 0° , as the droplet turns into a flat puddle [64]. Furthermore, contact angles are not limited to the liquid-vapor interface on a solid; they are also applicable to the liquid-liquid interface on a solid. Ideally, the shape of a liquid droplet is determined by the surface tension of the liquid. In a pure liquid, each molecule in the bulk is pulled equally in every direction by neighboring liquid molecules, resulting in a net force of zero. However, the molecules exposed at the surface do not have neighboring molecules in all directions to provide a balanced net force. Instead, they are pulled inward by the neighboring molecules (Fig. 3.2), creating an internal pressure. As a result, the liquid voluntarily contracts its surface area to maintain the lowest surface free energy. From everyday life, we know that small droplets and bubbles are spherical, which gives the minimum surface area for

a fixed volume. This intermolecular force to contract the surface is called the surface tension, and it is responsible for the shape of liquid droplets. In practice, external forces such as gravity deform the droplet; consequently, the contact angle is determined by a combination of surface tension and external forces (usually gravity). Theoretically, the contact angle is expected to be characteristic for a given solid-liquid system in a specific environment [65].



Fig. 3.2 Surface tension is caused by the unbalanced forces of liquid molecules at the surface.

3.2. Wettability of Biological Liquids with Metallic Nanoparticles

The wetting ability of the liquid changes introducing specific nanoparticles and the resulting adhesion of the liquid to a surface may be drastically modified. This aspect is of special interest in Biology and Medicine because it has been demonstrated that the wetting ability determines the protein absorption and the cellular response and represents a key parameter for the success of prostheses implantation and functionality in human body [66-67]. Some devices, such as removable catheters and orthopedically implants, intraocular lens and part of mobile prosthesis, need to have hydrophobic surfaces to avoid or reduce the cell growth on their surface. Other devices, instead, must be anchored permanently to the bone or to other tissues and must promote the cellular growth, thus their surface must be highly hydrophilic. The contact angle of the liquid in presence of nanoparticles may be altered depending on the surface properties, such as composition, chemical reactivity, roughness, crystalline structure, grain contours, permeability, etc. On this aspect our attention is focused because it is interesting to understand if the use of specific metallic nanoparticles in general enhances the properties of hydrophobic or hydrophilic behaviour of the used solution on specific surfaces. The goal of this investigation is that to study the effects of biocompatible nanoparticles when inserted in physiologic liquids or deposited on different biocompatible surfaces. The use of some biocompatible nanoparticles, species at low concentration in water, in physiological solutions and blood, determining a different wetting ability with respect to different substrate surfaces, will be presented and discussed.

3.2.1 Used Materials

Metallic nanoparticles of Ti, Cu, Ag and Au, with spherical shape and average diameter within 10 and 100 nm, produced by laser, were used in this experiment. Liquid solutions based on distilled water and saline solutions were used without and with addition of metallic nanoparticles. The physiological liquid (PL) is represented by a saline solution (Fresenius Kabi Italia 0.9%) composed of 9 gr NaCl dissolved in 1000 ml of water. The used concentrations in water and in PL were: 1.0 mg/15 ml for Ti; 1.7 mg /15 ml for Cu; 2.3 mg /15 ml for Ag; 5.6 mg /15 ml for Au. Flat and polished surfaces of different materials were considered for the presented study. They consist in high pure (99.9%) polyethylene (PE), polymethylmethacrylate (PMMA), Aluminum, Silicon, Titanium, Copper, and glass based on SiO₂. The polishing procedure in all substrates was performed accurately to obtain the minimum surface roughness. It was first mechanical, using hard abrasives with sub-micrometric size, and successively ionic by using ion sputtering processes obtained using an ion gun of nitrogen ions at the 1 keV energy and doses of the order of 1016/cm². Also human blood was used for this experiment. The blood was taken, from a healthy volunteer; in a laboratory of clinical analyzes and then stored in the original sterile tube (BD Vacutainer K3E) with 5.4mg Ethylenediaminetetraacetic acid (EDTA) at a temperature between 2–6°C. The liquid solution of EDTA binds calcium ions thus inhibiting the coagulation cascade, preserving the blood. In order to avoid the possible deterioration of blood, the measurements of contact angle were performed within 5 days from donation. Before the experiment, the tube was agitated to homogenise the solution and for a long time, until the room temperature was reached.

3.2.2 Methods of analysis

The used method to measure the wetting angles is the “sessile drop” that involves the profile observation of a liquid droplet deposited on a cleaned solid surface. The drop is generated depositing 1µl liquid on the flat and horizontal surface with a

microsyringe. A CCD camera (Pixera) connected to the eyepiece of an aligned optical microscope records the images of the drops and of the substrate cross-section. A dedicated software permits to calculate the contact angle and, for each substrate, to evaluate the angle between the horizontal line and the tangent line to the point where the drop curve liquid is in contact with the solid plane.

The wettability was measured using distilled water, physiological liquid and human blood. The wettability measurements were performed in three modes: using pure liquids on the different pure substrates; using liquids containing metallic nanoparticles (NPs) on the different substrates; and using liquids deposited on substrates whose surface was preventively covered by a layer of metallic nanoparticles. This coverage occurred through previous drops of water, containing little quantity of polyvinyl alcohol (1%) and nanoparticles, deposited on the cleaned surface and followed by a drying process obtained maintaining the substrate for 24h at a constant temperature of 50°C. The drop surface shape will depend on the resulting R of the cohesion forces, F_c (normal to the tangent to the profile of the liquid in P and facing the inside), and of the adhesion forces, F_a (normal to the solid surface in P facing towards it), applied to the point P, point of contact between the three surfaces: solid-gas (SSG), liquid-gas (SLG) and solid-liquid (SSL). The wettability is quantified as contact angle θ determined by the balance of forces at the interface of the three phases (solid, gas and liquid) and is defined by the Young equation. The measurements of contact angle, performed with an optical microscope, were very accurate and generally were acquired with an indetermination of about 2%. Measurements of surface roughness were carried out in order to correlate the wetting ability of the liquid with the morphology of the substrate. Such measurements were performed in a surface profiler (KLA-Tencon P10) having a depth resolution of 1nm, a maximum depth measurement of 300 microns and a maximum scansion length of 5 mm. The tip of the profiler has a vertical force between 1–50 mg. Generally six measures of surface roughness were carried out, of which it is calculated the average value. The errors about the roughness measurements were evaluated of about 6%. The density ρ of the solutions were measured weighing a known volume V taken by a syringe and using an electronic balance (Kern KB 120-3N, max 121 gr, $d=0.001$ gr) to determine the

mass m . Ten independent measurements of $\rho=m/V$ were taken and averaged (measure error 2%). Surface tension τ measurements were performed by the “method of the dropper” at room temperature and relative humidity (22°C and 35%, respectively), by dripping slowly, from a 1.2mm inner radius R of a glass dropper, the liquid drops on an electronic balance (Kern KB 120-3N, max 121gr, $d=0.001$ gr) to measure their average mass M . The surface tension $\tau=Mg/2\pi R$ was determined from 10 measurements (measure error 2%). Measurements of viscosity η were performed at 22°C by using a glass pipe and measuring the time of outflow of a known volume value of the solution. For each solution 10 measurements were performed relatively to the viscosity value of the distilled water ($\eta=1.0$ mPa s) and was given the average value with a standard deviation of 2%. The density, surface tension and viscosity of the blood depend on the hematocrit (Ht), that in our case, as certificated by the biological analysis laboratory, was $H_t=39.3\%$. The physical properties of the test liquids are summarized in the Table 3.1. SEM analysis and X-ray fluorescence induced by electrons (EDX) analysis were employed to observe the NPs deposited on different substrates using high resolution microscopy. SEM microscopy was performed by using a 20 keV electron beam, produced by a FEI QUANTA—mod. Inspect S microscope, at the Department of Physics *Sciences* of the Messina University. TEM analyses were performed with a FEI Morgagni 268D microscope equipped with a $1k\times 1k$ SiS CCD camera Megaview II, operating at the nominal accelerating voltage of 80 kV.

Table 3.1- Physical properties (density, surface tension and viscosity) of the liquids (human blood, physiologic saline solution and distilled water) used for the measurements of contact angle at room temperature ($T=22^\circ C$). The errors of the three parameters are of the order of 2%.

Liquids	Density [Kg/m ³]	Surface tension [10 ⁻³ N/m]	Viscosity [cP]
Whole Blood	1054 ± 21	62.00 ± 1.2	3.490 ± 0.07
Saline Solution	1063 ± 21	77.00 ± 1.5	0.985 ± 0.02
Distilled Water	997.8 ± 20	72.22 ± 1.4	1.000 ± 0.02

3.2.3 Results

The results of the wettability analysis using the Au NPs are reported, for useful comparison, in Table 3.2. The first line of the table shows that contact angle of the PL on pristine substrate decreases going from copper, to aluminium, polyethylene, titanium, polymethylmethacrylate, silicon and glass, where it was evaluated of 101°, 96°, 94°, 91°, 77°, 67° and 39.61°, respectively. Measurements demonstrate that a different behaviour is observed for use of Cu NPs. In fact, generally the contact angle increases using Cu NPs in the solution, except for Al substrate. In the case of Cu NPs deposited on the surfaces, the contact angle generally decreases, except for glass. The maximum value of the contact angle variation, higher than 100%, is obtained for glass using Cu NPs deposited on its surface. The effect of the surface roughness and surface tension of the solution with NPs (Au, Ti, Ag, Cu) changes the wettability increasing or decreasing the contact angle. All used substrates were employed after an accurate submicrometric polishing procedure tending to obtain a very low roughness at which, generally, high contact angle occurs. Figure 3.3a reports the value of the residual roughness measured in the polished surfaces of the different substrates used for the contact angle measurements. The mean roughness is 0.88 μm in polyethylene, 0.5 μm in glass, 0.1 μm in Al, 0.09 μm in Cu, 0.05 μm in Ti, 0.04 μm in PMMA and Si. The plot inset concerns a typical roughness profile relative to the polished copper surface. At room temperature of 22°C, a relative humidity of 35%, and 1atm environmental pressure, the liquid drops of 1 μl in volume, constituted by distilled water, saline solution or human blood, were deposited on the horizontal face of the polished and perfectly flat substrates. Six measurements of contact angle on drops of test liquids on different points of each substrate were performed; subsequently the average value was substrates.

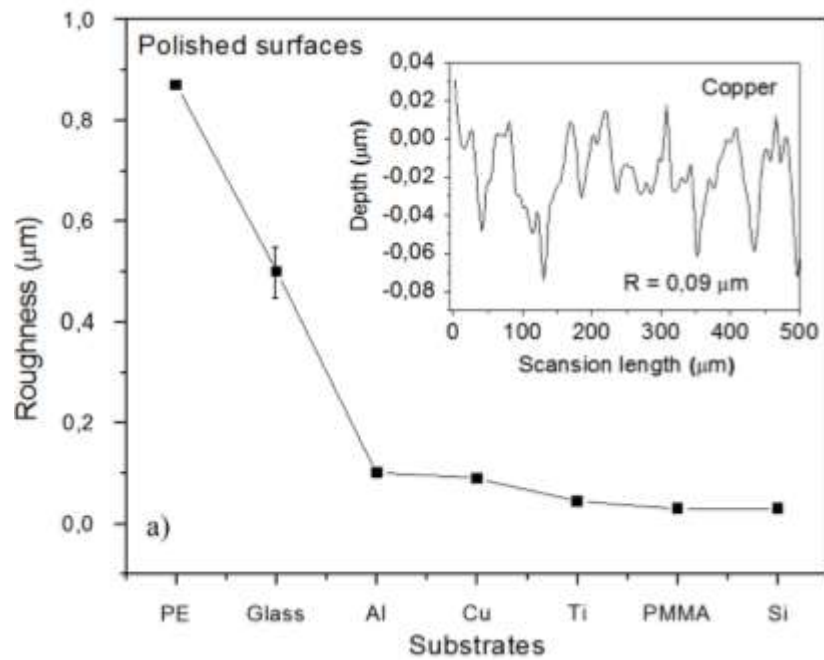




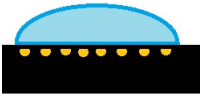





Fig. 3.3- Surface roughness as a function of the nature of the substrate submitted to submicrometric polishing procedure a) and a typical roughness profile in polished copper as inset picture. The vertical bar represents the experimental errors of the order of 6%. Contact angle of distilled water, physiologic saline solution and human blood, using a liquid in which 0.37mg Au NPs/ml were enclosed and deposited on a polished polyethylene surface b).

Six measurements of contact angle on drops of test liquids on different points of each substrate were performed; subsequently the average value was calculated. The reproducibility of the contact angle readings is $\pm 2^\circ$. The evaluated contact angles of the three liquids, containing 0.37 mg Au NPs/ml, with the polyethylene surface, as typical example, are reported in Fig. 3.3 for water (b), saline solution (c) and blood (d).

Table 3.2- Comparison of the experimental contact angles for physiological solutions deposited as they are, with addition of nanoparticles of Au, Ti, Ag and Cu as liquid solution and deposited on surfaces containing layers of nano particles. The errors of the contact angle are of the order of 2%.

Material	Contact angle (degrees)						
	Cu	Al	PE	Ti	PM MA	Si	Glass
Pure physiological liquid on the substrate	101	96	94	91	77	67	39,61
Au NPs							
Au NPs deposited on the substrate 	83	53	80	70	76	30	36
Liquid drops containing Au NPs 	79	84	85	76	70	42	33
Ti NPs							
Ti NPs deposited on the substrate 	84	67	56	70	69	44	40
Liquid drops containing Ti NPs 	87	86	79	73	73	41	46
Ag NPs							
Ag NPs deposited on the substrate 	89	37	51	19	42	16	21
Liquid drops containing Ag NPs 	93	88	90	59	76	59	43

	Cu NPs						
Cu NPs deposited on the substrate 	103	92	97	97	104	108	91
Liquid drops containing Cu NPs 	72	92	89	75	64	41	51

The wettability of the PE with the liquids containing Au NPs grows with increasing the viscosity of the fluid on the surface. The wetting ability increases going from distilled water to saline solution and to blood, i.e. for liquid viscosities growing from 1.0 to 0.985 cP up to 3.490 cP, respectively. Measurements demonstrate that the use of Au NPs decreases the contact angles above reported, enhancing the wetting ability of the surface. Generally the reduction is of the order of 10–20%, but for the Si substrate the reduction assumes a maximum value, of the order of 37 or 55%, depending if Au NPs are embedded in the solution or deposited as thin layer on the solid substrate surface, respectively (table second and third lines, respectively). A similar data comparison is obtained for PL without NPs, with Ti NPs at a concentration of 1.0 mg/15 ml (or with Ag NPs at a concentration of 2.3 mg/15 ml or with Cu NPs at a concentration of 1.7 mg/15 ml), and using PL deposited on the different surfaces on which a layer of Ti NPs (or Ag NPs or Cu NPs) has been previously deposited.

The results of the wetting ability analysis using the different NPs are reported, for useful comparison, in Table 3.2 for the different NPs. Measurements demonstrate that the use of Ti NPs generally decreases the contact angle, with respect to simple PL without NPs, enhancing the wetting ability of the surface, except for glass where the contact angle enhances of about 16%. The reduction assumes a maximum value for the Si substrate, of the order of 39 or 34%, using Ti NPs embedded in the solution or deposited as thin layer on the solid surface, respectively.

The use of Ag NPs also decreases the contact angle enhancing the wetting ability of the surface, except for glass using the solid surface NPs layers, where the contact angle enhances of about 8.6%. The reduction assumes a maximum value for the Si substrate, of the order of 12 or 76%, using Ag NPs embedded in the solution or deposited as thin layer on the solid surface, respectively. Figure 3.4 shows a comparison of liquid drops images on surfaces of Al, polyethylene (PE), polymethylmethacrylate (PMMA), Cu, Si, Ti and glass substrates obtained using a physiological liquid without NPs (a), using physiological liquids deposited on the different surfaces on which a layer of Au NPs has been deposited (b), and using a liquid containing the Au NPs at a concentration of 5,6 mg/15 ml (c). The measurements of wetting ability of biological liquids on biocompatible surfaces demonstrate that the studied surfaces, preventively submitted to polishing treatment up to maintain a roughness lower than 1 μm , generally have hydrophilic properties permitting a good adhesion to the liquid (contact angle lower than 90°). The contact angle of the liquid, for water, physiological solution, and human blood, can be modified if the liquid contains NPs at concentrations of the order of 1–6 mg/15 ml, i.e. of the order of 70–400 $\mu\text{g/ml}$. Such modifications generally consist of a decrement of the angle of contact in presence of NPs in the liquid drop or in the solid surface layers of the substrates.

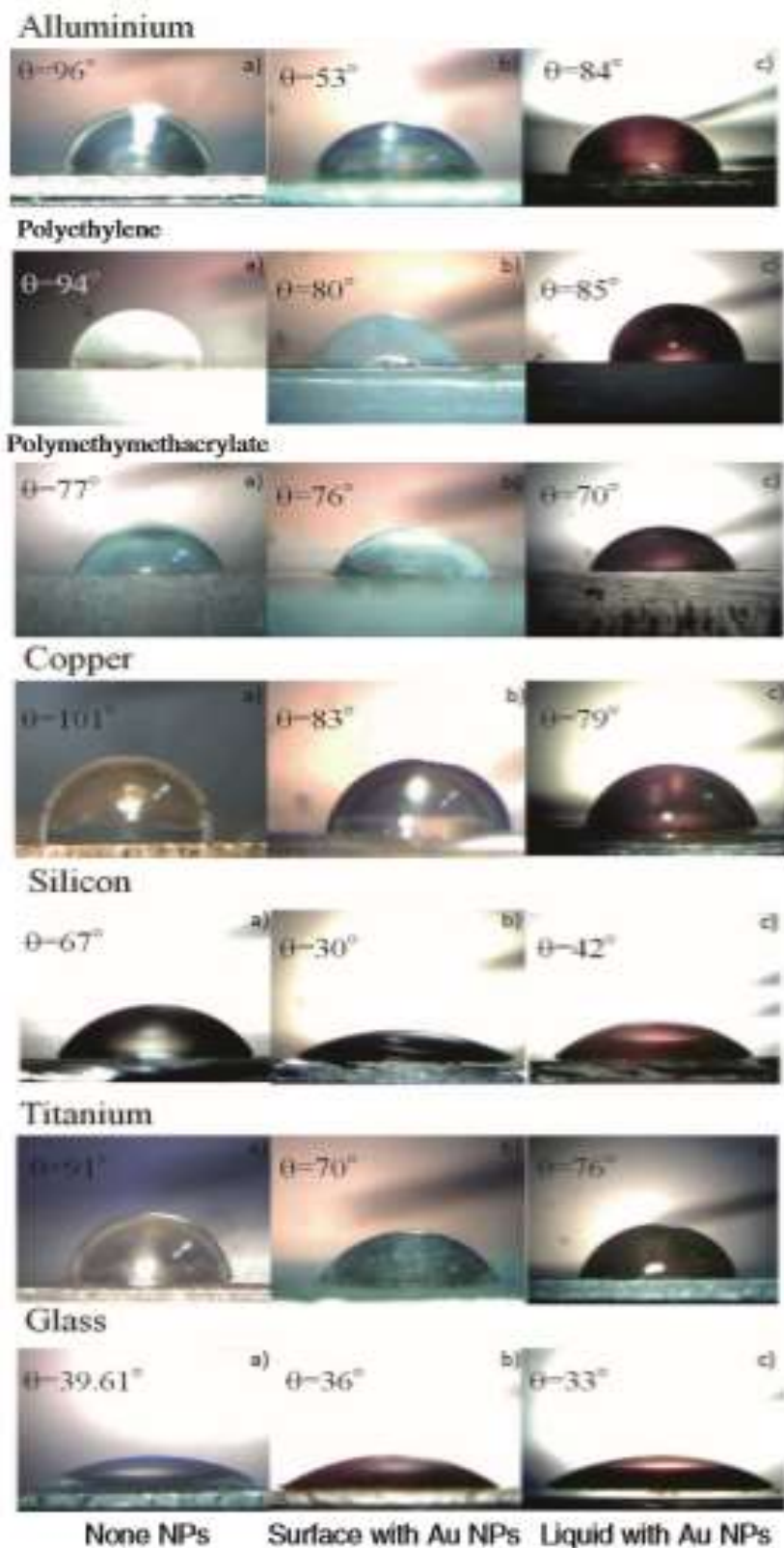


Fig. 3.4- Liquid drops images on different polished substrates of Al, polyethylene (PE), polymethylmethacrylate (PMMA), Cu, Si, Ti and glass, using a physiological liquid without NPs a), with Au NPs enclosed in the liquid c) and using Au NPs deposited in the solid substrate surface b). The contact angle measurements are affected by 2% errors.

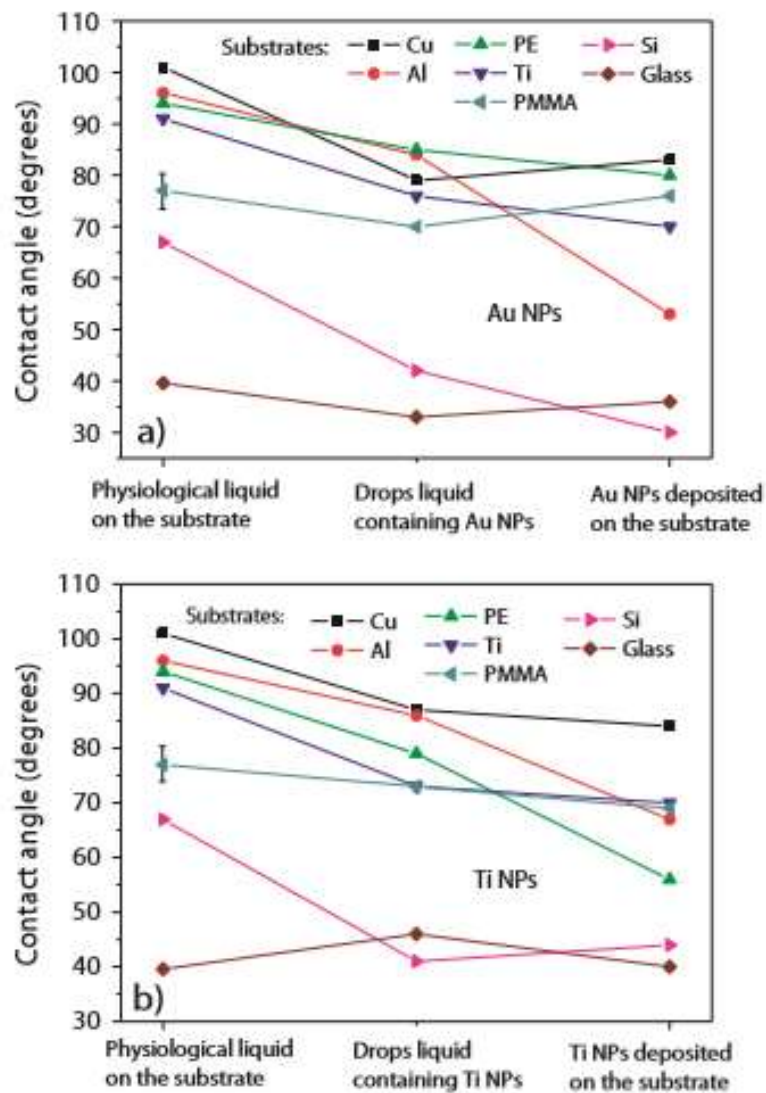


Fig. 3.5- Contact angles of physiological solutions without NPs, with NPs and with NPs deposited on the solid surfaces using Au NPs a) and Ti NPs b) for the different investigated substrates. The vertical bars represent the experimental errors of about 2%.

The many measurements performed can be described synthetically in the plots of Fig. 3.5 for Au NPs (a) and, Ti NPs (b), and in Fig. 3.6 for Ag NPs (a) and Cu NPs (b). The decrement of the contact angle i.e. the better wetting ability is due to the decrement of the surface tension of the liquid containing NPs, i.e. to the resulting attractive forces due to Van der Waals, electrostatic and dipolar, and Laplace pressure. However this decrement was not observed in some cases, such as for liquid drops containing Ti NPs deposited on glass, containing Ag NPs deposited on PMMA or glass and containing Cu NPs deposited on glass. The use of NPs as solid

surface layers deposited on the polished substrates may act in three different ways. As a first way as hydrophilic promoter, as in the case for liquid drops deposited on Au NPs on PE, Ti, Al, Si surfaces (Fig. 3.5a), Ti NPs deposited on Cu, Al, PE, PMMA, Ti surfaces (Fig. 3.5b), Ag NPs deposited on Cu, PE, PMMA, Ti, Si, glass surfaces (Fig. 3.6a), and Cu NPs deposited on Al surface (Fig. 3.6b). As a second way with the same action of the liquid drop containing the NPs, as in the case of Au NPs deposited on glass surface (Fig. 3.5a), Ti NPs deposited on Ti, Si and glass surfaces (Fig. 3.5b) and Cu NPs deposited on Al surface (Fig. 3.6b).

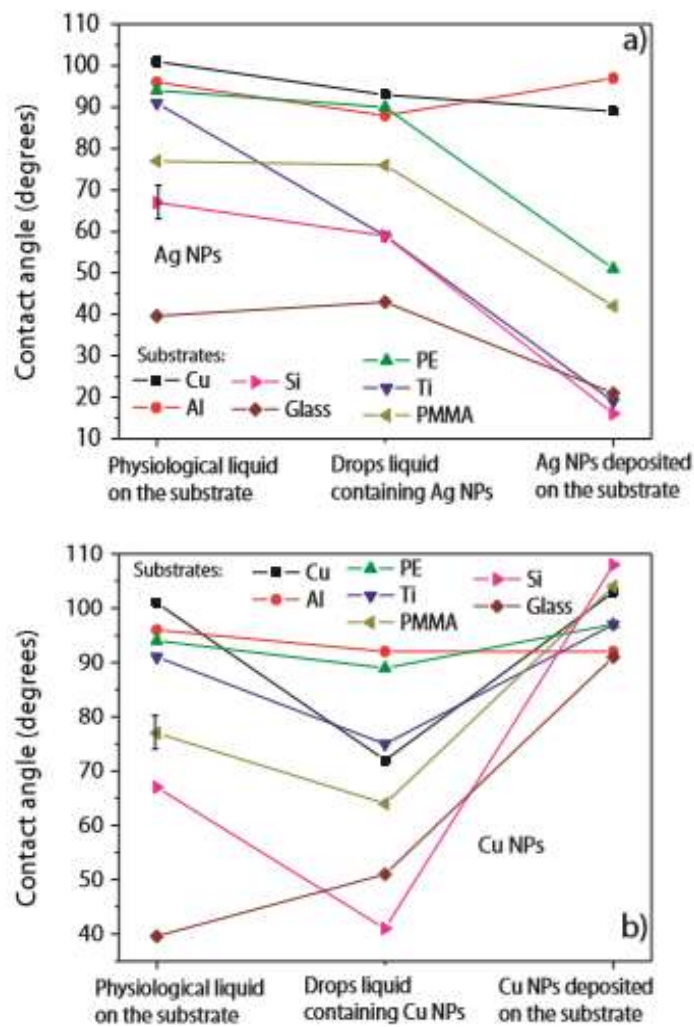


Fig. 3.6- Contact angles of physiological solutions without NPs, with NPs and with NPs deposited on the solid surfaces using Ag NPs a) and Cu NPs b) for the different investigated substrates. The vertical bars represent the experimental errors of about 2%.

As a third way, the use of NPs as solid surface layers of substrates can act as hydrophobic promoter, enhancing the contact angle, such as occurs for Au NPs deposited on PMMA surface (Fig. 3.5a), Ag NPs deposited on Al surface (Fig. 3.6a) and Cu NPs deposited on Si, PMMA, PE, Cu, Ti and glass surfaces (Fig. 3.6b). In conclusion the use of metallic NPs based on Ti, Cu, Ag and Au in biological liquids, such as water, physiological solution and blood, increases the wetting ability of the solution with many types of solid surfaces. This aspect can be very useful for many practical applications, such as that to enhance the anchorage of prosthesis to biological tissues and interface adhesions. Generally the wettability enhances when the NPs are previously deposited on the solid surface, but for special NPs as for Cu NPs, instead, it seem increase enhancing the surface hydrophobic properties. The more hydrophilic surfaces, characterized by low contact angle, have been glass and Si while the less hydrophilic ones have been the Cu, Al and PE surfaces. Intermediate trend was found for the Ti and PMMA substrates.

3.3. Optical and mechanical properties: Static and dynamic characterization of biomedical polyethylene laser welding using biocompatible nano-particles.

Polymeric joints of Ultra High Molecular Weight Polyethylene (UHMWPE) sheets were realized and welded by a diode laser operating at a 970 nm wavelength. One of the polymer sheet was doped, at different concentrations, with nano filler (carbon, titanium and silver nanoparticles) in order to enhance the absorption coefficient at the laser wavelength [68]. Laser operated in repetition rate with a 100 mJ maximum pulse energy, for times of the order of 1-60 s transporting the light through a fiber with 300 μm diameter. The laser light has been transmitted by the transparent first polymer and absorbed on the face of the second doped polymer. At the interface of the two polymer foils, 0.5 mm thickness each, the released energy induces melting, assisted by pressure, producing a fast and resistant welding. Single lap and double lap geometries have been performed and studied by means of mechanical static (shear stress) and dynamical analysis. Effect of the different particles nature on the mechanical features of the joints has been evaluated. Morphological observations of the jointed areas are presented and discussed. Joints could be useful in biomedical field for their special features. The growing development in many plastics industries and the increasing attention paid to the quality and aesthetics of products have defined new technological demands for components junction processes. Welds must be excellent in mechanical and aesthetic quality without residues in the welded area. Mechanical characterization is a very important aspect of materials knowledge since polymers are often used in applications that involve stresses, such as that of polymeric joints. So we must study the effect that stress has on them. In the field of mechanical characterization, static testing (load/displacement curves) and fatigue test (lifetime or durability analysis) are commonly employed. In our case, the mechanical properties of our joints have been studied to verify the resistance features of the laser welding effect. In particular, mechanical static and dynamic (fatigue) tests have been performed. We have considered a particular type of polyethylene, a biomedical grade Ultra High Molecular Weight-UHMWPE. It has a particular high viscosity and low friction

coefficient, and it's largely used for biomedical applications. Polyethylene itself is transparent to laser light. So, we have prepared single lap or double lap joints (welded by means of a diode laser) by employing fillers (nano particles) to make laser absorbing one polymeric sheet of the joint. The nanofillers have been suitably selected for type and quantity to keep color as close to white as possible for aesthetic requirement. The joints have been mechanically analyzed by means of static and fatigue tests in order to verify their strength and durability.

3.3.1 Materials

Polymeric nanocomposite sheets, 30mm x 20 mm x 0,5 mm thick, were obtained by dispersing the carbon nanofiller, titanium dioxide and silver nano particles inside the matrix (biomedical grade UHMWPE GUR 1020) with a solvent. The amount of fillers added to the UHMWPE polymer matrix was of 0.003-0.016-0.025-0.25-0.5-1.0% (for carbon nanoparticles, UH-NC code), 1-2-4-6 % (for titanium nanoparticles, UH-NTiO code) and 1-2-4% (for silver nanoparticles, UH-NAg code). Polymeric nanocomposites of carbon are filled with very low filler amount of nanoparticles, (0.003%, 0.016%, 0.025%,) so that it anyway appears of white color. The obtained nanocomposites were then molded into an hot press obtaining 60mm x 60mm and 0.5mm thick sheets. Single (SLJ) and double lap joints (DLJ) (Fig.3.7a) were obtained by a diode laser operating at 970 nm, CW continuous wave (0.5-7W), maximum energy of 100 mJ, for times of the order of 1-60 s. Optical fiber thickness: 300 μ m. Two types of welding geometry were created: points and grid (Fig.3.7b). The irradiation time to create welding by a diode laser varies from a dozen seconds (NC-doped material) to over 2 minutes (doped with NAg and NTiO).

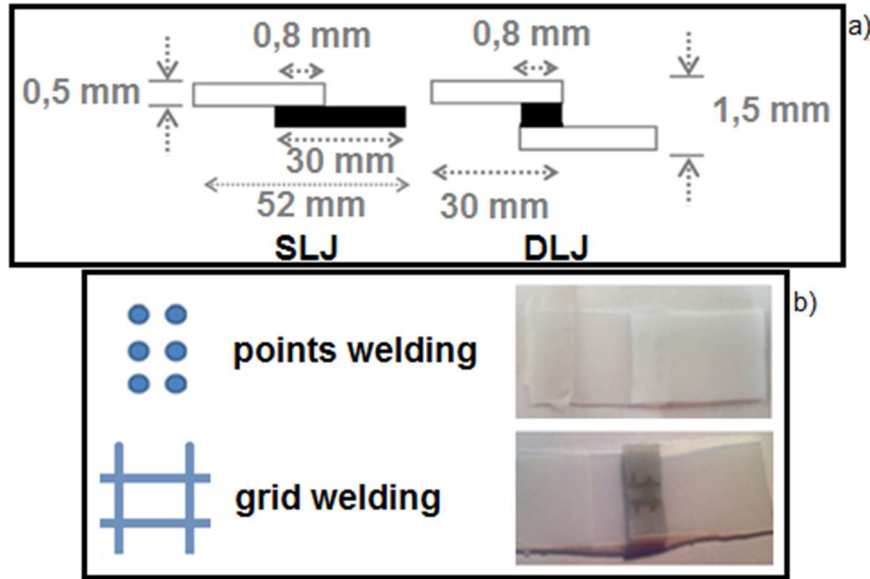


Fig. 3.7- a) Single-lap (SL) and double lap (DL) joint geometries; b) welding geometries and typical joint.

3.3.2 Physical Characterization

Optical absorption measurements: light absorption coefficients in pure and doped polymers with fillers were measured by using optical spectroscopy in the range from 150 nm to 800 nm. Absorption studies were performed by evaluating the absorption of characteristic peaks emitted by a Hg (Ar) lamp and detected by the high sensitivity optical spectrometer. The sample is placed on a suitable support, the incident light is perpendicular to the sample and the emerging light is measured in intensity with respect to the incident. The light beam emerging from the sample is captured by a fiber interfaced with the optical spectrometer (Horiba Jobin) that detects wavelengths between 220 nm and 1100 nm. The Lynear spectroscope software acquires 100 spectra per second and the average spectrum is then stored on a PC. Absorption coefficients, μ , have been experimentally calculated using the Lambert law:

$$\mu = \Delta x \cdot \ln \frac{I_T}{I_0}$$

where Δx = thickness, I_0 = incident laser intensity and I_T = transmitted laser intensity. Morphological Optical (MO) characterization: the Hirox Digital Microscope KH8700 optical microscope has been used for morphological observation of the nanocomposite materials surface with a low magnification, of 50x.

3.3.3 Mechanical Characterization

Static tensile tests have been conducted to evaluate how the presence of NC, NTiO and NAg at different concentrations in UHMWPE affects the mechanical properties of the final nanocomposite. The tests were performed according to the ASTM D638 standard with a Lloyd Universal Testing Machine (LR10K), imposing a traverse feed rate of 5 mm/min and a load cell of 500N. Load /displacement curves of the joints shear stressed during the tensile motion. The data are from the average of six specimens. EPJ Dynamic fatigue tests: the experimental setup allows to test the sample with fatigue loads, monitoring the mechanical and thermal behaviors. It consists of an electro mechanic testing system (Electropuls E300, Instron), equipped with two pneumatic grips (± 3 kN max) able to guarantee a grip force of 4.5 kN, a calibrated load cell (± 5 kN max), and an infrared camera (SC 7200, Flir). The fatigue tests were performed according to ASTM D7791 standard. They were carried out in load control at different maximum force values (fractions of the break load) with stress ratio (R) of 0.7 and a frequency of 1 Hz at room temperature (25 ± 2 °C and 50 ± 10 Relative Humidity). The mechanical parameters were acquired at 100 Hz with a defined reduction of the analyzed cycles: from 0 to 1000th cycle all ones were captured, between 1000th and 100000th cycle 1 every 4, finally after 100000th 1 every 40. IR images were obtained at an acquisition frequency of 100 Hz, monitoring the thermal effect at the maximum applied force of the characteristic cycles and assuming as negligible the small variation of the temperature room (± 2 °C) during the test.

3.3.4 Results

The presence of filler within the UHMWPE makes the nanocomposites less transparent to the laser radiation. Increasing the percentage of NPs filler concentration in the UHMWPE, 0.5 mm thick target, increases the absorbance at 970 nm laser wavelength. Instead pure polyethylene (UHMWPE) is a transparent material to laser light.

Fig. 3.8a shows the variation of light absorption coefficient in pure and doped polymers at different percentages by weight (0.003%, 0.016%, 0.025%, 0.25%, 0.5%, 1%) of nano carbon particles.

From Fig. 3.8b we observe how the light absorption coefficient in the polymer, for example, at 545 nm, grows with the growth of the amount of carbon nanostructures. A similar result has been obtained testing the other fillers.

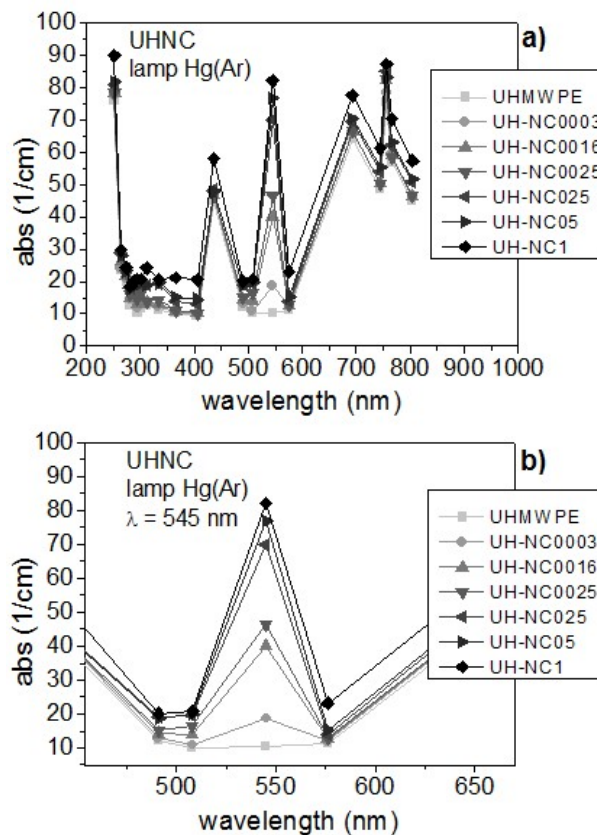


Fig. 3.8- a) Measure the absorption coefficient of pure polyethylene with doped with NC, b) measure the absorption coefficient at $\lambda = 545$ nm according to the NC filler percentage.

Regarding the static mechanical tests of the prepared joints, a previous experimentation (not shown for brevity) indicated to us that the optimal filler amount was of 0.016 wt% of CN, 1 wt% of TiO₂ and of 4 wt% of Ag. The static load/displacement curves show as the highest load of 169 N is reached in the NC filled joint and the lowest of 78 N in the Ag filled one (Fig.3.9).

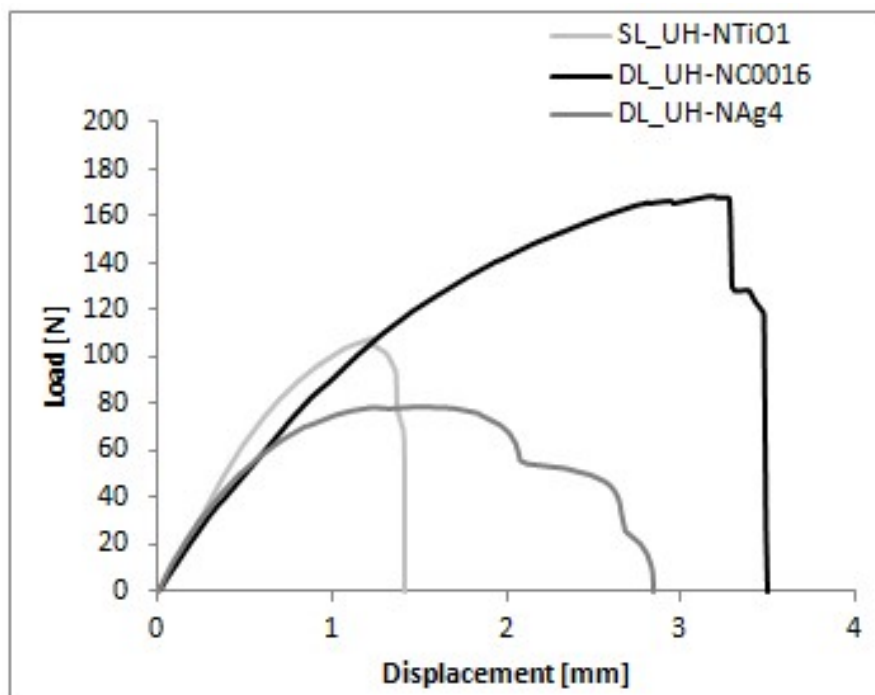


Fig. 3.9- Load /displacement curves of the joints with different filler types.

The morphological observation of the welded area of the UH-NC0016 joint (that exhibited the best static mechanical strength) is shown in Fig.3.10. The image highlights the melted track with the cross line shape. The laser contact with the polymer melts the materials, changing the starting smooth morphology of polyethylene surface. The great morphological modification indicates a deep interpenetration between the polymeric sheets confirming a good welding action, in agreement with mechanical results. Fig.3.11 highlights the displacement of the fatigue machine actuator, and so the elongation of two welded joints of UH-NC0016 sample, subjected to 90% of break load (FR). Three different regions can be identified by observing the displacement-number of cycles trend: (1) a first part

with elastic deformation due to polymeric structure orientation for the normal load; (2) a second step with stiffening of the basic material of the joints and progressive plastic deformation; (3) finally, a rapid damage and a break of the welded zone.

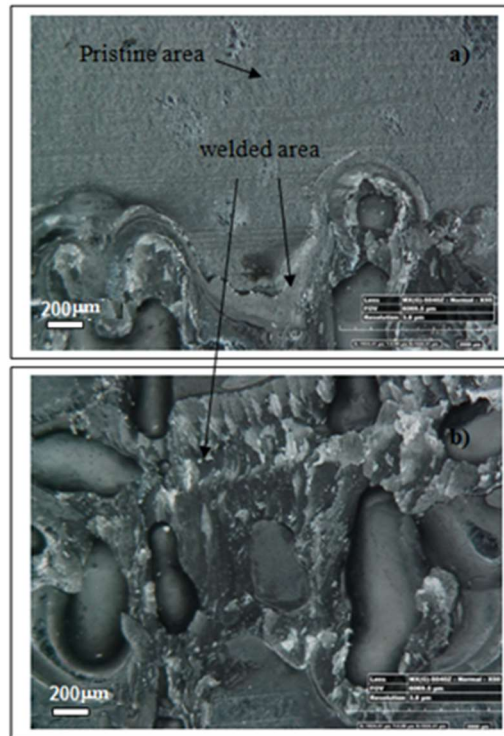


Fig. 3.10- Microscope images of UH-NC0016 welding junction a) of the pristine polymeric surface and b) of the laser irradiated surface.

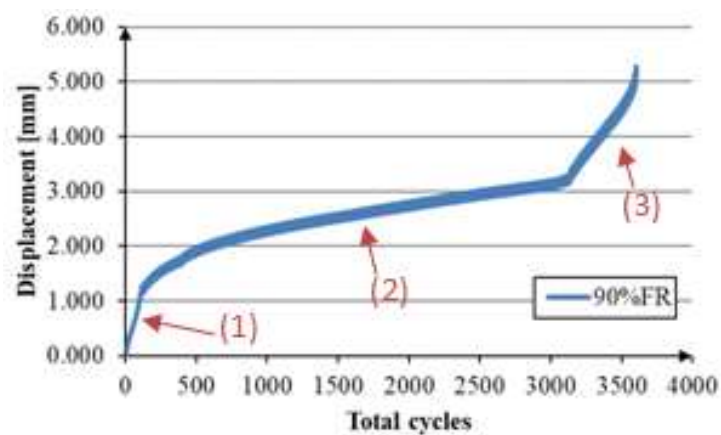


Fig. 3.11- Elongation of two welded joint

The fatigue limit of the UH-NC0016 joint is about 3500 cycles. Fig.3.12 shows the typical images of the thermal behaviors of the cyclic load at 90% FR, when the sample is subjected to the maximum load ($F_{max} = 130 \text{ N}$) on the fatigue test. In this condition, the thermal increase starts to the upper joint, locked at the machine fatigue actuator. Progressively, it evolves to the inferior joint and to twelded zone. Particularly, in the welded zone, the temperature growth is only placed closer to the melted area.

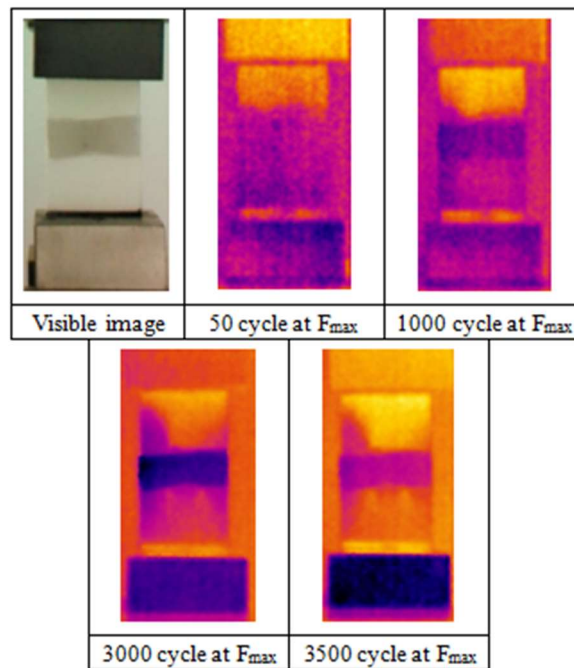


Fig. 3.12- Comparison between visible image and IR images at maximum load and specific cycle

Fig.3.13 displays the effect of the applied load on the measured elongation of the two welded joints. Different trends for compression and tensile are observed, defining a hysteric cycle. The hysteresis area grows when the number of fatigue cycles increases from 50 cycles (Fig.3.13a) to 3500 cycles (Fig.3.13c), putting into evidence the plastic deformation of the joints whose displacement improves from $\sim 1.45 \text{ mm}$ (Fig.3.13a), to $\sim 2.65 \text{ mm}$ (Fig.3.13b) and to $\sim 4.7 \text{ mm}$ (Fig.3.13c).

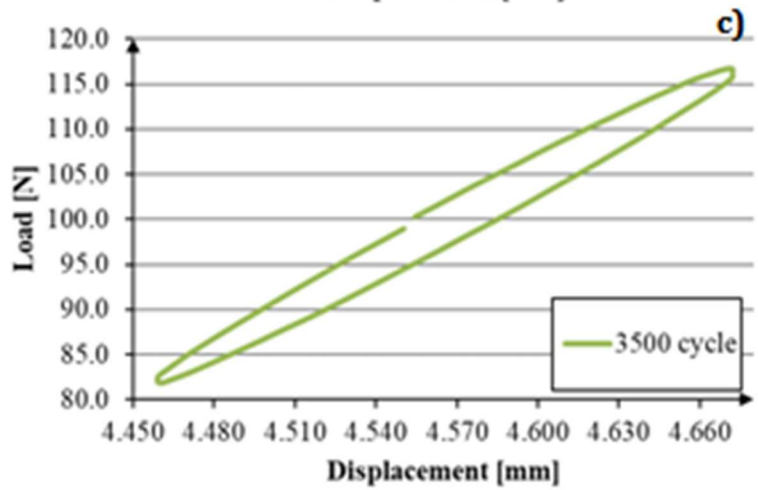
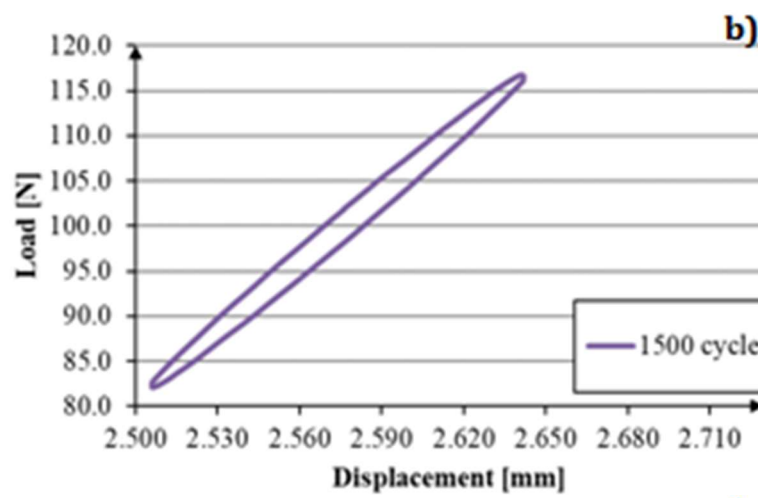
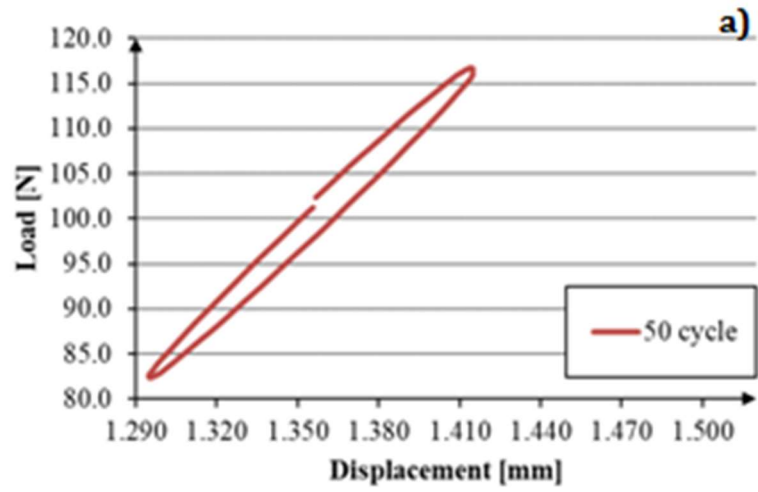


Fig. 3.13- Areas of hysteresis at 90%FR and different cycles a) 50, b) 1500, c) 3500.

3.4. Gold Nanoparticles produced by Laser Ablation in water and in graphene oxide suspension

In the last years, special attention has been paid to develop efficient methods for the production of carbon nanostructures [69,70] but most of the methods require high synthesis temperatures, high vacuum conditions, low structure growth rate and tricky control of the structure size. Moreover, the fast nucleation mechanism is a challenge for growth control and the material integration process. Laser interaction with solids placed in a confined liquid environment is an emerging process due to the undeniable advantage of this technique relative to the size, structure, concentration and morphology control by monitoring of the laser wavelength, fluence, pulse width, spot size, medium type, repetition rate and irradiation time. The pulsed laser ablation (PLA) process in liquids involves many steps: the delivered laser beam is focused on the surface of the target that is plunged into the liquid at a given depth. Due to the interaction between the laser beam and the target–liquid interface, plasma is generated, and violent boiling bubbles and cavitation formation occur in the heated liquid layer. The plasma plume formation and its confinement at the metal–liquid interface induce the enhancement of temperature and pressure and a localised melting of the solid surface layers. The increase in temperature results in a decrease in the surface tension with the formation of circular capillary waves of organised periodic surface structures and of mass removal; local cooling of the target surface and quick solidification of the melted layer are responsible for the formation of structures with nanometric granular morphology in the liquid. The localised laser pulse induces heating and the water causes fast cooling resulting in preferential crystallisation and grain growth. Recently, the PLA of a graphite target immersed in a liquid was proposed as a new method for producing graphene nanosheets. The result of laser ablation in the liquid depends on the optical properties of the liquid and at high concentration, generally, enhances its absorption of the laser light reducing the ablation yield. Presently, we propose laser ablation of a solid gold target immersed in a graphene oxide (GO) suspension in deionised water for the production of metallic nanoparticles (NPs) without the use of necessary surfactants to prevent their aggregations. The laser

light passing through the suspension of GO in deionised water is partially absorbed, it reduces GO and afterwards it reaches the metallic target immersed in the liquid by producing nanoparticles. The objective is to explore the effects of the environment and the laser parameters on the evolution of nanostructures, on their size and shape after the irradiation of the gold target in different liquids. The successful synthesis of graphene with metals free from any types of chemical contamination would be promising for the development of clinical biomarkers, immunosensors, nanodevices and others [71].

3.4.1 Experimental set up

The Nd:YAG laser of the ‘Plasma Physics laboratory’ at the University of Messina, operating at a 1064 nm wavelength and at a 3 ns pulse duration with the repetition rate of 1 Hz for 10 min was employed to perform two experiments [72]. Typically, the maximum output energy is 200 mJ, but presently in both cases, the laser delivered a pulsed energy of 80 mJ measured by a power/ energy meter. The fluence was of about 10 J/cm². It was calculated by considering the delivered pulsed energy and the beam spot size; the latter was measured by scanning electron microscope (SEM) analysis of the crater produced by a single pulse, and it was 500 µm in radius. The laser light was focused onto a high-purity solid gold (Au) target (99.95% pure, Goodfellow) submerged with 2.5 ml of deionised water (referred as DW) with a 500 mm focal length convergent lens to obtain 1 mm of spot diameter. The Au target was placed in a quartz cuvette of 9.8 cm height and 1.33 cm diameter through a tailored target holder. The thickness of the liquid layer above the target surface was 5 mm. The distance between the laser and the deflecting prism was 65 cm, while the distances between the prism and the lens and the lens and the target were 1.5 and 50 cm, respectively. In both experiments, the same configuration (see Figure 3.14(a)) was adopted: the laser beam impinged normal on the front face of the prism, then it was driven to wards the lens and finally it was focused on the target immersed in water. For a better understanding of the plasma behaviour inside the medium, we changed the medium transparency and performed optical

measurements on Au-NPs in DW, in a GO suspension in deionised water with a concentration of 4 mg/ml (referred as (DW+GO)) and in a diluted GO suspension in deionised water with a concentration of 0.6 mg/ml (referred as (DW+dGO)). Therefore, measurements were performed using different diluted solutions in order to change the laser absorption in the 5 mm solution thickness in front of the solid Au surface.

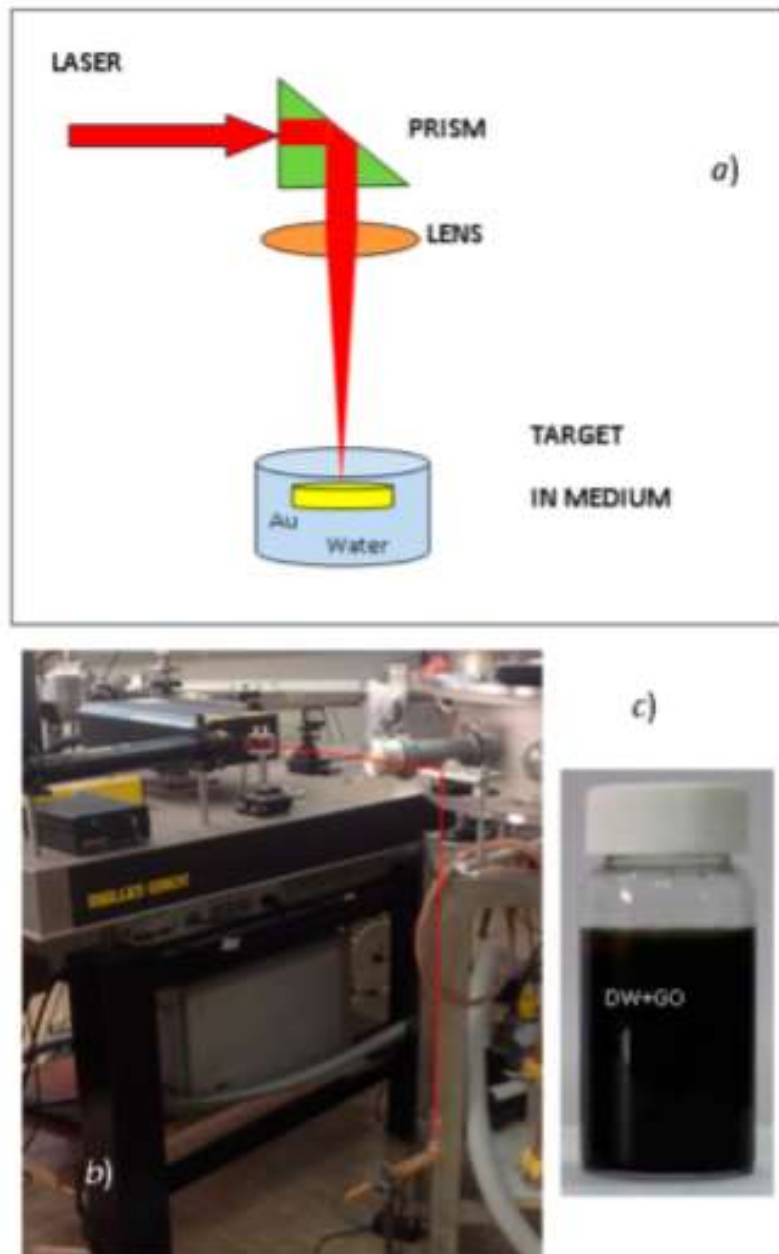


Fig. 3.14 - . Sketch of the laser ablation of a solid target plunged in a liquid medium (a), photos of the experimental set-up (b) and the (DW + GO) solution after the laser treatment (c).

Figure 3.14(b) reports a photo of the experimental set-up and Figure 3.14(c) a picture of the black (DW+GO) solution after the laser treatment. The experiments were performed at room temperature and at 1 atmosphere pressure. The obtained NPs colloidal suspension was placed as drops on a silicon substrate surface and dried (at 60°C) to be used for further physical investigations. UV–Vis–IR transmission spectra on the colloidal suspensions of Au-NPs were registered with the use of an AvaSpec-2048 spectrophotometer with an UB-600 lines/mm grating and a bandwidth from 195 to 757 nm. Halogen/deuterium lamps were employed as excitation sources and at an angle of incidence of 0° in the transmission mode. An accumulation time of 180 min was needed to get an acceptable signal-to-noise ratio in the acquired spectra by the spectrometer. Transmission electron microscope (TEM) images were recorded by the following procedure: 3 µl of specimen dilutions were applied on to freshly glow-discharged carbon-coated parlodion (pyroxylin purified strips, C12H16N4O18) membrane placed on 200 mesh copper grids. An FEI Talos TEM with an FEG gun and an FEI Ceta CMOS camera were used to acquire images, operating at 200 kV with magnifications ranging from 4300× to 310,000×, yielding pixel sizes from 0.05 to 5.5 nm. Images were taken with an exposure of 1 s. Physical characterisation used also SEM investigations, energy-dispersive X-ray spectroscopy (EDX) and Raman spectroscopy. SEM images and EDX analysis were performed using a field emission scanning electron microscope (FE-SEM ZEISS Merlin with Gemini II® column) with an acceleration voltage of 1.5 and 5.0 kV, respectively. Raman spectroscopy is a useful technique to obtain information about the electronic and structural properties of graphene and its related compounds [9]. Representative Raman peaks of graphene and GO are the D and G bands, located for GO at 1363 and 1594 cm⁻¹, respectively, which change in their relative intensity giving information about the GO reduction. In fact, in graphite the D band (ranging from 1330 to 1348 cm⁻¹) is related to the defect-induced breathing mode of A_{1g} symmetry and the G band (ranging from 1577 to 1580 cm⁻¹) comes from the E_{2g} mode that is the in-plane optical vibration of aromatic carbon rings and represents the relative degree of graphitization. The D band is related to the amount of disorder and its intensity shows the degree of edge chirality. Therefore, the intensity ratio of D and G band of the reduced graphene

oxide (rGO) indicates the degree of the disorder such as defects, ripples and edges. Moon et al. [73] in their Raman spectra on hybrids of graphene and gold nanoparticles observed that with GO and rGO, the G band was broadened and shifted to 1595 cm^{-1} because of the enhanced isolated double bonds and the D band became outstanding due to the enhanced disorder. Furthermore, they noted that when GO was reduced to rGO, the D/G intensity ratio, that would have to decrease depending on the restoration of sp^2 (aromatic) domains, increased on the contrary. They explained this as due to the decrease in the size of the sp^2 domains as the graphene sheet was broken into fragments during the photocatalytic reduction of GO. We collected Raman spectra from a Horiba-Jobin Yvon Raman system (model HR800) equipped with a confocal microscope and a 633.0 nm wavelength laser source. The laser power on samples was about 1 mW. Raman spectra were calibrated by using the 520 cm^{-1} band of silicon. The first- and second-order Raman regions were fitted to Lorentzian curves, while the Breit–Wigner–Fano function was used for the G band.

3.4.2 Results

The delivered laser beam is focused at the liquid–target interface plunged in the liquid; the target material ejected from the target surface generates a plasma plume which expands at high velocity. The plume confined by the liquid leads to an enhancement of the temperature and pressure inside the plasma, increasing the collisions probability between atoms and molecules and generating particles aggregation in the liquid, producing spherical nanostructures. The fast plasma localized heating and then the quick cooling are responsible for the atom aggregation to form nanoparticles, for crystallisation effects, for molecular scissions and grain growth. Figure 3.15(a–c) shows the pictures of the hand-made holders, containing 1 ml of DW (a), Au-NPs in DW (b) and in (DW+GO) (c), employed to perform optical analysis of the prepared solutions. The holders are made of polymethylmetacrylate (PMMA), they have 1 mm thickness and a total surface of $35 \times 35\text{ mm}^2$. A cylindrical cavity is formed with PMMA foils having $10\text{ }\mu\text{m}$

thickness as walls, with 10 mm in diameter and 1 mm in width, in which the liquid can be contained with a total volume of about 80 mm³ to be submitted to the optical analysis. The optical measurements, showing absorbance vs. the wavelength, were performed in pure deionised water (DW), in deionised water containing Au-NPs (DW+Au-NPs) and in deionised water containing GO (DW+GO) and Au-NPs. In the case of (DW+Au-NPs), these measurements evince an absorbance peak depending on the spherical diameter of the Au nanoparticles: it shifts to wards higher wavelength with an increase in their diameter as reported in the plot of Figure 3.15(d), in agreement with the literature [74,75]. In particular, Au-NPs at 10 nm average diameter have an absorbance peak at 510 nm, which shifts to 590 nm if the nanoparticles have an average diameter of 100 nm. The absorption peak is assigned to the gold surface plasmon resonance due to the induction of electric dipole on the gold nanoparticles by the incident electromagnetic wave.

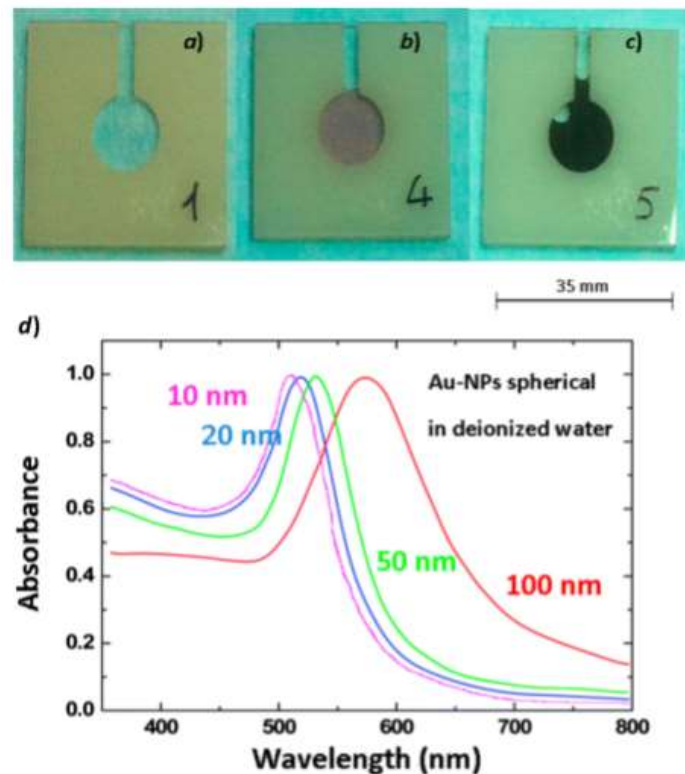


Figure 3.15- Holders containing (a)DW, (b)Au-NPs in DW and (c) in (DW+GO); absorbance spectra of colloidal suspensions in deionised water containing Au-NPs of different diameters(d) are also shown.

In fact, the electric field of the incident light causes electron oscillations on the gold nanoparticle surface with an associated electric dipole opposite to the incident one, enhancing thus the light absorption effect. Resonance absorption is possible when the incident radiation has a frequency equal to the plasmonic one. The presented absorbance curves are normalised to the maximum value of absorption and are obtained using a very little amount of sodium citrate (1 μ l/10 ml) that acts as the surfactant avoiding the gold nanoparticles coalescence.

The results of the UV–Vis–NIR transmission measurements show interesting spectra in the (300–757) nm range for the synthesised Au-NPs in two different solutions (DW and (DW+GO)), as reported in Figure 3.16. With respect to pure deionised water (higher curve), for the Au-NPs in DW (middle curve) negligible absorption is exhibited in the (400–522) nm wavelength range, while higher absorption, evaluated of the order of 10–15%, is observed at wavelengths higher than about 600 nm. Due to the low target thickness of 1 mm, this curve is not sufficiently sensitive to observe the Au-NPs absorption band expected around to 520 nm. The transmission spectrum registered for the Au-NPs in (DW+GO) (bottom curve) instead shows high absorption effects for the wavelength region from 300 up to 757 nm. The narrow transmission peaks are due to the optical properties of the used containers material (see the higher curve). The observed absorption difference between Au-NPs suspensions in DW and (DW+GO) is imputable to the presence of GO acting as a dense filter distributed in the solution reducing significantly the transmission of the light. This result shows that the solution of Au-NPs in DW +GO is characterised by low transmission and high absorption and that the laser light is strongly attenuated in the solution, which must be used with a minimum thickness of about 1–2 mm on the Au target in order to induce the requested ablation and to generate Au-NPs. Figure 3.17(a–c) reports the TEM images of the synthesised Au-NPs in DW (a) as well as in the (DW+dGO) (b) and (DW+GO) (c) suspensions revealing spherical and irregular shape nanostructures. In particular, in Figure 3.17(a), most of the Au-NPs are spherical in the 5–10 nm diameter range, while the rest of them do not exceed 25 nm in diameter.

In Figure 3.17(b), a low number of Au-NPs immobilised at the GO sheets are revealed due to a high GO dilution.

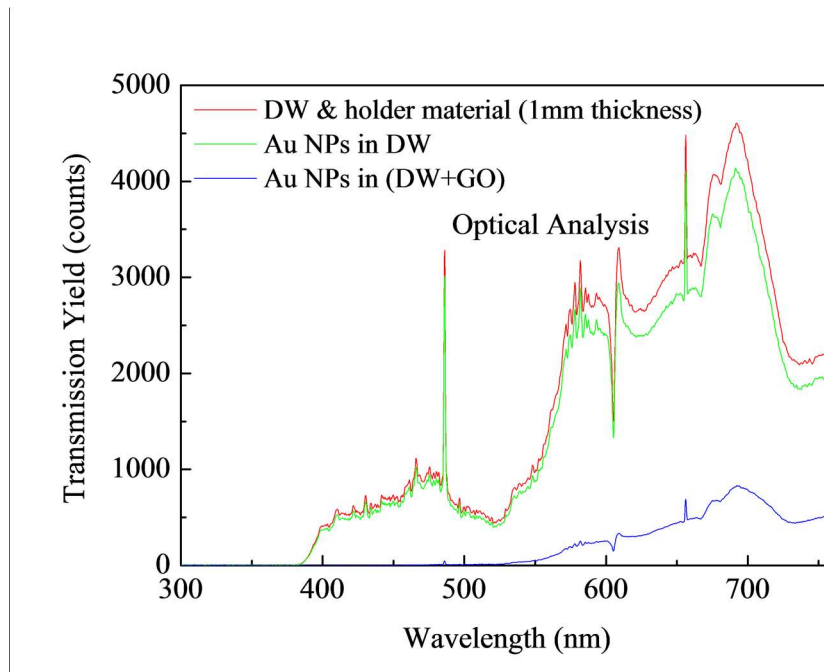


Figure 3.16- UV-Vis-IR transmission spectra of DW and holder material (higher curve), and of Au NPs in DW (middle curve) and in the (DW+GO) (bottom curve) suspension.

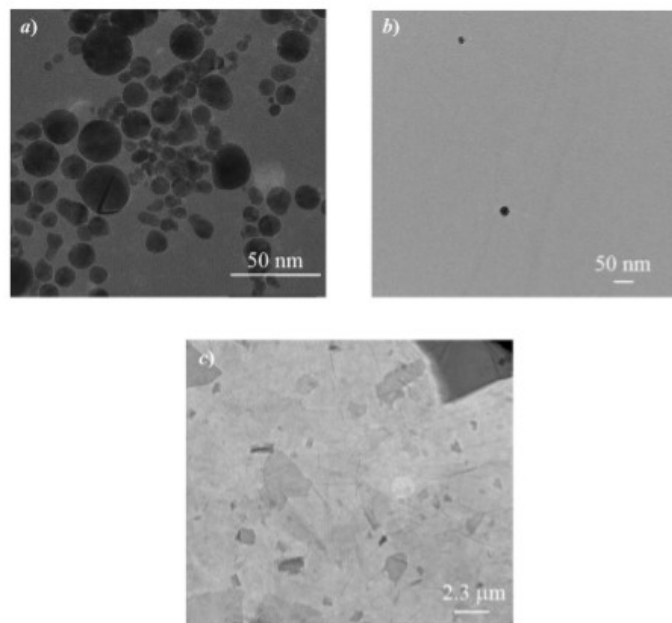


Figure 3.17 TEM images of the synthesised Au-NPs in DW (a) as well as in (DW+dGO) (b) and in (DW+GO) (c) revealing spherical and irregular shape nanostructures.

In Figure 3.17(c), only GO sheets are shown with irregular shape and large size distribution, from tens to thousands of nanometres. GO that does not interact with laser appears as a large size distribution of micrometric and under micrometric platelets. In the case of the (DW+GO) suspension, the solution has a high GO concentration, thus a high laser absorption results and the ablation effect produces micrometric and sub-micrometric platelets in water. The dimension of the Au-NPs generated in DW as well as the full size of Au-NPs anchored to the GO sheets and produced in (DW+dGO) (low GO concentration because it is diluted) are comparable. This means that low Au-NPs size has been obtained during the PLA in (DW+dGO). For high GO concentration, (DW+GO), no Au-NP has been produced as GO acts as a ‘dense filter’ that impedes the delivering of the full laser fluence on the Au target by being part of this energy absorbed by the matter in front of the target. Some SEM images of the pure GO solution drops deposited on a silicon substrate are reported in Figure 3.18. The images indicate that a thin GO film (some nanometres in thickness) is deposited on the silicon substrate, as observed at different magnifications (a, b, c, d).

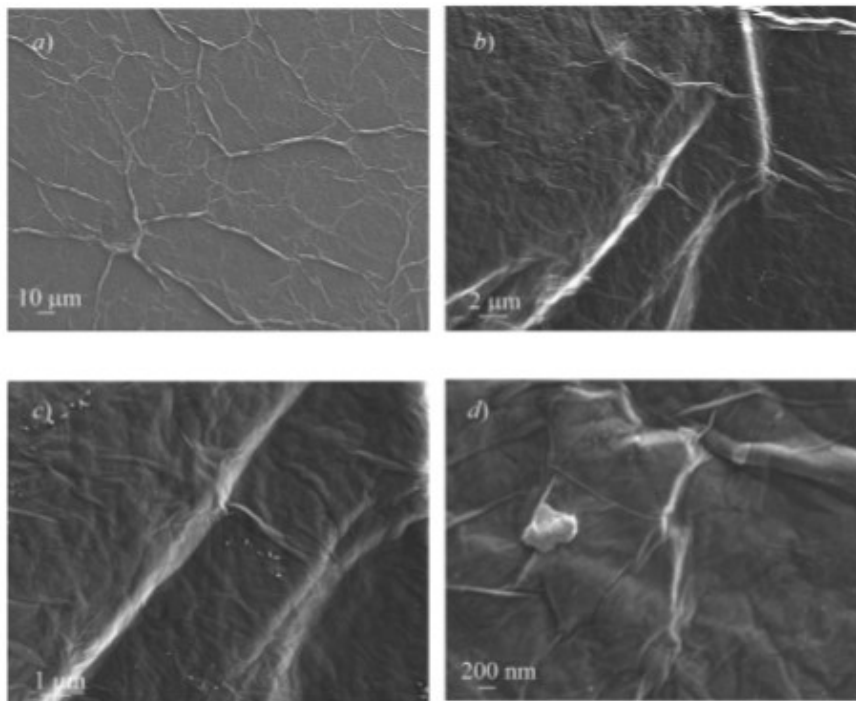


Figure 3.18- SEM photos of the GO thin film deposited on a Si-substrate at different magnifications.

The SEM investigations have considered also the Au-NPs produced in deionised water, as reported in Figure 3.19(a), indicating two main groups of nanoparticles with about 6 nm (75%) and 25 nm (25%) in diameter, according to a previous our study [18]. Practically the laser ablation of Au in the high concentrated GO solution (4 mg/ml), referred as (DW+GO), is almost absent, due to the high absorption coefficient of the solution, and only micrometric and sub-micrometric platelets of GO are present, as are sult of the laser fragmentation effects on the GO platelets, as reported in the SEM photo of Figure 3.19(b). Instead the low concentrated GO solution (0.6 mg/ml), referred as (DW+dGO), shows a low Au-NPs concentration and a lower presence of micrometric and sub-micrometric platelets of GO, as are sult of lower laser absorption in the solution and higher lasera blation of the Au solid target, as reported in the SEM photo of Figure 3.19(c). In this case, the Au-NPs have an average diameter not greater than 25 nm and their composition has been confirmed by the EDX analysis illustrated in Figure 3.19(d) that shows the characteristic X-ray M-lines of the Au atoms at about 2.1 keV. Thus the Au-NPs generation is inhibited in high concentrated GO solutions, referred as (DW+GO), it is facilitated in DW solutions and it occurs, with a minor yield, in low concentrated GO solutions, referred as (DW+dGO). The average size of the Au NPs in the DW solution is about 5–10 nm and it is of about 10–20 nm in DW+dGO. The Au ablation yield, evaluated from the target mass reduction after a prolonged laser irradiations of 30 min, is about 1 and 0.5 mg in DW and in the diluted (DW+dGO) solution, respectively, and it is about zero in the concentrated (DW+GO) solution. The optical absorption of the solution at the used laser wavelength is responsible of this result. EDX spectra, including also the characteristic X-ray K lines of the C and O atoms, at about 277.0 and 525.0 eV, respectively, provide information on the oxidation state of the analysed graphene material. In particular, Figure 3.20 reports a comparison between the EDX spectra performed in the deionised water solution containing Au-NPs (a), in the GO solution (b), in the concentrated GO solution that is laser irradiated to produce Au-NPs, reported as (DW+GO) (c), and in the diluted GO solution, referred as (DW+dGO), wheretheAu-NPs are effectively produced byt he laser irradiation (d).

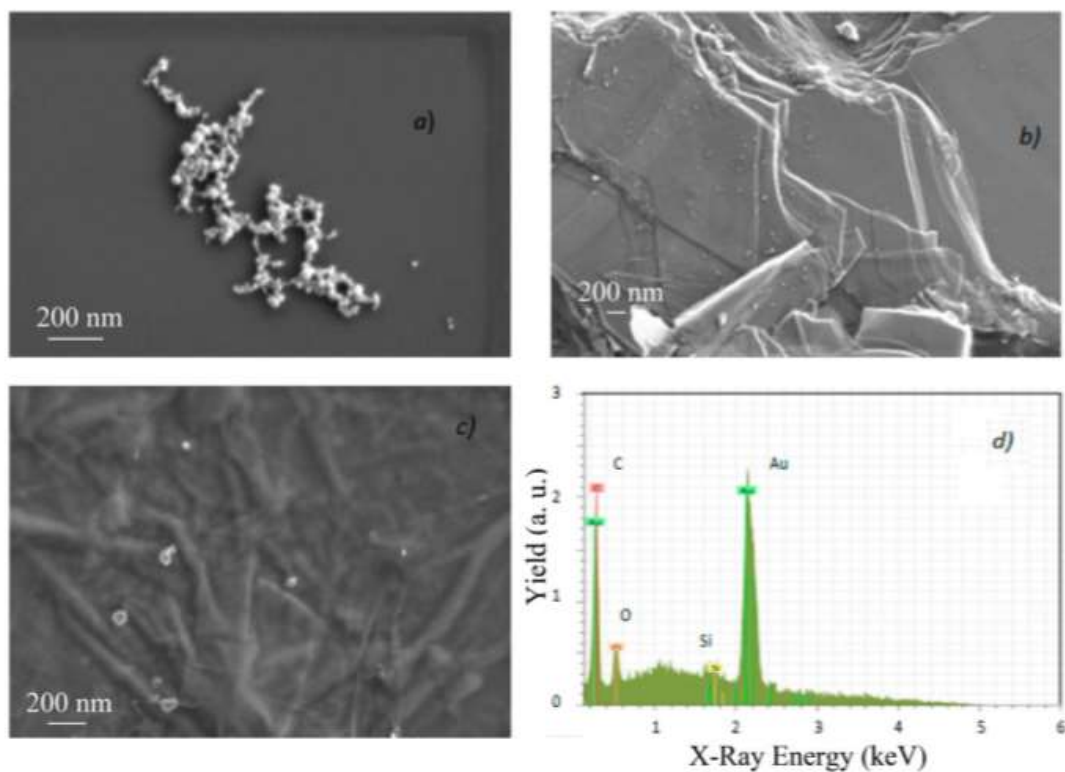


Figure 3.19- SEM photos of the Au-NPs produced in DW(a), in the concentrated GO solution (DW+GO) (b) and in the diluted GO solution (DW+dGO) (c). The EDX spectrum of the Au-NPs suspension in (DW+dGO) is also shown (d).

The comparison shows that the oxygen content in GO decreases when the solution is investigated by the repetition laser pulses, demonstrating that laser induces the formation of rGO. This last result is in agreement with the recent literature; lately, in fact, a series of excellent results with the photochemical loading of gold nanoparticles on the rGO sheets have been obtained. Furthermore, a green photocatalytic synthesis of gold NPs-rGO nanocomposites for sensing and other applications is provided. Raman spectroscopy has been employed to investigate if laser induces the GO reduction as indicated by the EDX spectra. Figure 3.21 shows the Raman spectra of the thin films obtained by depositing the different solutions drops on silicon substrates. In particular, Figure 3.21(a) reports a Raman spectra comparison between the pure GO (bottom curve), (DW+GO) (middle curve) and (DW+ dGO)+AuNPs (higher curve) films at 633.0 nm. A quick look at the figure points out that from the GO film to the (DW+GO) one as light increase in the D band intensity occurs, while the use of diluted GO (the (DW+dGO) film) shows higher Raman peak intensities. In order to understand better what happened, we

fitted our data as indicated in the experimental section and illustrated in Figure 3.21(b), where the experimental data are represented by circles, the sub-bands by dashed lines, the best fit by continuous line. As expected, the GO film Raman spectrum (see b1) displays a D band at about 1332.1 cm^{-1} , a G band at ca. 1591.9 cm^{-1} , a 2D band around 2633.4 cm^{-1} , a D+G band at about 2903.6 cm^{-1} and a C band at ca. 3167.5 cm^{-1} . This last feature is attributed to the C–H stretching mode of aromatic carbons. The Raman band at about 1720.0 cm^{-1} is assigned to irregular rings such as Stone-Waled defects.

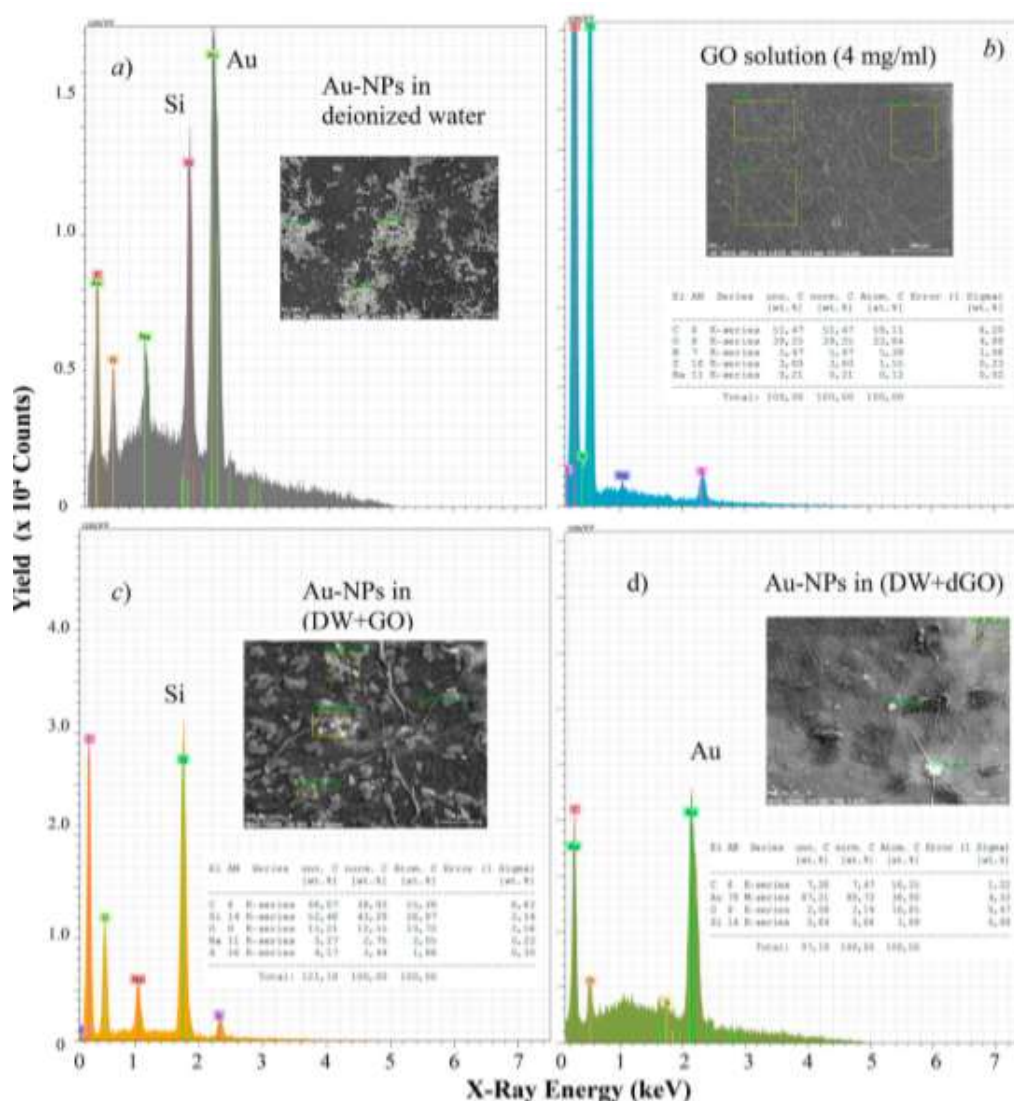


Figure 3.20- EDX spectra of Au-NPs in deionised water (DW) (a), of the GO solution (b), of the GO solution after the laser treatment (DW+GO) (c) and of the Au-NPs in the diluted GO suspension (DW+dGO) (d), in which the Au-NPs are laser produced.

Also the Raman spectrum of the (DW+GO) film (b2) presents a D band at about 1333.7 cm^{-1} , a G band at ca. 1588.1 cm^{-1} , a 2D band around 2622.2 cm^{-1} , a D+G band at about 2899.6 cm^{-1} and the band at ca. 1720.0 cm^{-1} . An increased D/G intensity ratio (1.4) is observed as compared to that obtained for pure GO (1.1). As

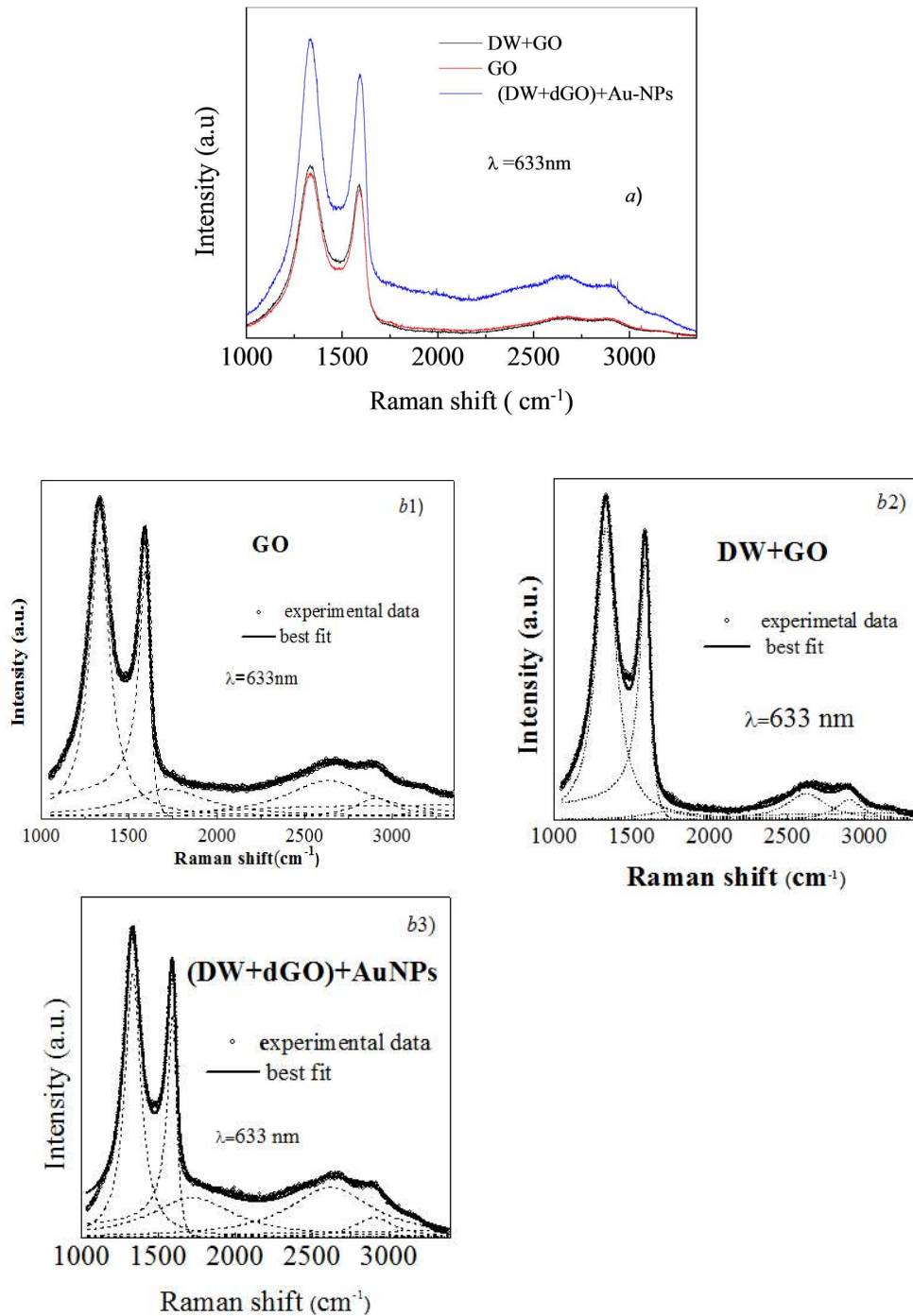


Figure 3.21- Raman spectra comparisons between the following thin films: pure GO, (DW+GO), and (DW+dGO) +Au-NPs, at 633.0 nm (a) and their fits (b).

already said, this increase is typical of the reduction of GO since new numerous smaller in size graphitic domains are created by the laser ablation process. In fact, as shown in Figure 3.19 (b), during the laser treatment the GO sheets are broken into fragments and the size of the sp^2 domains decreases. So the new graphitic domains are smaller in size to the ones present in GO but more numerous. The lack of the C band in the (DW+GO) film Raman spectrum (see Figure 3.21(b)) due to the C–H stretching mode of aromatic carbons indicates partial removal of the oxygen-containing functional groups, thus confirming that GO is partially reduced owing to the laser irradiation. This is in agreement with the decrease in the oxygen content observed in the EDX spectra (see Figure 3.20). The Raman spectrum of the (DW +dGO)+Au-NPs film (b3) shows a D band at about 1334.7 cm^{-1} , a G band at ca. 1592.8 cm^{-1} , a 2 D band around 2620.0 cm^{-1} , a D+G band at about 2903.8 cm^{-1} , a C band at 3168.5 cm^{-1} , the band at ca. 1720.5 cm^{-1} and a D/G intensity ratio of 1.2. Therefore, the D/G intensity ratio increases on going from the pure GO film (1.1) to the (DW+dGO) one (1.2), to the (DW+GO) one (1.4). This rise is due to a greater reduction of GO when it is IR laser treated. As regards the higher Raman peak intensities observed in the diluted GO with Au-NPs, they are due to the gold NPs that are effectively produced by laser irradiation, as already suggested by EDX spectra. The presence of Au-NPs could be also the cause of the slight up shift of the G band and with respect to GO probably due to electron–phonon coupling.

4. Use of Metallic Nanoparticles for Biological and Medical Diagnostics

4.1. Contrast Agents in X-ray imaging and computed Tomography

By diagnostics we mean that complex of manual, instrumental and laboratory, aimed at formulating the diagnosis of a disease. It is distinguished in diagnostic imaging and interventional diagnostics. The former uses the radiological methods for the visualization of lesions at the level of the different organs; the latter uses, instead, surgical techniques for the study of such lesions. The early diagnosis of cancer is very important: for many forms of cancer, in fact, the therapy is far more effective and less disabling if the tumor is treated when it is small and has not had time to cause metastases in other body areas. Prevention is our best weapon to win cancer: healthy eating and a healthy lifestyle, associated with periodic medical checks could limit the appearance of these diseases. The concept of prevention has begun to be emphasized, above all because the incidence of tumors has clearly increased. For an enhanced image quality and a more in-depth investigation into the characteristic biological phenomena, contrast agents have been widely used in imaging technologies. A diagnostic method that has recently assumed a certain importance, is to use metallic nanoparticles as contrast agents: they allow to identify tumor cells. Contrast media (mdc) are substances used in diagnostics for images, mainly in radiology or magnetic resonance, they alter the contrast of an organ, a lesion, or any other structure with respect to its surroundings, in such a way as to make visible details that otherwise would not be appreciable. If an organ absorbs little radiation or in the same way as the surrounding organs, it will not be visible in a useful way on the image (eg. stomach, liver, kidneys and other abdominal organs). Contrast media are therefore administered, in order to make visible the organs containing them, or by direct filling (gastrointestinal viscera, veins, arteries, etc.) or by selective elimination (kidneys and urinary tract). The contrast effect has a transitory duration; in fact, the radiographic examination must be performed immediately or shortly after the contrast medium has been taken.

The thus highlighted organs take on characteristic aspects, which in many cases are of great help in reaching an early diagnosis of even serious diseases [76]. The

contrast media in radiology are classified according to their chemical constitution, which determines their possible uses.

Among the most used and often responsible contrast agents of reactions adverse, there are the iodate one; they are particularly useful in the study of the uro-gynecological apparatus and for angiography studies.

Iodine, as well as barium, is part of the radio-opaque contrast media; this means that increase the resistance to the passage of X-rays; it is characterized by a high atomic number, small in size and is soluble in water. The iodinated contrast medium is not a dye, but a substance that temporarily changes the way in which the radiation interacts with the body and internal organs. In fact, when iodine is introduced into the body during a radiological examination, it improves the visibility of specific organs, blood vessels and tissues.

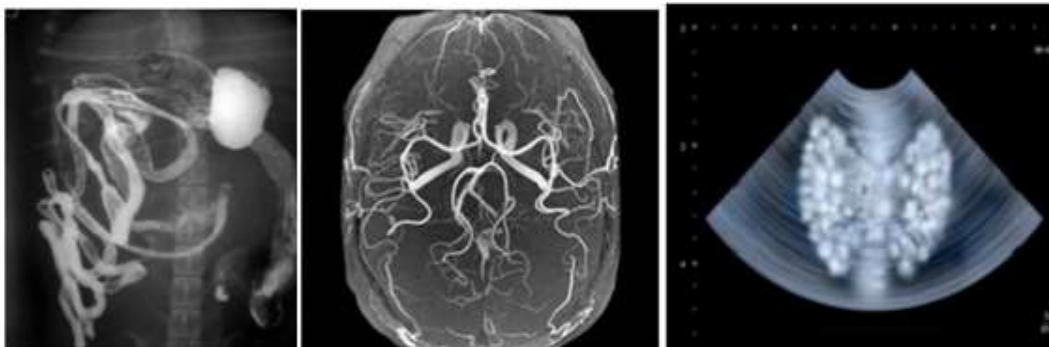


Fig. 4.1- Examples of different means of contrast: radiography of the digestive tract improved thanks to the combination with opaque contrast medium (in this case barium sulfate), encephalic magnetic resonance with contrast. The contrast agent used in this case is gadolinium, a diagnosis of thyroid cancer. The used contrast medium is sodiumpertechnetate (NaTcO_4).

4.1.1 Contrast agents for CT

X-ray contrast agents were introduced in order to enhance the contrast between tissues with similar and/or low x-ray attenuation by increasing the signal to-noise ratio without increasing the radiation dose to the patient. X-ray contrast agents used clinically include barium sulfate suspensions and iodinated molecules. Barium sulfate was first introduced as a clinical contrast agent in 1910 and is currently used for gastrointestinal imaging after oral administration. Thus, barium sulfate contrast agents are a mature technology and are not presently an active area of research. Iodinated molecules were first used as a contrast agent in 1923 and have undergone

significant improvements since then. The first water-soluble contrast agents utilized sodium iodide, which was toxic at the concentrations necessary for imaging contrast. Current agents are most commonly low-molecular weight iodinated aromatics, which are highly water soluble and exhibit low toxicity. Active targeting has been enabled by the conjugation of functional ligands onto the aromatic rings. Iodinated molecules are most commonly used as vascular contrast agents. However, iodinated contrast agents exhibit a relatively short blood circulation time and rapid clearance through the kidneys, leading to a short imaging window, which may require multiple injections. A recent clinical report associated sudden exposure to high levels of iodinated contrast agents with a risk of developing thyroid dysfunction, although further investigation is necessary to determine a casual relationship and the general population risk.

4.1.2 Gold nanoparticles as x-ray contrast agents

Over the last decade, gold nanoparticles (AuNPs) have gained attention as an x-ray contrast agent following initial reports. Subsequent research and clinical interest, as gauged by the annual number of publications on AuNPs as x-ray contrast agents, have grown steadily due to a number of favorable properties of AuNPs. Gold exhibits a relatively high x-ray attenuation coefficient compared with both barium sulfate and iodine, especially at the energy levels used for clinical CT [77]. Furthermore, AuNPs exhibit a longer vascular retention time compared with iodinated molecules, due to their higher molecular weight, which potentially increases the available imaging window. AuNPs are readily surface functionalized for enhanced colloidal stability and/or targeted delivery. In fact, a sharp increase in the annual number of research publications on AuNPs as x-ray contrast agents occurred in 2010, when several groups demonstrated active targeting in vivo with surface-functionalized AuNPs, which could enable molecular imaging capabilities with CT. Investigations of AuNPs as an x-ray contrast agent can be categorized by three potential applications in diagnostic imaging: blood pool, passive targeting and active targeting (Figure 4.2). Blood pool contrast agents are designed to remain in the blood stream for a prolonged amount of time by limiting diffusion through the

vascular endothelium in order to enable a longer imaging window. Passive targeting relies on the nonspecific accumulation of AuNPs within a site of interest by leveraging the enhanced permeability and retention effect, in which appropriately sized molecules or nanoparticles accumulate more readily in tumor tissues compared with normal surrounding tissues.

Tumor vasculature is described as ‘leaky’ due to a distortion of the endothelial layer of blood vessels, allowing AuNPs to escape the vasculature and enter the tumor microenvironment. Active targeting is the ability to deliver and retain a contrast agent at a specific site of interest through surface functionalization with molecules, such as peptides or antibodies, which exhibit a specific affinity for that site. AuNPs have been targeted to cancer cells and tumors by exploiting the overexpression of a number of receptors on cancer cells compared with normal cells.

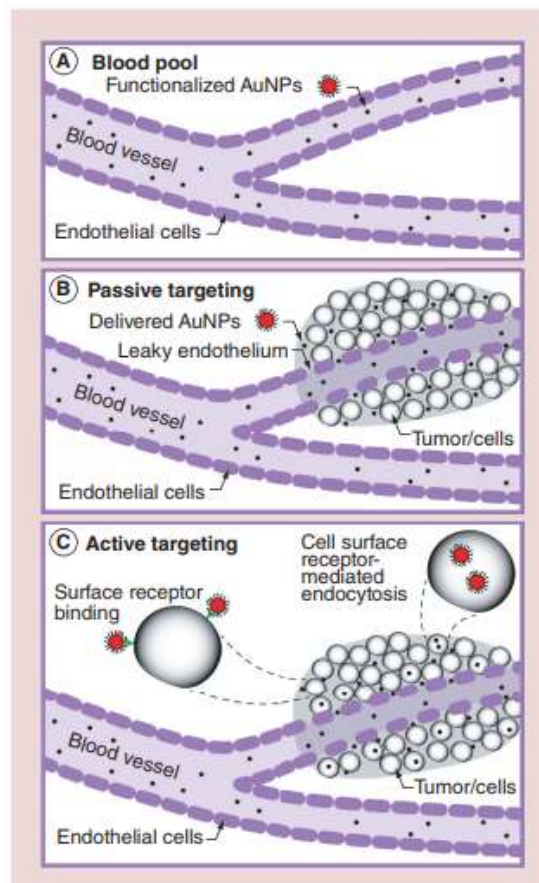


Fig. 4.2- Three applications for the use of gold nanoparticles as x-ray contrast agents in diagnostic imaging. (A) Blood pool, (B) passive targeting and (C) active targeting [77].

4.1.3 Contrast enhancement

X-ray imaging is based on the absorption or scattering of photons as a collimated x-ray beam passes through a specimen. As x-ray photons are absorbed or scattered, the intensity (I) of the x-ray beam is reduced as:

$$I = I_0 e^{-x\mu/\rho} \quad (4.1)$$

where I_0 is the initial intensity of the x-ray beam, x is the thickness of the specimen, μ is the linear x-ray attenuation coefficient (cm^{-1}) of the specimen material or tissue and ρ is the material or tissue bulk density (g/cm^3). In CT, X-ray attenuation is measured in Hounsfield units (HU) by calibration with water (0 HU) and air (-1000 HU) as:

$$HU = \frac{\mu - \mu_{\text{water}}}{\mu_{\text{water}}} \cdot 100 \quad (4.2)$$

where μ is the linear x-ray attenuation coefficient of the material or tissue and μ_{water} is the linear x-ray attenuation coefficient of water. Image contrast is derived from differences in the linear x-ray attenuation coefficient and the thickness of two neighboring materials or tissues (e.g., muscle and bone, where bone attenuates a proportionally greater number of x-rays, leading to a greater degree of incident intensity reduction, or greater x-ray attenuation). Materials or tissues with high atomic number (Z) and bulk density (ρ) generally absorb more x-rays. Therefore, high atomic number elements, such as barium, iodine or gold, exhibit a high mass attenuation coefficient (μ/ρ), and are thus good candidates as X-ray contrast agents in soft tissues (Figure 4.4). Gold ($Z = 79$) has a higher atomic number compared with iodine ($Z = 53$) or barium ($Z = 56$) and can thus absorb more x-rays at specific energy levels (Figure 4.4). X-ray attenuation is also dependent on the x-ray photon energy, which governs the initial intensity (I_0) and also independently influences the x-ray attenuation coefficient. The mass attenuation coefficient is decreased as incident photon energy from the X-ray source is increased (Figures 4.4). Therefore differences in the X-ray attenuation coefficient between two different materials are greater at lower tube potentials, but the radiation dose is also greater.

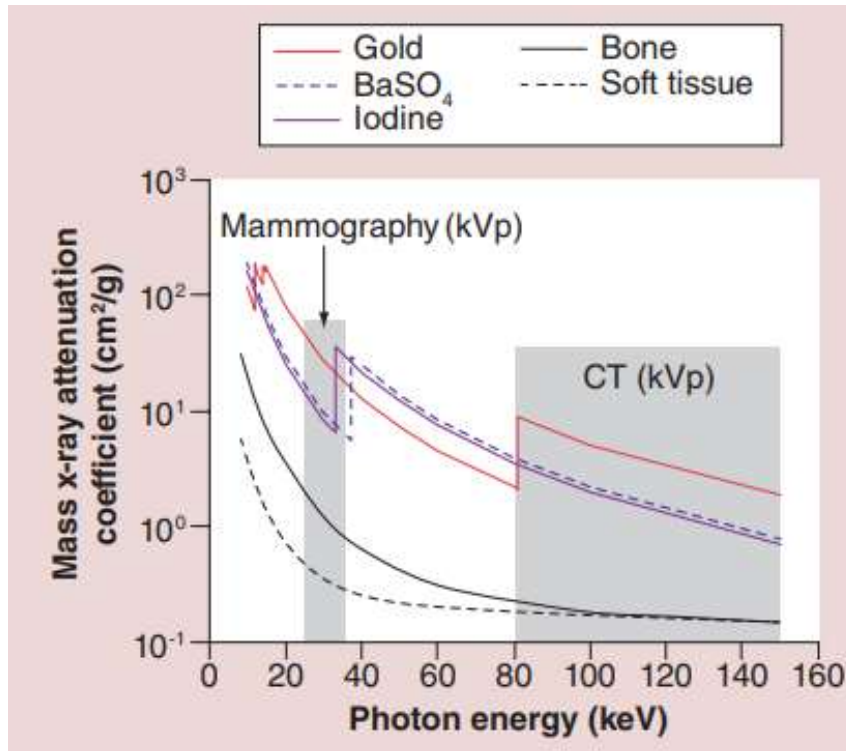


Figure 4.3- Energy-dependent differences in the mass x-ray attenuation coefficient (μ/ρ) of gold compared with current clinical contrast agents (BaSO_4 and iodine) and tissues. In clinical mammography and CT systems, gold nanoparticles due to exhibiting a greater x-ray attenuation compared with both barium sulfate and iodine at the energy levels used for clinical imaging [77] .

The incident x-ray photon energy spectrum is controlled by setting the peak tube potential (kVp), which corresponds to the maximum photon energy in the beam. Beam filtration is used to tune the energy spectrum by limiting the number of low-energy photons (<15 keV), and also high-energy photons in mammography, using a filter material (commonly aluminum, copper or molybdenum, among others). Therefore, the peak tube potential range is typically 25–35 kVp in mammography, 50–80 kVp in clinical radiography and 80–150 kVp in clinical CT in order to achieve sufficient contrast while minimizing the radiation dose. The high x-ray attenuation coefficient of gold compared with both iodine and barium within these energy ranges (Figure 4.4) suggests that gold can enable improved contrast enhancement. The mass attenuation coefficient also exhibits a step increase, called an ‘absorption edge’, when incident x-ray photons possess a greater energy than the binding energy of the inner-shell electrons of an element in the material, such that an electron is ejected and the vacancy filled by an outer-shell electron. At the photon energy levels utilized in CT and other x-ray imaging systems, K-shell electrons may

be ejected, resulting in a K-edge (Figure 4.4). The K-edges for iodine, barium and gold are located at 33.2, 37.4 and 80.7 keV, respectively. Thus, the contribution of absorption edges to x-ray attenuation is greatest when the mean energy of the source spectrum is near the contrast agent K-edge. Moreover, absorption edge subtraction can be used to increase the signal-to-noise ratio by subtracting images taken at energy levels above and below the K-edge of a material or contrast agent. At the photon energy ranges used in radiography and CT (10–140 keV), the X-ray attenuation of high atomic number elements is primarily governed by the photoelectric absorption due to differences in mass concentration. A greater mass concentration will lead to greater x-ray attenuation; therefore, the delivery of a larger mass payload to the site of interest will increase the contrast enhancement. However, large doses of exogenous contrast media may cause adverse side effects in vivo, including toxicity. Therefore, an appropriate dose must be determined in order to enhance contrast without inducing cytotoxicity.

4.1.4 Design of AuNPs as x-ray contrast agents

AuNPs must be designed to meet the necessary functional requirements for a contrast agent in a particular clinical or preclinical application.

These functional requirements include (Figure 4.4):

Delivery: “Go where we want.” The contrast agent must be able to be delivered in vivo and transported to the site of interest.

Nontoxic: “Do not harm along the way.” The contrast agent must not cause adverse side effects to organs during delivery and clearance.

Targeting or localization: “Stay where we want.” The contrast agent must accumulate and be retained at site(s) of interest (e.g., blood pool, tumor or microcalcification, among others).

Contrast enhancement: “Show what we want.”

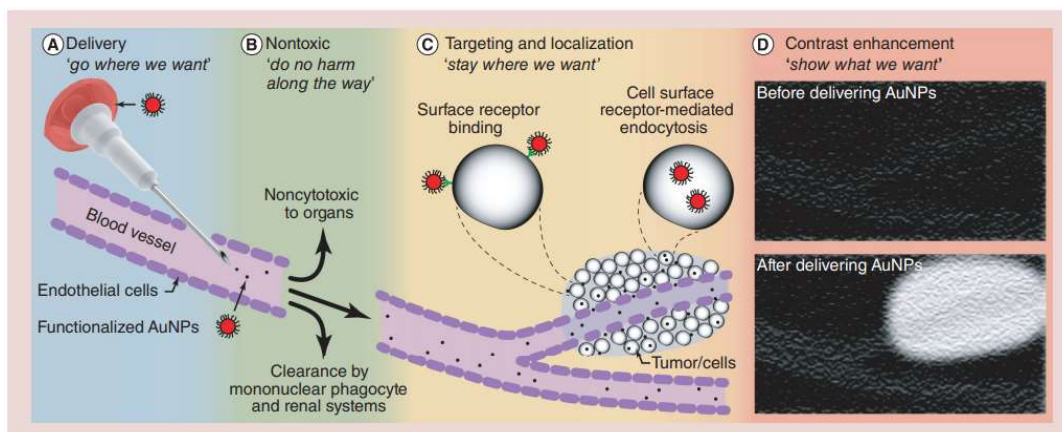


Figure 4.4- Schematic diagram (not to scale) showing the necessary functional requirements for gold nanoparticle x-ray contrast agents: delivery (A), nontoxic, targeting (B) and localization (C) and contrast enhancement (D) [77].

The contrast agent must increase the x-ray attenuation of the site of interest compared with surrounding tissues. These functional requirements can be achieved by designing nanoparticles to have specific properties through control over structural characteristics. Key properties include the X-ray attenuation coefficient, colloidal stability in physiological media and during storage, vascular retention time, biodistribution and cytotoxicity. These physical, colloidal and biological properties are governed by structural characteristics, including the nanoparticle composition, mass concentration, size, morphology and molecular functional groups. The composition of an x-ray contrast agent directly affects the number of X-rays that can be attenuated and therefore the ability to enhance contrast. The X-ray attenuation of a contrast agent is dependent on the atomic number, bulk density, X-ray source energy spectrum and presence or location of x-ray absorption edges.

4.2. Laser-produced Au nanoparticles as X-ray contrast agents for diagnostic imaging

Recently, Au nanoparticles (NPs) have been finding many potential applications in different scientific fields like physics to chemistry and biology, reaching from material sciences and catalysis to biomedicine, particularly thanks to the variety of their peculiar properties [78]. For instance, they promote surface plasmon resonance (SPR) permitting induction of resonant absorption at specific electromagnetic wavelength bands from visible to IR regions. Furthermore, they can be employed to improve welding, thanks to enhancement of wetting and adhesion of adjacent surfaces; they can be also employed to modify mechanical, optical, and electrical properties of many different materials, from polymers to glass and ceramics; or they can be used to prepare advanced targets for laser irradiation and plasma production at high density and temperature. Particular interest is devoted to Au NPs due to the high atomic number and atomic weight of Au, their high biocompatibility and chemical passivation, and high atomic and electronic density. Au significantly changes the absorption of X-rays during radiography; therefore, if suitably introduced into liquid and biological tissues, it may produce high-contrast imaging of biological systems and enhance the absorbed dose during radiotherapy expositions. In bio-medicine, Au nanoparticles find high interest, also thanks to the increase of the dose released by the ionizing radiation during the radiotherapy and the induction of localized heating during the photothermal therapy. Most importantly perhaps, Au nanoparticles have been also widely investigated as carriers for targeted drug delivery. The image contrast produced by Au maybe higher than the one of iodine due to its higher mass X-ray absorption coefficient [79].

Moreover, Au NPs do not induce the cause of severe adverse effects in some patients during their injection, as well as can be for iodine molecules, and due to their small size, they may travel through the microscopic capillaries of the circulatory system, facilitating their intravenous use. NPs speed, deposition, coagulation, agglomeration, and endothelial penetration under viscous pulsatile

flow represent complex phenomena. The transport of NPs in the circulatory system, whether major blood vessels or microcapillaries, is still not a well investigated and understood phenomenon but it is plausible. Au NPs form various structures, including nanorods, nanoclusters, nanoshells, nanocages, nanocubes, nanoprisms, and nanospheres, which can be well conveyed and spread if in nanometric dimensions. We propose a method for the preparation of Au nanoparticles using the pulsed laser ablation of solid Au targets placed in liquids (water, physiological solutions, biocompatible liquids, etc.); they are investigated using the optical spectroscopy, SEM and TEM, and the enhancement of contrast and radiotherapeutic dose in X-ray diagnostic imaging in the presence of Au NPs. The energy released by the laser pulse generates plasma with an emission of atomic ionized particles. Due to the high density of the surrounding liquid, the plasma cannot expand freely, as in vacuum, and therefore it promotes strong collisions between atoms and molecules, which lead to the generation of nanoparticles in the liquid. Shape, size, and density of the produced NPs depend on the following:

- the laser parameters: wavelength, pulse duration, pulse energy, intensity, repetition rate, polarization, etc.,
- the irradiation conditions: focal spot, focal point with respect to the target surface, incidence angle, target depth in the liquid, etc.
- the target and liquid properties.

We also present a study of the mechanisms of X-ray absorption in liquids and tissues with and without insertion of Au NPs at different concentrations. The data are based on the dependence of the X-ray absorption coefficient of the absorber material at a specific energy [81].

This phenomenon is described by the Lambert–Beer law, which is valid in the case of narrow beams of monoenergetic photons for plane-parallel beams incident on slab geometry:

$$I_T = I_0^{-\left(\frac{\mu}{\rho}\right)\rho \cdot d} \quad (4.3)$$

where I_T is the intensity of the transmitted X-ray radiation, I_0 is the intensity of the incident X-ray radiation, $\frac{\mu}{\rho}$ (cm^2/g) is the mass X-ray absorption coefficient, ρ is the material density (g/cm^3), and d is the thickness (cm) of the irradiated material. Furthermore, at the X-ray energy lower than 100 keV which we used in our experiments, the main absorption is generated by the photoelectric effect, depending strongly on the atomic number of the target. The Compton scattering will be also present but its cross section is less relevant because the dependence is linear with the atomic number of the target. Therefore, the mass X-ray absorption coefficient is a function of the X-ray energy, and the physical and chemical properties of the sample material are given by the following:

$$\frac{\mu}{\rho} = \frac{N_A \sigma_{tot}}{A} \approx \frac{Z^4}{AE^3} \quad (4.4)$$

where N_A is the Avogadro number, σ_{tot} is the total cross section given by the sum over contributions from the principal photon interactions (coherent (Rayleigh) and incoherent (Compton) scattering, photoelectric effect, electron-positron production, and photonuclear cross section), A is the gram atomic weight of the target element, Z is the effective atomic number of the target, and E is the X-ray energy.

At the used X-ray energies lower than 100 keV, the major contribution comes from the photoelectric effect and the Compton effect, although present, can be neglected only in a first approximation.

The mass absorption coefficient is then proportional to the high power of the effective atomic number and inversely proportional to the high power of the X-ray energy.

In mixtures and compounds, the values of the mass attenuation coefficient, μ/ρ , can be evaluated by the simple additive law:

$$\frac{\mu}{\rho} = \sum_i w_i \left(\frac{\mu}{\rho} \right)_i \quad (4.5)$$

where w_i is the fraction by weight of the i^{th} atomic constituent, and the $\left(\frac{\mu}{\rho}\right)_i$ values are relative to the i -th element of the compound. The mass X-ray absorption coefficient in Au is higher than iodine, which means that gold provides greater X-ray contrast per unit weight than iodine. Additionally, since it has an optimal X-ray absorption coefficient at 50–100 keV, which reduces interference of contributions from the bone and soft tissue absorption. We will present and discuss the qualities of X-ray images in the presence or absence of Au NPs in living mice. The advantages of Au NPs in comparison to other contrast agents will be discussed in major detail for in vivo studies. For example, their surface, shape, and dimensions can be modified in order to tailor their specificity. For example, suitable coatings (e.g., polymers, silica) and other compounds may provide advanced nanoparticles with increased circulation half-life and improved functionality. Therefore, fluorescent markers or therapeutic agents of suitable size and shape can be introduced in extra- and intracellular liquids of different tissues and organs. Another advantage of Au NPs is their use as X-ray contrast agents increasing the effective atomic number of the target. Considering the number of functionalities that can be incorporated, the NP size becomes a critical parameter. For example, a NP with not only imaging but also targeting functionalities requires a diameter of about 100–10 nm. This is approximately the diameter of many cell structures such as ribosomes, microtubules, nuclear pores, diameter of a DNA Alpha helix, and proteins, which, analogously, have several recognitions and effects or sites. For molecular imaging, NPs <150 nm are preferred because they can easily undergo endocytosis. For other imaging applications, well-stabilized NPs up to 500 nm in size are typically used because they selectively accumulate at tumor sites as a result of the enhanced permeability and retention (EPR) effect, which describes the abnormal form and architecture of the tumor.

4.2.1 Used Materials

A Nd:YAG laser, operating at a 1064 nm wavelength, 3ns pulse duration, 150 mJ pulse energy, 10 Hz repetition rate, 1 mm² spot size on the target, an intensity of 5×10^9 W/cm², was employed to generate Au NPs. The horizontal laser beam was

deflected at 90° by a prism and focused on the target through a convergent lens with a 50 cm focal distance. The Au target, 1 mm in thickness, was placed inside a glass beaker. In order to avoid vibrations of the Au target, it was retained within the beaker by an interlocking polyethylene, and 2.5 ml of distilled water was introduced in the beaker with a micro-syringe. Irradiations were conducted at step of 10 min, during which a Au ablation of 1 mg is obtained. Generally, solutions of NPs were produced using an irradiation time ranging between 10 min and 60 min to obtain different concentrations of Au NPs in solution. The Au target has been weighed before and after the laser irradiation to calculate the total amount of gold released in the solution. Concentrations of 1 mg/ml up to 10 mg/ml of Au NPs were obtained in a total volume of the order of 2.5 cm³. The freshly prepared solution of NPs was immediately submitted to optical spectroscopy analysis in order to measure the absorbance as a function of the wavelength. To test the suitability of the prepared NPs for medical diagnostics, we injected 0.01 ml of NPs solution per gram of the mouse weight to healthy mice from their tail vein 1 h after the solution preparation. Thus, at a mouse with 100 g weight was injected 1.0 ml solution. X-ray images were observed at different times (from 3 min up to 3 days) from the injection using a new X-ray imaging system emitting photons at a mean energy of about 20 keV with different exposition times and recording the images on a CCD digital recorder (Bruker-In vivo imaging system MS-FX PRO). The system uses X-rays at energy selectable between 20 and 45 kV, a maximum electron current of 500 μA, a spot of 60 μm, and with a beryllium window filter. Using 45 kV tube bias the typical X-ray spectrum due to electron Bremsstrahlung shows an average X-ray energy peaked at about 20 keV photons. The exposition of 1.2 s can be acquired either as a single capture or as a summation of up to 32 frames. The output is typically a grayscale image, which may be thought of as a shadow of the object in the path of the X-ray beam. In a classic X-ray image with film, areas that appear white represents dense tissues (like bone or inflammation and infected lung tissue that can obstruct the passage of X-ray energy). Meanwhile, tissue that is not dense (like the lungs, which are filled with air) will have contrast at the opposite end of the grayscale spectrum and appear black. Tissues containing Au NPs during the X-ray tube exposition appear white colored due to the induced characteristic X-ray

fluorescence. Measurements with and without Au NPs were performed in order to evaluate the contrast agent introduced in the living system. The theoretical studies of the X-ray absorption in the different biological tissues and in the prepared solution were performed using the CXRO and NIST databases.

4.2.2 Mechanism of X-ray absorption in liquids and tissue

Using the absorption coefficients given by the NIST database, it was possible to evaluate the absorption in water, soft tissues, and bones with and without the use of the Au NPs solution at 20 keV X-ray energy, which is typically employed in biological diagnostics. The mass absorption coefficients in the three media are 0.2476, 0.2476, and 0.54485 cm²/g for water, soft tissue (ICRU-44 [82]), and hard bone tissue (ICRU-44), respectively. The absorption enhancement due to Au NPs concentration is a consequence of the higher cross-section of the photoelectric effect, which is proportional to a high power of the equivalent atomic number of the target, and the density of the target increased by the presence of Au NPs. Figure 4.5 shows the calculated absorption in water (1 g/cm³ density), in soft tissue (mammary gland, 1.02 g/cm³ density), and in bone (cortical bone adult 1.92 g/cm³ density) with growing concentration of Au NPs, from 0 up to 100 mg/ml. Generally, the used concentrations in this study range from 1 to less than 10 mg/ml, which is reduced to values of the order of microgram per millilitre (µg/ml) just injected in blood as estimated from the detected concentrations obtained from blood or drug transport measurementstopeculiar organs. However, higher concentration can be obtained at interfaces between different tissues as result of diffusion processes, filtering, local injection, segregation, restraint, coalescence, mechanical and/or chemical activation, or other processes. The mass absorption coefficient in tissues was calculated onthe basis of its value in the tissue andingold, weighted for the concentration of the tissue and of the gold in the target.

For instance, for the soft tissue with the concentration of 10mg/ml Au NP at 20 keV (mean X-ray energy used), the calculation using the NIST database has been performed as follows:

$$\begin{aligned} \left(\frac{\mu}{\rho}\right)_{softtissue+AuNp} &= (0.99 \cdot 82.30) \frac{cm^2}{g} + (0.01 \cdot 78.83) \frac{cm^2}{g} \\ &= 1.6031 \frac{cm^2}{g} \end{aligned} \quad (4.6)$$

The density ρ soft tissue containing the Au Nps can be approximately as follows:

$$\rho_{softtissue+AuNp} = (0.99 \cdot 1.02) \frac{g}{cm^3} + (0.01 \cdot 19.3) \frac{g}{cm^3} = 1.203 \frac{g}{cm^3} \quad (4.7)$$

The transmitted intensity of a 2 cm tissue thickness doped with the Au NPs, for example, corresponds to as follows:

$$I_{T-softtissu +Au} = I_0 e^{-\frac{\mu}{\rho} \rho \cdot d} = 100 \cdot e^{-1.6 \cdot 1.2 \cdot 2} = 15.4\% \quad (4.8)$$

$$I_{T_{soft tissue+AuNp}} = I_0 e^{-\frac{\mu}{\rho} \rho \cdot d} = 100 \cdot e^{-3,3463 \cdot 1.203 \cdot 3} = 28.656\% \quad (4.9)$$

And the corresponding absorption value is:

$$Abs = 100 - I_{T_{soft tissue+AuNp}} = 84.6\% \quad (4.10)$$

The comparison of the normalized absorption data for the different targets shows that the absorption increases with the Au NPs concentration. The absorption of Au NPs in water and soft tissue is similar due to the comparable mass absorption coefficients and densities. The 1 mg Au NPs/ml solution does not show significant enhancement with respect to the pristine water or biological tissue, while the 10 mg/ml or higher indicates important enhancement of the radiation absorption at 20 keV X-rays. The relative increment is higher in the case of water and soft tissue due to the low density of the pristine medium. At the high concentration of 100 mg/ml, Au NPs produce about 100% X-ray absorption starting from 0.5 cm target thickness or higher. The effect of the increasing absorption of the X-rays in tissues with higher concentration of Au NPs can be used in diagnostics and therapy. Increase of the absorption coefficient leads to an increment of local dose released by the irradiation. Therefore, the presence of Au NPs enhances there leased energy in the medium. If disease tissues are doped with Au NPs, they are more likely to be destroyed.

An increment of X-ray absorption by 55%, as occurs, for example, for soft tissue at 1 cm depth containing 10 mg Au NPs/ml, with respect to the tissue without Au NPs (see Fig. 4.5 b), means an increment of the absorbed energy and dose by 55 %.

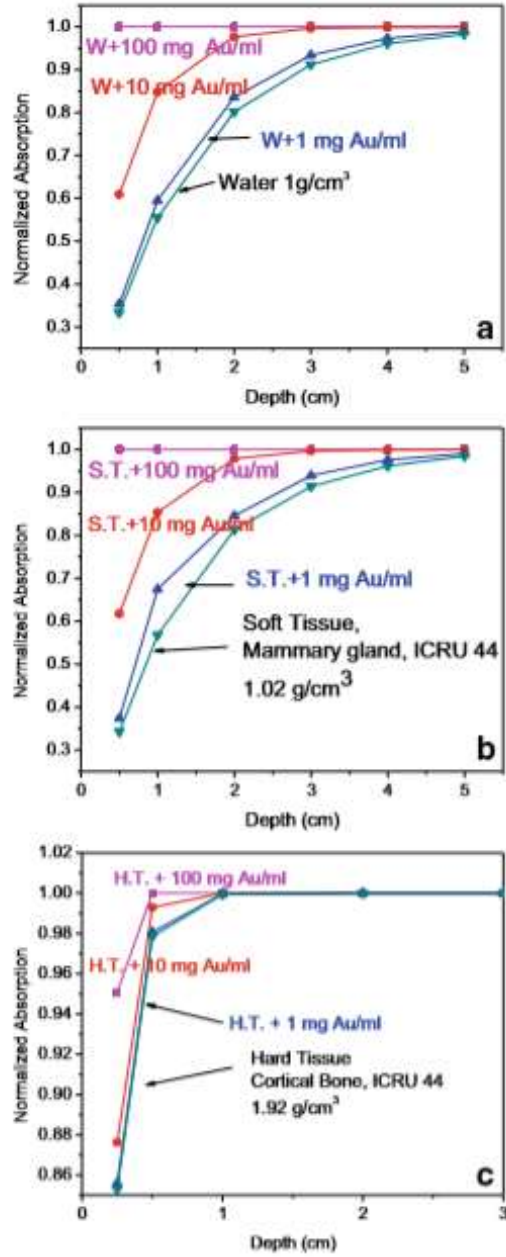


Fig. 4.5- Normalized absorption of 20 keV X-rays as a function of the depth in water (a), soft tissue (b), and cortical bone (c) for different Au NPs concentrations, from 0 up to 100 mg Au/ml.

4.2.3 X-ray diagnostic enhanced by Au NPs

The Au NPs transported by blood flux increase in many organs with the administered dose indicating an efficient tissue uptake proportional to the flux. Although the brain is the organ containing the lowest quantity of injected Au NPs, literature data suggest that Au NPs are able to cross the blood–brain barrier and accumulate in the neural tissue. Importantly, no evidence of toxicity was observed in any of the diverse studies performed, including survival, behavior, animal weight, organ morphology, blood biochemistry, and tissue histology. In pulmonary imaging, the bones of the rib cage and vertebral bodies will appear white, the lungs will appear black, and the heart will possess shades of gray. Dense lung tissue, as a consequence of pulmonary fibrosis, atelectasis, or pulmonary edema, appears in lighter shades of gray in a chest X-ray image, while the normal lung tissue appears black. With modern digital X-ray technology, these color scales can be optimized to achieve the best contrast for a given feature/disorder. Figure 4.6 shows a comparison of three typical images of a mouse, performed with the Bruker-In vivo imaging system MS-FX PRO, at $t = 3$ min just after the injection of 1 cm^3 solution at 1 mg/ml through the tail vein (a), at $t = 45$ min after the injection (b), and at 48 h after the injection (c). Image acquisition was obtained with 45 kVp 1 bias, beam filtering, 400 μA current, and 15 multi acquisition of 1.2 s each. The images indicate that the Au NPs uptake is higher at times of the order of 45 min in the colon of the mouse. The uptake is fast in the first minutes after the injection and about absent at times of about 48 h after the injection.

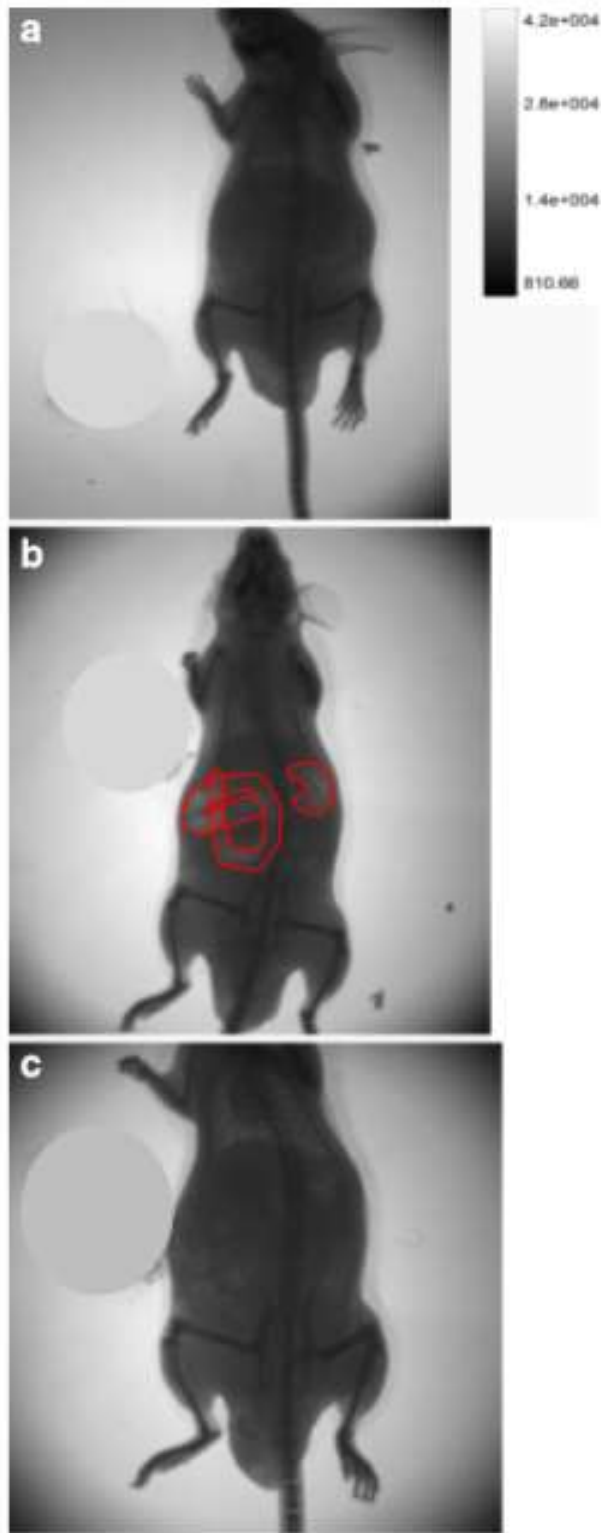


Fig.4.6- 20 keV X-ray image of a mouse at 3 min(a), at 45 min(b), and at 48 h(c) from the injection time in the tail vein (the gray circle on the left is an artefact due to localized burn of CCD pixels)

A good X-ray image contrast increment due to the Au NPs uptake is visible also in other organs, such as kidneys and bladder. Unfortunately, the CCD X-ray detector sensitivity and the image resolution are not sufficiently able to observe the contrast in the veins of the mouse in the beginning of the experiment, as reported in similar investigations. This deficiency can be due to both the used low concentration of 1 mg Au NPs/ml and to the fast dilution in the veins before to be accumulated in the excretory organs.

The produced colon contrast image is due mainly to the X-ray fluorescence of the gold targeting more than to the X-ray absorption effect, as demonstrated by the whiter color, opposite to the black color of the high absorbent bones. The X-ray fluorescence is due to the characteristic L-lines emitted at 9.7 keV ($L\alpha$), 11.5 keV ($L\beta$), and 13.4 keV ($L\gamma$) produced at high photoelectric cross section by the incident 20 keV X-rays tube. The gray scale X-ray images can be also quantitatively analyzed in order to characterize the uptake of Au NPs. Figure 4.7 shows a typical curve of the uptake of the Au NPs agent in colon walls of a rat in 45 min, followed by a decay phase. Assuming that the decay follows an exponential law, the biological decay constant τ is as follows:

$$\tau = t \cdot \ln \frac{Y_0}{Y} \quad (4.11)$$

where t is the time, Y_0 is the maximum value of the relative contrast gray, and Y is the relative contrast at t time from the maximum value. Value $\text{soft}=2000$ min and $\tau=2773$ min can be calculated from Fig. 4.7. Therefore, the biological decay constant in the rat is weak and of the order of 46 h. The contrast enhancement in colon, bladder, and kidney clearly points out to a quick clearance of the mouse body on the time-scale of hours.

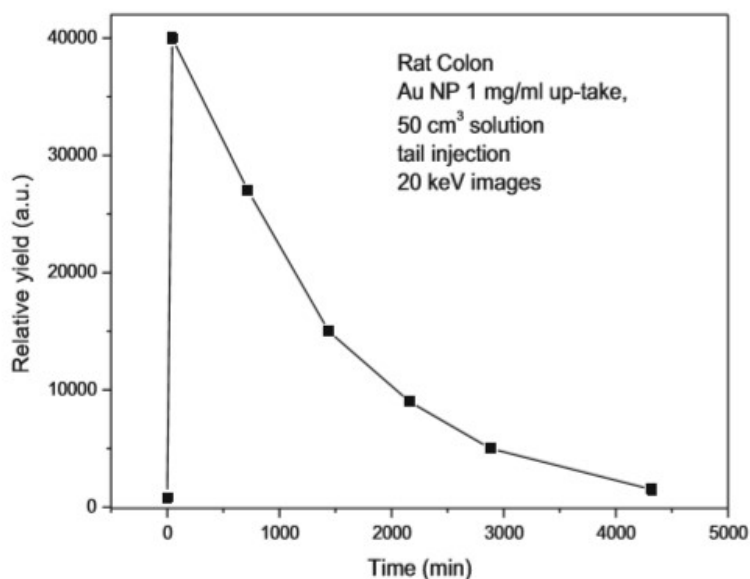


Fig. 4.7- Typical curve showing the uptake and decay times of the Au NPs concentration in the colon of the mouse.

During such decay, the diagnostic images can result of high interest for the description of the biofunctionality of the organism or of specific excretion organs. Moreover, within this decay time, it is possible to use radiotherapy in order to have an optimization of the effect on localized disease in the colon, bladder, and kidney. In other sprinkled blood organs, instead, radiotherapy can be employed before that Au NPs clearance appears in the excretion organs. A first evaluation about the theoretical dose released by X-ray irradiation with 50 to 200 keV for radiotherapeutical purposes with and without Au NPs has been performed by using the CXRO and NIST databases. The results indicate that the X-ray energy can be optimized in order to release high dose at the diseased tissues, depending on their depth, volume, shape, and density, and by assuming the Au NPs to be uniformly distributed in their volume. For example, preliminary results demonstrated that the use of 100 keV X-ray irradiation may enhance the released dose up to 100% with respect to the tissue without Au NPs when their concentration, at 3 cm depth, is high, of the order of 100 mg/ml, for water, soft tissues, and bones. This enhancement decreases to about 30% and 5% for Au NPs concentration of the order of 10 and 1 mg/ml, respectively.

4.3. Comparison between Au and Ag Nanoparticles generated by laser in liquid as contrast medium.

In recent years, technological development has allowed us to prepare, manipulate and characterize, more nano-sized materials. Metallic nanoparticles (NPs), based on Ti, Au, Ag, Bi and others, have numerous fields of applications: from electronics (detectors, solar cells, optoelectronics devices, sensors, nanoacoustic) to telecommunications (nonlinear optics, nanophotonics, nanothermic), biology and medicine (photothermal therapy, radiation and biological imaging diagnostics) and physical-chemistry (catalysts, preparing targets). Metallic nanoparticles embedded in an insulating medium behave like ionizing radiation absorbing centres, being able to show certain absorption resonances bands at specific wavelengths, thank to the Surface Plasmon Resonance (SPR) absorption effect. Their size distribution in a fluid changes the electronic and mass density and the equivalent atomic number of the material. The choice of gold as a starting material to prepare nanoparticles is not accidental. Gold, in fact, is stable, not oxidable and biocompatible for humans and, more in general, also for other living beings. In the light of these results, the medicine demonstrates a particular interest to the gold and silver nanoparticles for different aspects concerning prosthesis, interface adhesion, contrast medium for X-ray images and high Z-element for high absorbent radiations. In the present study it was determined experimentally the behaviour of Au and Ag nanoparticles (Au NPs and Ag NPs) in therapy and in diagnostics, in particular by calculating the ratio of the dose delivered to a given depth and the dose delivered to the surface in various media (water, adipose tissue and compact bone) in presence or not of the nanoparticles. The anticancer potential of the gold and silver nanoparticles is generated by the different physical-chemical properties advantages. Numerous studies [83] have demonstrated the safety and biocompatibility of Au and Ag both in vitro and in vivo, suggesting that the gold nanoparticles can be administered safely with minimal inflammatory activation and few local or systemic side effects enhancing the equivalent Z-value of the treated tissues at significant nanoparticle concentrations.

4.3.1 Used Materials

The Au-Ag NPs were produced by laser ablation in our laboratory, as explained previously. The system uses X-rays at energy selectable between 20 and 45 keV, a maximum electron current of 500 mA, spot diameter of 60 mm, with a beryllium window filter. The exposition time can be in single capture of 1.2 s, or in multiple captures overlapping up to the 32 image captures. Fig. 4.8 shows a scheme of the X-ray absorption image used in our laboratory. In order to avoid the nanoparticle aggregation phenomenon, in water we have added a biocompatible solution of 1 $\mu\text{g/ml}$ of sodium citrate that permits their uniform dispersion minimizing the collateral effect of coalescence.

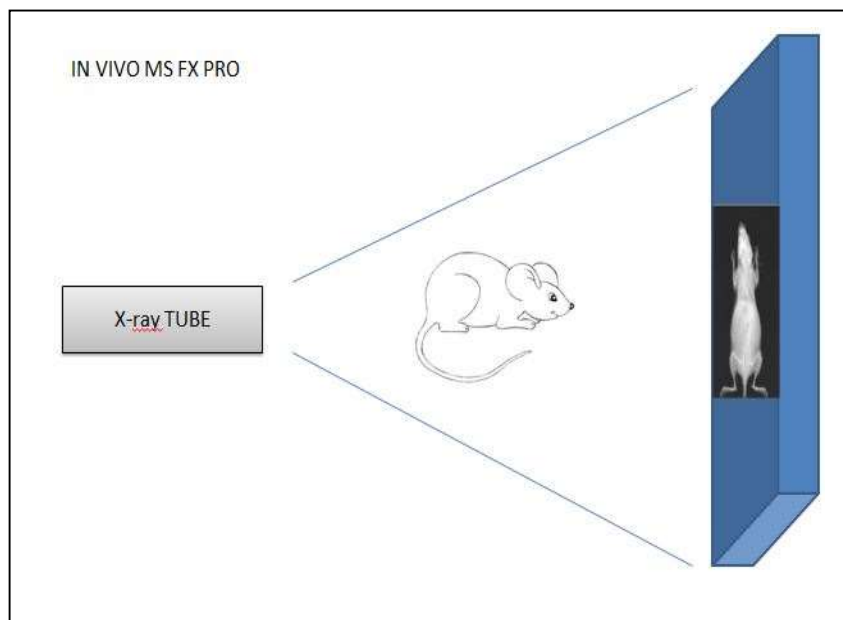


Fig. 4.8- Scheme of the X-rays imaging system

The output image is typically grayscale and may be obtained thought of as a shadow of the object in the path of the X-ray beam. In a classic X-ray image with film, areas that appear white represent dense tissues (like bone or inflammation and infected lung tissue that can obstruct the passage of X-ray energy). Meanwhile, tissue that is not dense (like the lungs, which are filled with air) will have contrast at the opposite end of the grayscale spectrum and appear black. The new used X-ray

image system records images on a CCD detector through different filters, such as beryllium, aluminum and other thin films, in order to improve the signal-to-noise ratio.

This tool has allowed us to carry out animal measurements to verify the effectiveness of high-Z metallic nanoparticles as a potential contrast medium injectable by intravenous, peritoneal or ingestion way. It permits to record X-ray images not only using transmitted X-rays but also using secondary X-ray characteristic fluorescence emission lines, as obtained using Au and Ag NPs.

4.3.2 Results

Water solutions containing gold and silver nanoparticles, both generated by ablation in water and analyzed through SEM and TEM microscopies, giving an average diameter of about 50 nm, were injected in healthy mice. The administration of 0.01 ml solution containing nanoparticles per gram of mouse weight was given through intraperitoneal way. The Fig. 4.9 shows the differences between the X-rays of fluorescence images obtained using gold and silver nanoparticles injected in mice. Once injected gold nanoparticles are quickly absorbed and after about 120 minutes they are deposited in the colon (middle images), after 24 hours there is a remainder accumulated in the livers (bottom images). Instead, measurements demonstrated that silver nanoparticles are absorbed more slowly and the first visible results are found after 24 hours with a significant build up in the colon of the mouse. This result leads us to conclude that blood circulation of silver nanoparticles produces a slower up-take than that relative to gold nanoparticles. Thus the two kind of nanoparticles have a different metabolic up-take effect

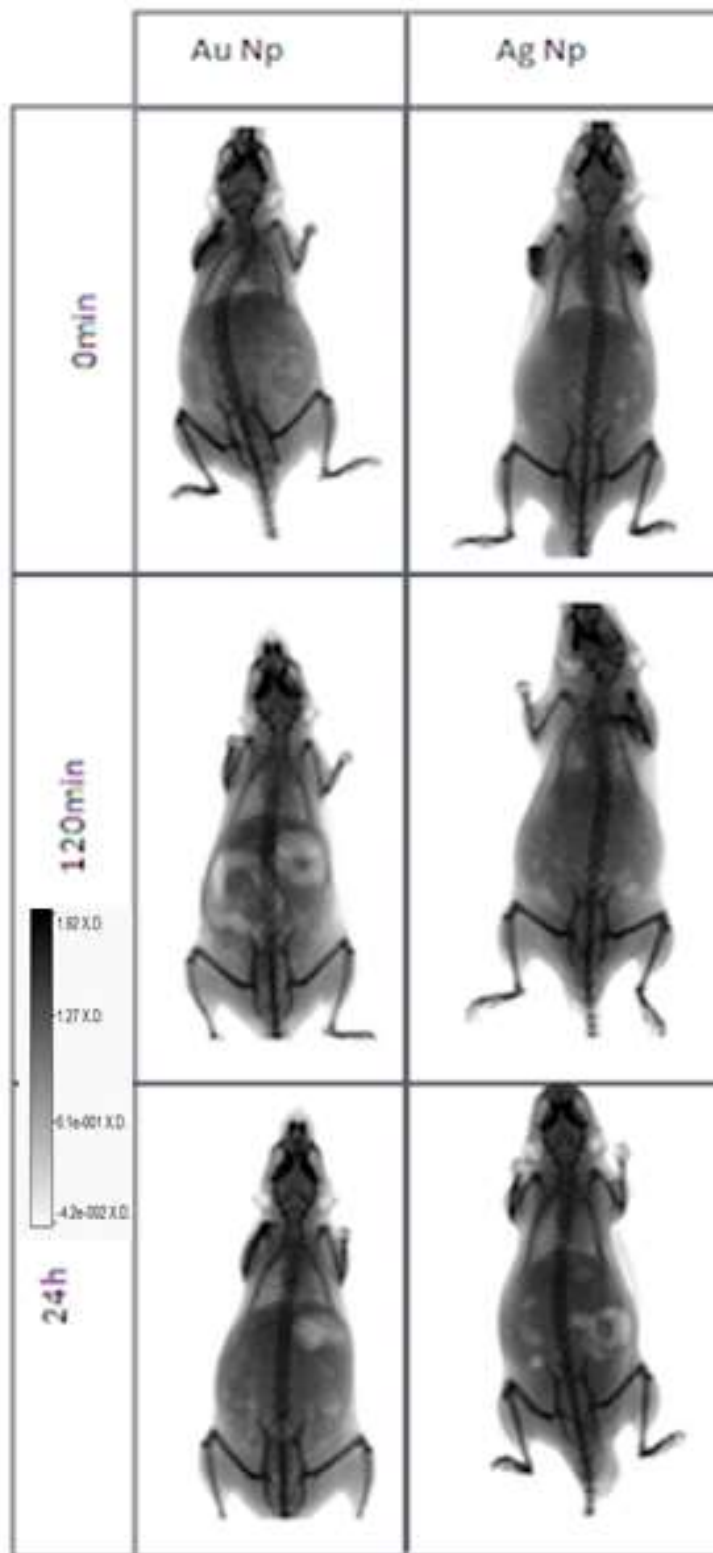


Fig. 4.9 - X-rays fluorescence images of Au and Ag in mice as a function of the time from the peritoneal injection.

4.4. Laser-generated Bismuth Nanoparticles for application in Imaging and Radiotherapy.

Bismuth is a pentavalent post-transition metal, it has atomic number is 83, an electronegativity of 2.02 in the Pauling scale, a melting point of 271.5°C and a boiling point of 1564°C. It is the most natural diamagnetic element, and exhibits the lowest values of thermal conductivity among metals. Its density is of 9.78 g/cm³, it has a rhomboidal structure, a thermal expansion of 13.4 μm/mK at 25°C, a thermal conductivity of 7.97 W/mK and an electrical resistivity of 1.29 μΩm at 20°C [84]. It is a brittle metal with white color when freshly produced, but its color turns pink as a consequence of the surface oxidation. The thickness variations of the surface oxide layer cause interference of the different light wavelengths upon reflection, displaying a rainbow of colors on its crystalline surface. Bismuth compounds are used in cosmetics, as pigments, and a few pharmaceuticals. Other Bi-based compounds, such as Bi-subnitrate ($\text{Bi}_5\text{O}(\text{OH})_9(\text{NO}_3)_4$) and Bisubcarbonate ($\text{Bi}_2\text{O}_2(\text{CO}_3)$), are also used in medicine for other different aims, such as to treat syphilis, to treat some gastro-intestinal diseases and to acts such as a basic salt. Even if bismuth is an heavy metal, it has unusually low toxicity. As the toxicity of lead has become more apparent in recent years, there is an increasing use of bismuth alloys as a replacement for lead. Bismuth, as a dense element of high atomic weight, is used in bismuth-impregnated latex shields to shield from X-ray in medical examinations, such as CTs, mostly as it is considered non-toxic. Bismuth oxide is occasionally used in dental materials to make them more opaque to X-rays than the surrounding tooth structure. The mass absorption coefficients of X-ray and the stopping powers for electrons and ions versus the energy shows a significant increment of the values for heavy Bi element with respect to other contrast media, such as iodine, gold and calcium, demonstrating the best behaviour for its use as contrast medium and as targeting elements in biological cancer tissues for suitable radiotherapy expositions. Several nanoparticulated CT contrast agents are based on iodine, gold and silver nanoparticles, core-shell iron oxide/tantalum oxide nanoparticles and others alloy nanoparticles. Nanoparticulated CT contrasts bearing bismuth, in particular bismuth sulphide nanoparticles, have obtained

special attention due to a combination of low price, low toxicity and a high x-ray attenuation coefficient. This material has been successfully prepared to be used as contrast breast cancer, as reported in literature [85]. Many researchers are using Bi as metal [86], Bi₂O₃ oxides [87], as FeBi as magnetic nanoparticles, as Bi₂S₃ as sulfides [88], and other Bi compounds, as nanoparticles in liquid solution to be used as X-ray computed tomography (CT) imaging and to generate fluorescence imaging. However, high Bi concentrations in solution are demonstrating to have a minimum level of toxicity, thus the concentration must be accurately evaluated before to introduce the solution in living systems [89]. Our study on Bi was conducted both to improve the image spatial resolution using it as contrast medium in biological environment, and to enhance the equivalent atomic number of the targeted tissues where the element is concentrated in order to be prepared for an efficacious radiotherapy treatment, as presented in similar papers previously published [80] by our group. The Bi-NPs introduction in the in-vivo environment can be performed in different ways, by using the injection of the prepared solution in the blood flux, by injecting directly the solution in the organ of interest.

4.4.1 Materials

Metallic bismuth nanoparticles (Bi-NPs) were prepared using the technique of the pulsed laser ablation in liquids. The metal, as sheets of about 3 cm² surface and 1 mm thickness, was placed on the bottom of a glass beaker. A volume of 5 ml of distilled water was added and 1 µg of tensioactive was employed as stabilizer in order to avoid fast particle coalescence. Using 70 mJ pulse energy and an irradiation time of 10 min and covering the Bi sheet surface with 4 mm liquid, the ablated mass was of 4 mg, thus in these conditions a solution concentration of 4 mg/5 ml, that is 0.8 mg/ml, was obtained. The ablation yield, in terms of removed mass per laser shot, was controlled by the laser fluence and solution concentration, because the increment of the laser fluence enhances the ablation yield while the high solution concentration absorbs laser energy and decreases the ablation yield. Generally, using exposition times of the order of 20 min and repetitive laser shots, a total ablation of about 1 µg mass per laser shot was produced in the form of nanoparticles in water at fluence of 5 J/cm². The Bi laser ablation in water was evaluated in term

of removed mass per laser shot as a function of the laser pulse energy, as reported in Fig. 4.10. Above the ablation threshold, the ablation yield grows approximately linearly with the laser energy and the use of low pulse energy, above the ablation threshold, is chosen to maintain low (below about 100 nm diameter) the dimensions of the produced nanoparticles. The inset of the plot shows a photo of a typical crater produced by the 10 Hz repetition rate laser beam after 20 min irradiation time in water. The removed atoms in the laser-generated plasma and in the water environment condense in nanometric particulate. The nanoparticles tend to aggregate forming micrometric nanoparticles but the presence of the tensioactive liquid stops the aggregation phase. The produced solution of Bi-NPs in water changes color during the laser ablation from white transparent to white opaque, to brown and to dark brown color at high concentration. Fig. 4.11 shows the Bi-NPs in water before (a) and after 10 min (b) of laser irradiation time ($C=0.8$ mg/ml). The Bi-NPs were characterized at the Department of Physics Sciences of Messina University (MIFT) laboratories and at the Messina IPCF CNR ones by using FESEM microscopy, X-ray diffraction analysis (XRD), X-ray fluorescence analysis induced by electron beam (EDX), UV-Vis absorption and Raman spectroscopy. In particular the bismuth nanoparticles solutions were diluted with water before taking the UV-Vis absorption spectra. Deionized water was used as reference. To observe the Bi-NPs morphology and composition a drop of the resulting solution was dried onto a silicon or glass substrates and a field emission scanning electron microscope (FESEM), operating at 1.5 and 3.0 kV, as well as the energy-dispersed X-ray spectrometry (EDX) used with a 5 KeV electron beam energy, a Bruker D8Advance X-ray diffractometer, using the Cu $K\alpha$ radiation ($\lambda = 1.54 \text{ \AA}$) at 40 kV and 40 mA in the $5^\circ \leq 2\theta \leq 60^\circ$ range, and the micro-Raman spectroscopy using a He-Ne 633 nm laser source, were employed. The prepared Bi-NPs were injected in specific organs of living systems (mice) and their spatial location and contrast were controlled using the fluorescence induced by a (20÷45) kV X-ray tube of the Bruker-in vivo MS-FX PRO system.

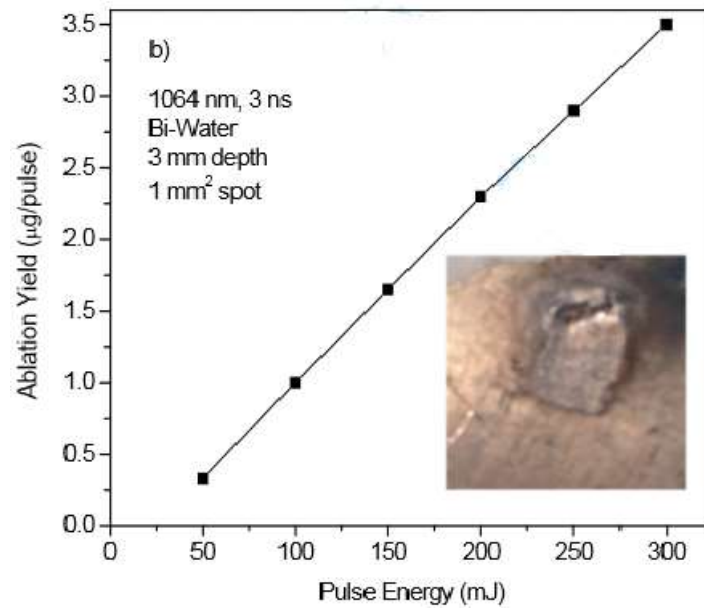


Fig. 4.10 - The inset reports a crater produced in Bi sheet by the laser ablation.

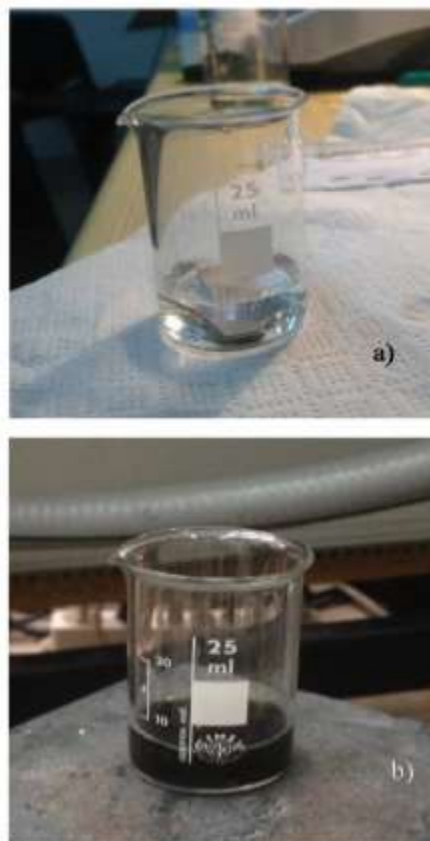


Fig. 4.11- Bi-NPs solution in the beaker before (a) and after the laser ablation (b) (20 min, 10 Hz).

4.4.2 Results

The presence of the metallic nanoparticles in the solution induces surface plasmon resonance (SPR) absorption effects showing absorption wavelength bands depending strongly on the particle shape, dimensions, concentration and nature of liquid medium. The resonant absorption is due to the light induction of dipole and electron oscillations on the surface of the metallic nanoparticles. The plasmon bands fall in the UV region for very little nanoparticles and in the visible region for nanoparticles from about 50 nm up to about 100 nm diameter. Fig. 4.12 reports the UV-Vis absorption spectrum of the diluted aqueous solution of Bi-NPs containing the tensioactive stabilizer. It shows a poorly resolved shoulder at about 269 nm; this feature can be assigned to the surface plasmon resonance (SPR) absorption peak of the Bi NPs that gradually broadens as the size of Bi NPs decreases. Since the Bi clusters with diameter below 10 nm do not show any SPR absorption band, while the larger nanoparticles (>100 nm) show a strong absorption peak at about 280nm, our spectrum seems to indicate that the Bi-NPs shape is a sphere, with a diameter greater than 10 nm but smaller than 100 nm, in agreement with the SEM and XRD data that will be illustrated in the following. Since the Bi-NPs aggregation producing larger nanoparticles shifts the band from the near UV up to the VIS region, the presence of another little absorption band at about 380 nm seems to indicate that some nanoparticles have an ellipsoidal shape even if not visible in the SEM images. Fig. 4.13 (a, b, c, d) report a lot of SEM images of the Bi-NPs deposited with the solution on the Si substrate after prolonged drying (6 h). The nanoparticles have spherical shape with a diameter distribution going from about 10 nm to 100 nm and an average value of about 25 nm, as reported in the size distribution of Fig. 4.13e. A typical EDX spectrum, performed during SEM analysis using a 5 keV electron beam, is illustrated in Fig. 4.14a. It is relative to a group of Bi-NPs, reported in the SEM image of the inset. The spectrum shows the characteristic M-lines of Bi, at about 2.4 keV ($M\alpha$), the K-lines of Si due to the silicon substrate, the presence of O and C (K-lines) as substrate's contaminants and the presence of Na, coming from the tensioactive compounds at very low concentration.

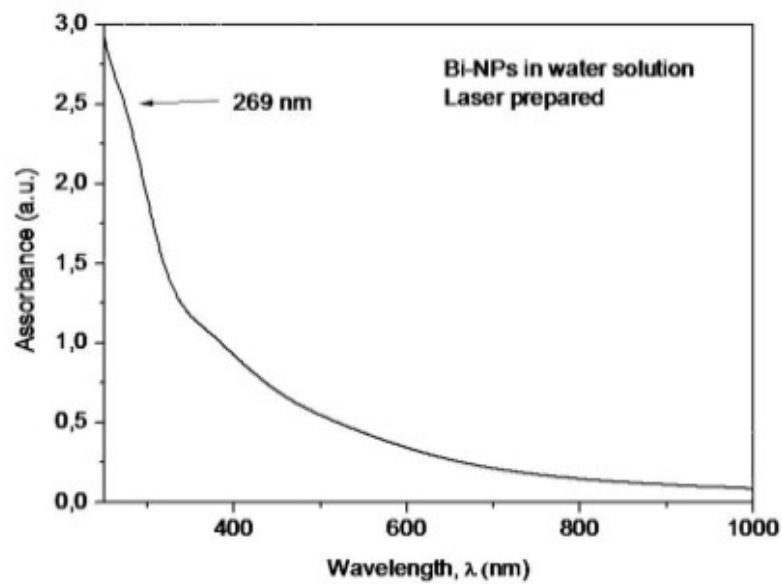


Fig. 4.12- Absorbance measurements vs. wavelength for the Bi-NPs solution in water.

The O low presence indicates that the Bi is metallic and not oxidized (other while the oxygen should have been higher), in agreement with the Raman spectrum, reported in Fig. 4.14b, relative to a solution drop deposited and dried on a Si cleaned surface and obtained by using an exciting laser beam operating at 633 nm. The characteristic peaks at 69.5 and 96.0 cm^{-1} are due to the Eg and A1g first order Raman modes characteristic of rhombohedral bismuth and reveal the crystalline state of the formed nanoparticles. The blue shift of the Raman lines (they are located at 69 and 94 cm^{-1} respectively in Bi bulk) can be due to the phonon confinement. The broad shoulder at about 130 cm^{-1} corresponding to the Bi-O stretches of $\beta\text{-Bi}_2\text{O}_3$ indicates a very slight oxidation of the Bi NPs [90, 92]. Thus the microRaman spectrum confirms the presence in the solution of metallic Bi nanoparticles for the most part in agreement with the above mentioned measurements of X-ray fluorescence analysis from SEM investigations on some observed nanoparticles.

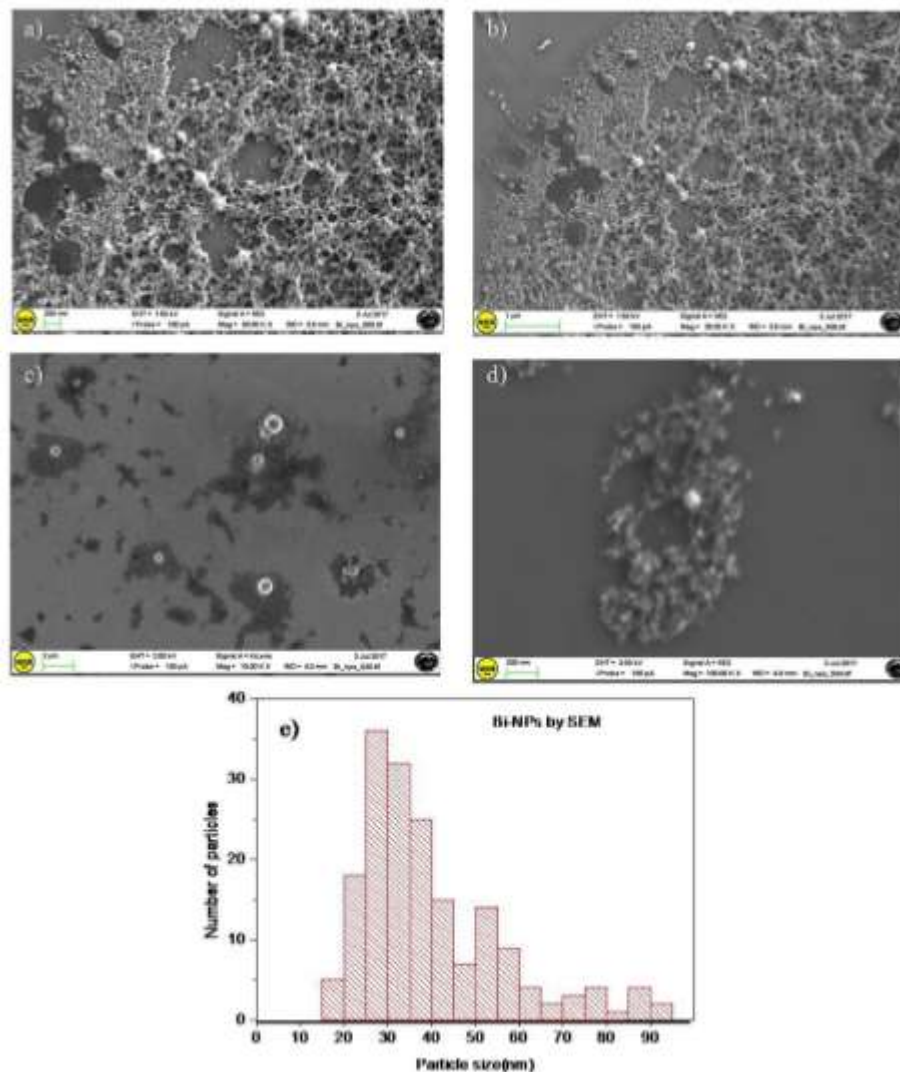


Fig. 4.13- SEM photos of the dried Bi-NPs deposited on a silicon surface (a, b, c, d) and relative diameter distribution (e).

The use of Bi-NPs as contrast medium in living tissues was tested in mice injecting the prepared biocompatible solution in some organs and observing the Bi fluorescence image induced by the Bruker X-ray tube. Fig. 4.15a shows the image when the solution was injected in the heart. The image shows very well the organ (observed in dark gray scale such as X-ray transmission) and the nearest blood irrigated tissues as very bright due to the X-ray induced fluorescence. Fig. 4.15b reports the image when the solution was directly injected directly in the Sx kidney. The image illustrates very well the organ (observed in gray scale such as X-ray transmission) and the nearest blood irrigated tissues are very bright due to the X-

ray induced fluorescence. The obtained medical images are well contrasted and the interested organ shows high spatial resolution of the zones where the Bi-NPs are localized. At this stage the up-take and the decay of the Bi as a function of the time were not studied, a work is in progress on this aspect. The aim of the study was to distinguish the interested organ in order to be observed it in detail before that a successive radiotherapy procedure can be applied on the diseased tissues. From this point of view at the moment no radiotherapy was performed on mice, it will be performed in a next investigation.

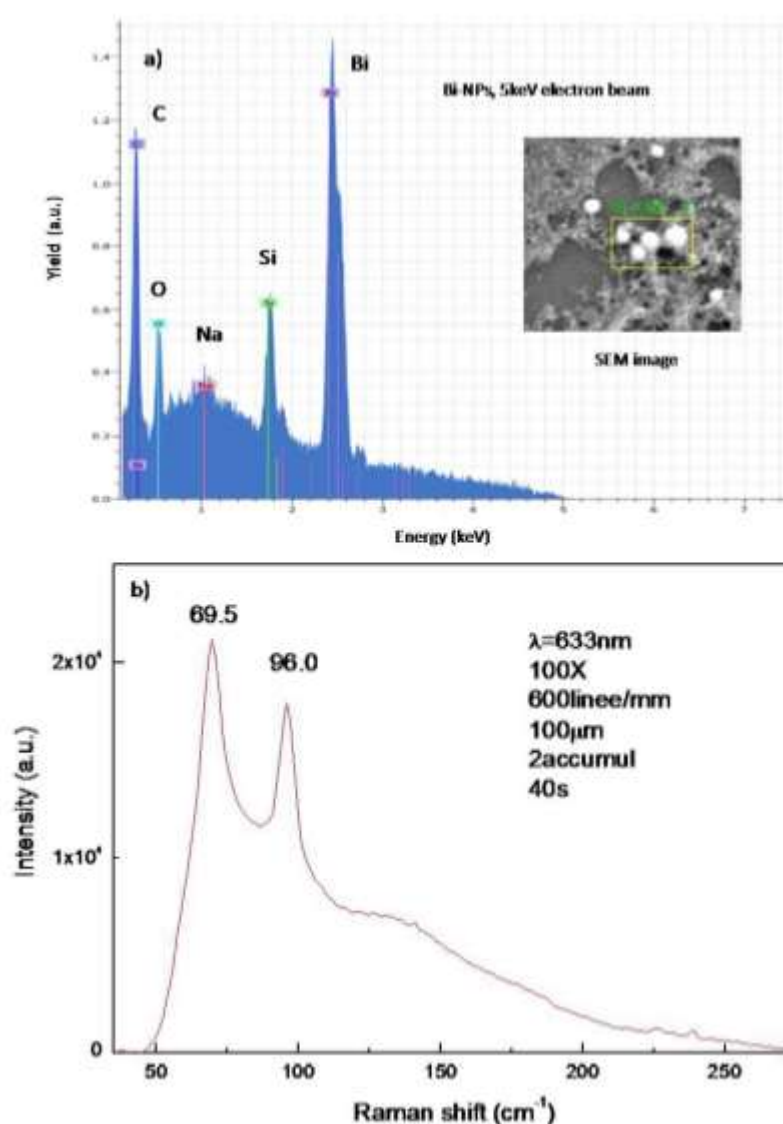


Fig. 4.14- Typical XRF analysis of the Bi-NPs deposited on the Si-substrate (a) (the inset report the analyzed zone) and Raman spectrum of the analyzed thin Bi-NPs film (b)

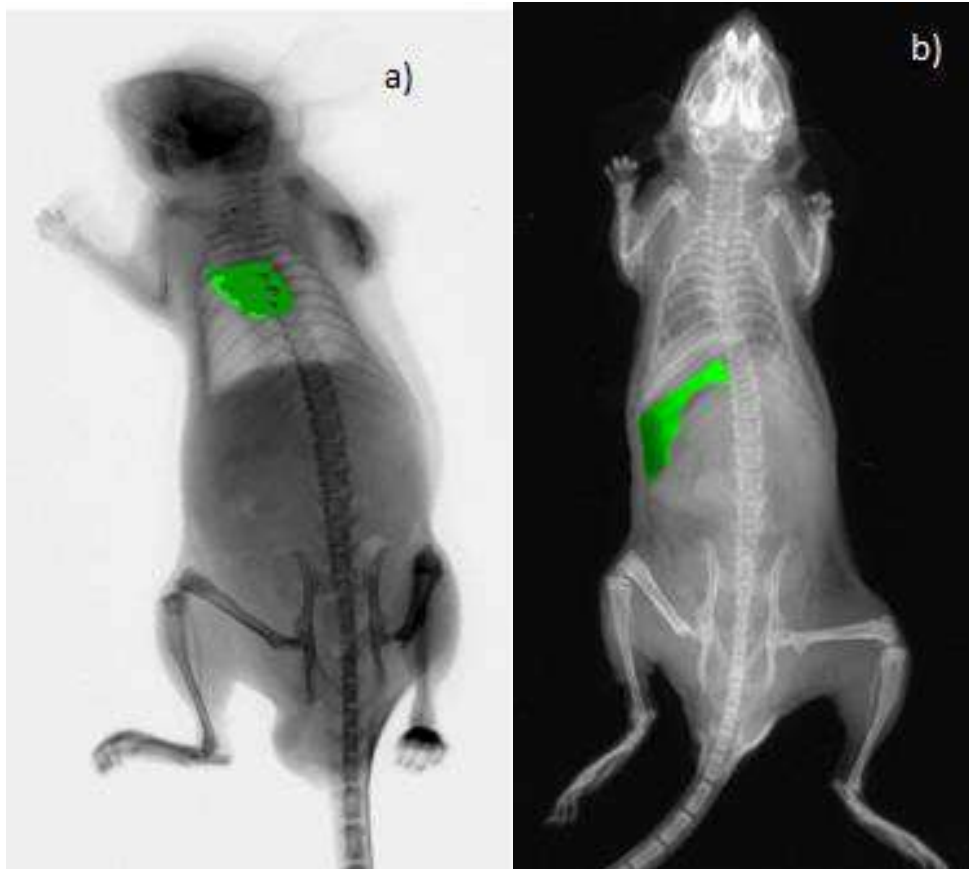


Fig 4.15- X-ray fluorescence image showing the Bi-NPs for an injection of solution in heart(a) and Sx kidney(b).

In conclusions, Bi-NPs can be used in alternative to Au-NPs on the base of their higher Z atomic number and on the base of the lower mass density to obtain a similar improvement of the contrast imaging resolution and of the radio and thermal therapy efficacy in cancer tissues. The most difficult aspect of their use is the transport of the NPs up to the tissues and organ interested by the disease without diffusion toward the healthy tissues around the target of interest. To this further studies must be conducted using functionalized nanoparticles in collaboration with biologists, pharmacologists, chemists and doctors.

4.5. Comparing different types of Nanoparticles as X-ray contrast agents for diagnostics imaging

Nanoparticle systems, primarily organic and inorganic nanoparticles (NPs), have found potential applications in different diagnostic imaging techniques because of their potential to target specific tissues and organs within the body [93]. In this way, it is possible to highlight the region of interest, increase the overall efficiency of the procedure and reduce the side effects. Medical imaging is designed to diagnose and examine diseases by imaging images of the body's internal structures. It also provides valuable information before starting an appropriate treatment and then following its effectiveness. One way to improve the efficiency of imaging studies is the development of improved X-ray contrast agents, which are commonly used molecules in radiographic procedures to ensure high image contrast based on strong X-ray attenuation properties of the elements radiopaque. Since X-rays have a short wavelength, which is in the range of 0.1-10 nm, they can detect subtle differences in the electronic density of a material that are not visible using other absorption-based techniques. Currently, X-ray contrast agents are predominantly based on small iodinated molecules. Iodine (I) assumed the main role in the synthesis of X-ray contrast agent due to its high X-ray absorption coefficient ($1.94 \text{ cm}^2 \cdot \text{g}^{-1}$ to 100 keV) and its chemical versatility. The evolution in the structure of iodinated X-ray contrast agents designed to reduce the adverse effects associated with the clinical use of these molecules. For example, non-ionic molecules have a lower tendency to interact with cell membranes, peptides and other biological structures, so that they are less toxic than ionic molecules. The dimers show lower osmolality than the monomers; this reduces pain and sensation of heat at the injection site and decreases the incidence of contrast nephrotoxicity (CMN), which is a common condition in patients with pre-existing renal failure, cardiovascular complications (eg irregular heart rate and blood pressure) and osmotic diuresis. However, dimers tend to exhibit higher viscosities than monomers, which is a cause for concern because the higher the viscosity of the X-ray contrast agent, the slower the injection and excretion rate. Furthermore, rates of slow excretion were associated in preclinical studies with upregulation of markers for renal impairment. Iodized X-ray contrast agents with

high osmolality and viscosity are normally administered intravascularly by intra-arterial injection, which requires the use of a catheter or intravenous injection. Thus, a balance between osmolality and viscosity values must be found for each developing X-ray contrast agent. An active research field is the development of alternative X-ray contrast agent formulations, most of which use NPs to improve the effectiveness of the materials that generate the contrast. However, in order to determine whether they are suitable for diagnostic imaging applications, an accurate evaluation of their properties is required. The development of NP-based X-ray contrast agents is providing an increasing contribution to the field of diagnostic and molecular imaging. An ideal contrast agent should selectively accumulate at the site of interest to be able to physically, chemically, biochemically and functionally interact with the target and, by these means, improve the image contrast. The use of NP offers numerous advantages over widely used iodinated contrast solutions. For example, their surface can be modified by adding appropriate coatings (e.g. polymers, silica) to improve their specificity by attacking targeting portions, to increase their half-life of the circulation and improve its functionality by adding other components, including fluorescent markers and therapeutic agents. (Fig. 4.13).

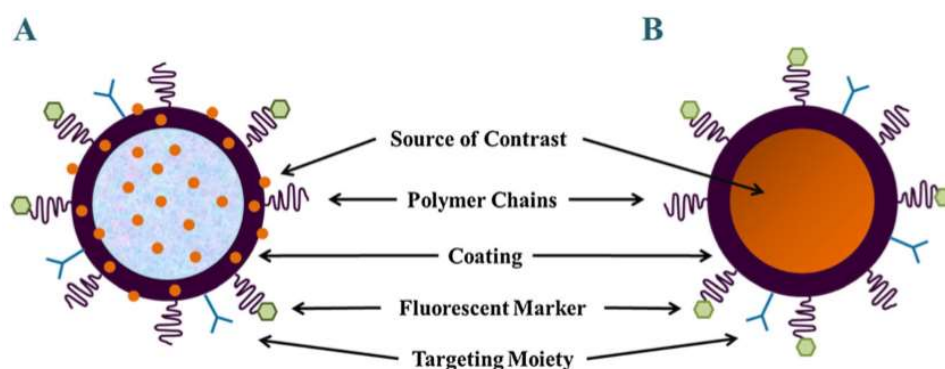


Figure 4.13- Different strategies to design NP-based X-ray contrast agents. The source of contrast can be either (A) a polymer-based NP in which the radiopaque element is loaded into the core, included within the coating or attached to the surface or (B) an inorganic NP made from an element that exhibits X-ray attenuation properties [93].

Gold has garnered a lot of attention in the development of iodine-free NP-based X-ray contrast agents because it possesses several properties that make it suitable for medical imaging applications. It has a higher atomic number ($Z_{\text{Au}}=79$) and a higher mass X-ray absorption coefficient ($5.16 \text{ cm}^2 \text{ g}^{-1}$ at 100 keV) than iodine. This means that gold provides about 2.7 times greater X-ray contrast per unit weight than iodine and, additionally, it has an optimal X-ray absorption coefficient at 80–100 keV, reducing interference from bone and soft tissue absorption.

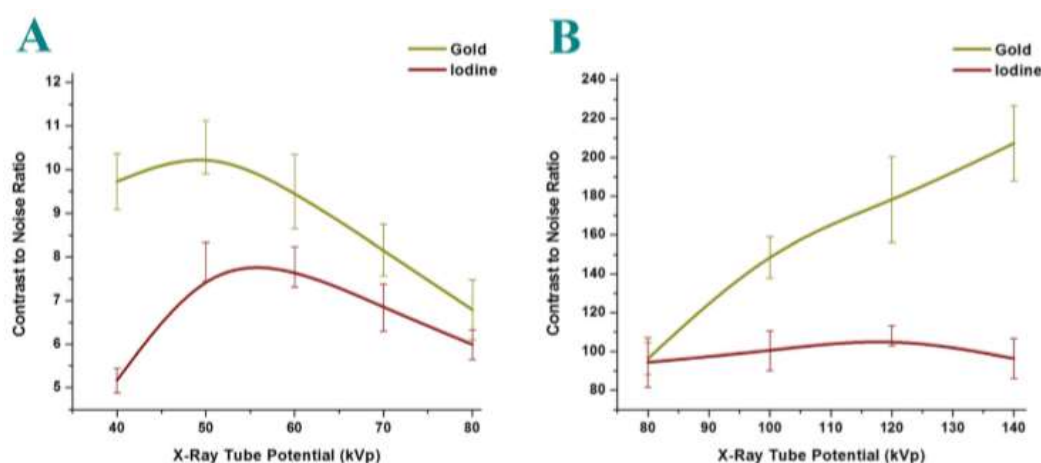


Figure 4.14- Comparison of the contrast-to-noise ratio of AuNPs and an iodine-based X-ray contrast agent at different X-ray tube potentials. The graphs show that the contrast-to-noise ratio of AuNPs and Ultravist® imaged by (A) CR and (B) CT is dependent on the X-ray tube potential applied [93].

The contrast enhancement of a solution of Au NPs with a mean diameter of 1.9 nm was compared with Ultravist® (iopromide, 300 mg of I per mL), a clinically approved iodinated contrast agent, at various X-ray tube potentials in an imaging phantom. An imaging study was performed at medium (40–80) kVp and high (80–140) kVp X-ray tube potentials using computed radiography (CR) and CT, respectively. It was observed that Au NPs provided more contrast enhancement than the iodinated X-ray contrast agent (Fig. 4.14). However, the specific improvement reached by replacing iodine with gold as the radiopaque element was dependent on the utilized X-ray tube potential. For example, in the CR scans, the contrast enhancement was higher at low X-ray tube potentials (<50 kVp; Fig. 4.14 A), whereas in the CT scans, it was higher at high X-ray tube potentials (>100 kVp; Fig. 4.14 B).

Additionally, it was observed that the AuNPs cleared through the kidneys in less than 1 h and they did not accumulate in the liver and the spleen (Fig. 4.15). The aforementioned results suggest that iodinated X-ray contrast agents and AuNPs differ in their pharmacokinetic properties.

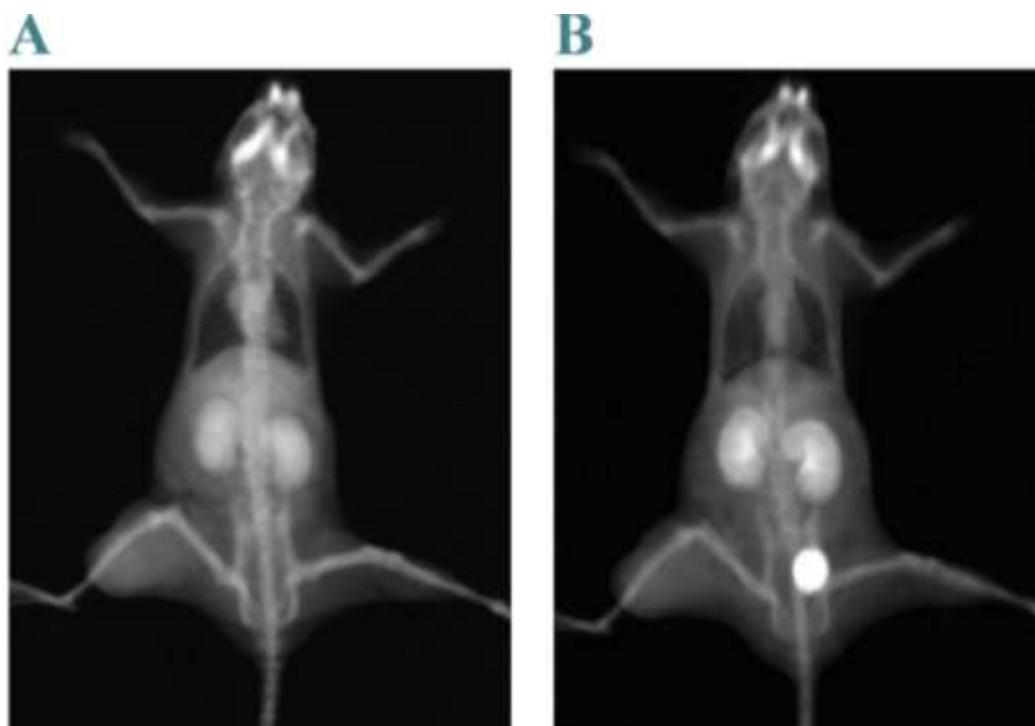


Figure 4.15-Biodistribution and contrast enhancement of AuNPs by planar imaging. Following administration into the tail vein of Balb/C mice bearing EMT-6 subcutaneous mammary tumors, 1.90±0.10 nm AuNPs exhibited high contrast enhancement of angiogenic and hypervascularized regions for approximately 1 h and clearance through the kidneys and the bladder. The pictures depict the biodistribution of AuNPs (A) 2 and (B) 45 min after injection [93].

The former are rapidly excreted through the kidneys, whereas the latter are extensively retained in tumors after blood clearance. For this reason, AuNPs may be useful for enhanced tumor detection. Even though AuNPs overcome some limitations of clinically used X-ray contrast agents, gold is more expensive than iodine, which can limit its utilization for large-scale applications.

Consequently, other elements with high atomic numbers and biological tolerance have started to gain importance for the development of NP-based X-ray contrast agents.

The PEG-NaYbF₄:Tm³⁺ NPs, with a mean diameter around 20 nm, exhibited both high in vitro and in vivo performance in CT and near-infrared fluorescence imaging

compared with iobitridol. Furthermore, enhanced hepatic imaging was observed with the use of PEG-NaYbF₄:Tm³⁺ NPs owing to rapid uptake by phagocytic cells in the liver (Fig. 4.16). Hence, as a result of the passive targeting by the EPR effect in tumors, these NPs have interesting applications for imaging of hepatic tumors. Related to multimodal contrast agents they are hybrid NP-based X-ray contrast agents, which are synthesized by combining into a single carrier various elements with adequate X-ray attenuation capabilities but different K-edge values. As a result of the differential attenuation of X-ray photons, this strategy allows engineering X-ray contrast agents that provide optimal contrast enhancement at different X-ray tube potentials.

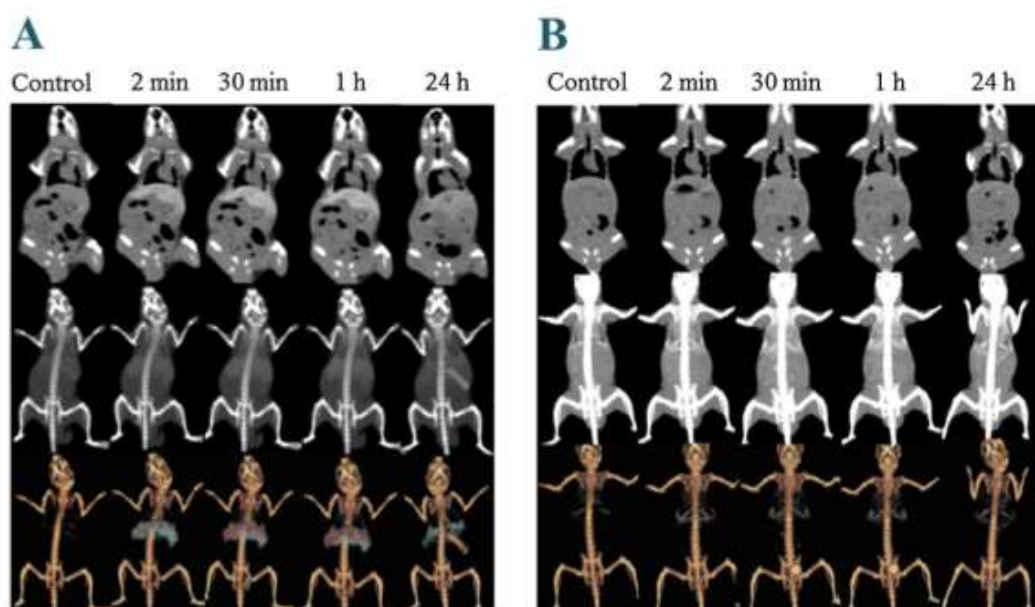


Figure 4.16- Comparison of the biodistribution and contrast enhancement of PEG-NaYbF₄:Tm³⁺ NPs and an iodine-based X-ray contrast agent by CT imaging. The pictures show the biodistribution and contrast enhancement of (A) 20 nm PEG-NaYbF₄:Tm³⁺ NPs and (B) iobitridol. The CT slices were acquired after an intravenous injection of 150 μ L of either a physiological saline solution of PEG-NaYbF₄:Tm³⁺ NPs (20 mg of Yb per mL) or iobitridol (25.6mg of I per ml) into Kunming mice. The control refers to mice before injection. Top, serial CT coronal views; middle, maximum intensity projection; and bottom, 3D volume rendering CT images [93].

5. Radioterapy and Thermotherapy

5.1. Radiotherapy

For the correct therapeutic treatment of a neoplasm it is necessary to know in addition to the type, also the degree of atypia of the neoplastic tissue and its stage, the extension of the pathological process at the time of diagnosis. The staging allows us to identify immediately what is the correct therapy to follow. There are several forms of cancer therapy (surgery, pharmacotherapy, radiotherapy): usually the treatment of a tumor, especially if it is malignant, uses more than one procedure with an approach that is called "multi-disciplinary" (i.e. based on the integration of different techniques for obtaining a better result). From the physical point of view, important results have also been achieved in the therapy, thanks to the use of NPs (in the diagnostic the NPs have assumed one considerable importance as contrast agents). In particular, NPs can make significant improvements in Thermo-therapy and Radiotherapy.

In recent years radiotherapy has become increasingly effective and complex through the introduction of new techniques such as intensity-modulated radiotherapy (IMRT) and stereotaxic radiosurgery (SRS), through the use of dedicated equipment such as tomotherapy. These techniques use fields (of radiations) much smaller than those of a time, or extended fields composed of a multitude of smaller fields that allow the optimization of the delivery of the dose to the target volume and the minimization of dose to adjacent healthy structures. Radiotherapy is a clinical discipline that uses ionizing radiation for the treatment of various diseases, including tumors. Ionizing radiation is a physical energy capable of damaging the neoplastic cells; such cancer cells that are first hit and damaged by these radiations, are subsequently destroyed and eliminated by the body itself. Nowadays, for the treatment of tumors we have different therapies available: surgery, chemotherapy, radiotherapy, hormone therapy, immunotherapy, all techniques that are often integrated together to obtain a better result. The incident radiation on neoplastic tissues destroys the tumor cells (Figure 5.1).

The currently used radiation are:

- High-energy Photon (KeV-MeV) that are able to reach deep regions in the tissues.
- Electrons (MeV) which concentrate on superficial regions, rapidly attenuating with depth.
- Protons (MeV) that deposit most of the energy in depth

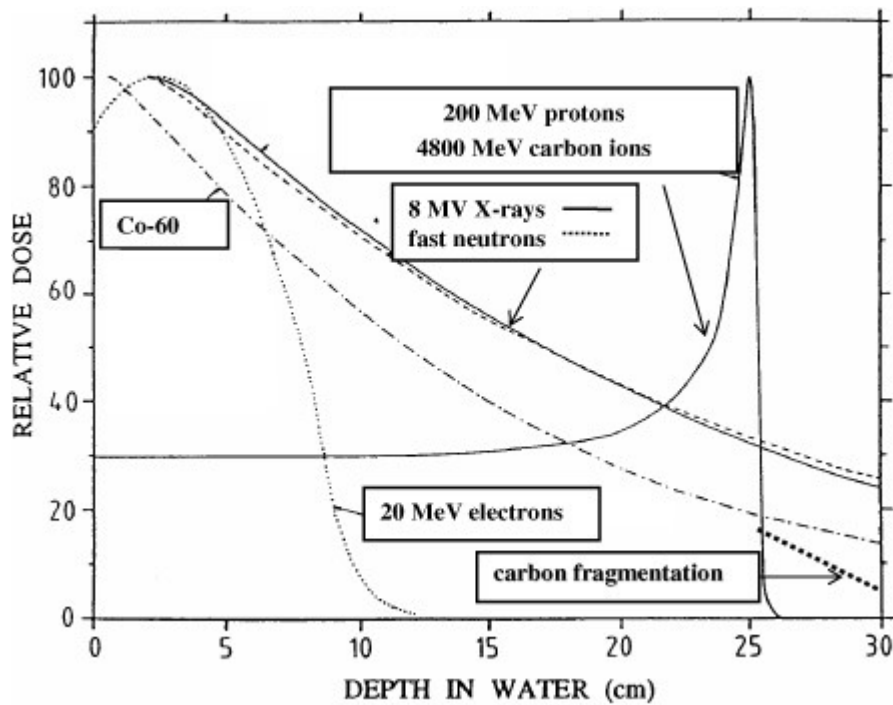


Fig. 5.1- Depth dependence of the deposited dose for different radiations[94].

The beams of photons, and in a similar manner the neutron beams produced by the collision of protons on particular targets, show a decreasing trend with exponential shape of the dose as a function of depth, with the energetic peak at the most superficial region (maximum at 2 cm for photons energy equal to 8 MeV). The electrons, instead, are characterized by the fact that the maximum dose is released a few centimeters from the surface and that the maximum penetration value (calculated at the point where the relative dose is equal at about 5% of the maximum dose) expressed in cm is equal to about half of the numerical value of their initial energy (in MeV), with a tail that extends towards low intensity and is due to bremsstrahlung photons.

Proton beams present, instead, the volume selection capacity where the released dose is concentrated, as it is evident from the particular shape of the dose-depth curve: a practically flat input region (plateau) is followed by a high and narrow dose peak (peak of Bragg), with an amplitude equal to about 3-4 times the value of the entrance plateau, which is released in depth at the end of the path (end-point). Therefore the tissues that are located before the target, placed at the peak, receive a low dose rate, while those located at a greater depth virtually do not receive, given the steep fall to zero of the curve.

5.1.1 Radiation with Photons

- Radiotherapy with γ -ray: are produced by the decay of radioactive isotopes of elements such as Cobalt-60 and Radio.
- Radiotherapy with X-ray: the rays are originated by a machine that excites electrons using a cathode tube, or a linear particle accelerator.

Figure 5.2 reports the dose dependence from the depth for the photons X and γ ; as you can see from the chart you create a zone called "Build up" which is the phenomenon for which the layer of fabric that absorbs the greatest energy is not located in the immediate surface, but at increasing depths in relation to the energy of radiation (esample for ^{60}Co the build up is at 5 mm). An observation to be made looking at the graph is that the ratio between the dose in depth and the dose on the surface is less than one

$$\frac{D_{depth}}{D_{surface}} < 1 \quad (5.1)$$

so most of the radiation is absorbed on the surface and less in depth.

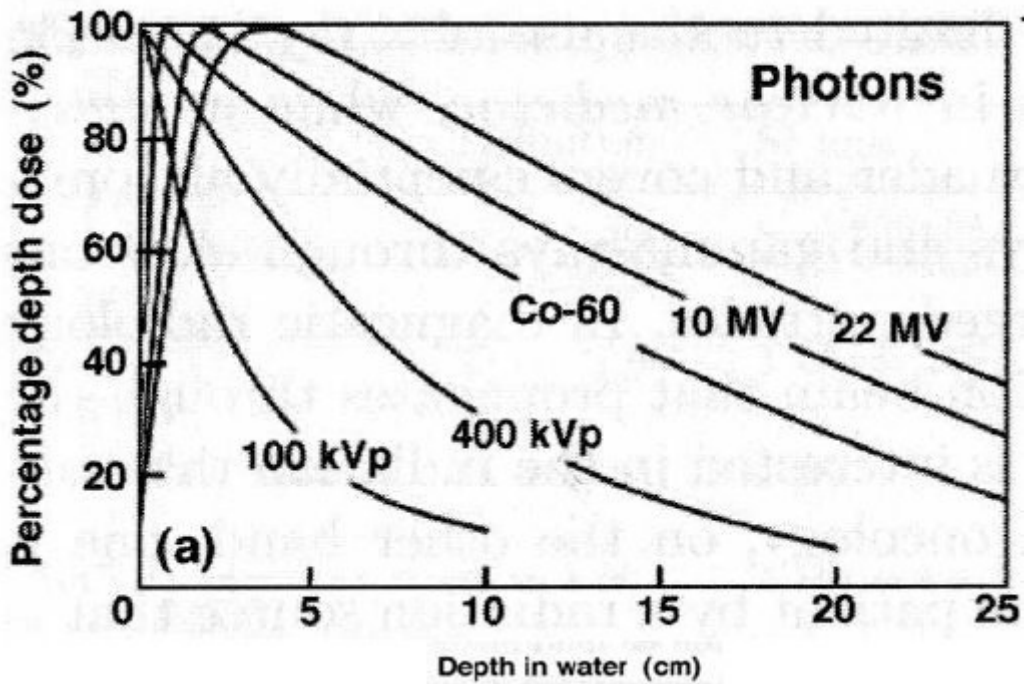


Fig. 5.2- Dose against depth in water for photon beams in the range from 100 kVp to 22 MV [95]

5.1.2 Radiotherapy with Electrons

Electron radiation is a type of external radiation therapy in which electron beams are directed towards a target in the human body, such as a tumor site. Due to the characteristics of the interaction of the electron beams with matter, the therapy is able to electrically hit the skin cells without affecting the deeper regions, thus saving the underlying organs and tissues. Electron beam therapy is administered using particles produced by a linear accelerator, the electron beam is collimated with another element of the apparatus, known as an additional applicator or collimator, made from a low melting point metal alloy. The electron beams have a limited range of interaction with the matter, after which they are quickly attenuated. Those characteristics allows them to be used for the irradiation of only superficial layers of matter, without touching the deeper layers. In external irradiation therapy, it is useful when only the superficial layers of the body, those to be hit, are to be killed, while the deepest healthy tissues are to be saved. The depth of treatment can be adjusted by choosing the most appropriate energy for the emitted beams. The used energy for radiotherapy with electrons ranges from 5 to

21 MeV depending on the thickness of the surface to be irradiated. Figure 5.3 shows the graph of the dose as a function of distance: as can easily be seen the electrons are rapidly absorbed and therefore this allows only superficial irradiation. In the case of electrons the ratio between the dose in depth and the dose on the surface is less than one.

$$\frac{D_{depth}}{D_{surface}} < 1 \quad (5.2)$$

Here too, most of the dose is deposited at the beginning of the path, then on the surface.

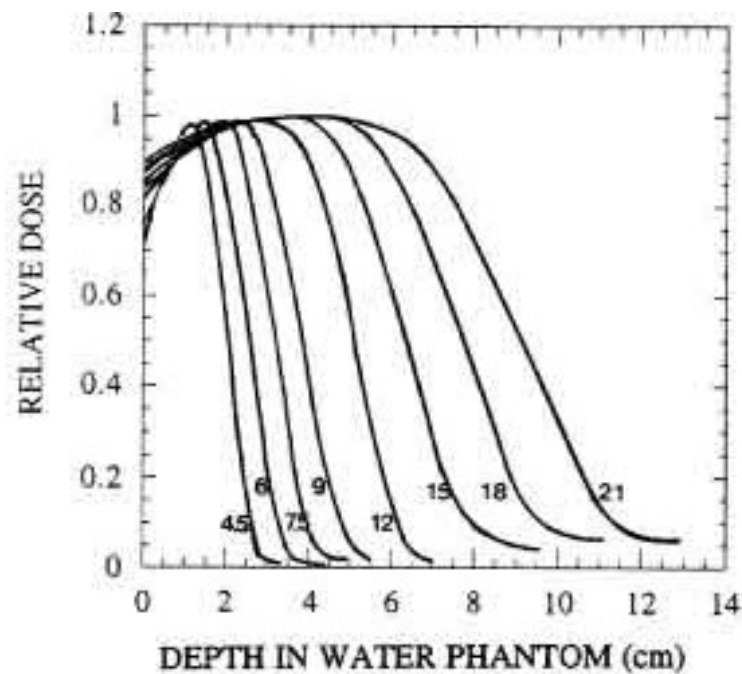


Fig. 5.3- Dose vs depth curve for the Electron sof energy between 4.5 and 21 MeV [96].

5.1.3 Protontherapy

The use in radiotherapy of proton beams is due to their favorable distribution of dose absorbed in depth. The protons release a massive dose of concentrated radiation at a single point of their path (Bragg peak). Little energy is released as the particles enter deep, and a lot of energy instead in the Bragg peak. We can then

adjust the intensity of the radiation so as to focus the Bragg peak on the tumor and release the radiation there.

So the release of energy takes place in a very limited area to a depth that we determine by art and the radiation does not cross the whole body, but it shuts off shortly after the Bragg peak (Figure 5.4). In this case the ratio between the dose in depth and the dose on the surface is > 1 .

$$\frac{D_{depth}}{D_{surface}} > 1 \quad (5.3)$$

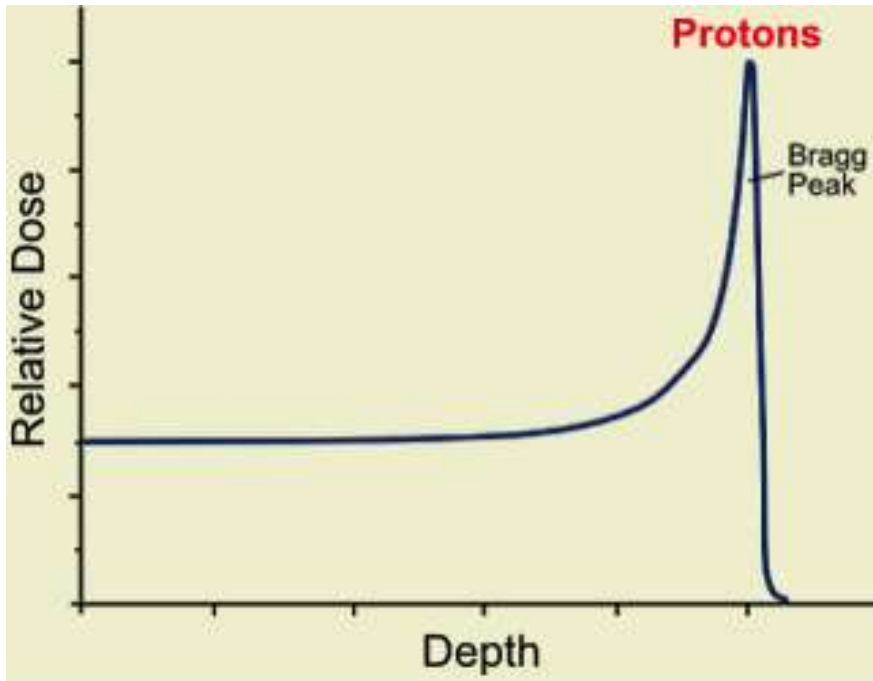


Fig 5.4- Dose vs depth curve for Protons [97].

The characteristic curve of the dose distribution in depth, in which the so-called Bragg peak is present, is usually the starting point from which the modulated trend originates. This is due to the fact that the thickness of the tumor target, sometimes unfortunately, is relatively large and, therefore, the beam range must be appropriately adapted to these dimensions. Modular means to use absorbent objects, of different thickness and rotating, which are arranged on the bundle in such a way that the overall effect is to sum the various pure Bragg peaks corresponding to them.

This sum translates into a single enlarged peak, the so-called SOBP Spread-Out Bragg Peak (Figure 5.5).

There is another method, defined time active, in which the SOBP is realized through the use of controllable, or adjustable energy radiation beams. In this mode not only the depth profile, the so-called longitudinal dose, but also the transverse or lateral dose profile is changed.

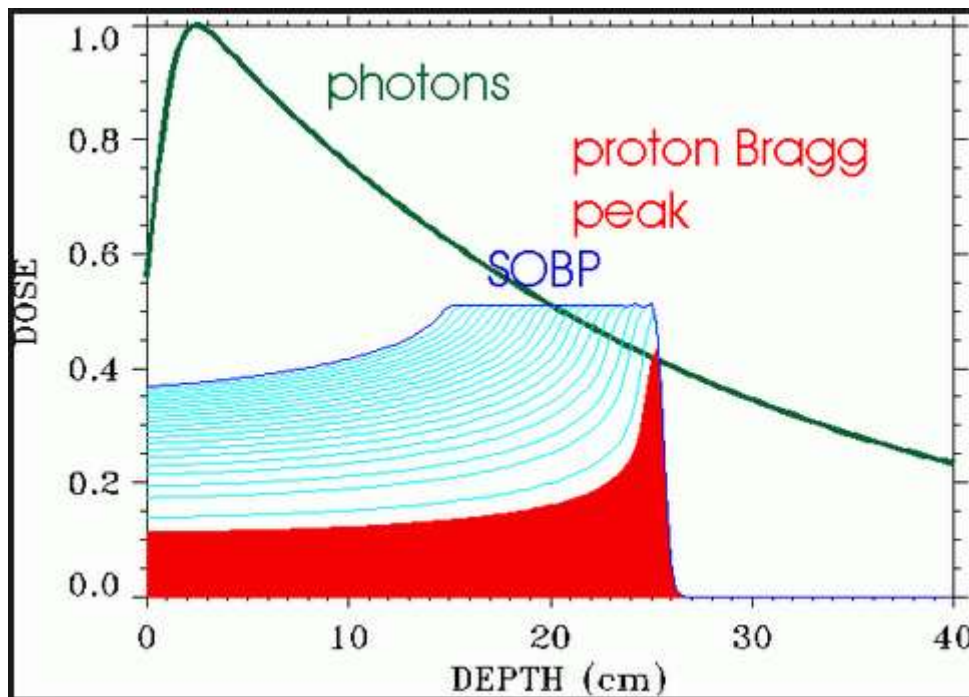


Fig. 5.5- Development of depth dose distribution and definition of the modulation.

5.2. Different Types of radiotherapy

Approximately half of all cancer patients must undergo any form of radiotherapy in course of anti-tumor therapy: for some of them radiotherapy is carried out as treatment curative (hopefully that therapy treats the neoplasm, or eliminating it and/or preventing recurrences): in this case it can be used alone, or in combination with the surgery and /or the chemotherapy.

Radiation therapy can also be used as a palliative treatment, which does not cure the tumor, but it is limited to relieving symptoms and pain: it can be carried out for palliative purposes, for example in these cases:

- Radiation targeted to the brain to circumscribe the metastasis (tumor cells that have spread in the brain, coming from another part of the organism).
- Radiation aimed at circumscribing a tumor that presses on the spine or is developed inside a bone.
- Radiation aimed at circumscribing a tumor near the esophagus, which can interfere with the normal patient nutrition.

Radiation can be administered by an external device that surrounds the body of the patient (external radiotherapy), or it can be produced by a radioactive substance that enters in the patient's organism (internal radiotherapy, also called "brachytherapy").

Systemic radiotherapy uses one or more radioactive substances (administered orally or via drip), such as radioactive iodine, which move into the patient's organism via the systemic circulation and, thus being able to reach the tissues of the whole organism, kill the cells cancer.



Fig. 5.6- Image guide Radiotherapy

The type of radiotherapy prescribed by the oncologist depends on several factors, among which we remember:

- type of tumor;
- tumor size;
- position of the tumor;
- proximity of the tumor to healthy tissues sensitive to radiation;
- path that the radiation must perform in the body;
- general health status and medical history of the patient;
- need to undergo other anticancer therapies;
- all other factors (age of the patient, other pathologies in progress, etc.).

5.3. Radiotherapy Techniques and Criteria

The patient who has been diagnosed with a tumor, treatable with external beam radiotherapy, enters the radiotherapy department and, after a first visit by the radiotherapist, performs a simulation session with a radiographic device, called a simulator, or better with a more modern TAC with virtual simulation program. To perform a complete treatment requires a large number of sessions, ranging from 25 to 35, normally made for 5 days / week, for 4 to 7 weeks. The patient can receive radiation therapy before, during or after surgery. Some patients will have to undergo radiotherapy only, without surgery or other therapies; others, on the other hand, will have to undergo radiotherapy and chemotherapy at the same time. The time of start of radiotherapy depends on the type of tumor to be treated and the purpose of therapy (curative therapy or palliative therapy). Radiotherapy performed before surgery is called preoperative or neoadjuvant radiotherapy: it can be used to decrease the size of a tumor before surgery and therefore the risk of relapse. Radiotherapy administered during surgery is called intraoperative radiotherapy (IORT), and can be external (with photons or electrons) or internal. When radiation is administered during surgery, the surrounding healthy tissues can be shielded, thus avoiding exposure to radiation. IORT is used in some cases when the normal tissues are too close to the tumor and therefore it is not advisable to resort to external radiotherapy. Radiotherapy performed after surgery is called postoperative or adjuvant radiotherapy: particularly after some complicated operations (especially in the abdominal or pelvic area) radiotherapy could cause too many side effects, so it is considered safer to carry out the procedure before the operation. The combination of chemotherapy and radiotherapy administered simultaneously can be called radiochemotherapy. For some types of cancer, it is able to kill more cancer cells, thus increasing the effectiveness of the treatment, but it can also cause more side effects. After anti-tumor therapy, patients must undergo regular cancer controls to check their health and rule out any cancer recurrence.

5.3.1 Doses given to the Patient

The radiotherapist develops the patient's healing plan (assigned to him by the oncologist) through therapeutic planning, which starts with a simulation. During the simulation, detailed images of the patient's body are taken, to find out where the tumor is and where there are healthy tissues. Images are usually taken using the TAC (computed tomography), or even with an MRI scan (Magnetic Resonance Imaging), a PET (positron emission tomography) or an ultrasound. During the simulation and the radiotherapy sessions it is essential that the patient is always in the same position with respect to the equipment that emits the radiation or processes the images. It is possible to build fingerprints, masks, that help keep the head still and ensure that the patient does not change position between a session and the next, or other devices that help the patient to stay still. To position the patient with the utmost precision, doctors use removable marks on the skin or the species of tattoos. After the simulation the oncologist decides which is the exact area to be treated, the total dose of radiation that will hit the tumor, the maximum dose allowed for healthy tissues around the tumor and the angles of incidence (the paths) safer for the administration of radiation. The radiation dose for antitumor therapy is measured in gray (Gy): 1 gray is equivalent to the amount of 1 J of absorbed energy by 1 kg of human tissue; different doses of radiation are needed to eliminate the different types of cancer cells. Radiation can damage some tissues with particular ease: for example, the reproductive organs (testes and ovaries) are more sensitive to radiation than bones; however, the radiotherapist will take this into account when planning therapy. If a certain area of the body has already been subjected to radiotherapy, the patient will probably not be able to undergo a second radiotherapy in the same area; any contraindication depends on the administered dose of radiation in the first cycle.

If an area of the organism has already received the maximum permitted dose of radiation, it is possible to treat another area provided it is sufficiently distant. The area to be treated usually includes all the tumor and a small amount of neighboring healthy tissue; healthy tissue should be treated for two reasons:

- patient movements due to respiration (respiratory gating) and all movements of the internal organs, they can change the position of the tumor between a session of radiotherapy and the next;
- it is necessary to reduce the risk of recurrence due to tumor cells that may have spread to the tissues surrounding the tumor (microscopic diffusion). Patients who undergo external radiotherapy usually have to go to the hospital or clinic five days a week for several weeks. Every day, patients are given a fraction of the expected total radiation dose; only in some cases two doses are given a day.

Most types of external radiotherapy are administered as a single dose for these reasons:

- to minimize damage to healthy tissues;
- to increase the likelihood that cancer cells will be exposed to radiation at the time of the cell cycle where there is a greater probability of DNA damage.

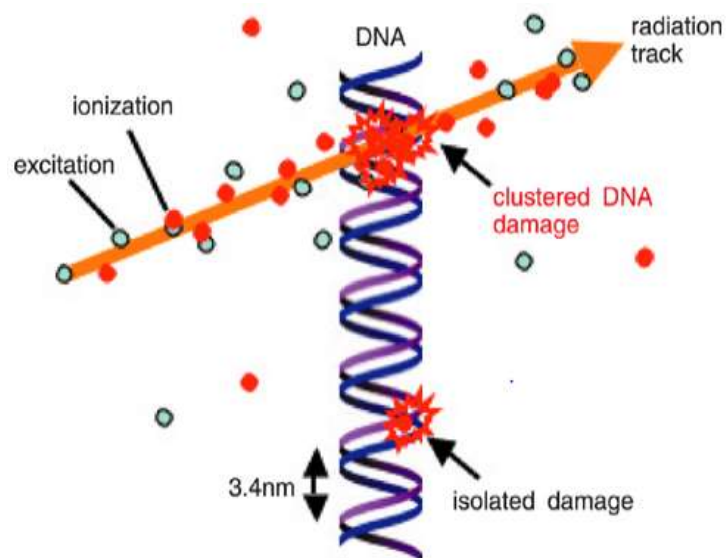


Fig. 5.7- DNA damage by ionizing radiation

Dose fractionation in radiation therapy involves a therapeutic gain; it increases the tolerance of normal tissues (for repair and repopulation phenomena) and at the same time eliminates the radioprotective effects of hypoxia on the tumor (due to the reoxygenation phenomenon). Standard fractionation involves 5 fractions per week of about 2 Gy each 24hour interval, for 5/6 weeks.

The variations compared to the standard are represented by fractions of larger dose, we speak of hypofractionamento (es. palliative treatments), or minor fractions, in this case we speak of hyperfractionation (es. melanoma). Regarding the duration of treatment, if the dose is given at a rate greater than 10 Gy per week, it is called accelerated treatment while a slower treatment, obtained by introducing programmed breaks during the course of therapy is called "split course".

5.4. Radiotherapy enhancement with Gold Nanoparticles

Radiation therapy is one of the main methods of cancer therapy. Despite the progress made in this field, radiation therapy may still fail to eradicate tumors [98]. A sufficient dose may render cancer cells harmless, but radiotherapy doses are limited by potential radiotoxicity to the surrounding healthy tissues in the beam pathway. A further limitation of radiation is that cellular damage is cumulative; that is, DNA strand breaks that are not repaired or other damage to cells can not kill a healthy cell, but additional irradiation can eventually induce its disappearance. This means that a dose deposited in the tumor that inevitably also reaches the surrounding healthy tissue creates a damage, for this reason it can not be repeated with subsequent irradiations (for example 6 months after the regrowth of the tumor).

If it were possible to deposit high-Z metal nanoparticles in the tumor tissues / organs, this would result in a larger dose of the cancerous tissue than the dose received from the normal tissue during a radiotherapy treatment. For example, gold is an excellent X-ray absorber, if the tumors were loaded with gold nanoparticles, X-rays deposit a greater amount of beam energy into the tumor cells, saving healthy cells.

5.4.1 Properties of gold nanoparticles

The potential advantages in the use of gold nanoparticles are:

- Gold absorbs ~ 3 times more than iodine at 20 and 100 keV.
- The dose increase factor (DEF) for gold can be between 1.2 and > 5 depending on the radius energy and the amount of gold delivered.
- The range of the enhancement effect can be on multiple cells, for example 100 μm , thus releasing the requirement that gold be delivered to all tumor cells. Tumors are known to be heterogeneous.
- Gold is relatively inert and can be biocompatible.
- Nanoparticles release blood less rapidly than small molecules, such as iodine contrast agents that are considered extravascular and exit quickly from the vascular system. The nanoparticles can remain in the blood for hours if they are designed to do so, thus improving the delivery of the tumor.
- The nanoparticles are known to permeate the leaking angiogenic endothelium, thus providing a certain specificity of the tumor, the so-called permeability and retention effect (EPR).
- Nanoparticles have a low osmolality.
- Effective tumor targeting with antibodies, peptides or drugs may be possible with nanoparticles.
- Gold nanoparticles can be produced on a wide range of sizes (1-1000) nm and designed for the best penetration and delivery of the tumor.
- Gold nanoparticles have a number of surface ligands, allowing flexible design and multi-functionality by incorporating mixed ligands for optimal properties.

- Biodistribution of gold can be resumed before a therapeutic dose is delivered and used for treatment planning and quantified dose improvement prediction.
- Other high-Z metal nanoparticles, in addition to gold nanoparticles, can be used with similar characteristics.

The potential disadvantages of gold nanoparticles are:

- The high cost of gold.
- More comprehensive toxicity studies are needed to evaluate human use.
- More comprehensive efficacy studies are needed to evaluate human use.

Some of the properties of gold nanoparticles are due to the size from 0.4 to 5000 nm. However, since gold is inert and unmetabolized, many of the properties, such as biocompatibility and pharmacokinetics, are determined by the stabilizing organic coating and possible surface functionalization [99]. The final size will be greater and will increase the time spent in the blood. Small particles can be rapidly disposed of through the kidneys, while larger ones avoid renal filtration. Toxicity can also be controlled by size and surface coating. Because elemental gold is biologically non-reactive, its intrinsic toxicity is low, yet all substances become toxic beyond a certain level. The right design can reduce toxicity. Large amounts of material to be delivered to the tumor are required to increase the radiation dose to the tumor with high-Z materials. A gold concentration of 0.5% by weight should give a DEF of ~ 1.6, but better results would be obtained if 1-5% were deposited in the tumor; but such concentration is too high compared to the doses necessary for drugs to kill tumors.

5.4.2 Physics of Metal-Enhanced Radiotherapy

When X-rays hit matter, different processes can occur (Figure 5.8). Relevant emissions are scattered photons (X-rays), photoelectrons, Compton electrons, Auger electrons and fluorescence photons. When an incident photon ejects an electron from an inner shell of an atom, this photoelectron acquires a kinetic energy that determines its distance traveled in the tissue, which can be for example 100 μm or about 10 cell diameters for an electron of about 100 keV of energy.

When x-rays impinge on matter, a number of processes can result

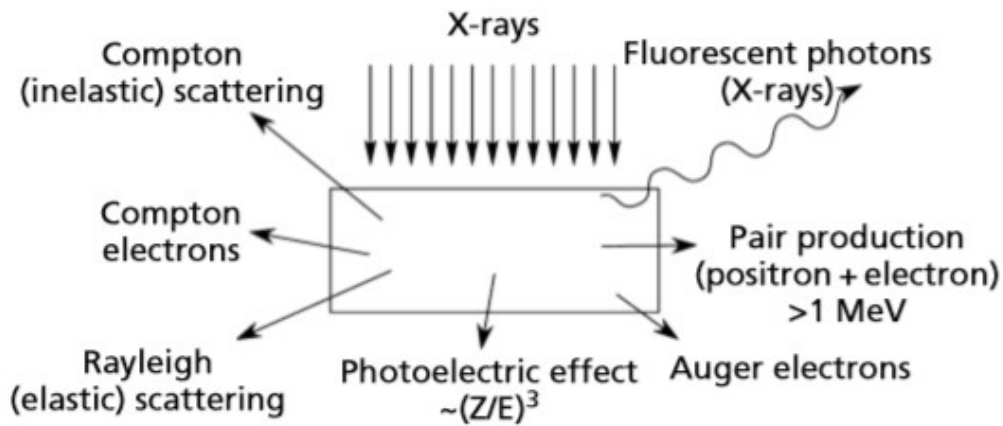


Figure 5.8- Interaction of X-rays with matter.

This photoelectric effect varies approximately as $\left(\frac{Z}{E}\right)^3$, where E is the incident photon energy and Z is the atomic number of the target. For high-Z elements it dominates the interaction with matter at energies $< 0.5\text{MeV}$. The relative effect of gold ($Z=79$) to soft tissue ($Z=7.4$) in the energy range above gold's K-edge (80.75keV) is then approximately 1217 (i.e. $79^3/7.4^3$); the ratio is more complicated at lower energies, but still a large number. The photoelectric effect, and in some cases also the inelastic (Compton) scattering, produces atoms in excited states due to the ejected electron. The missing electrons are then restored by electrons falling from higher orbits, which release energy either as fluorescent photons or Auger electrons.

Fluorescent photons can travel longer ranges (up to centimetres), so, depending on the tumour size, they may or may not provide the desired localized tumour effect. On the other hand, Auger electrons, which are weakly bound electrons ejected as a result of electronic shell rearrangements, can be effective in producing very high local ionization density. However, they travel much shorter distances, typically $\sim 10\text{nm}$, and several of them can be emitted from the same atom practically simultaneously. To take advantage of the Auger effect, the emitting atom must be only atoms away from the target molecule to be damaged, for example high-Z atoms intercalated in DNA to cause double-strand breaks. The Auger effect is greater in atoms of medium and high Z.

5.4.3 Therapy using Gold Nanoparticles in mice

The use of Au NPs in radiotherapy was tested on mice carrying EMT-6 breast cancers. The combination of Au NPs, injected intravenously 5 min before irradiation, and radiotherapy has been shown to prolong survival in mice [100].

The Au NPs used have a 1.9 nm size, the therapy was performed with a radiation of 250 kVp. Different types of treatment are performed: untreated tumor, tumor treated with Au NPs alone, tumor treated with irradiation alone and tumor treated with Au NPs and irradiation together (Fig. 5.9).

The mice received a single dose of 30 Gy with radiation of 250 kVp alone or in combination with high concentrations of AuNP ($1.35\text{ g of Au kg}^{-1}$). There is an actual growth delay of the radiation-induced tumor alone; however, radiation and AuNPs together have actually led to a drastic reduction in tumor growth once assessed 1 month after treatment. Au NPs alone had no effect on tumor growth. The encouraging result leads to a second dose of lower radiation (26 Gy), always respecting the different types of treatment. Mice with radiation only and mice were then treated in which two different concentrations of Au NPs were injected ($1.35\text{ g of Au kg}^{-1}$ and $2.7\text{ g of Au kg}^{-1}$).

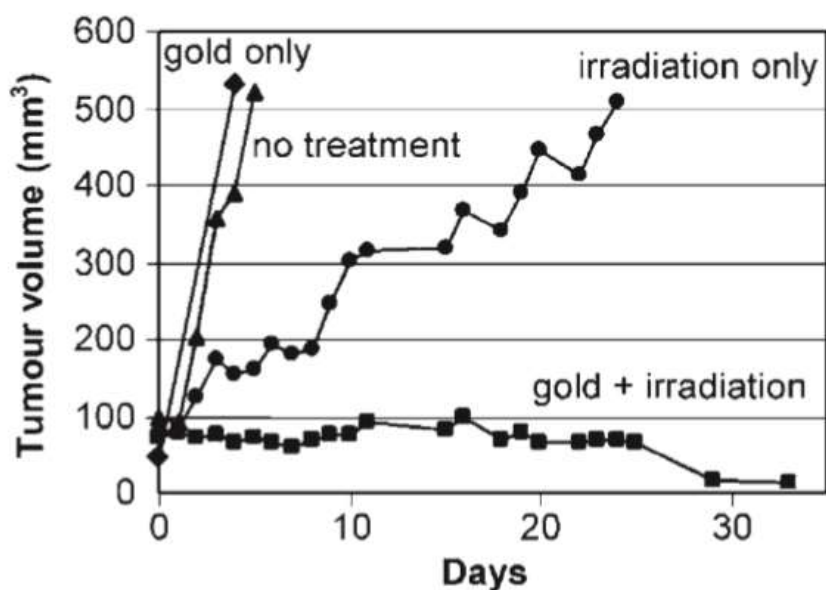


Figure 5.9- Curves tumour growth after: no treatment; treatment with only gold; treatment with only radiation (30Gy); and treatment with gold and radiation [100].

The results show that 50% of the mice that received the 1.35 g concentration of Au kg⁻¹ and 86% of the mice that received the 2.7 g concentration of Au kg⁻¹ treated with radiation survived for 1 year compared to 20% of mice treated with radiation alone and 0% treated with only gold or without treatment (Figure 5.10). Pharmacokinetics have shown that gold concentrations peaked in tumor vasculature 7 minutes after injection. In addition Au NPs are eliminated twice as fast from the surrounding muscle tissue and from the tumor.

AuNPs appeared to accumulate more in the tumour periphery than in the main tumour mass, with concentrations peaking at 6.5 mg of Au g⁻¹ of tumour. Au NPs concentrations shortly after injection were higher in tumours than in the liver; however, more detailed information on biodistribution and Au NPs tissue extravasation is required. In this study, surviving mice remained alive for 1 year after treatment with no obvious long-term toxicities.

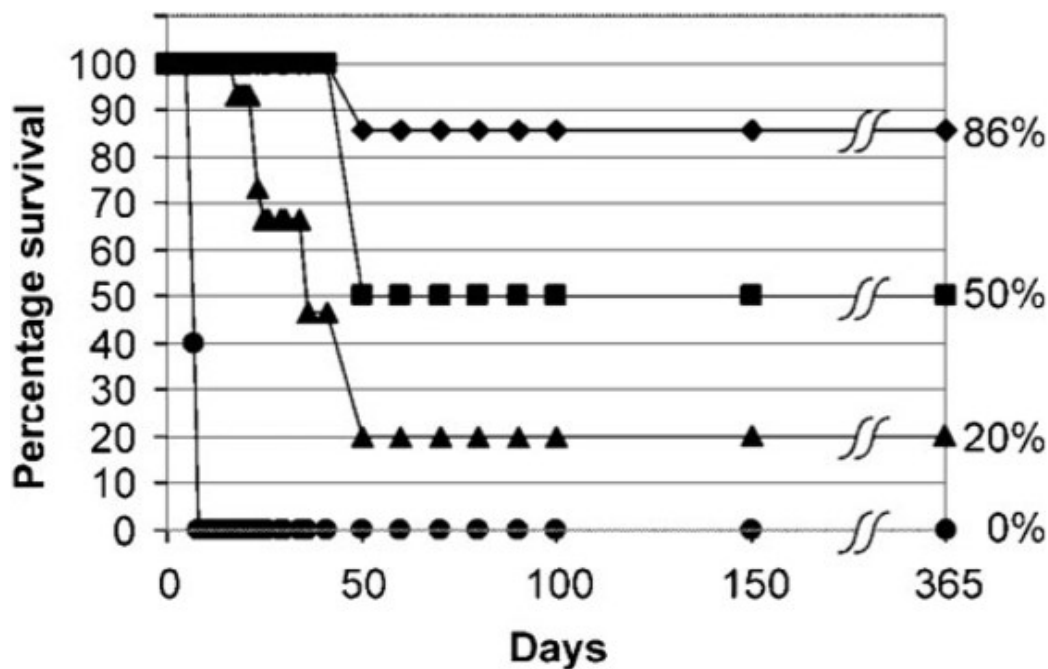


Figure 5.10- Survival Circles: no treatment or gold alone; treatment with only radiation; treatment with radiation after 1.35 g of Au kg⁻¹ injection; and treatment with radiation after of 2.7 g of Au kg⁻¹ injection [100].

A further in vivo study using 1.9 nm Au NPs. In this study, a highly radioresistant murky squamous cell carcinoma, SCCVII, was used in mice irradiated with filtered photons produced in a synchrotron. 68 keV photons were used, and significant delay in tumor growth and long-term tumor control were observed when Au NPs were combined with 42 Gy of radiation compared to radiation-only treatment. This effect was not observed using 30 Gy of radiation. Further clinical evaluations are still needed, including the efficacy shown in larger animals and humans, with more comprehensive toxicity studies ensuring the safety of Au NPs treatment.

5.5. Thermaltherapy (Hyper-Thermia)

The use of high temperature heat in a therapeutic setting or simply “hyper-thermia” is an emerging treatment tool in the field of cancer (i.e. a field known as thermal medicine) [102]. It has been shown that cancer cells (i.e. both leukemia & solid tumors) are more sensitive to hyperthermia than normal tissue cells. “Heat and cancer do not get along”. This has given researchers greater hope of using medically supervised high temperature heating as a treatment tool against cancer.

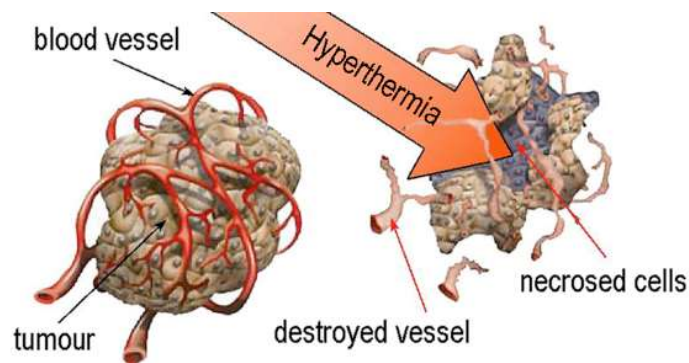


Fig. 5.11- Graphical representation of what hyperthermia involves at the tumor cell level (cell death)

For hyperthermic therapy or clinical hyperthermia s "means the induction, in the biological tissues, of temperatures slightly higher than the physiological one (from 40-41 ° C up to 45 ° C). In oncology, hyperthermia is a therapeutic modality used in association with the most traditional therapies used up to now, ie with radiotherapy and chemotherapy. Through the use of electromagnetic fields the tumor tissue is heated up to a temperature near or above 43 ° C and for a time interval of about one hour. The treatment, ie heating at the aforementioned temperatures, is performed one or more times according to the protocol applied, but generally it is not repeated more than twice a week to avoid the phenomenon of thermotolerance, that is to say a greater resistance of the cells to heat in the first two days following the therapy.

The heat enhances the effects of radiotherapy and chemotherapy on the tumor, without excessively increasing the side effects (ie the inevitable debilitating effects on healthy tissues and organs resulting from the cytotoxicity of chemotherapy and radiotherapy) allowing a significant improvement in the control of the lesion (ie of the target tumor mass). Hyperthermia is under clinical trials (research study with people) and is not widely available. However, while receiving those combination therapies, only few have shown increased survival in patients.

Various techniques of hyperthermia (Figure 5.12) are presently under investigation, that include local, regional and whole body hyperthermia. Many of these have shown a significant depression in tumor size when hyperthermia is combined with other treatment or therapy. Attaining temperature above the systemic temperature (37 °C) in a specified target volume is a challenge and still under development. High temperature is induced by applying a power density specific absorption rate (SAR; measured in W/kg).

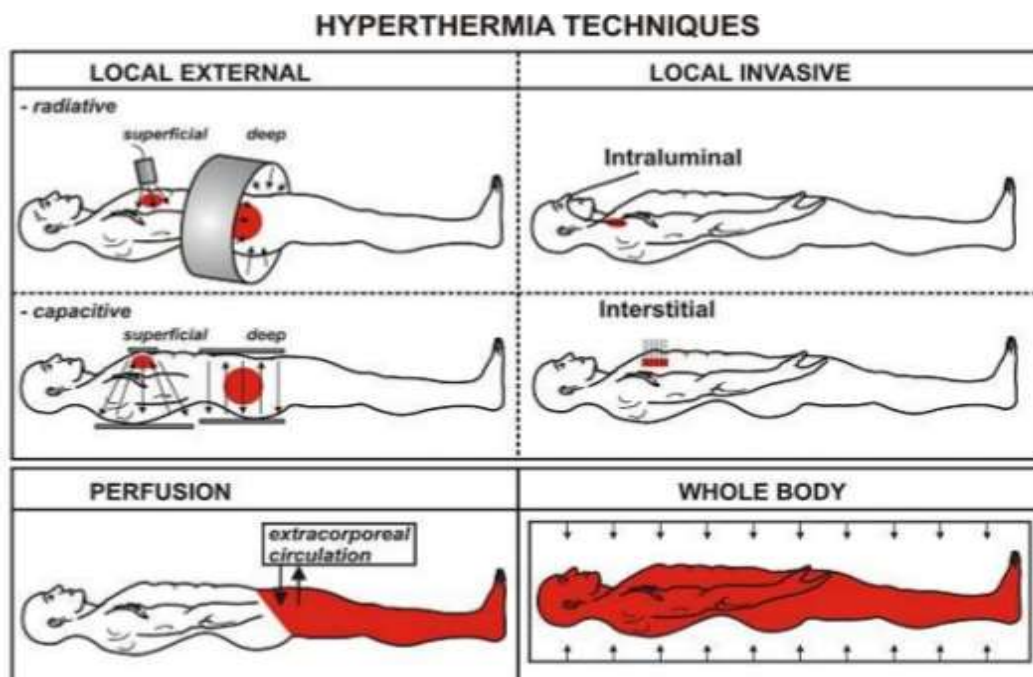


Figure 5.12- Various Hyperthermia techniques.

In hyperthermia it is important to take into account some quantities.

Considering Fick's law for the thermal conductivity in the material, the heat flux J (W/m^2) is given by the equation:

$$J = -K \frac{\Delta T}{\Delta x} \quad (5.4)$$

Where K is the thermal conductivity ($\text{W}/\text{m}\cdot\text{k}$.), and $\Delta T/\Delta x$ is the temperature gradient.

In biological environment the K value is low, for example it is $K=0.606 \text{ W}/\text{m}\cdot\text{K}$ in water and $K=0.64 \text{ W}/\text{m}\cdot\text{k}$.in bone.

SAR (Specific Absorption Rate) is a measure of the amount of energy absorbed by the body when exposed to radio-frequency (RF) electromagnetic field. It is defined as the power absorbed by fabric mass and has units of watts per kilogram (W/kg). It has various measurement expressions.

The most used [103]:

$$SAR = \frac{\sigma E^2}{\rho} \quad (5.4)$$

where σ is electrical conductivity (S/m), E is electric field (N/C), ρ is density of the material (kg/m^3).

Literature [103] reports that in the case of biological tissues the SAR value is calculable using the following equation:

$$SAR = C \frac{\partial T}{\partial t} \quad (5.5)$$

where C is thermal capacity of the sample (J/K), and $\frac{\partial T}{\partial t}$ represents the temperature increment velocity.

Equating the two expressions for SAR

$$SAR = C \frac{\partial T}{\partial t} = \frac{\sigma E^2}{\rho} \quad (5.7)$$

from this equation we can be noticed that the temperature increment velocity is proportional to $\sigma/C \cdot \rho$ and to E^2 , with the trend, as reported in Fig 5.14.

Normal basal metabolism of human is above 1 W/kg. Perfusion counteracts the elevated temperature. In humans perfusion rate is around 5–15 ml per 100 g per min, but they differ widely. To reach the elevated temperature approx 42 °C at least in some parts of the body tumors requires a power density of approx 20–40 W/kg at the target region. In hyperthermia, two quantities are of equal importance in determining cell survival at heat exposure: temperature and application time. The heat acts in a predictable and repeatable way, allowing the total survival of the cells for temperatures lower than 42 °C and causing a increase in cell death as temperature and exposure time increase.

Furthermore, in a first approximation, there is a relation to the linear one between temperature and time. This means that for an increase of one degree of temperature over 41°C, just half the exposure time to kill the same number of cells. The need to provide the right amount of heat to the affected area is clear if we think that the survival of very few cancer cells could lead to the reappearance of the tumor.

The goal is to achieve the most uniform heating possible, avoiding the formation of cold spots (areas whose temperature is lower than the therapeutic one due to the presence of a large blood vessel) and hot spots (areas at temperatures above the maximum allowed).

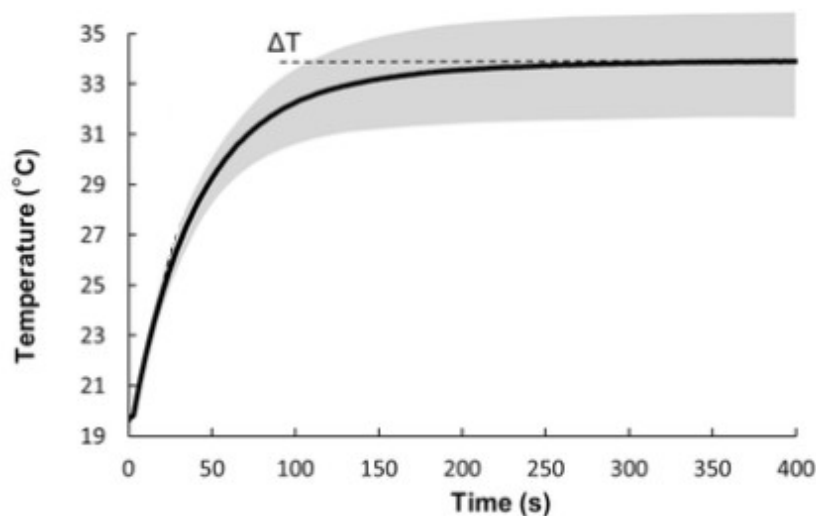


Fig. 5.14- A typical temperature-time curve from a hyperthermia experiment [104].

6. Theoretical Case Study: Radiotherapy with Gold Nanoparticles of Breast Cancer

This study aims to demonstrate the effective efficacy of the use of gold nanoparticles to improve radiotherapy. We decided to examine the case of breast cancer.

Patient: woman age: 68 years

Test material: right breast, supero-central quadrant, widening of the areolar side.

Macroscopic description: quadrant subcutaneous mammary cm 5 x 4 x 2.5, presence of land mark in correspondence of which is found area of increased consistency diameter 0.5 cm, distant 0.4 cm from the areolar margin; 0.5 cm from the upper margin cystic-hemorrhagic nodular area diameter 1.5 cm. Enlargement of the areolar margin: two non-oriented fragments of a mammary parenchyma diameter 3 cm. (Figure 6.1).

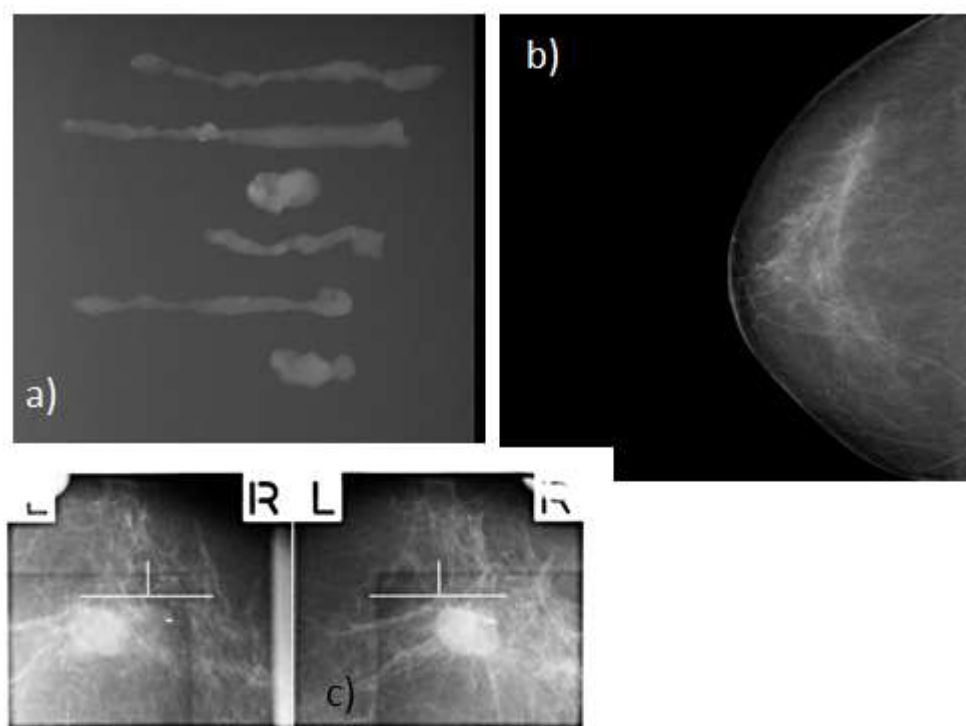


Fig 6.1-a) Microhistological samples using a mammotome system with an needle 8G on a group of microcalcifications (b) Incribed in the right retroareolar site; c) Positioning of metal clips on the biopsied zone.

The following diagnosis is obtained from the histological report of the operating piece: intraductal carcinoma of comedones with multiple microcalcifications. Outbreaks of analogous neoplasia in one of the fragments of the prenext enlargement of the areolar margin. Blood pseudocyst with adjacent small residual outbreak of a blackhead carcinoma. In particular, nuclear receptors for estrogen: 20%, nuclear receptors for progesterone: negative, Ki 67: 5%.

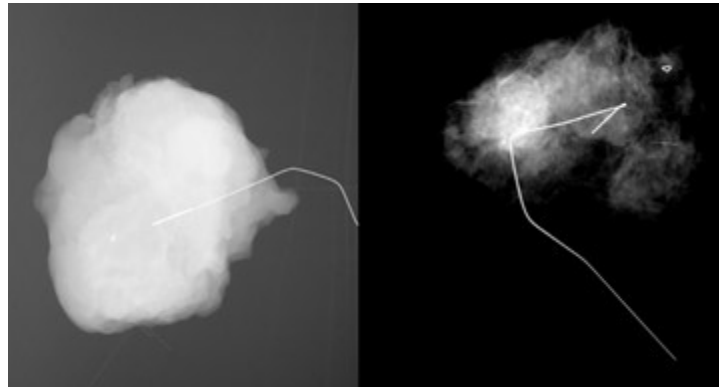


Fig. 6.2- RX operating piece breast.

The patient after surgery is subjected to Radiotherapy:

Technique: static conformational **Energy:** 6 MeV X-photons + 9 MeV electrons

Total dose delivered: 60 Gy of which 50 Gy on right breast and 10 Gy boost tumor bed.

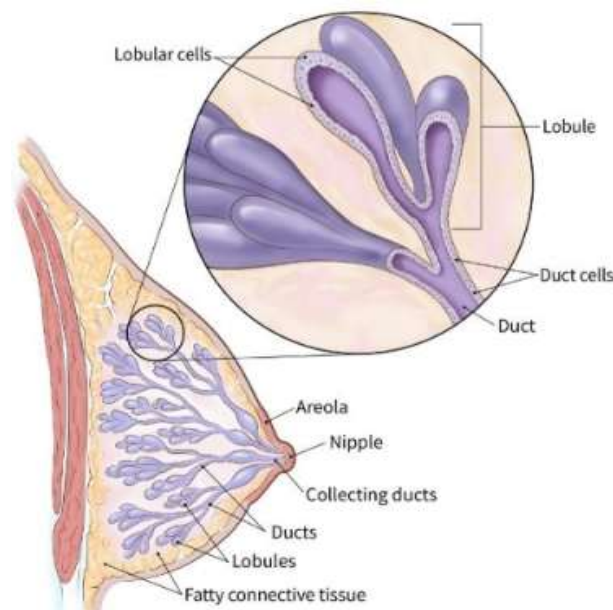


Fig. 6.3- Breast Anatomy

Regular mammograms are the best way to find breast cancer early. Breasts are made up of lobules, ducts, and fatty and fibrous connective tissue. Your breasts will be seen as dense if you have a lot of fibrous or glandular tissue and not much fat in the breasts. On mammograms, dense breast tissue looks white. Breast masses or tumors also look white, so the dense tissue can hide some tumors. In contrast, fatty tissue looks almost black. On a black background it's easier to see a tumor that looks white. The Breast Imaging Reporting and Database Systems, or BI-RADS, which reports the findings of mammograms, also includes an assessment of breast density. BI-RADS classifies breast density into four groups:

- **Mostly fatty:** The breasts are made up of mostly fat and contain little fibrous and glandular tissue. This means the mammogram would likely show anything that was abnormal.
- **Scattered density:** The breasts have quite a bit of fat, but there are a few areas of fibrous and glandular tissue.
- **Consistent density:** The breasts have many areas of fibrous and glandular tissue that are evenly distributed through the breasts. This can make it hard to see small masses in the breast.
- **Extremely dense:** The breasts have a lot of fibrous and glandular tissue.

6.1. Calculation of the Dose Ratio between the surface and the depth at which the tumor is located.

For the therapeutic use of directly or indirectly radiation ionizing, we propose to calculate the ratio R between the dose that is released at the depth of the tumor and the dose released on the surface in the case study in question. As mentioned above, in the presence of a tumor the breast tissue modifies its density which normally is equal to 1.02 g/cm^3 . When microcalcifications occur this density value increases up to about 1.5 g/cm^3 . Only for demonstrative purposes we choose a particular geometry (Fig. 6.4a), which can then be changed for more in-depth analysis with other more or less complex geometries. The chosen geometry considers the tumor localized at 0.5 cm of distance from the areolar margin and thickness 3 cm . In the 3 cm of tumor will be placed the gold nanoparticles that will increase the effectiveness of radiotherapy Fig. 6.4b.

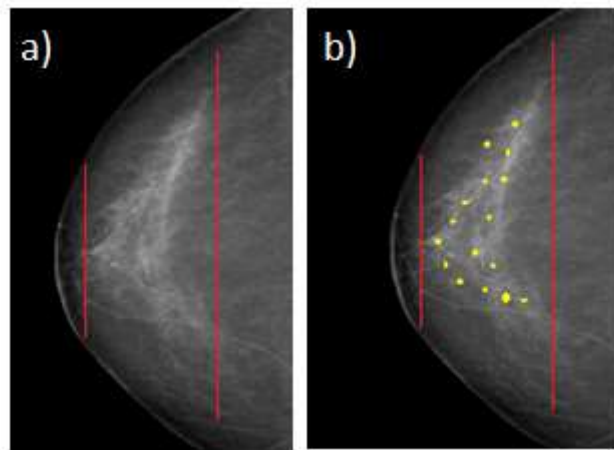


Fig. 6.4- a) Geometry of the tumor in breast tissue. b) geometry of the tumor with Au NPs in breast tissue.

When it comes to a compound (i.e. a material composed of multiple elements), we must consider the actual atomic number Z_{eff} , (sometimes called effective nuclear charge) of an atom that is the number of protons that an electron in the element effectively sees thanks to the screening by electrons in the inner shell. It is a measure of the electrostatic interaction between electrons and protons in the atom.

The atomic number of the material presents a strong and fundamental relationship with the nature of the interactions of radiation within a medium.

An actual atomic number is equivalent to the atomic number but used for compounds (eg water) and mixtures of different materials (such as tissues and bones), depending on the context, can be calculated in different ways. Such methods include a simple weighted mass mean, a power law type method with a certain relationship to the radiation interaction properties or methods involving calculations based on cross-sections of interaction. The latter is the most accurate method [105], and the other more simplified approaches are often inaccurate. The proposed formula for the actual atomic number, Z_{eff} , is:

$$Z_{eff} = \sqrt[2,94]{f_1 \times (Z_1)^{2,94} + f_2 \times (Z_2)^{2,94} + f_3 \times (Z_3)^{2,94} + \dots} \quad (6.1)$$

where f_n is the fraction of the total number of electrons associated with each element, and Z_n is the atomic number of each element.

Three cases are presented separately related to the three different types of used radiation for radiotherapy (protons, electrons and photons).

6.1.1 Protons

The NIST data book [106] is used, referring to the Stopping / Range Tables section for protons, extrapolating the various graphs related to total stopping power, considering an energy of about 65 MeV able to reach up to 3.5 cm; where exactly is the tumor.

The stopping power of ions in a compound can be evaluated using the Bragg rule, i.e. calculating the stopping power in the single elements and weighting them for the content in the compound and for the compound density. This rule is reasonably accurate, and the ion stopping in measured compounds usually differs less than 20%

from that predicted by the Bragg rule. The accuracy of the Bragg rule is limited because the loss of energy of electrons in any material depends on the detailed structure of the orbital and the excitation of the matter, and the differences between the bonds in elementary materials and in compounds brings the Bragg rule to become inaccurate.

$$\varepsilon_{A+B} = \frac{A}{A+B} \varepsilon_A + \frac{B}{A+B} \varepsilon_B \quad (6.2)$$

Where ε_{A+B} is the stopping power of the compound under examination, ε_A is the stopping power of element A of the considered compound and ε_B is the stopping power of element B [107].

In the first 0.5 cm of tissue there is no tumor so we consider the density of the breast tissue, fixed to 1.02 g/cm^3 , as in literature.

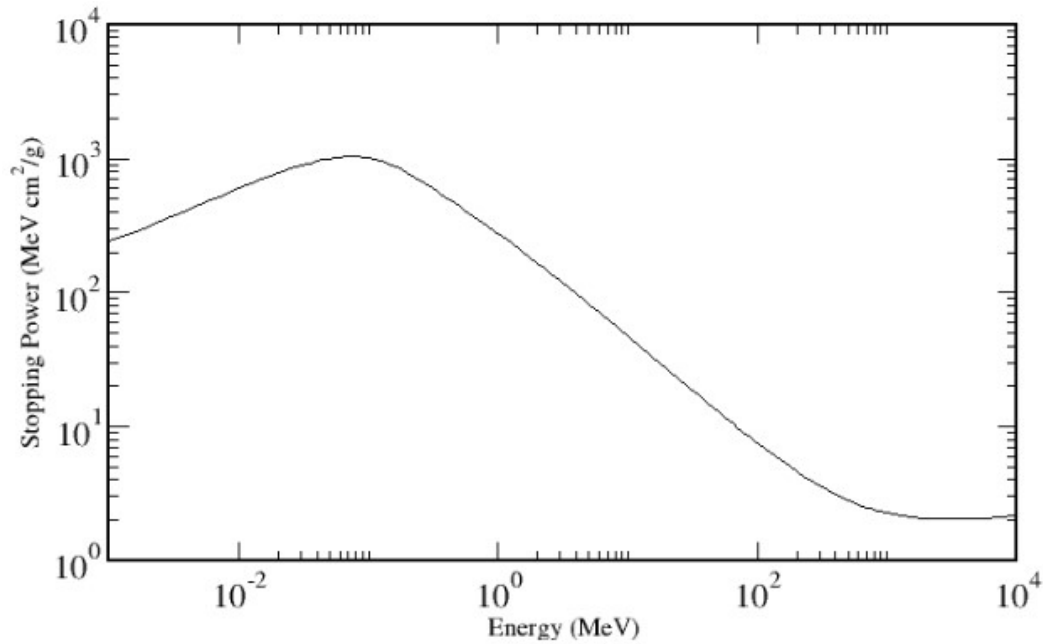


Fig.6.5- Stopping power of Breast Tissue for Protons [108].

The stopping power of protons in the healthy tissue at the depth of 3.5 cm is relative to a proton energy of about 15 keV, at the Bragg peak position, at which it is:

$$S_{dept \text{ breast tissue}} = 605.3 \frac{\text{MeV} \cdot \text{cm}^2}{\text{g}} \cdot 1.02 \frac{\text{g}}{\text{cm}^3} = 617.406 \text{ MeV} \cdot \text{cm}^{-1} \quad (6.3)$$

The stopping power of protons in the tissue at the surface is relative to a proton energy of 65 MeV, at which it is:

$$\begin{aligned} S_{sup\ breast\ tissue} &= 10.42\ MeV \cdot cm^2/g \cdot 1.02\ \frac{g}{cm^3} & (6.4) \\ &= 10.628\ MeV \cdot cm^{-1} \end{aligned}$$

Thus the ratio between the stopping powers in the 3,5 cm depth with respect to the first superficial layers is:

$$R_{tissue} = \frac{S_{depth}}{S_{sup}} = \frac{617.406\ MeV \cdot cm^2/g}{10.628\ MeV \cdot cm^2/g} = 58.09 \quad (6.5)$$

Assuming now that in the first 0.5 cm the tissue is healthy with a density of 1.02 g/cm³ and that in the successive 3 cm depth there is the tumor, as reported in the scheme of Fig. 6.6, we can calculate the relationship of the stopping power in the tumor with respect to the surface if one considers that in the tumor tissue the density is increased due to calcification processes at which the density increases up to 1.5 g/cm³.

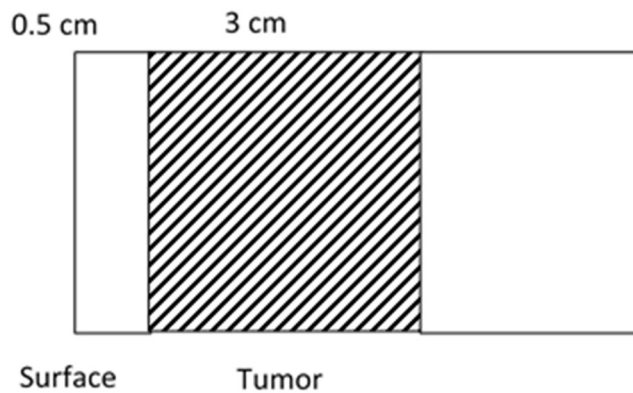


Fig.6.6- Geometry used in the considered case

Thus in this contest we have:

$$S_{depth\ tumor\ tissue} = 605.3 \frac{MeV \cdot cm^2}{g} \cdot 1.5 \frac{g}{cm^3} = 907.95 MeV \cdot cm^{-1} \quad (6.6)$$

Thus with respect to the surface stopping power now the ratio values increases to:

$$R_{tumor\ tissue} = \frac{S_{depth}}{S_{sup}} = \frac{907.95 MeV \cdot cm^{-1}}{10.628 MeV \cdot cm^{-1}} = 85.43 \quad (6.7)$$

Increment in the released energy or dose with respect to the healthy tissue is of about 47%.

If we add the Au Np in the tumor, let's see how the relationship between the stopping power changes. In particular Au nanoparticles (size 1.9 nm) are added up to 2.7 g Au/kg body weight, i.e. at a concentration of 0.27% in weight.

Through NIST database ^[96] we obtain the stopping power values for pure gold. At the Bragg peak, assuming the proton energy to be near 15 keV its value is:

$$S_{depth\ Au} = 47.45 MeV \cdot cm^2 / g$$

Thus, by using the Bragg rule for the addition of the stopping power in the material constituted by 99.73% of cancer tissue with a density of 1.5 g/cm³ and for 0.27% of gold with a density of 19.3 g/cm³, we obtain at the Bragg peak position:

$$\begin{aligned} S_{depth\ breast\ tissue+Au} &= (99.73 \cdot S_{depth\ tissue}) + (0.27 \cdot S_{depth\ Au} \cdot \rho_{Au}) \quad (6.8) \\ &= (99.73 \cdot 907,95) + (0.27 \cdot 47.45 \cdot 19.3) \\ &= 90549.85 + 247.26 = 90797.11 MeV \cdot cm^{-1} \end{aligned}$$

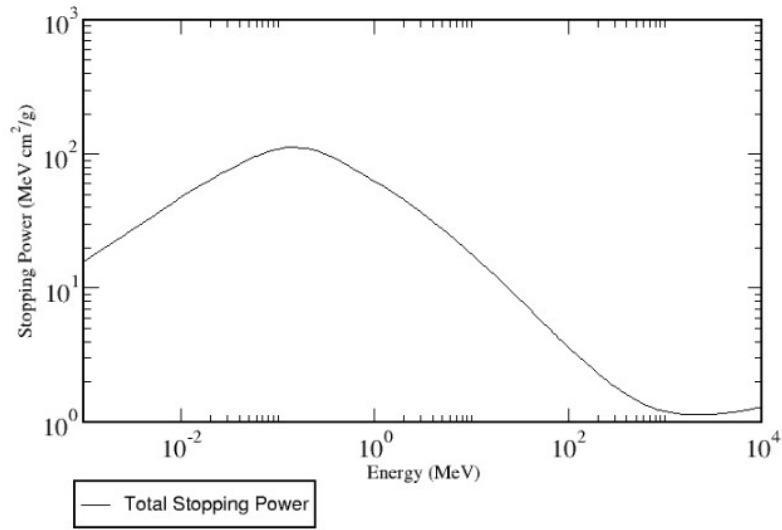


Fig 6.7- Stopping Power of Gold for Protons [109]

Thus, the surface depth stopping power ratio increases to the value:

$$R_{breast\ tissue+Au} = \frac{S_{depth\ breast\ tissue+Au}}{S_{sup} \rho_{tissue}} = \frac{90797.11\ MeV \cdot cm^{-1}}{10.628\ MeV \cdot cm^{-1}} \quad (6.9)$$

$$= 8543.19$$

It is possible to observe such in this case the ratio increased with respect to the case without Au NPs of about a factor 100. This result is very interesting because the deposited dose can be increased of about two orders of magnitude with respect to the case without Au NPs.

6.1.2 Electrons

In the same way, such as for proton beams in radiotherapy, we proceed with the electron beam for an evaluation of the dose increment in radiotherapy in healthy, cancer and tissue with Au NPs tissue.

From the NIST data Base [110], referring to the Stopping / Range Tables section for electrons, we extrapolate the various graphs related to the total stopping power, considering an incident electron beam energy of 9.0 MeV.

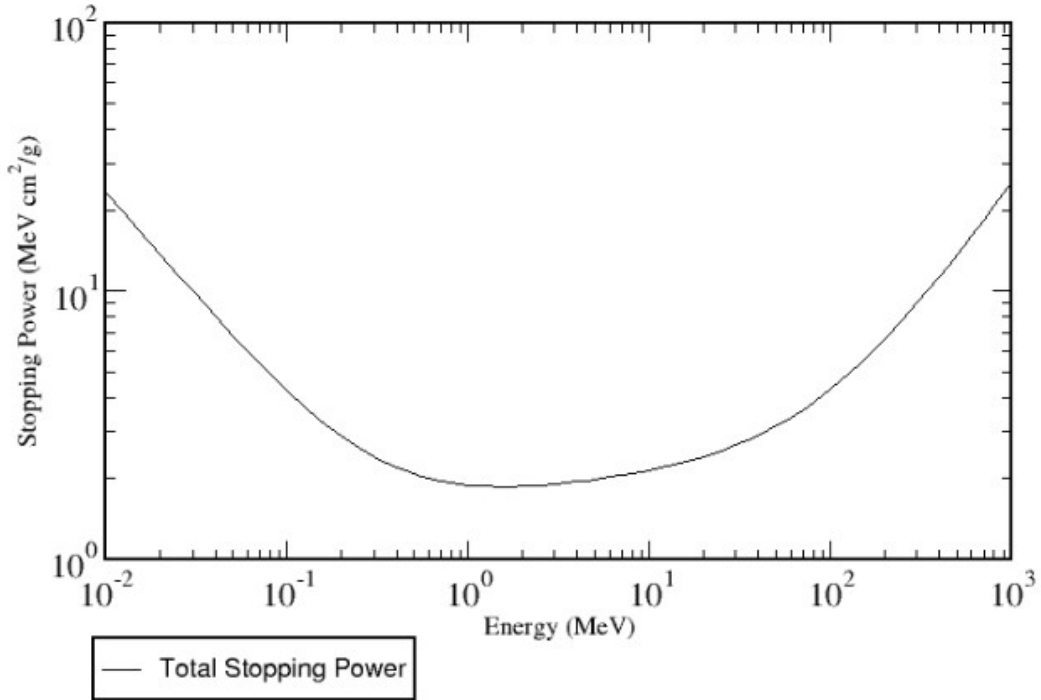


Fig. 6.8- Stopping Power of Breast Tissue for Electrons [111].

At this energy and at the healthy surface tissue the stopping is:

$$S_{sup\ breast\ tissue} = 2.121\ MeV \cdot cm^2/g$$

Using the NIST database and using a tissue density of 1.02 g/cm³, at 3.5 cm depth the electron beam energy decreases up to about 2 MeV.

Thus, at the 3.5 cm tissue depth in the healthy tissue we have:

$$S_{depth\ breast\ tissue} = 1.83\ MeV \cdot cm^2/g$$

With such data the stopping power ratio between the depth and the surface is:

$$R_{breast\ tissue} = \frac{S_{depth}}{S_{sup}} = \frac{1.83}{2.121} = 0.863 \quad (6.10)$$

This means that the released energy in surface is higher with respect to that released in depth, as expected for electron beams.

Assuming now to have a tumor tissue, with a density of 1.5 g/cm^3 , starting at 0.5 cm depth up to 3.5 cm depth, as reported in previous Fig. 6.6, we can calculate the relationship of the stopping power in the tumor with respect to the surface. In this case the electron energy at 0.5 cm depth is 7.92 MeV at which the linear electron stopping power is:

$$\begin{aligned} \frac{\Delta E}{\Delta x} &= S(7.92 \text{ MeV}) \cdot \rho_{\text{tumor tissue}} = 2.06 \text{ MeV} \cdot \frac{\text{cm}^2}{\text{g}} \cdot 1.5 \frac{\text{g}}{\text{cm}^3} & (6.11) \\ &= 3.09 \text{ MeV} \cdot \text{cm}^{-1} \end{aligned}$$

Thus at a 1.5 cm depth the energy decreases to 4.83 MeV. Calculating the new stopping power is $\Delta E/\Delta x = 2.9 \text{ MeV/cm}$. Thus at a 2.5 cm depth the electron energy decreases to 1.93 MeV. Calculating the new stopping power, is $\Delta E/\Delta x = 2.75 \text{ MeV/cm}$. It means that at a 3.2 cm total depth the electron beam energy goes to zero. Calculating the stopping power at a 2.5 cm depth, at which the electron energy is 1.93 MeV, we have:

$$S_{\text{depth tumor tissue}} = 1.83 \text{ MeV} \cdot \text{cm}^2/\text{g}$$

Thus the stopping power ratio between depth and tissue becomes:

$$R_{\text{tumor tissue}} = \frac{S_{\text{depth}}}{S_{\text{sup}}} = \frac{1.83}{2.121} = 0.863 \quad (6.12)$$

It means that the depth/surface dose ratio practically not changes in healthy and cancer tissues and it is little higher in the surface layers which respect to the depth ones.

If we add the Au NPs in the tumor, let's see how the relationship between the stopping power changes. In particular adding Au nanoparticles (size 1,9 nm) up to 2,7 g Au/kg body weight. Through NIST (above reported Fig. 6.8) we obtain the stopping power values for gold calculated at a 2 MeV electron beam energy of:

$$S_{depth Au} = 1.255 \text{ MeV} \cdot \text{cm}^2 / \text{g}$$

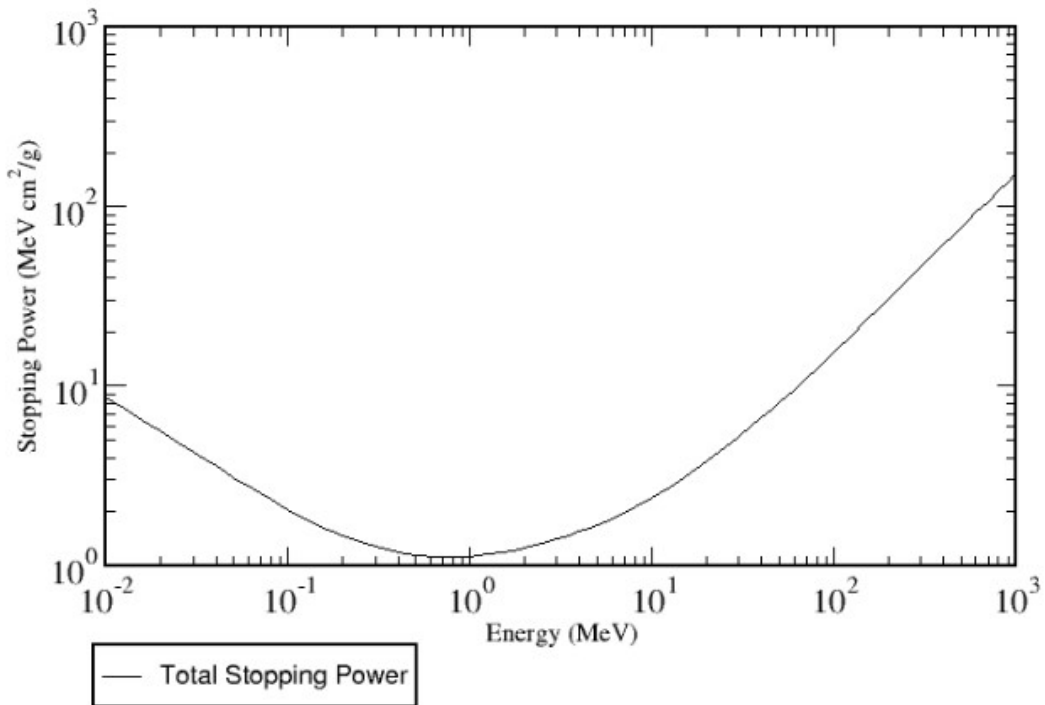


Fig. 6.9- Stopping Power of Gold for Electrons [112].

$$\begin{aligned}
 S_{depth tumor tissue+Au} &= (99.73 \cdot S_{depth tissue}) + (0.27 \cdot S_{prof Au} \cdot \rho_{Au}) \\
 &= (99.73 \cdot 1.83) + (0.27 \cdot 1.255 \cdot 19.3) \\
 &= 190.58 \text{ MeV} \cdot \text{cm}^{-1}
 \end{aligned}
 \tag{6.13}$$

$$R_{tumor\ tissue+AuNp} = \frac{S_{depth}}{S_{sup}} = \frac{190.58}{2.121} = 89.85 \quad (6.14)$$

Also this result is very interesting because it is demonstrating that the electron energy deposition in tumor depth containing high Au NPs concentration is about a factor 86 times higher than in surface, i.e. the dose to the tumor enriched of Au NPs is higher with respect to that given to the healthy surface layers. This result is similar to that obtainable using protontherapy, as reported in the discussion relative to the eq. (6.9). It is due to the increment of the electron density of the disease tissue rich in Au NPs.

6.1.3 Photons

The NIST database [113] is used also in this case as reference of the absorption coefficient for X-rays in radiotherapy. In particular have been used the X-Ray Mass Attenuation Coefficients and Mass Energy-Absorption Coefficients section for X-ray photons.

Assuming to use a high X-Ray energy beam with **6 MeV photons**, by NIST in soft tissues (ICRU-44 components) we find an energy mass absorption coefficient:

$$\left(\frac{\mu_{en}}{\rho}\right)_{tissue} = 1.773 \times 10^{-2} \frac{cm^2}{g}$$

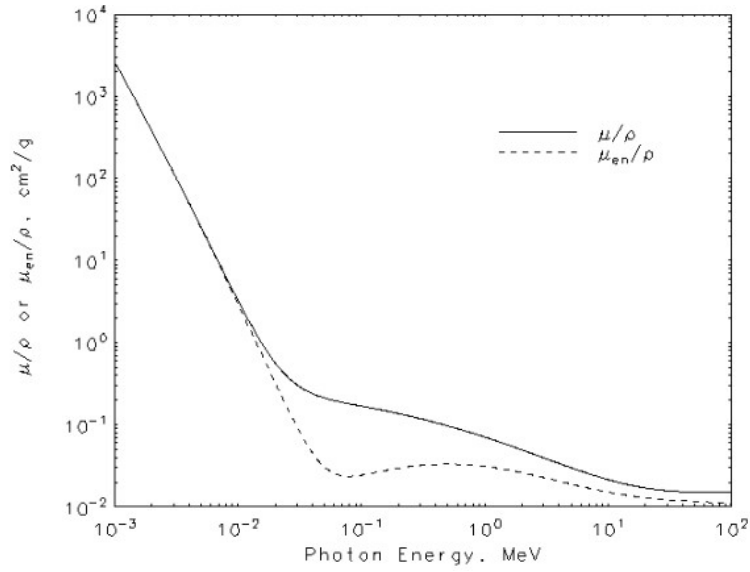


Fig. 6.10- X-Ray Mass Attenuation Coefficients for Breast Tissue [114]

Using the scheme previously reported in Fig. 6.10, we make the following considerations.

Thus, by considering the energy mass absorption coefficients, the transmitted photon intensity I_0 at a depth of 0.5 cm of healthy tissue (1.02 g/cm^3 density) is:

$$I(E) = I_0(E) \cdot e^{-\frac{\mu_{en}}{\rho} \rho \cdot \Delta x} = 6 \cdot e^{-0.01773 \cdot 1.02 \cdot 0.5} = 5.95 \text{ MeV} \quad (6.15)$$

If all the tissue is healthy we will have a transmitted energy and a dept / surface ratio equal to:

$$\begin{aligned} I(E)_{trasmtissue} &= I(E)_0 \cdot e^{-\frac{\mu_{en}}{\rho} \rho \cdot \Delta x} = 5.95 \text{ MeV} \cdot e^{-0.1773 \cdot 1.02 \cdot 3} \\ &= 5.64 \text{ MeV} \end{aligned} \quad (6.16)$$

$$I(E)_{abs} = I(E)_{incidente} - I(E)_{trasm} = 5.95 - 5.64 = 0.314 \text{ MeV} \quad (6.17)$$

the total energy difference is:

$$\Delta E = (6 - 5.95) \text{ MeV} = 0.05 \text{ MeV} \quad (6.18)$$

Dividing for the 6 layers of 0.5 cm each we have in average:

$$\Delta E = \frac{0.314}{6} = 0.052 \text{ MeV} \quad (6.19)$$

Finally we can calculate the energy released in 0.5 cm depth with respect the same depth in surface layers:

$$R_{tissue} = \frac{DE_{dept}}{DE_{surface}} = \frac{0.052}{0.05} = 1.05 \quad (6.20)$$

Thus, the photon intensity hitting the healthy tissue (1.02 g/cm³ density) placed at a 0.5 cm depth and at 3 cm depth practically is similar. The dose in surface, in the healthy tissue, and in depth, practically is the same.

Now we consider the tumor as in the geometry of Fig. 6.6, with a density of 1.5 g/cm³. The photon beam transmitted by the tumor tissue thickness having 1.5 g/cm³ density is:

$$\begin{aligned} I(E)_{trasmtissue} &= I(E)_0 \cdot e^{-\frac{\mu_{en}}{\rho} \cdot \rho \cdot \Delta x} \quad (6.21) \\ &= 5.95 \cdot e^{-0.01773 \cdot 1.5 \cdot 3} = 5.49 \text{ MeV} \end{aligned}$$

Thus the intensity absorbed in the 3 cm tissue (tumor) thickness is:

$$\begin{aligned} I(E)_{abs} &= I(E)_{incidente} - I(E)_{trasm} = 5.95 - 5.49 \quad (6.22) \\ &= 0.49 \text{ MeV} = 490 \text{ keV} \end{aligned}$$

In order to compare the absorbed energy in the surface layers and in the depth it is possible to evaluate the absorbed energy in the first 0.5 cm of healthy tissue $\Delta E_{surface} = 0.05$ and that released to 0.5 cm thickness in the tumor tissue at 3 cm depth, calculated as average energy released in 6 layers of 0.5 cm thickness each, $\Delta E_{depth} = 0.49/6 = 0.082$

$$R_{tissue} = \frac{DE_{dept}}{DE_{surface}} = \frac{0.082}{0.05} = 1.63 \quad (6.23)$$

It means that in this case the released dose in the tumor in this case is 63% higher with respect to that released in the tumor, due only to the difference in density of the tumor with respect to the healthy tissue.

Now, by adding Au nanoparticles (size 1.9 nm) up to 2.7 g Au/kg body weight the absorption coefficient will increase due to the higher effective atomic number of the material. In pure gold at a 6 MeV energy is (see Fig. 6.11):

$$\left(\frac{\mu_{en}}{\rho}\right)_{Au} = 3 \times 10^{-2} \frac{cm^2}{g}$$

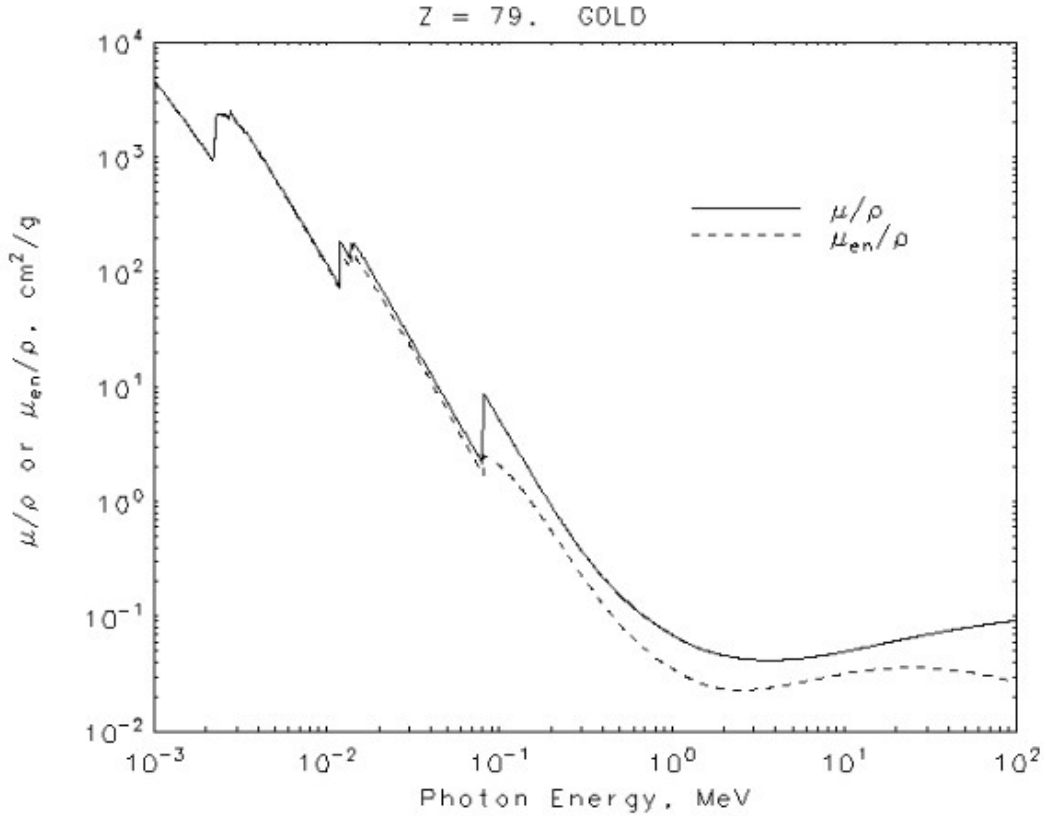


Fig. 6.11- X-Ray Mass Attenuation Coefficients for Gold [115].

$$\begin{aligned} \left(\frac{\mu_{en}}{\rho}\right)_{tissue+Au} &= \left[(9973 \cdot 0.01773) \frac{cm^2}{g} + (0.27 \cdot 0.03) \frac{cm^2}{g} \right] / 100 \quad (6.24) \\ &= 0.0176 \frac{cm^2}{g} \end{aligned}$$

The density of healthy tissue is 1.02 g/cm^3 , that of the calcified cancer tissue about 1.5 g/cm^3 .

The insertion in this cancer tissue of 0.27% Au NPs comports a little increment of the tissue density which can be evaluated from the following relation:

$$\begin{aligned}\rho_{tissue+Au} &= \frac{\left[(99.73 \cdot 1.5) \frac{g}{cm^3} + (0.27 \cdot 19.3) \frac{g}{cm^3} \right]}{100} & (6.25) \\ &= \frac{149.6 + 5.21}{100} = 1.55 \frac{g}{cm^3}\end{aligned}$$

Thus now it is possible to evaluate the photon transmission through 3 cm tumor thickness with this new density:

$$\begin{aligned}I(E)_{transm\ tissue+Au} &= I(E)_0 \cdot e^{-\frac{\mu}{\rho} \rho \cdot \Delta x} & (6.26) \\ &= 5.95 \cdot e^{-0.0176 \cdot 1.55 \cdot 3} = 5.48\ MeV\end{aligned}$$

$$\begin{aligned}I(E)_{abs\ in\ 0.5\ cm} &= I(E)_{incidente} - I(E)_{transm} & (6.27) \\ &= \frac{5.95 - 5.48}{6} = \frac{0.47}{6} = 0.078\ MeV\end{aligned}$$

Thus, in such conditions, the energy loss in the surface with respect to the depth gives again a too low value ratio:

$$R_{tissue} = \frac{0.078}{0.05} = 1.56 \quad (6.28)$$

It means that the tumor is hit with high dose, 56% higher, with respect to the surface layers, but the results are similar to that obtained for the case without Au NPs. It means that the photon energy of 6 MeV is too high to be employed to enhance the dose in the tissue in which AuNPs are injected; Compton and couple effects predominate on the photoelectric effects.

In order to increase the ratio it needs to use a less energetic X-ray beam in manner to maintain high the photoelectric cross-section effect specially in the tumor site where the atomic effective number has been increased thanks to the use of the Au-NPs.

In fact, now we repeat the evaluation considering an X-ray photon beam of **100 keV energy** obtaining the following considerations.

Assuming to use an X-Ray beam with **100 keV photons**, by NIST in soft tissues (ICRU 4 components) we find an energy mass absorption coefficient:

$$\left(\frac{\mu_{en}}{\rho}\right)_{tissue} = 2.443 \times 10^{-2} \frac{cm^2}{g}$$

Thus the transmitted photon intensity I_0 at a depth of 0.5 cm of healthy tissue (1.02 g/cm³ density) is:

$$\begin{aligned} I(E)_{trasmtissue} &= I(E)_0 \cdot e^{-\frac{\mu_{en}}{\rho} \rho \cdot \Delta x} = 100 \text{ keV} \cdot e^{-0.02443 \cdot 1.02 \cdot 0.5} \quad (6.29) \\ &= 98.76 \text{ keV} \end{aligned}$$

If all the tissue is healthy we will have a transmitted energy and a dept / surface ratio equal to:

$$\begin{aligned} I_{trasmtissue} &= I_0 \cdot e^{-\frac{\mu_{en}}{\rho} \rho \cdot \Delta x} = 98.76 \text{ keV} \cdot e^{-0.02443 \cdot 1.02 \cdot 3} \quad (6.30) \\ &= 91.65 \text{ keV} \end{aligned}$$

$$I_{abs} = I_{incidente} - I_{trasm} = 98.76 - 91.65 = 7.11 \text{ keV} \quad (6.31)$$

$$\Delta E_{surface} = (100 - 98.76) \text{ keV} = 1.24 \text{ keV} \quad (6.32)$$

$$\Delta E_{surface} = \frac{7.11 \text{ keV}}{6} = 1.19 \text{ keV} \quad (6.33)$$

$$R_{tissue} = \frac{DE_{dept}}{DE_{surface}} = \frac{1.19}{1.24} = 0.95 \quad (6.34)$$

Thus at this photon energy the released dose in surface and in depth is very similar having a little maximum in surface with respect to the depth.

The intensity hits the tumor tissue (1.5 g/cm³ density) placed at 0.5 cm depth and with 3 cm thickness after which there is healthy tissue. The transmitted photon beam by the tumor tissue thickness having 1.5 g/cm³ density is:

$$\begin{aligned}
I_{trasm\text{tissue}} &= I_0 \cdot e^{-\frac{\mu_{en}}{\rho} \cdot \rho \cdot \Delta x} = 98.76 \text{ keV} \cdot e^{-0.02443 \cdot 1.5 \cdot 3} \\
&= 88.48 \text{ keV}
\end{aligned} \tag{6.35}$$

Thus the absorbed intensity in the 3 cm tissue thickness is:

$$I_{abs}(E) = I_{incid}(E) - I_{trasm}(E) = 98.76 - 88.48 = 10.28 \text{ keV} \tag{6.36}$$

Of course this absorbed energy is very low with respect to that calculated using eq. (6.21).

In order to compare the absorbed energy in the surface layers and in the depth it is possible to evaluate the absorbed energy in the first 0.5 cm of healthy tissue

$$\Delta E_{surface} = (100 - 9.86) = 1.24 \text{ keV} \tag{6.37}$$

and that released to 0.5 cm thickness in the tumor tissue at 3 cm depth

$$\Delta E_{depth} = \frac{10.28 \text{ keV}}{6} = 1.71 \text{ keV} \tag{6.38}$$

$$R_{tissue} = \frac{DE_{dept}}{DE_{surface}} = \frac{1.71}{1.24} = 1.4 \tag{6.39}$$

Those are indicating an increment of dose to the cancer tissue of 40% higher with respect to the surface, due only to the increment of tissue density.

Now, adding Au nanoparticles (size 1.9 nm) up to 2.7 g Au/kg body weight the absorption coefficient will increase due to the higher effective atomic number of the material. In pure gold at a 100 keV energy is:

$$\begin{aligned}
\left(\frac{\mu_{en}}{\rho}\right)_{Au} &= 2.074 \frac{cm^2}{g} \\
\left(\frac{\mu_{en}}{\rho}\right)_{tissue+Au} &= \frac{[(99.73 \cdot 0.02443) \frac{cm^2}{g} + (0.27 \cdot 2.074) \frac{cm^2}{g}]}{100} \\
&= 0.02996 \frac{cm^2}{g}
\end{aligned} \tag{6.40}$$

Thus now it is possible to evaluate the photon transmission through a 3 cm tumor thickness with this new density:

$$I_{transm\ tissue+oro} = I_0 \cdot e^{-\frac{\mu}{\rho} \rho \Delta x} = 98.86\ keV \cdot e^{-0.02996 \cdot 1.55 \cdot 3} \quad (6.41)$$

$$= 86.39\ keV$$

in 0.5 cm healthy tissue

$$I_{abs}(E) = I_{incid}(E) - I_{transm}(E) = (100 - 98.86)\ keV = 1.14\ keV \quad (6.42)$$

in 0.5 cm cancer tissue + AuNPs

$$I_{abs}(E) = I_{incid}(E) - I_{transm}(E) = (98.86 - 86.39)\ keV = 12.47\ keV \quad (6.43)$$

Thus, in such conditions the energy loss in the surface with respect to the depth gives a ratio:

$$R_{tissue} = \frac{12.47}{1.14} = 10.94 \quad (6.44)$$

Thus, also in this case, such as calculated for ions and electrons, the deposited energy in the cancer using Au-NPs is higher for the tumor with respect to the surface healthy tissue. The increment is about a ten factor higher with respect to that released to the more superficial layers of healthy tissue.

However the deposited energy by such photon beams are too low and in order to increase the deposited energy in the tumor site it will be useful or to enhance the exposition time or the photon beam energy.

For this purpose we repeat again the calculations but this time using an intermedium energy between 100 keV and 6 MeV, i.e. using an energy of 1 MeV and 500 keV.

Assuming to use an X-Ray beam with **1 MeV photons**, by NIST in soft tissues (ICRU 4 components) we find an energy mass absorption coefficient:

$$\left(\frac{\mu_{en}}{\rho}\right)_{tissue} = 3.108 \times 10^{-2} \frac{cm^2}{g}$$

Thus the transmitted photon intensity I_0 at a depth of 0.5 cm of healthy tissue (1.02 g/cm³ density) is:

$$I_{trasmtissue} = I_0 \cdot e^{-\frac{\mu_{en}}{\rho} \rho \cdot \Delta x} = 1 \text{ MeV} \cdot e^{-0.03108 \cdot 1.02 \cdot 0.5} \quad (6.45)$$

$$= 984 \text{ keV}$$

If all the tissue is healthy we will have a transmitted energy and a depth / surface ratio equal to:

$$I_{trasmtissue}(E) = I_0(E) \cdot e^{-\frac{\mu_{en}}{\rho} \rho \cdot \Delta x} = 984 \text{ keV} \cdot e^{-0.03108 \cdot 1.02 \cdot 3} \quad (6.46)$$

$$= 894 \text{ keV}$$

$$I_{abs}(E) = I_{incid}(E) - I_{trasm}(E) = 984 - 894 = 89.3 \text{ keV} \quad (6.47)$$

$$\Delta E_{surface} = (1000 - 984) \text{ keV} = 16 \text{ keV} \quad (6.48)$$

$$\Delta E_{depth} = \frac{89.3 \text{ keV}}{6} = 14.8 \text{ keV} \quad (6.49)$$

$$R_{tissue} = \frac{DE_{dept}}{DE_{surface}} = \frac{14.8}{16} = 0.925 \quad (6.50)$$

The transmitted photon beam by the tumor tissue thickness having 1.5 g/cm³ density is:

$$I_{trasmtissue}(E) = I_0(E) \cdot e^{-\frac{\mu_{en}}{\rho} \rho \cdot \Delta x} = 984 \text{ keV} \cdot e^{-0.03108 \cdot 1.5 \cdot 3} \quad (6.51)$$

$$= 855.6 \text{ keV}$$

Thus the absorbed intensity in the 3 cm tissue thickness is:

$$I_{abs}(E) = I_{incidente}(E) - I_{trasm}(E) = 984 - 855,6 \quad (6.52)$$

$$= 128.4 \text{ keV}$$

In order to compare the absorbed energy in the surface layers and in the depth it is possible to evaluate the absorbed energy in the first 0.5 cm of healthy tissue

$$\Delta E_{surface} = (1000 - 984)keV = 16 keV \quad (6.53)$$

and that released to 0.5 cm thickness in the tumor tissue at 3 cm depth

$$\Delta E_{depth} = \frac{128.4 keV}{6} = 21.4 keV \quad (6.54)$$

$$R_{tissue} = \frac{DE_{dept}}{DE_{surface}} = \frac{21.4}{16} = 1.3375 \quad (6.55)$$

Now, adding Au nanoparticles (size 1.9 nm) up to 2.7 g Au/kg body weight the absorption coefficient will increase due to the higher effective atomic number of the material. In pure gold at 1 MeV energy is:

$$\begin{aligned} \left(\frac{\mu en}{\rho}\right)_{Au} &= 3.525 \times 10^{-2} \frac{cm^2}{g} \\ \left(\frac{\mu en}{\rho}\right)_{tissue+Au} &= \frac{[(99.73 \cdot 0.03108) \frac{cm^2}{g} + (0.27 \cdot 0.03525) \frac{cm^2}{g}]}{100} \\ &= 0.03109 \frac{cm^2}{g} \end{aligned} \quad (6.56)$$

Thus now it is possible to evaluate the photon transmission trough 3 cm tumor thickness with this new density:

$$\begin{aligned} I_{trasm\ tissue+Au} &= I_0 \cdot e^{-\frac{\mu}{\rho} \cdot \rho \cdot \Delta x} = 984 keV \cdot e^{-0.03109 \cdot 1.55 \cdot 3} \\ &= 851.5 keV \end{aligned} \quad (6.57)$$

in 0.5 cm healthy tissue

$$I_{abs}(E) = I_{incid}(E) - I_{trasm}(E) = (1000 - 984) keV = 16 keV \quad (6.58)$$

in 0.5 cm cancer tissue + AuNPs

$$I_{abs}(E) = I_{incidente}(E) - I_{trasm}(E) = (984 - 851.5)keV = 132.5keV \quad (6.59)$$

Thus, in such conditions the energy loss in the surface with respect to the depth gives a ratio:

$$R_{tissue} = \frac{132.5}{16} = 8.28 \quad (6.60)$$

Thus we observe that the increment of dose to the tumor with respect to the surface is 8.3 times higher, an interesting result that permits to give high doses to the tumor using 1 MeV photons, optimizing the radiotherapeutic effect.

Finally, assuming to use an X-Ray beam with **500 keV photons**, by NIST in soft tissues (ICRU 4 components) we find an energy mass absorption coefficient:

$$\left(\frac{\mu_{en}}{\rho}\right)_{tissue} = 3.304 \times 10^{-2} \frac{cm^2}{g}$$

Thus the transmitted photon intensity I_0 at a depth of 0.5 cm of healthy tissue (1.02 g/cm³ density) is:

$$\begin{aligned} I_{trasmtissue} &= I_0 \cdot e^{-\frac{\mu_{en}}{\rho} \rho \cdot \Delta x} = 500 \text{ keV} \cdot e^{-0.03304 \cdot 1.02 \cdot 0.5} \quad (6.61) \\ &= 491.65 \text{ keV} \end{aligned}$$

If all the tissue is healthy we will have a transmitted energy and a depth / surface ratio equal to:

$$\begin{aligned} I_{trasmtissue}(E) &= I_0(E) \cdot e^{-\frac{\mu_{en}}{\rho} \rho \cdot \Delta x} = 491.5 \text{ keV} \cdot e^{-0.3304 \cdot 1.02 \cdot 3} \quad (6.62) \\ &= 444.37 \text{ keV} \end{aligned}$$

$$I_{abs}(E) = I_{incid}(E) - I_{trasm}(E) = 491.65 - 444.37 = 47.27 \text{ keV} \quad (6.63)$$

$$\Delta E_{surface} = (500 - 491.65) \text{ keV} = 8.35 \text{ keV} \quad (6.64)$$

and that released to a 0.5 cm thickness in the tumor tissue at a 3 cm depth

$$\Delta E_{depth} = \frac{47.27 \text{ keV}}{6} = 7.87 \text{ keV} \quad (6.65)$$

$$R_{tissue} = \frac{DE_{dept}}{DE_{surface}} = \frac{7.87}{8.35} = 0.94 \quad (6.66)$$

The transmitted photon beam by the tumor tissue thickness having 1.5 g/cm³ density is:

$$\begin{aligned} I_{trasm}(E) &= I_0(E) \cdot e^{-\frac{\mu_{en}}{\rho} \cdot \rho \cdot \Delta x} = 491.65 \text{ keV} \cdot e^{-0.03304 \cdot 1.5 \cdot 3} \quad (6.67) \\ &= 423.73 \text{ keV} \end{aligned}$$

Thus the intensity absorbed in the 3 cm tissue thickness is:

$$\begin{aligned} I_{abs}(E) &= I_{incid}(E) - I_{trasm}(E) = 491.65 - 423.73 \quad (6.68) \\ &= 67.92 \text{ keV} \end{aligned}$$

In order to compare the absorbed energy in the surface layers and in the depth it is possible to evaluate the absorbed energy in the first 0.5 cm of healthy tissue

$$\Delta E_{surface} = (500 - 491.65) \text{ keV} = 8.35 \text{ keV} \quad (6.69)$$

and that released to a 0.5 cm thickness in the tumor tissue at a 3 cm depth

$$\Delta E_{depth} = \frac{67.92 \text{ keV}}{6} = 11.32 \text{ keV} \quad (6.70)$$

$$R_{tissue} = \frac{DE_{dept}}{DE_{surface}} = \frac{11.32}{8.35} = 1.35 \quad (6.71)$$

Now, adding Au nanoparticles (size 1.9 nm) up to 2.7 g Au/kg body weight the absorption coefficient will increase due to the higher effective atomic number of the material. In pure gold at 1 MeV energy is:

$$\left(\frac{\mu_{en}}{\rho} \right)_{Au} = 8,523 \times 10^{-2} \frac{\text{cm}^2}{\text{g}}$$

$$\begin{aligned} \left(\frac{\mu_{en}}{\rho}\right)_{tissue+Au} & \quad (6.72) \\ & = \left[(99.73 \cdot 0.03304) \frac{cm^2}{g} + (0.27 \cdot 0.08523) \frac{cm^2}{g} \right] \\ & /100 = 0.03318 \frac{cm^2}{g} \end{aligned}$$

Thus now it is possible to evaluate the photon transmission through a 3 cm tumor thickness with this new density:

$$\begin{aligned} I_{trasm\ tissue+Au} & = I_0 \cdot e^{-\frac{\mu}{\rho} \rho \cdot \Delta x} = 491.65\ keV \cdot e^{-0.03318 \cdot 1.55 \cdot 3} \quad (6.73) \\ & = 421.36\ keV \end{aligned}$$

in 0.5 cm healthy tissue

$$\begin{aligned} I_{abs}(E) & = I_{incidente}(E) - I_{trasm}(E) = (500 - 491.65)\ keV = \quad (6.74) \\ & = 8.35\ keV \end{aligned}$$

in 0.5 cm cancer tissue + AuNPs

$$\begin{aligned} I_{abs}(E) & = I_{incidente}(E) - I_{trasm}(E) = (491.65 - 421.36)\ keV \quad (6.75) \\ & = 70.29\ keV \end{aligned}$$

Thus, in such conditions the energy loss in the surface with respect to the depth gives a ratio:

$$R_{tissue} = \frac{70.29}{8.35} = 8.42 \quad (6.76)$$

obtaining a similar result to that obtained using 1 MeV photon beam. Thus, compressively, the radiotherapist should use an energy of the photon beam within 500 keV and 1 MeV to optimize the dose release in the tumor with respect to the surface layers and to the layers placed after the tumor site.

A comparison between the calculated values is represented in the following table 6.1:

Table 6.1- Comparison of calculated values obtained through NIST data book for Protons, Electrons and Photons.

Beam	R(d/s) Healthy T.	R(d/s) Tumor/Healthy	R(d/s) Tumor+AuNPs/Healthy
Protons	58.09	85.43	8543.19
Electrons	0.863	0.863	89.85
Photons (100keV)	0.95	1.4	10.94
Photons (6 MeV)	1.2	1.63	1.56
Photons (1 MeV)	0.925	1.3375	8.28
Photons (500 keV)	0.94	1.35	8.42

CONCLUSIONS

The presented thesis work reports preliminary results on the use of metallic NPs for biomedical diagnosis and therapy in mice. In particular five aspects are discussed: (i) the preparation of different metallic nanoparticles by laser ablation in water; (ii) the characterization of their optical, morphological and structural properties by means of various spectroscopic techniques; (iii) absorption calculations in water, soft tissues, and bones with and without the Au or Bi NPs solution of the typical biological diagnostics X-ray radiation energy (20 keV), using the absorption coefficients given by the NIST database; (iv) the improvement of contrast imaging produced by NPs in living mice, which takes place to a fast uptake and a slow decay in the mouse colon, as reported in Figs. 4.6 and 4.7; (v) the calculation of the Dose Ratio between the surface and the depth at which the tumor is located.

Our measurements have demonstrated that the concentration of 10 mg/ml or higher is the best one for the improvement of the images contrast and for enhancing the absorbed dose, being lower concentrations low efficient. In fact the concentration of 1mg/ml is resulted too low to give a detectable image of the veins and of other organs in the mouse, but it is well tolerated by mice that continue to live normally. A higher concentration should be used to give a better diagnostic image, as works in progress prove hopefully.

As reported in the literature, 10 nm Au NPs or smaller can be moved well through the blood and filtered by the kidneys and spleen without problems, flowing through the capillaries without causing thrombi and transported to all the organs depending on the blood supply. They can be transported to the extracellular fluid, bear to the cell membrane and even pass through the membrane, and reach the nucleus of the cell. Moreover, Au NPs generally are non-toxic, biocompatible, and non-irritating when ingested, because they are inert to all chemicals that encounter inside the body (ingested gold cannot be attacked by stomach acid). On the basis of these

informations we have evaluated the 5-20 nm Au NPs uptake and decay times in the colon, from the radiographs analysis obtaining times of the order of 45 minutes and of 2000 minutes respectively. This has permitted us to assert that in case of disease or cancer to the colon apparatus or to the bladder or to the kidneys, the radiotherapy should be applied within these 2000 minutes to release and enhance high ionizing radiation doses only to the diseased colon. For different diseased organs, radiotherapy should be applied within the first 45 min, before the Au NPs are absorbed by the excretion organs.

Further biological investigations necessary for explaining why the metallic NPs are more concentrated in the colon walls instead than in other organs will be performed in future.

Many aspects of the Au NPs production and applications should be further investigated because they are strongly dependent on the properties of the Au NPs solution. Infact, not only water but also other solutions, molecular species, and drugs can be employed to contain nanoparticles, so that they can be injected into an organism and conveyed through specific molecules. The size, shape, and the used solution can strongly modify the final effects of the higher absorbed concentration changing the final imaging and the possible therapy. Of course, the contrast imaging should be investigated in more depth in animals or cell lines before any protocol of application in the human body. In this direction, the work is in progress at the University of Messina in collaboration with other national and international research centers.

Finally, our preliminary studies concerning the dose of ionizing radiations released to the tissues containing the Au NPs can be very useful if the target is a diseased tissue because in this case a significant increment of released dose to the target can be obtained using adapt X-rays or electron or ion beams, greatly improving the results of conventional radiotherapy in the fight against cancer.

Bi-NPs can be used in alternative to Au-NPs on the base of their higher Z atomic number and on the base of the lower mass density to obtain a similar improvement of the contrast imaging resolution and of the radio and thermal therapy efficacy in

cancer tissues. The most difficult aspect of their use is the transport of the NPs up to the tissues and organ interested by the disease without diffusion toward the healthy tissues around the target of interest. For this reason further studies must be conducted using functionalized nanoparticles in collaboration with biologists, pharmacologists, chemists and doctors.

Our measurements of contact angle of physiological liquids with and without use of NPs have demonstrated that the hydrophobic or hydrophilic action can be controlled depending on the nature of the NPs and of the used solid surface. Sub-micrometric polished Cu, Al, PE and Ti substrates show contact angles with physiological liquids higher than 90° : therefore they can be considered as hydrophobic surfaces. However their behavior can be modified inserting metallic NPs at low concentration in the used solutions or depositing NPs as thin layers on their surface. On the contrary, PMMA, Si and glass SiO_2 based surfaces have hydrophilic action, because their contact angle with biological fluid is less than 90° . Also in this case the contact angle can be modified using adapt metallic NPs. In many cases the contact angle can be reduced in all investigated substrates adding metallic NPs to the solution and a further reduction can be obtained if the solid surface contains a layer of nanoparticles. However in some cases, for example using Cu NPs, the contact angle can be increased promoting the hydrophobic action of the surface. In conclusion the use of metallic NPs based on Ti, Cu, Ag and Au in biological liquids, such as water, physiological solution and blood, increases the wetting ability of the solution with many types of solid surfaces. This aspect can be very useful for many practical applications, such as to enhance the anchorage of prosthesis to biological tissues and to interface adhesions.

Finally, our theoretical study of a breast cancer treated with radiotherapy has shown the effectiveness in the use of gold nanoparticles coupled to radiotherapy and proton therapy, calculating in particular the ratio between the released dose at the tumor depth and the released dose on the surface. Furthermore we have observed in the case of protons an increased ratio of about a factor 100 with respect to the case without Au NPs. This result is very interesting because the deposited dose can be increased of about two orders of magnitude with respect to the case without Au

NPs. In the case of electrons, the result is very interesting because it demonstrates that the electron energy deposition in tumor depth containing high Au NPs concentration is about a factor 86 times higher than in surface, i.e. the dose to the tumor enriched of Au NPs is higher than the given one to the healthy surface layers. In the case of photons, the increment of dose to the tumor with respect to the surface is 8.3 times higher, an interesting result that permits to give high doses to the tumor using 1 MeV photons, optimizing the radiotherapeutic effect. With 500 keV photons we have gotten a similar result to that obtained using 1 MeV photon beam. Thus, complessly, the radiotherapist should use an energy of the photon beam between 500 keV and 1 MeV to optimize the dose release in the tumor with respect to the surface layers and to the layers placed after the tumor site.

The future goal is to use a minimal ionizing radiation dose to damage the DNA of the cancer cells without damaging, or making a minimal damage, the healthy cells, improving the spatial resolution confinement of the volume of the tumor site target to be irradiated.

REFERENCES

- [1] Garcia M A, A Tiwari and S Pilla, "Surface Plasmons in biomedicine Recent Developments in Bio-Nanocomposites for Biomedical Applications" (New York: Novascience Publishers) ISBN 978-1-61761-008-0, (2010).
- [2] F. Jay et al. "Gold nanoparticles in radiation research: potential applications for imaging and radiosensitization" *Transl Cancer Res* ;2(4):280-291 (2013).
- [3] L. Torrisi, et al. "Effect of metallic nanoparticles in thin foils for laser ion acceleration" *Phys. Scripta* 9 (2015).
- [4] S.K. Ghosh and T. Pal, "Interparticle Coupling Effect on the Surface Plasmon Resonance of Gold Nanoparticles": From Theory to applications, *Chem. Rev.* 107, 4797–4862 (2007).
- [5] Tzoneva-Velinova R. "The wettability of biomaterials determines the protein adsorption and the cellular responses". PhD Thesis, Institute of Chemistry, Universität Potsdam (Germany, 2003).
- [6] Van Wachem PB, Beugeling T, Feijen J, Bantjes A, Detmers JP, van Aken WG. "Interaction of cultured human endothelial cells with polymeric surfaces of different wettabilities", *Biomaterials*, 6(6):403–8, (1985).
- [7] G. Schmid, "Nanoparticles: From Theory to Applications", Wiley, (2004).
- [8] L. Nicolais and G. Carotenuto, "Metal-polymer nanocomposites", Wiley, Hoboken, (2005).
- [9] L. Nicolais, G. Carotenuto "Nanocomposites: in situ synthesis of polymer-embedded nanostructures", Wiley-Interscience (2013).
- [10] M. A. Garcia "Surface Plasmon in metallic nanoparticles: Fundamental and applications." *Journal of Physics: Applied Physics* 44, 28 (2011).
- [11] Kreibig U and Vollmer M, "Optical Properties of Metal Clusters" (Springer Series in Material Science vol 25) (Berlin: Springer) 1995.
- [12] Fritzsche W and Taton T A, "Nanotechnology" 14 R63 (2003).
- [13] Brongersma M L and Kik P G, "Surface Plasmon Nanophotonics" (Berlin: Springer). (1988).

- [14] Maier S A, “Plasmonics: The Promise of Highly Integrated Optical Devices” Browse Journals & Magazines, Vol. 12 Issue: 6, (2006).
- [15] A. Heilmann, “Polymer Films with Embedded Metal Nanoparticles”, Springer, Berlin Heidelberg New York, (2003).
- [16] Pillai S, Catchpole K R, Trupke T and Green M A, J. Appl. Phys. 101 093105 (2007).
- [17] Atwater H A and Polman A 2010 Nature Mater. 9 205, (2010).
- [18] Matheu P, Lim S H, Derkacs D, McPheeters C and Yu E T, “Metal and dielectric nanoparticle scattering for improved optical absorption in photovoltaic devices”, Appl. Phys. Lett. 93, 113108 (2008)
- [19] Pillai S, Catchpole K R, Trupke T, and Green M A, J. Appl. Phys. 101 093105, (2007).
- [20] Atwater H A and Polman A, Nat. Mat. 9 205, (2010).
- [21] Matheu P, Lim S H, Derkacs D, McPheeters C, and Yu E T, App. Phys. Lett. 93 113108, (2008).
- [22] Homola J, “Surface Plasmon Resonance Based Sensors” (Springer Series on Chemical Sensors and Biosensors) (Heidelberg: Springer), (2006).
- [23] Maier S A, “Plasmonics Fundamentals and Applications” (Berlin: Springer), (2007).
- [24] Raether H, Surface Plasmons on Smooth and Rough Surfaces and on Gratings (Berlin: Springer), (1988).
- [25] Sambles J R, Bradbery G W and Yang F, Contemp. Phys, (1991).
- [26] Mie G Ann. Phys. 25 377 (1908).
- [27] Dynich R A and Ponyavina A. N, J. Appl. Spectrosc. (2008).
- [28] Link S, Burda C, Nikoobakht B and El-Sayed M A, J. Phys. Chem. B 104 6152 (2000).
- [29] Huang W, Qian W and El-Sayed M A, J. Appl. Phys. 98 114301 (1998).
- [30] Chang S S, Shih C W, Chen C D, Lai W C and Wang C R C, Langmuir 15 701 (1999).
- [31] Deepen et. al/ Materials Today: Proceedings 4 3534–3541, (2017).
- [32] Brian Love, Metallic Biomaterials, in Biomaterials, (2017).

- [33] L.G. Griffith, *Polymeric biomaterials*, Acta Materialia, Volume 48, Issue 1, 1 January, Pages 263-277, (2000).
- [34] Alejandro Sáenz, Eric Rivera-Muñoz, Witold Brostow and Victor M. Castaño, CERAMIC BIOMATERIALS: AN INTRODUCTORY OVERVIEW, *Journal of Materials Education* 21(5-6):297-306, (1999).
- [35] Anu Mary Ealias and Saravanakumar M P, A review on the classification, characterisation, Synthesis of nanoparticles and their application, *IOP Conf. Series: Materials Science and Engineering* 263, (2017).
- [36] Yadav, T.P., Yadav, R.M., Singh, D.P.: Mechanical Milling: A Top Down Approach for the Synthesis of Nanomaterials and Nanocomposites. In: *Nanoscience and Nanotechnology* 2 No. 3, p. 22-48, (2012).
- [37] Ozbay E, *Science* 311:189-193 (2006).
- [38] Myungjoon Kim, SahoOsone, Taesung Kim, Hideni Higashi and Takafumi Seto, Synthesis Nanoparticles by Laser Ablation: a review, *KONA Power and Particle Journal* n° 34 (2017).
- [39] J. F. Ziegler, J. P. Biersack, and U. Littmark. *The Stopping and Range of Ions in Matter*. Pergamon, New York, (1985).
- [40] L. Torrasi, M. Cutroneo, G. Ceccio, *Physica Scripta* 90, (9pp) (2005).
- [41] L. Torrasi, *Nuclear Instruments and Methods in Physics Research B* 183 271-278, (2001).
- [42] V. Dudoitis, V. Ulevičius, G. Račiukaitis, N. Špirkauskaitė, and K. Plauškaitė, GENERATION OF METAL NANOPARTICLES BY LASER ABLATION, *Lithuanian Journal of Physics*, Vol. 51. No. 3, pp. 248–259 (2011).
- [43] T.V. Kononenko, V.I. Konov, S.V. Garnov, R. Danielius, A. Piskarskas, G. Tamoshauskas, and F. Dausinger, Comparative state of the ablation of materials by femto second and pico- or nanosecond laser pulses, *Quantum Electron.* 29(8), 724–728 (1999).
- [44] N.B. Dahotre and S.P. Harimkar, in: *Laser Fabrication and Machining of Materials*, Springer Science, pp. 34–65, (2008).
- [45] B.N. Chichkov, C. Momma, S. Nolte, F. von Alvensleben, and A. Tünnermann, Femtosecond, picosecond and nanosecond laser ablation of solids, *Appl. Phys. A* 63(2), 109–115 (1996).

- [46] A. Baladi and R. Sarraf Mamooory, Effect of Laser Wavelength and Ablation Time on Pulsed Laser Ablation Synthesis of Al Nanoparticles in Ethanol, *International Journal of Modern Physics: Conference Series* Vol. 5, 58:6 (2012).
- [47] Jin-Woo Jeon, Sangwoo Yoon, HaeWoon Choi, Joohan Kim, Dave Farsonand Sung-Hak Cho “The Effect of Laser Pulse Widths on Laser Ag Nanoparticle Interaction: Femto- to Nanosecond Laser” *Applied Sciences* (2018).
- [48] HODA MAHDIYAN MOMEN, Effects of particle size and laser wavelength on heating of silver nanoparticles under laser irradiation in liquid, *Pramana – J. Phys.* 87: 26 (2016).
- [49] Daria Riabinina, Jianming Zhang, Mohamed Chaker, Joelle Margot, and Dongling Ma, Size Control of Gold Nanoparticles Synthesized by Laser Ablation in Liquid Media *ISRN Nanotechnology* Volume 2012, Article ID 297863, 5 pages (2012).
- [50] M. Lassithiotaki, A. Athanassiou, D. Anglos, S. Georgiou, C. Fotakis, Photochemical effects in the UV laser ablation of polymers: Implications for laser restoration of painted artworks, *Appl. Phys. A* 69, 363–367 (1999).
- [51] Harihar Nath Verma, Praveen Singh and R. M. Chavan, Gold nanoparticle: synthesis and characterization, *Veterinary World*, EISSN: 2231-0916 (2014).
- [52] Dr. Benjamin Michen, Dr. Sandor Balog, Prof. Barbara Rothen- Rutishauser, Prof. Alke Petri- Fink, Dr. Dimitri Vanhecke. “TEM Sample Preparation of Nanoparticicles in Suspensions”. *Imaging e Microscopy*. Jul. 07, (2014).
- [53] Goldstein, J. I., et al. *Scanning Electron Microscopy and X-ray Micronalysis*, 3rd ed, Plenum Press, New York (2003).
- [54] Russ, J. C. *Fundamentals of Energy Dispersive X-ray Analysis*, Butterworths. London (1984).
- [55] Perkampus, Heinz-Helmut, *UV-VIS Spectroscopy and Its Applications*, Springer Lab Manual, (1992).
- [56] Christopher G. Pope, X-Ray Diffraction and the Bragg Equation, *J. Chem. Educ.*, 74 (1), p 129, (1997).
- [57] R. Singh, S. Sahu, M. Thangaraj, Biosynthesis of Silver Nanoparticles by Marine Invertebrate (Polychaete) and Assessment of Its Efficacy against Human Pathogens, *Journal of Nanoparticles* (2):1-7, (2014).

- [58] Gurvinder Singh Bumbrah Rakesh Mohan Sharma, Raman spectroscopy – Basic principle, instrumentation and selected applications for the characterization of drugs of abuse, *Egyptian Journal of Forensic Sciences* 6, 209–215 (2016).
- [59] Y. Cai, X. Piao, W. Gao et al., Large-scale and facile synthesis of silver nanoparticles: Via a microwave method for a conductive pen, *RSC Advances* 7(54):34041-34048, (2017)
- [60] Scolaro C. Study, physical characterization and wetting ability aspects of biomaterials. PhD Thesis, Doctorate in Physics, University of Messina Publ. (Italy), (2014).
- [61] Thaxton CS, Rosi NL, Mirkin CA: Optically and chemically encoded nanoparticle materials for DNA and protein detection. *MRS Bull* 30(5), 376–380 (2005).
- [62] Glomm WR: Functionalized gold nanoparticles for applications in bionanotechnology. *J. Disp. Sci. Technol.* 26(3), 389–414 (2005).
- [63] Aksay IA, Hoge CE, Pask JA, Wetting under chemical equilibrium and nonequilibrium conditions. *J PhysChem* 78: 1178-1183 (1974).
- [64] A. Lafuma, D. Quere, *Nat. Mater.* 2, 457 (2003).
- [65] J H. Snoeijer, B. Andreotti, *Phys. Fluids* 20, 057101 (2008).
- [66] **L. Torrisi, C. Scolaro, N. Restuccia, “Wetting ability of biological liquids in presence of metallic nanoparticles”, *J Mater Sci: Mater Med* (2017).**
- [67] **L. Torrisi, C. Scolaro and N. Restuccia, Wetting ability of human blood in the presence of gold nanoparticles *Gold Bulletin* (2018).**
- [68] **A. Visco, C. Scolaro, T. Terracciano, Roberto Montanini, A. Quattrocchi, L. Torrisi and N. Restuccia “Static and dynamic characterization of biomedical polyethylene laser welding using biocompatible nano-particles”, *EPJ Web of Conferences* 167, 05009 (2018).**
- [69] S.E. Iyuke, T. A. Mamvura, K. Liu, V. Sibanda, M. Meyyappan, and V.K. Varadan, Process synthesis and optimization for the production of carbon nanostructures, *Nanotechnology* 20, pp. 16–20, (2009).
- [70] J.I. Tapia and M. Quintana, Carbon nanostructures produced by liquid phase exfoliation of graphite in the presence of small organic molecules, *Mesoporous Biomater* 3, pp. 76–82, (2016).

[71] S. Campuzano, M. Pedrero, G. Nikoleli, J. Pingarrón, and D. Nikolelis, Hybrid 2Dnanomaterials-based electrochemical immunosensing strategies for clinical biomarkers determination, *Biosens Bioelectron.* 89 pp. 269–279, (2017).

[72] **L. Torrisi, M. Cutroneo, L. Silipigni, N. Restuccia et al. “Gold nanoparticles produced by laser ablation in water and in graphene oxide suspension”, *Philosophical Magazine*,98: pp. 2205-2220, (2018).**

[73] G. Moon, Y. Park, W. Kim, and W. Choi, Photochemical loading of metal nanoparticles on reduced graphene oxide sheets using phosphotungstate, *Carbon N. Y.* 49, pp. 3454–3462, (2011).

[74] J.R. Kalluri, T. Arbnesi, S.A. Khan, A. Neely et al., Use of gold nanoparticles in a simple colorimetric and ultrasensitive dynamic light scattering assay: Selective Detection of Arsenic in Groundwater, *Angew Chem Int Ed Engl.*;48(51):9668-71 (2009).

[75] A. Zubera, M. Purdeya, E. Schartnera, C. Forbes, B. van der Hoek, D. Giles, A. Abella, T. Monro, and H. Ebendorff-Heidepriem, Detection of gold nanoparticles with different sizes using absorption and fluorescence based method, *Sensor Actuat B.* 227, pp. 117–127, (2016).

[76] G. P. Feltrin - M. Zandonà - V. Borile - C. Rettore - D. Miotto, “Fondamenti sui mezzi di contrasto iodati e reazioni avverse”. *La Radiologia Medica - RadiolMed* 107 (Suppl 1 al N. 4): 8-31, (2004).

[77] Lisa E Cole, Ryan D Ross, Jennifer MR Tilley, Tracy Vargo-Gogola and Ryan K Roeder. “Gold nanoparticles as contrast agents in x-ray imaging and computed tomography”. *Nanomedicine (Lond.)*, 10(2): 321–34, (2015).

[78] L. Torrisi. “Evaluation of the radiotherapy and protontherapy improvements using gold nanoparticles”. *Gold Bulletin*, 50:299–311 (2017).

[79] **L. Torrisi, M. Cutroneo, G. Ceccio, A. Cannavò, N. Restuccia et al., ”Nanoparticles by laser and their applications in Nuclear Physics”, *LNS Report activity 2017.***

[80] **L. Torrisi, N. Restuccia, S. Cuzzocrea, L. Kovacik et al. “Laser-produced Au nanoparticles as X-ray contrast agents for diagnostic imaging”, *Gold Bulletin* 50(1) 51–60 (2017).**

[81] **L. Torrisi, N. Restuccia, I. Paterniti “Gold Nanoparticles by Laser Ablation for X-Ray Imaging and Protontherapy Improvements”, *Recent Pat Nanotechnol.* 14;12(1):59-69, (2018).**

- [82] ICRU, Tissue Substitutes in Radiation Dosimetry and Measurement. Report 44, International Commission on Radiation Units and Measurements, Bethesda, MD, (1989).
- [83] **N. Restuccia, L. Torrasi “Nanoparticles generated by laser in liquids as contrast medium and radiotherapy intensifiers”, The European Physical Journal Conferences (2018).**
- [84] **L. Torrasi, L. Silipigni, N. Restuccia, S. Guglielmino et al., Laser-generated bismuth nanoparticles for applications in imaging and radiotherapy, Journal of Physics and Chemistry of Solids, (2018).**
- [85] S. Veintemillas-Verdaguer, Y. Luengo, C. J. Serna, M. Andrés-Vergés, M. Varela, M. Calero, A. Lazaro-Carrillo, A. Villanueva, A. Sisniega, P. Montesinos, M. P. Morales, Bismuth labeling for the CT assessment of local administration of magnetic nanoparticles. *Nanotechnology* 26 (10pp) (2015).
- [86] F. Xia, X. Xu, X. Li, L. Zhang, L. Zhang, H. Qiu, W. Wang, Y. Liu, J. Gao Preparation of Bismuth Nanoparticles in Aqueous Solution and its Catalytic Performance for the Reduction of 4-Nitrophenol *Ind. Eng. Chem. Res.* 53: 10576–10582 (2014).
- [87] I. Uddin, S. Adhynthaya, A. Syed, K. Selvaraj, A. Ahmad, P. Poddar Structure and Microbial Synthesis of Sub-10 nm Bi₂O₃ Nanocrystals *Journal of Nanoscience and Nanotechnology* 8:1–5, (2008).
- [88] S. Nambiar, E.K. Osei, J.T.W. Yeow, Bismuth Sulfide Nanoflowers for Detection of X-rays in the Mammographic Energy Range, *Scientific Reports* 5 9440, (2015).
- [89] A. Slikkerveer and F.A. de Wolff, Pharmacokinetics and Toxicity of Bismuth compounds *Med. Toxicol. Adverse Drug Exp.* 4(5) 303-323 (1989).
- [90] K. Trentelman, A note on the characterization of bismuth black by Raman microspectroscopy. *J. Raman Spectrosc.* 40 585–589 (2009).
- [91] L. I. Vera-Robles, L. Escobar-Alarcon, M. Picquart, J.L. Hernandez-Pozos, E. Haro-Poniatowski, A Biological Approach for the Synthesis of Bismuth Nanoparticles: Using Thiolated M13 Phage as Scaffold, *Langmuir* 32:3199–3206, (2016).
- [92] L. Kumari, J.H. Lin, Y.R. Ma, Laser oxidation and wide-band photoluminescence of thermal evaporated bismuth thin films, *J. Phys. D: Appl. Phys.* 41 (7pp) (2008)

- [93] José Carlos De La Vega and Urs O. Häfeli, “Utilization of nanoparticles as X-ray contrast agents for diagnostic imaging applications”, *Review Contrast media and molecular imaging* (2014).
- [94] Ugo Amaldi and Gerhard Kraft, “Radiotherapy with beams of carbon ions”, *Reports on Progress in Physics*, Volume 68, Number 8, IOP Publishing Ltd (2005).
- [95] Adrie J.J. Bos, “Fundamentals of Radiation Dosimetry”, Conference: CONCEPTS AND TRENDS IN MEDICAL RADIATION DOSIMETRY, DOI: 10.1063/1.3576156 (2011).
- [96] Tapley N, ed. “Clinical applications of the electron beam”. New York: John Wiley & Sons, (1976).
- [97] Frederik Vernimmen Sandra Sinske, *Arteriovenous Malformations: “A comprehensive guide to Natural History, Diagnosis, and Management”*. Chapter: Heavy charged particle beam radiosurgery for arteriovenous malformations of the brain Publisher: Nova publishers Editors: D Ding (2015).
- [98] E.B. Podgorsak, *Radiation Oncology Physics: A Handbook for Teachers and Students*, Technical Editor (2005).
- [99] James F. Hainfeld, F. Avraham Dilmanian, Daniel N. Slatkin and Henry M. Smilowit, “Radiotherapy enhancement with gold nanoparticles”, *Journal of Pharmacy and Pharmacology* (2008).
- [100] James F Hainfeld, Daniel N Slatkin and Henry M Smilowitz. “The use of gold nanoparticles to enhance radiotherapy in mice”. *Phys. Med. Biol.*, 49: 309–315, (2004).
- [102] Sheeta IJha, Pramod Kumar Sharma Rishabha Malviya, *Hyperthermia: Role and Risk Factor for Cancer Treatment* Sheetal Jha *, Pramod Kumar Sharma, Rishabha Malviya, “Hyperthermia: Role and Risk Factor for Cancer Treatment”, *Achievements in the Life Sciences* 10 (2016).
- [103] Varshini Karthik and T. Rama Rao, “Estimation of Specific Absorption Rate Using Infrared Thermography for the Biocompatibility of Wearable Wireless Devices”, *Progress In Electromagnetics Research M*, Vol. 56, 101–109, (2017).
- [104] A. Cervadoro, C. Giverso, R. Pande, “Design Maps for the Hyperthermic Treatment of Tumors with Superparamagnetic Nanoparticles”, *PLoS ONE* 8(2):57332 (2013).
- [105] M. L. Taylor et al, "Robust calculation of effective atomic numbers: The Auto-Zeff software", *Medical Physics* 39 1769-1778 (2012).

- [106] <https://physics.nist.gov/PhysRefData/Star/Text/PSTAR.html>
- [107] L. Torrasi “Gold Nanoparticles Enhancing Protontherapy Efficiency” Recent Patents on Nanotechnology, 9, 1-10, (2015).
- [108] https://physics.nist.gov/cgi-bin/Star/ap_table.pl
- [109] https://physics.nist.gov/cgi-bin/Star/ap_table.pl
- [110] <https://physics.nist.gov/PhysRefData/Star/Text/ESTAR.html>
- [111] https://physics.nist.gov/cgi-bin/Star/e_table.pl.
- [112] https://physics.nist.gov/cgi-bin/Star/e_table.pl
- [113] <https://www.nist.gov/pml/x-ray-mass-attenuation-coefficients>
- [114] <https://physics.nist.gov/PhysRefData/XrayMassCoef/ComTab/adipose.html>
- [115] <https://physics.nist.gov/PhysRefData/XrayMassCoef/ElemTab/z79.html>
- [116] Boisselier E, Astruc D, “Gold nanoparticles in nanomedicine: preparations, imaging, diagnostics, therapies and toxicity”. Chem Soc Rev 38:1759–1782 (2009).

Acknowledgments

I would like to thank Professor Lorenzo Torrisi, my tutor in the present research work and already my thesis supervisor. My thanks go to a person who has always been available and present and who made the realization of this work possible, believing in me and mine capacity.

I thank Prof. Sara Ronca for her great availability and the great scientific support provided to my thesis.

I thank Prof. Anna Mackova for the precious scientific help and for the priceless suggestions.

I thank Prof. Lilly Silipigni for the precious and always timely advice that they have me allowed to carry out this work with completeness and precision.

I thank Dr. Maria Cutroneo for scientific and friendly support, always present.

I thank the group of the U.O.C Health Physics of the Policlinico G. Martino of Messina and in particular the Dr. Ielo that has accompanied me, with its cordiality and professionalism during the initial phases of the research activity.

I thank the Department of Clinical and Experimental Medicine of the University of Messina, in particular Dr. Paterniti and Dr. Cordaro for supporting me in my research with their knowledge and experimental skills.

I thank Prof. Annamaria Visco for our collaboration during my second year of my Doctorate.

I also want to thank my colleagues and friends, Ph.D. Cristina Scolaro, Giovanni Ceccio, Giuseppe Costa and Antonino Cannaò, whose company has made this experience more pleasant.

A special thanks goes to my family, for their support unconditional during this long period of work. They knew how to give me courage, strength and help for my work.

Nancy Restuccia

Messina, Settembre 2018.